Systems Biology Perspectives on Calcium Signaling and DNA Repair

DISSERTATION
zur Erlangung des akademischen Grades
doctor rerum naturalium
(Dr. rer. nat.)
im Fach Biophysik

eingereicht an der
Mathematisch-Naturwissenschaftlichen Fakultät I
Humboldt-Universität zu Berlin

von

Diplom–Biophysiker Antonio Politi

geboren am 29.10.1975 in Florenz

Präsident der Humboldt-Universität zu Berlin:
Prof. Dr. Christoph Markschies

Dekan der Mathematisch-Naturwissenschaftlichen Fakultät I:
Prof. Dr. Christian Limberg

Gutachter:

1. Prof. Thomas Höfer, PhD
2. Prof. Dr. Hanspeter Herzel
3. Prof. Dr. Hermann-Georg Holzhütter

eingereicht am: 6. November 2006

Tag der mündlichen Prüfung: 26. März 2007

Abstract

This work deals with two paradigms of cellular signaling: a change in the intracellular Ca^{2+} concentration represents often one of the first steps in the transduction of incoming stimuli; the ability to properly respond to external injuries and repair damaged DNA is an essential component for life. The approaches used to investigate Ca^{2+} signaling and DNA repair bear common points. Mathematical models are used to asses system properties, such as efficiency in the signal processing, specificity of the response, and design principles behind the different pathways. A close collaboration with experimentalist made it possible to directly compare model predictions and experimental data, and to test different mechanistic hypothesis.

The first part of this thesis focuses on the phosphoinositide-dependent Ca^{2+} signaling. Hormones that act through the Ca^{2+} releasing messenger, inositol 1,4,5-trisphosphate (IP_3), cause intracellular Ca^{2+} oscillations, which have been ascribed to Ca^{2+} feedbacks on the IP_3 receptor. Recent studies have shown that IP_3 levels oscillate together with the cytoplasmic Ca^{2+} concentration. To investigate the functional significance of this phenomenon, mathematical models of the interaction of both second messengers have been developed. The models account for both positive and negative feedbacks of Ca^{2+} on the phosphoinositide metabolism, mediated by Ca^{2+} activation of phospholipase C and IP_3 3-kinase, respectively. The theoretical analysis shows that each of these Ca^{2+} feedbacks substantially expands the range of oscillation frequencies of a core oscillator based on Ca^{2+} and IP_3R dynamics, compared to Ca^{2+} fluctuations obtained with clamped IP_3 (Chapter 2). The action of the feedbacks depends on the turnover rate of IP_3. To shape the oscillations, positive feedback requires fast IP_3 turnover, whereas negative feedback requires slow IP_3 turnover. This suggests to perturb the IP_3 turnover in order to study the feedbacks present (Chapter 3): Whereas increasing the IP_3 turnover by overexpressing IP_3 metabolizing enzymes gives no information on the underlying feedbacks, slowing the IP_3 dynamics with an IP_3 binding protein can reveal positive feedback. This theory has been tested in chinese hamster ovary cells by transiently expressing an IP_3 binding protein. The overexpression of this fusion protein exerted a dose-dependent suppression of agonist-induced Ca^{2+} oscillations that is consistent with an oscillator model including positive feedback of Ca^{2+} on IP_3 generation. This prominent role of the IP_3 dynamics in modulating Ca^{2+} oscillations demanded a more deeper analysis of the fate of the IP_3 precursor, phosphatidylinositol-4,5-bisphosphate (PIP_2).

To this end, a detailed model for the phosphoinositide pathway based on measured metabolite concentrations has been developed (Chapter 4). The model illustrates the importance of futile (de)phosphorylation cycles for regenerating PIP_2 during stimulation, an essential property to support long-lasting Ca^{2+} signals. Alternatively, when futile cycling is weak, the presence of positive feedback of Ca^{2+} on the IP_3 production also allows to regenerate the PIP_2 pool. Taken together, the experimental data and theoretical analysis presented in this thesis indicate that IP_3 oscillations are an essential component of the Ca^{2+} oscillator, they are physiologically important for supporting the efficient frequency encoding of hormone dose and the long-lasting Ca^{2+} signals observed in many cell types.

The second part of the thesis is devoted to nucleotide excision repair (NER). It is a versatile DNA repair mechanism that can remove different type of lesions, such as UV light induced pyrimidine dimers and bulky adducts caused by chemical agents. It requires the concerted action of many different proteins that assemble at sites of damaged DNA. Despite our detailed biochemical knowledge about NER, many questions concerning its dynamic behavior remain unanswered, in particular, it is controversial whether repair factors are assembled sequentially or in a random way at the site of damage, or whether they exist as a holocomplex. Therefore, to understand the mechanisms underlying the protein assembly and the performance of repair, a mathematical model, delineating hallmarks and general characteristics of NER, has been developed. First, the binding and dissociation kinetics of repair factors are related to the structural properties of the system, such as the sequential order in which the factors enter repair (Chapter 7). Second, using *in vivo* kinetic data for the recruitment of three different protein factors at local damaged nuclei, the model parameters are determined and the dynamic behavior of the repair process is scrutinized in detail. The observed saturation of NER is predicted to rely on the high engagement of the recognition factor in repair. Furthermore, the model predicts a quiescent phase, where the amounts of factors involved in repair remains high and constant for a long time period, a forecast that has been validated experimentally. The theoretical analysis of repair performance indicates that a sequential assembly process is remarkably advantageous in terms of repair efficiency and can show a marked selectivity for the damaged substrate (Chapter 8). Alternative mechanisms for repairosome formation, including random assembly and preassembly, can readily become kinetically unfavorable. Based on the model, new experiments are proposed to gain further insight into the early and late steps of this complex process and to critically test model predictions (Chapter 10). Taken together, this thesis provides a kinetic framework for NER and rationalizes why many processes within the nucleus show a sequential assembly strategy.

Zusammenfassung

Diese Arbeit behandelt, anhand von zwei Beispielen, wie Zellen auf äußere Reize antworten: Eine Änderung der Ca^{2+}-Konzentration wird häufig beobachtet, wenn Zellen stimuliert werden; die Fähigkeit die DNS zu reparieren, wenn sie beschädigt wurde, ist eine essentielle Komponente für die fehlerfreie Weitergabe der genetischen Information. Die Vorgehensweisen, um die Eigenschaften und Mechanismen der Calciumsignale und der DNS-Reparatur zu erforschen, haben einige Parallelen. Es wurden mathematische Modelle entwickelt, um die Effizienz in der Verarbeitung der Signale, die Spezifität der Antworten und die Designprinzipien der verschiedenen Wege zu erforschen. Die enge Kooperation mit experimentellen Arbeitsgruppen erlaubte den direkten Vergleich zwischen Modellvorhersagen und Daten. Außerdem war das Testen von verschiedenen Hypothesen möglich.

Der erste Teil dieser Doktorarbeit konzentriert sich auf Calciumsignale, die von Phosphoinositiden abhängen. Hormone, die über den calciumfreisetzenden Botenstoff Inositol 1,4,5-trisphosphat (IP_3) wirken, induzieren intrazelluläre Calciumoszillationen. Diese Oszillationen werden zurückgeführt auf die Wirkung von Ca^{2+} auf den IP_3-Rezeptor. Jüngste Studien zeigten, dass die IP_3-Konzentration zusammen mit der Ca^{2+}-Konzentration oszilliert. Um die funktionelle Bedeutung dieses Phänomens zu untersuchen, wurden mathematische Modelle aufgestellt, die die Interaktion zwischen diesen Botenstoffen einbeziehen. Die Modelle beinhalten sowohl die positive als auch die negative Rückkopplung von Calcium auf den Metabolismus der Phosphoinositiden. Diese beiden Rückkopplungen werden durch Ca^{2+}-Aktivierung von PLC bzw. IP_3 3-Kinase bewirkt. Die theoretischen Untersuchungen zeigen, dass jede dieser Rückkopplungen die Reichweite der Oszillationsfrequenzen eines Oszillators, der auf den Interaktionen von Ca^{2+} und IP_3-Rezeptoren basiert, stark vergrößert (Kapitel 2). Die Wirkungsweise der beiden Rückkopplungsmechanismen hängt sehr stark von der Geschwindigkeit der IP_3-Dynamik ab. Die positive Rückkopplung benötigt, um die Ca^{2+}-Oszillationen zu prägen, eine schnelle IP_3-Dynamik, wohingegen die negative Rückkopplung eine langsame IP_3-Dynamik benötigt. Diese Ergebnisse deuten darauf hin, dass mit Hilfe einer Störung der IP_3-Dynamik die Art der Rückkopplung bestimmt werden kann (Kapitel 3). Zwei Strategien wurden simuliert: die Beschleunigung der IP_3-Dynamik mit IP_3-abbauenden Enzymen bzw. die Verlangsamung mit IP_3-bindenden Molekülen. Nur die zweite Strategie ergab Hinweise über die Anwesenheit und Wirkung einer positiven Rückkopplung. Diese Vorhersage wurde in Eizellen von Chinesischen Hamstern getestet, die ein IP_3-bindendes

Protein exprimieren. Die Überexpression dieses Konstrukts kann agonistinduzierte Calciumoszillationen stoppen. Diese Wirkung ist im Einklang mit einem Oszillatormodell, das positive Rückkopplung von Ca^{2+} auf die IP_3-Produktion beinhaltet. Um die Rolle der IP_3-Oszillationen weiter zu verstehen, wurde ein Modell für den Metabolismus des IP_3-Vorläufers Phosphatidylinositol-4,5-bisphosphat entwickelt (Kapitel 4). Das Modell, das auf gemessenen Metabolitenkonzentrationen basiert, wurde dazu benutzt um die Eigenschaften dieses Weges zu untersuchen. Es zeigt sich, dass die angeblich nutzlosen Phosphorylierungs/Dephosphorylierungszyklen eine wichtige Rolle für den PIP_2-Haushalt spielen. Sie ermöglichen, durch das Nachliefern von PIP_2 während der Stimulation, anhaltende Calciumsignale. Interessanterweise kann eine positive Rückkopplung von Ca^{2+} auf die IP_3-Produktion ebenfalls dazu beitragen das Reservoir von PIP_2 zu regenerieren. Somit zeigen die theoretischen und experimentellen Analysen dieser Arbeit, dass IP_3-Oszillationen eine essentielle Komponente für den Ca^{2+}-Oszillator sind. Sie spielen eine wichtige physiologische Rolle für die effiziente Frequenzkodierung des Hormonsstimulus und die Aufrechterhaltung der Calciumsignale.

Der zweite Teil meiner Arbeit beschäftigt sich mit einem wichtigen DNS-Reparaturweg, die Reparatur mittels Entfernung von Nukleotiden (NER). Dieser Reparaturmechanismus ist sehr vielseitig und entfernt Pyrimidinpaare, die durch UV-Strahlung erzeugt wurden, oder Schäden, die durch chemischen Agenten erzeugt wurden. NER benötigt eine große Anzahl von Proteinen, die an der beschädigten DNS rekrutiert werden. Heutzutage sind eine Fülle von biochemischen Details bekannt, trotzdem bleiben mehrere Fragen hinsichtlich des dynamischen Verhaltens unklar. Insbesondere ist die Art und Weise wie Faktoren an der DNS rekrutiert werden umstritten. Es wurden sowohl sequentielle als auch zufällige Mechanismen vorgeschlagen, und weiterhin Preassemblierung als einen Holokomplex diskutiert. Um diese Frage zu klären, wurde ein Modell, das die Grundeigenschaften von NER beschreiben soll, entwickelt. Erstens wurde untersucht, wie die Kinetik der Bindung und der Freisetzung der Reparaturfaktoren mit den strukturellen Eigenschaften des Systems, wie zum Beispiel die Bindungsreihenfolge, zusammenhängen (Kapitel 7). Zweitens sind die Modellparameter anhand von *in vivo* gemessenen Rekrutierungskinetiken von drei Proteinfaktoren bestimmt worden. Diese Kinetiken wurden in Zellkernen gemessen, die einen Lokalschaden erlitten haben. Das so gefittete Modell sagt unter anderem eine Sättigung von NER durch den Verbrauch des Erkennungsfaktors vorher. Außerdem wurde eine lang andauernde Phase, in der die Menge der involvierten Faktoren hoch bleibt, prognostiziert. Die zweite Vorhersage wurde experimentell bestätigt. Die theoretischen Untersuchungen deuten daraufhin, dass ein sequentieller Assemblierungsmechanismus bezüglich Effizienz und Spezifität gegenüber den beschädigten Substrat sehr vorteilhaft sein kann (Kapitel 8). Alternative Mechanismen für die Bildung des Repairosoms, wie z.B. zufällige Bindung oder Preassemblierung, können schnell kinetisch unvorteilhaft werden. Anhand des Modells wurden neue Experimente vorgeschlagen, um die ersten und letzten Schritte des Reparaturpozesses besser zu verstehen und Modellvorhersagen kritisch zu testen (Kapitel 10). Diese Arbeit hilft die kinetischen Randbedingungen für NER zu verstehen und macht ersichtlich, warum viele Prozesse, die im Zellkern stattfinden, eine sequentielle Strategie verfolgen.

Contents

Part I

Dynamics of Calcium and IP$_3$: Feedbacks, Oscillations, and Futile Cycling

Chapter 1

Introduction to the phosphoinositide and calcium signaling

One of the essential cellular functions is the ability to sense the external environment and respond appropriately to incoming informations. To perform these tasks, the cellular plasma membrane is equipped with a palette of different protein receptors. A signaling cascade can be initiated by the binding of ligand to these receptors and, eventually, the desired response, such as changes in the metabolic activity, expression of specific genes, and secretion of signaling molecules, is obtained.

Over the years many molecular players in the signaling cascades have been identified and the emerging picture is a very dynamic one. It turns out that the information resides both in the timing of the signals as well as in the downstream targets of the receptors. To finely control the time course of the target proteins a series of self-regulatory mechanisms, such as activatory and inhibitory feedbacks, have evolved. Mathematical modeling has proved a useful tool for the quantitative understanding of the dynamics of signaling cascades. It allowed, among other things, to test specific mechanistic hypothesis and experimental protocols, and rationalize why certain pathway features can be (dis)advantageous for the signaling efficiency.

In this part of my thesis, I concentrate on the phosphoinositide-dependent Ca^{2+} signaling, a pathway which is of central importance because many cellular processes are controlled by Ca^{2+} ions and phosphoinositide derivates. In the mid of the eighties, the discovery that the cytoplasmic Ca^{2+} concentration changes periodically [195], was an additional indication that, together with at that time already known glycolytic and cAMP oscillations [47, 126], biochemical rhythms are a frequent phenomena in life. Since then, oscillations in several signaling pathways have been found (e.g. circadian rhythms, p53 oscillations, mitotic oscillations) and to understand their molecular basis both experimental as well as theoretical approaches have been used (see e.g. [19, 48, 88, 90]).

Below, I will briefly summerize some of the known experimental facts in the phosphoinositide-dependent Ca^{2+} signaling and point towards the still controversial questions after 20 years of research.

1.1 Signal transduction via phosphoinositides and calcium

After binding of ligand to the plasma membrane receptor, and activation of their proximate effector (e.g. the G_α subunit of trimeric G-proteins), the next steps in the signaling cascade often involve enzymes which generate lipid-derived second messengers. This relays the information arriving at the plasma membrane into the inner of the cell.

Phosphoinositides are undoubtedly one the most prominent source for lipid-derived second messengers, they comprise a family of eight species, which differ in their combination of phosphate groups at the inositol ring. Among these phosphatidylinositol-4,5-bisphosphate (PIP_2) represents a focal point in phosphoinositide-dependent signaling [31, 188]. PIP_2 itself is involved in the regulation of the actin cytoskeleton and membrane trafficking [77, 105]. Its phosphorylation by phosphatidylinositol 3-kinase generates phosphatidylinositol-3,4,5-trisphosphate (PIP_3), a lipid which is responsible for the recruitment and eventually activation of a variety of PH-domain containing proteins at the inner surface of the cell membrane. These proteins have been found to be involved in cytoskeleton remodeling, mitogenesis, cell growth, and survival [176, 178]. The hydrolysis of PIP_2 by phospholipase C (PLC) produces two important second messengers inositol 1,4,5-trisphosphate (IP_3) and diacylglycerol (DAG). The former is a potent activator of intracellular Ca^{2+} channels, the IP_3-receptors, the latter activates protein kinase C (PKC). A quick look through any physiology book show that both Ca^{2+} and PKC are involved in several cellular processes such as secretion of neurotransmitters, activation of transcription factors, and energy metabolism. Ca^{2+} can bind directly to proteins and so regulate their activity, or act via the protein calmodulin. Calmodulin is found as part of larger proteins or freely diffusing and changes its conformation upon Ca^{2+} binding.

The intracellular Ca^{2+} concentration is tightly regulated by a combination of Ca^{2+} channels and pumps. In a resting cell, the Ca^{2+}-ATPases in the ER and plasma membrane keep the Ca^{2+} concentration in the cytoplasm low ($\sim$ 100 nM), compared to the concentration in the ER ($\sim$ 20 μM) and the Ca^{2+} concentration outside the cell ($\sim$ 1 mM). Binding of agonist to its receptor at the the plasma membrane activates PLC, which produces IP_3. This messenger in turn activates the IP_3-receptor Ca^{2+} channels (IP_3R) located in the ER membrane and causes their opening and an outflow of Ca^{2+} into the cytoplasm. The increase in cytoplasmic Ca^{2+} concentration ($[Ca^{2+}]_c$) further activates the IP_3R, a phenomenon called calcium induced calcium release (CICR). This leads to an explosive rise of $[Ca^{2+}]_c$ to values up to $\sim$ 1 μM.

In a multitude of cell types, one does not observe a simple increase of $[Ca^{2+}]_c$ to a new steady state but a sequence of Ca^{2+} spikes, or Ca^{2+} oscillations. The strength of the extracellular stimulus is encoded primarily in the frequency of the Ca^{2+} oscillations, which increases with the degree of stimulation. For example, in rat hepatocytes, the periods of Ca^{2+} oscillations range over one order of magnitude, from above 250 s for low concentrations of hormones, such as vasopressin and noradrenalin, to about 30 s for higher hormone doses [138]. Ca^{2+} signals usually originate from a specific site in the cell and propagate through the cell as intracellular Ca^{2+} waves [9, 86, 139]. The signals can also propagate between neighboring cells, these intercellular Ca^{2+} waves have been observed in several cell preparations, which maintain a certain functional integrity. The propagation can rely on the secretion of extracellular messengers/hormones as well as on the diffusion of messengers via gap junctions (see e.g. [118, 121, 122, 137, 172, 202]).

1.2 Mechanisms underlying Ca^{2+}/IP_3oscillations

A long-standing question has been whether the oscillations are generated by the cellular Ca^{2+} transporters and channels themselves or whether they originate upstream in the signal transduction machinery, between hormone binding to its receptor and the activation of Ca^{2+} fluxes. It has been proposed that the periodic release of Ca^{2+} ions from the endoplasmic reticulum (ER) can be brought about through the regulatory properties of the IP_3 receptor (IP_3R), the main type of ER calcium release channel in non-excitable cells [10, 51, 101, 203]. Mathematical models have demonstrated how fast activation and delayed inhibition of the IP_3R by cytoplasmic Ca^{2+} can drive repetitive Ca^{2+} spiking [36, 80, 144]. In these models, IP_3 is required to initially open the IP_3R and sensitize the channel toward feedback activation by cytoplasmic calcium. Therefore, Ca^{2+} oscillations can occur when IP_3 concentration is held at a constant value. However, models based on a simple description of the IP_3R dynamics generally produce $[Ca^{2+}]_c$ oscillations with short periods ($\sim$ 10-60 sec) and, thus do not reproduce the long inter-spike intervals observed experimentally. Long-period oscillations have been obtained when additional mechanisms, such as the regulation of IP_3R by phosphorylation, stochastic gating phenomena or slow calcium buffer, are included [41, 102, 153].

Recently, it has become possible to monitor IP_3 changes in intact cells. These experiments have shown that, for some of the agonists used, the IP_3 concentration is highly dynamic and can oscillate together with cytoplasmic calcium [61, 112, 171, 201]. This raises the intriguing possibility that a coupled IP_3-Ca^{2+} oscillator may generate long-period oscillations and underlie the efficient frequency-encoding of the hormone dose.

The existence of both positive and negative feedbacks of Ca^{2+} on IP_3 metabolism could mediate fluctuations in cellular IP_3 levels. The production of IP_3 is catalyzed by a diverse family of phosphoinositide-specific PLC isoforms [135]. All PLC isoforms are activated by Ca^{2+} ions, although their sensitivities to $[Ca^{2+}]$ vary greatly [55, 134]. This feedback can have an important role in Ca^{2+} wave propagation [33, 65, 177, 181]. IP_3 is removed by either phosphorylation or dephosphorylation through IP_3 3-kinase ($IP_3$3K) or IP_3 5-phosphatase ($IP_3$5P), respectively. IP_3 removal by $IP_3$3K is activated by Ca^{2+} [22, 111, 194]. Moreover, it has also been suggested that protein kinase C (PKC), which is activated by receptor-mediated increases in Ca^{2+} and diacylglycerol, may inhibit IP_3 production by inactivating agonist receptors [25, 112].

1.3 Research objectives

It is presently not clear, which of the above described Ca^{2+} feedbacks on the IP_3 metabolism influences the Ca^{2+} dynamics, and what effects they will have on the Ca^{2+} oscillations and on the phosphoinositide metabolism as a whole.

Previous mathematical models have shown that IP_3-mediated Ca^{2+} release coupled to Ca^{2+}-activated PLC can generate oscillations, without any requirement of IP_3R regulation by Ca^{2+} [25, 104]. These models have been criticized because in some cell types Ca^{2+} oscillations can also be elicited when the $[IP_3]$ is clamped or its non-metabolizable analogs are used [51, 100, 185]. The incorporation of Ca^{2+}-activation of PLC into a Ca^{2+} oscillator model based on the above-described IP_3R properties has been reported to modulate Ca^{2+} oscillations [28], while the inclusion of $IP_3$3K has been found to have practically no effect [34, 38]. The complete absence, in all these models, of the reactions leading to the IP_3 precursor PIP_2 does not allow to fully appreciate the implications of

Ca^{2+} feedbacks on the phosphoinositide metabolism. The few models that have been developed for this pathway [106, 140, 197] omit some of the essential reactions and metabolites. Thus the dynamic view of the whole phosphoinositide metabolism is only partial.

In the present work, I have carried out a systematic modeling study of the interaction between cellular Ca^{2+} transports and phosphoinositide metabolism. In a first model I include the dynamics of IP_3, Ca^{2+}, and IP_3R and take into account positive and negative feedback of Ca^{2+} on the IP_3 metabolism. These are mediated by Ca^{2+} activation of IP_3 generation through PLC and Ca^{2+} activation of IP_3 removal by IP_33K, respectively. To better understand the role of oscillations in the phosphoinositide metabolism, I developed, based on the measured metabolite concentrations, a detailed model for this pathway and coupled it to the Ca^{2+} dynamics. With these models following questions have been addressed:

(*i*) Do the Ca^{2+}-dependent feedback mechanisms on the phosphoinositide metabolism serve a physiological role?

(*ii*) Which requirements have to be met by the Ca^{2+} and the phosphoinositide pathway for these feedbacks to be effective?

(*iii*) Is there a way to distinguish, experimentally, between the different feedbacks?

(*iv*) Which are the design principles of the phosphoinositide pathway and how does it respond to activation of PLC and periodic modulation of the Ca^{2+} concentration?

I begin by analyzing the role of Ca^{2+} feedbacks on the phosphoinositide metabolism in modulating the properties of a core oscillator based on Ca^{2+} and IP_3R dynamics, in particular, under which conditions these feedbacks can modify the frequency encoding of the hormone signal. The model analysis indicated which are the critical parameters that could be modified experimentally in order to identify the type of feedbacks present (Chapter 2). I, therefore, simulated two experimental protocols: The overexpression of IP_3 metabolizing enzymes and the expression of IP_3 binding proteins. The predictions of the latter experiment were compared to experiments in a mammalian cell line (Chapter 3). In the last chapter, I studied the phosphoinositide metabolism in detail and investigated, which reactions control the PIP_2 pool during stimulation, and how the whole metabolism is influenced by Ca^{2+} feedbacks (Chapter 4).

This theoretical work has been done in close collaboration with the group of Prof. A.-P. Thomas and Prof. L.D. Gaspers (University of Medicine and Dentistry of New Jersey, Newark, USA), which provided the experimental data presented here.

Chapter 2

Ca^{2+} feedbacks on IP_3 improve frequency encoding of the stimulus

2.1 Materials and methods

2.1.1 Mathematical model

The model accounts for the formation and degradation of IP_3, the main Ca^{2+} fluxes across the ER and plasma membrane, and the $\mathrm{IP}_3\mathrm{R}$ dynamics (see Fig. 2.1). It is formulated in terms of four variables: the IP_3 and Ca^{2+} concentration in the cytoplasm, p and c, respectively; the calcium concentration in the ER stores, s; and the fraction of $\mathrm{IP}_3\mathrm{R}$ that have not been inactivated by Ca^{2+}, r.

IP_3 dynamics: IP_3 is produced by PLC, whose activity depends on agonist dose and Ca^{2+}. The Ca^{2+} sensitivity of PLC can be modeled by [11]

$$v_{PLC} = V_{PLC}\frac{c^2}{K_{PLC}^2 + c^2}. \tag{2.1}$$

The maximal rate V_{PLC} depends on the agonist concentration, whereas K_{PLC} characterizes the sensitivity of PLC to Ca^{2+}. IP_3 is removed through dephosphorylation by IP_3 5-phosphatase ($\mathrm{IP}_3$5P) and phosphorylation by IP_3 3-kinase ($\mathrm{IP}_3$3K) which is modeled as

$$v_{deg} = v_{5P} + v_{3K} = \left(k_{5P} + k_{3K}\frac{c^2}{K_{3K}^2 + c^2}\right)p, \tag{2.2}$$

where k_{5P} and k_{3K} are the IP_3 dephosphorylation and phosphorylation rate constants, respectively. The Ca^{2+} dependence of the $\mathrm{IP}_3$3K is described by a Hill function with the

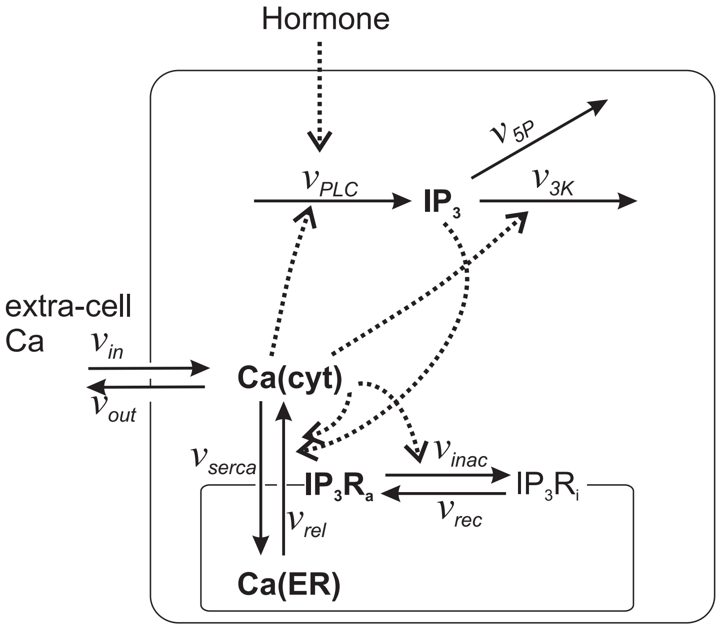

Figure 2.1: Interactions between Ca^{2+} transport processes and IP_3 metabolism included in the model. The solid and dashed arrows indicate transport/reaction steps and activations, respectively. The bold quantities indicate the model variables: IP_3, cytoplasmic IP_3; Ca(cyt), free cytoplasmic Ca^{2+}; Ca(ER), free Ca^{2+} in the ER; IP_3R_a, active conformation of the IP_3R. The other abbreviations denote: IP_3R_i, inactive conformation of the IP_3R; v_{rel}, rate of Ca^{2+} release through the IP_3R; v_{serca}, active Ca^{2+} transport into the ER; v_{inac} and v_{rec} rate of Ca^{2+} induced IP_3R inactivation and recovery rate, respectively; v_{PLC}, production rate of IP_3; v_{5P} and v_{3K} rates of IP_3 dephosphorylation and phosphorylation, respectively; v_{in} and v_{out}, rates of Ca^{2+} influx and extrusion across the plasma membrane, respectively.

half-saturation constant K_{3K} [22]. According to Fink et al. [43] and Sims and Allbritton [150] one can assume that the two enzymes are not saturated with IP_3, justifying the linear rate law.

For the purpose of the subsequent analysis, we write the balance equation for the IP_3 concentration in the following form

$$\begin{aligned}\frac{dp}{dt} &= v_{PLC} - v_{deg} \\ &= \frac{1}{\tau_p}\left[\overline{V}_{PLC}\frac{c^2}{K_{PLC}^2 + c^2} - \left(\eta\frac{c^2}{K_{3K}^2 + c^2} + (1-\eta)\right)p\right], \end{aligned} \tag{2.3}$$

where I introduce the characteristic time of IP_3 turnover

$$\tau_p = 1/(k_{3K} + k_{5P}), \tag{2.4}$$

and the ratio of the maximal IP$_3$3K rate to the total maximal degradation rate of IP$_3$

$$\eta = k_{3K}/(k_{3K} + k_{5P}). \tag{2.5}$$

The strength of the positive feedback will be tuned by changing K_{PLC} (the Ca^{2+} sensitivity of PLC), and the strength of the negative feedback will be tuned by changing η (the relative expression level of IP$_3$3K). Although both feedbacks can be present simultaneously, it is useful to first analyze them separately. Therefore, I define the "positive-feedback model" in which PLC is sensitive to Ca^{2+} ($K_{PLC} > 0$) and IP$_3$3K is not expressed ($\eta = 0$), and the "negative-feedback model" in which IP$_3$3K is present ($\eta > 0$) and PLC is assumed insensitive to physiological Ca^{2+} changes ($K_{PLC} = 0$). Note that the rescaled maximal PLC activity $\overline{V}_{PLC} = V_{PLC}\tau_p$ equals the steady-state concentration of IP$_3$ that would be attained in the absence of positive and negative feedbacks.

IP$_3$R and Ca^{2+} dynamics: Ca^{2+} release flux through the IP$_3$R is modeled according to Li and Rinzel [91]

$$v_{rel} = \left(k_1 \left(r \frac{c}{K_a + c} \frac{p}{K_p + p}\right)^3 + k_2\right)(s - c). \tag{2.6}$$

The model by Li and Rinzel is a simplification of the De Young and Keizer model which considered eight different states for each IP$_3$R subunit [28]. The cubic term represents the open probability of the IP$_3$R, which is assumed to open when 3 or 4 subunits of the tetrameric IP$_3$R are in the gating state. The gating state is attained when IP$_3$ and Ca^{2+} bind to their respective activating binding sites, which accounts for the sensitization by IP$_3$ and calcium induced calcium release (CICR), and the inactivating binding site is devoid of Ca^{2+}. Whereas the first two events are assumed to be fast, allowing for a quasi-steady state approximation, the inhibition occurs on a slower time scale. The fraction of IP$_3$Rs that have not yet been inactivated by Ca^{2+} follows

$$\frac{dr}{dt} = v_{rec} - v_{inac} = \frac{1}{\tau_r}\left(1 - r\frac{K_i + c}{K_i}\right) \tag{2.7}$$

where $\tau_r = 1/k_{rec}$ gives the characteristic time of receptor recovery after inactivation.

The rate equation for active transport of Ca^{2+} across the ER membrane by the sarco endoplasmic reticulum Ca^{2+}-ATPase (SERCA) follows Lytton et al. [97]

$$v_{serca} = V_{serca}\frac{c^2}{K_{serca}^2 + c^2}.$$

The rate equation for the active transport of Ca^{2+} by the plasma membrane Ca^{2+}-ATPase (PMCA) follows Camello et al. [15]

$$v_{out} = \varepsilon V_{pm} \frac{c^2}{K_{pm}^2 + c^2}.$$

The calcium influx includes a leak into the cell and a stimulation dependent influx which is assumed proportional to the maximal PLC activity

$$v_{in} = \varepsilon(v_0 + \phi \overline{V}_{PLC}).$$

The dimensionless parameter ε measures the relative strength of the plasma membrane fluxes, which is known to be cell-type specific. With these rate expressions the balance equation for cytoplasmic Ca^{2+} reads

$$\begin{aligned} \frac{dc}{dt} &= v_{rel} - v_{serca} + v_{in} - v_{out} \\ &= \left(k_1 \left(r \frac{c}{K_a + c} \frac{p}{K_p + p}\right)^3 + k_2\right)(s - c) - V_{serca} \frac{c^2}{K_{serca}^2 + c^2} \\ &\quad + \varepsilon \left(v_0 + \phi \overline{V}_{PLC} - V_{pm} \frac{c^2}{K_{pm}^2 + c^2}\right). \end{aligned} \tag{2.8}$$

I first carry out the model analysis for the simpler case that the plasma membrane fluxes are negligible. By setting $\varepsilon = 0$ the total Ca^{2+} concentration in the cell is conserved and can be expressed as $c_{tot} = c + \beta s$, where β is the ratio of effective cytoplasmic volume to effective ER volume (both accounting for Ca^{2+} buffering). Therefore, I can insert for the ER calcium in Eq. (2.8) $s = (c_{tot} - c)/\beta$. In the presence of plasma-membrane fluxes ($\varepsilon > 0$) this conservation no longer holds and a kinetic equation for s must be added:

$$\frac{ds}{dt} = \frac{1}{\beta}\left[V_{serca} \frac{c^2}{K_{serca}^2 + c^2} - \left(k_1 \left(r \frac{c}{K_a + c} \frac{p}{K_p + p}\right)^3 + k_2\right)(s - c)\right]. \tag{2.9}$$

The meaning and numerical values of the kinetic parameters are given in Tab. 2.1. The half-activation constant of PLC and $IP_3$3K were taken from [11] and [22], respectively. The IP_3 degradation rate constants were chosen in accordance to [43, 150]. In the positive-feedback model (Ca^{2+} activation of PLC), the parameters for the Ca^{2+} transport processes and the IP_3R were taken from [91]. In the negative-feedback model (Ca^{2+} activation of $IP_3$3K), no substantial effect of the $IP_3$3K on the oscillations is obtained with these parameters. However, for different parameters (as given) the $IP_3$3K effects

	Reference parameter values	
	Positive feedback	Negative feedback
IP_3 dynamics parameters:		
Half-activation constant of $IP_3$3K, K_{3K}	0.4 μM	0.4 μM
IP_3 phosphorylation rate constant, k_{3K}	0	0.1/s
IP_3 dephosphorylation rate constant, k_{5P}	0.66/s	0
Half-activation constant of PLC, K_{PLC}	0.2 μM	0
Ca^{2+} transport and structural parameters:		
Ratio of effective volumes ER/cytosol, β	0.185	0.185
Maximal SERCA pump rate, V_{serca}	0.9 μM/s	0.25 μM/s
Half-activation constant, K_{serca}	0.1 μM	0.1 μM
Maximal PMCA pump rate, V_{pm}	0.01 μM/s	0.01 μM/s
Half-activation constant, K_{pm}	0.12 μM	0.12 μM
Constant influx, v_0	0.0004 μM/s	0.0004 μM/s
Stimulation-dependent influx, ϕ	0.0047/s	0.045/s
Strength of plasma membrane fluxes, ε	0	0
Total Ca^{2+} concentration (for $\varepsilon = 0$), c_{tot}	2 μM	2 μM
IP_3R parameters:		
Maximal rate of Ca^{2+} release, k_1	1.11/s	7.4/s
Ca^{2+} leak, k_2	0.0203/s	0.00148/s
Ca^{2+} binding to activating site, K_a	0.08 μM	0.2 μM
Ca^{2+} binding to inhibiting site, K_i	0.4 μM	0.3 μM
IP_3 binding, K_p	0.13 μM	0.13 μM
Characteristic time of IP_3R inactivation, τ_r	12.5 s	6.6 s

Table 2.1: The table gives the reference parameter set. Changes are indicated in the respective figure legends. The maximal rate of PLC, V_{PLC}, is taken as the stimulation-dependent control parameter.

were pronounced. The differences in the Ca^{2+} fluxes between the two models can be accounted for by variations in the expression of the involved proteins. The differences in the Ca^{2+} binding properties to the activating site of the IP_3R can be due to differences in the expression of IP_3R subtypes, with IP_3R subtype 1 having a higher Ca^{2+} dissociation constant for the activating site than subtypes 2 and 3 [99, 129]. Numerical solutions of the differential equations system Eqs. (2.3), (2.7)–(2.9) were obtained using a 4th order Runge-Kutta algorithm implemented in XPPAUT (http://www.math.pitt.edu /bard/xpp/xpp.html). Bifurcation analysis were done using the program AUTO2000 [29]. Calcium waves with the local kinetics given by Eqs. (2.3), and (2.7)–(2.9) and diffusion of Ca^{2+} and IP_3 in the cytoplasm were calculated numerically with a finite-difference Crank-Nicholson scheme (see Appendix F). Wavespeeds for solitary waves were evaluated using AUTO2000.

2.1.2 Experimental procedures

Cell culture: Chinese Hamster Ovary cells (CHO) were cultured in Ham's F-12 media supplemented with 10% fetal bovine serum (FBS) and antibiotics. Cells were seeded onto poly-D-lysine coated glass coverslips (25 mm) and maintained in culture until 70-80% confluent prior to experimental protocols.

Plasmid construction and transfection protocols: The cDNA encoding 620 amino acids of the N-terminal rat type 1 IP_3 receptor [13] was ligated in-frame to the C-terminus of the enhanced green fluorescent protein gene in the plasmid pEGFP-C1 (Clontech, Palo Alto CA, USA) to generate the plasmid pEGFP-LBD. Cell cultures were transiently transfected with either pEGFP-LBD (EGFP-LBD) or pEGFP-C1 (EGFP) using Lipofectamine 2000 (Invitrogen, Carlsbad, CA, USA) according to the manufacturer's protocols. Agonist-evoked $[Ca^{2+}]_c$ responses were recorded in transfected cultures following a 16-48 hour incubation period.

Imaging measurements of $[Ca^{2+}]_c$ and fluorescent proteins: Calcium imaging experiments were performed in an HEPES-buffered physiological saline solution (HBSS) comprised of (in mM): 25 HEPES (pH 7.4 at 37 °C), 121 NaCl, 5 $NaHCO_3$, 4.7 KCl, 1.2 KH_2PO_4, 1.2 $MgSO_4$, 2.0 $CaCl_2$, 10 glucose, 0.1 sulphobromophthalein and 0.25% (w/v) fatty acid-free BSA. Cell cultures were loaded with fura-2/AM by incubation with 5 μM fura-2/AM plus Pluronic F-127 (0.02% v/v) for 20–40 min in HBSS. The cells were washed and transferred to a thermostatically regulated microscope chamber (37

°C). Fura-2 fluorescence images (excitation, 340 and 380 nm, emission 420-600 nm) were acquired at 3-4 s intervals with a cooled charge-coupled device (CCD) camera as previously described [51]. Fura-2 fluorescence intensities were corrected for GFP spillover prior to calculating fluorescence ratio values, by quenching cytosolic fura-2 with $MnCl_2$. Cells expressing recombinant proteins were selected by screening for GFP fluorescence (excitation 488 nm, emission 525 nm). EGFP-LBD concentration was estimated from a standard curve constructed with known concentrations of 6 His-tagged EGFP (Clontech, Palo Alto CA, USA; molecular weight 27 kDa). Calibration solutions were prepared by diluting the recombinant protein in PBS. An aliquot (5 μl) was mixed with low-density mineral oil then sandwiched between two glass coverslips. EGFP containing "bubbles" ranging in size from 10 to 50 μm (the approximate range of cell diameters observed in CHO cultures) were imaged with a Nikon 20x, 0.75 NA Plan Apo objective on a wide-field microscope. The fluorophore protein concentration was converted into molar value assuming a molecular weight of 27 kDa for His-tagged EGFP.

2.2 Frequency encoding and period control

2.2.1 Positive- and negative-feedback models exhibit frequency encoding of agonist dose

In many cell types, one observes a strong dependence of the frequency of Ca^{2+} oscillations on the dose of the applied receptor agonist, while the oscillation amplitude remains nearly constant [138]. A stepwise increase of the agonist concentration is accompanied by a prompt rise of the oscillation frequency. In the model, the maximal rate of PLC, V_{PLC}, is a measure of agonist concentration. The positive-feedback model, with Ca^{2+} activation of PLC, and the negative-feedback model, with Ca^{2+} activation of $IP_3$3K, were subjected to stepwise increases in V_{PLC}. The responses are shown in Fig. 2.2A, B, respectively, with the time points of increase indicated by arrowheads. Both models exhibit a large range of oscillation frequencies with little change in $[Ca^{2+}]_c$ amplitude (Fig. 2.2A, B; top traces). The pronounced increase in the rate of spiking with increasing stimulus is the hallmark of the experimentally observed frequency encoding. For very large stimuli, a plateau of elevated $[Ca^{2+}]_c$ is reached, again in agreement with experimental data.

The $[Ca^{2+}]_c$ oscillations in both models consist of a series of sharp spikes with baseline interludes (Fig. 2.2A, B). The peak values of $[Ca^{2+}]_c$ and $[IP_3]$ occur nearly at the same time. The shape of the $[IP_3]$ oscillations in the two models is different. In the positive-

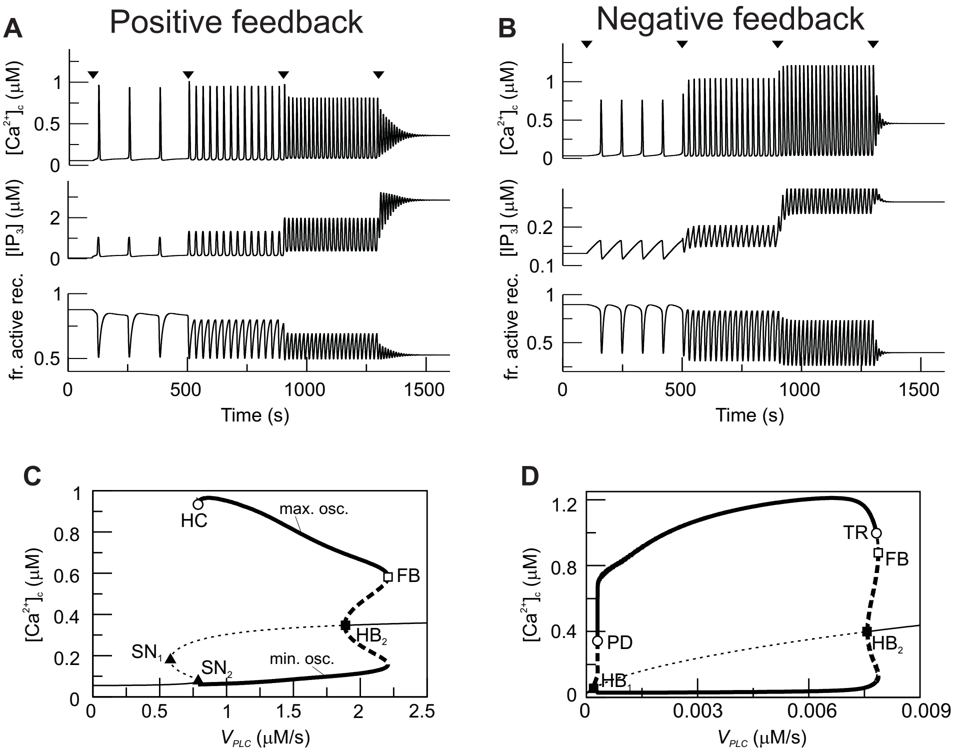

Figure 2.2: Agonist-induced IP_3 and Ca^{2+} oscillations in the positive- and negative-feedback models. (A) Positive-feedback model with Ca^{2+} activation of PLC. Changes in $[Ca^{2+}]_c$, $[IP_3]$ and in the fraction of active receptors (upper, middle and lower panels) after stepwise increases in the agonist concentration (arrowheads), modeled by an increase in the maximal rate of PLC ($V_{PLC} = 0.3$ μM/s for $t < 100$ with successive increases to 0.787, 1, 1.5 and 2.5 μM/s). (B) Negative-feedback model with Ca^{2+} activation of $IP_3$3K. The response is shown for a step-protocol with $V_{PLC} = 0.1$ nM/s for $t < 100$, followed by increases to 0.45, 2.5, 5.8 and 10 nM/s. (C) Bifurcation diagram for the positive-feedback model; shown are the maxima and minima of the $[Ca^{2+}]_c$ oscillations (thick lines) and the $[Ca^{2+}]_c$ steady states (thin lines) as a function of the stimulus (V_{PLC}). Solid and dashed lines indicate stable and unstable states, respectively. HB, Hopf bifurcation; HC, homoclinic bifurcation; SN, saddle node bifurcation; FB, saddle node of periodics. (D) Bifurcation diagram for the negative-feedback model. PD, period doubling; TR, torus bifurcation. Between PD and HB_1 as well as between TR and FB there exist complex oscillations (omitted for clarity). The parameter values are listed in Table 2.1.

feedback model, $[IP_3]$ exhibits baseline-separated spikes (Fig. 2.2A). In contrast, in the negative-feedback model, $[IP_3]$ follows a zig-zag pattern: the occurrence of a $[Ca^{2+}]_c$ spike leads to an abrupt decrease in $[IP_3]$, after which $[IP_3]$ slowly builds up again over the whole oscillation period (Fig. 2.2B). The IP_3R activities show similar dynamics in both models.

The behavior of the two model systems for different stimulation strengths can be summarized in bifurcation diagrams (Fig. 2.2C, D), where the steady states of $[\mathrm{Ca}^{2+}]_c$ and the maxima and minima of $[\mathrm{Ca}^{2+}]_c$ oscillations as a function of V_{PLC} have been computed. For very low PLC activity, both models show a stable steady state of low $[\mathrm{Ca}^{2+}]_c$; similarly, an elevated $[\mathrm{Ca}^{2+}]_c$ plateau is reached at relatively high PLC activity (these stable steady states are indicated by thin solid lines). For an intermediate range of V_{PLC}, the steady states are unstable (thin dashed lines). In these regions, both models exhibit oscillations ($[\mathrm{Ca}^{2+}]_c$ maxima and minima in stable oscillations are depicted by thick solid lines). The oscillations arise either via Hopf bifurcations (HB), or, in the case of the positive-feedback model, also by a homoclinic bifurcation (HC). Further bifurcations are indicated and referred to in the figure legend. In particular, a homoclinic bifurcation is associated with the existence of multiple steady states, which arise through saddle-node bifurcations (Fig. 2.2C, SN). Such multistationarity is typical for models that neglect the plasma-membrane fluxes of calcium; this point will be discussed in more detail below. In the negative-feedback model, there are two regions near the Hopf bifurcations HB_1 and HB_2 (prior to the point PD and after the point TR in Fig. 2.2D) where irregular and bursting oscillations are observed. Because these two regions are extremely narrow compared to the total stimulation range in the negative-feedback model, our focus will be on the regular oscillations.

In the two bifurcation diagrams, one notices that the values required for oscillations are considerably smaller in the negative-feedback model than in the positive-feedback model. This is primarily a consequence of the different feedback mechanisms. First, in the positive-feedback model the actual PLC activity is Ca^{2+}-dependent and, therefore, V_{PLC} is lower than at resting $[\mathrm{Ca}^{2+}]_c$. Second, owing to the calcium activation of $\mathrm{IP}_3$3K in the negative-feedback model, the IP_3 degradation rate at resting $[\mathrm{Ca}^{2+}]_c$ is much smaller than in the positive-feedback model, requiring a smaller rate of IP_3 production to raise the $[\mathrm{IP}_3]$ and induce oscillations.

2.2.2 The wide range of oscillation periods is due to interactions of IP_3 and Ca^{2+} dynamics

To elucidate whether the IP_3 dynamics participate in frequency encoding, I compared the oscillation periods in models without any Ca^{2+} feedback on IP_3 (resulting in a constant $[\mathrm{IP}_3]$) and in the two feedback models (with $[\mathrm{IP}_3]$ oscillations).

I begin by discussing the positive-feedback model, where the Ca^{2+} activation of an agonist-dependent PLC is considered. The strength of the positive feedback can be tuned by changing the value of the Ca^{2+} activation constant, K_{PLC}. For K_{PLC} being much lower than the basal $[Ca^{2+}]_c$, PLC is always saturated with Ca^{2+} and its activity is independent of variations in $[Ca^{2+}]_c$. In particular, by setting $K_{PLC} = 0$ positive feedback will effectively be eliminated. This model with constant $[IP_3]$ shows fast calcium oscillations with a period of 10-15 s (Fig. 2.3A, dashed line). Introducing positive feedback by setting $K_{PLC} > 0$ causes oscillations with long periods at low stimulation. The frequency encoding of the stimulus becomes very pronounced when the sensitivity of PLC to changes in $[Ca^{2+}]_c$ is just above basal $[Ca^{2+}]_c$ (Fig. 2.3A, solid lines, $K_{PLC} = 0.1$ and 0.2 μM).

For the negative-feedback model, I recall that there are two removal pathways for IP_3, one catalyzed by the Ca^{2+}-insensitive IP_3 5-phosphatase ($IP_3$5P) and the other by the Ca^{2+}-activated IP_3 3-kinase ($IP_3$3K). The strength of the negative feedback is modified by taking different concentration ratios of $IP_3$5P and $IP_3$3K. The feedback strength is expressed by the ratio of the maximal $IP_3$3K rate to the total degradation rate of IP_3; $\eta = k_{3K}/(k_{3K}+k_{5P})$, where $k_{3K}+k_{5P}$ has been kept constant in the following calculations. The oscillation periods in the absence of negative feedback ($\eta = 0$), and therefore constant $[IP_3]$, are shown in Fig. 2.3B (dashed line). When η is sufficiently high, the negative feedback has a pronounced effect on the range of oscillations periods; for approx. $\eta \geq 0.6$ there is an increase in the period range (Fig. 2.3B, solid lines).

Note that the two models without feedback are not identical in their ability to frequency encode the stimulus (compare Fig. 2.3A and B). Simulations indicate that the $IP_3$3K has an impact on the oscillation period only when the Ca^{2+} fluxes between ER and cytoplasm are comparatively slow and the IP_3R is less sensitive to Ca^{2+} activation. To expose the period effect of the negative feedback, different parameter values than in the positive-feedback model has been chosen (see Tab. 2.1). The differences in sensitivity towards the PLC activity observed in the two graphs have been explained above (Section 2.2.1).

In the positive-feedback model, arbitrarily long periods can be obtained (exceeding the 200 s shown), which are due to the onset of the oscillations via a homoclinic bifurcation (see also Fig. 2.2C). In the model, the homoclinic bifurcation specifically occurs when the plasma-membrane fluxes of Ca^{2+} are neglected, which is a valid simplification for many cell types in which the contribution of these fluxes to Ca^{2+} oscillations is small [154]. The more general case when the plasma-membrane Ca^{2+} fluxes are included has also being studied ($\varepsilon > 0$, see materials and methods Section 2.1). Then there is a unique steady state and the homoclinic bifurcation no longer exists. Nevertheless, long-

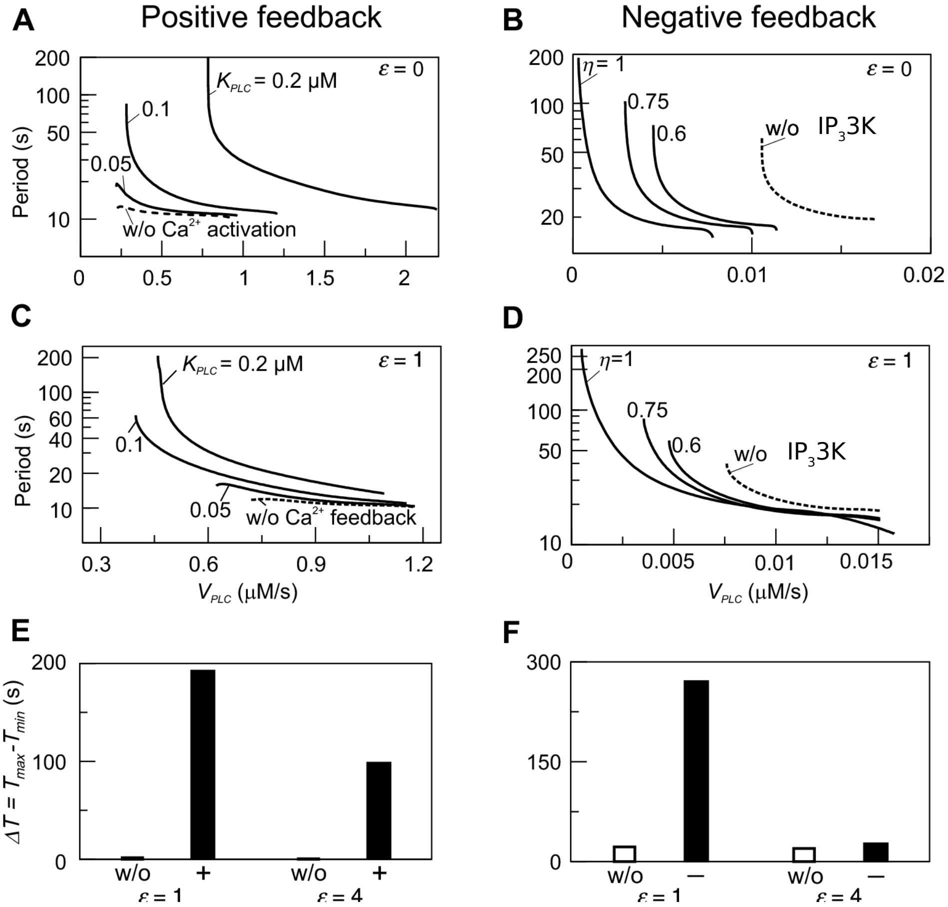

Figure 2.3: Frequency encoding of agonist stimulus. (A) Positive feedback. Oscillation periods observed at different stimulation strengths (varying V_{PLC}). Increasing the half-saturation constant of PLC for Ca^{2+}, K_{PLC}, from 0 (no functional positive feedback) to 0.2 μM (functional feedback) greatly enhances frequency encoding. (B) Negative feedback. Increasing the amount of IP$_3$3K relative to IP$_3$5P (η) enhances frequency encoding. (C, D) The feedback effects shown in A and B are preserved when plasma-membrane fluxes of Ca^{2+} are included ($\varepsilon = 1$). (E) Range of oscillation periods, $\Delta T = T_{max} - T_{min}$, in the presence (+) and absence (w/o) of positive feedback for two different strengths of the plasma-membrane Ca^{2+} fluxes ($\varepsilon = 1$, 4). (F) Range of oscillation periods in the presence (−) and absence (w/o) of negative feedback for two different strengths of the plasma-membrane Ca^{2+} fluxes ($\varepsilon = 1$, 4).

period oscillations are present (Fig. 2.3C). Importantly, the dependence of the period range of the oscillations on K_{PLC} remains very similar.

The plasma-membrane fluxes of Ca^{2+} have also been introduced into the negative-feedback model (Fig. 2.3D). One observes a similar picture as without plasma membrane fluxes, provided that the plasma-membrane fluxes are comparatively moderate. However, when the plasma-membrane Ca^{2+} fluxes are large enough, the effect of $IP_3$3K on the oscillation period practically disappears. In contrast, the period behavior in the positive-feedback model is less affected by changes in the magnitude of the plasma-membrane Ca^{2+} fluxes. To show this, I evaluated the range of oscillation periods $\Delta T = T_{max} - T_{min}$, where T_{max} and T_{min} are the maximal and minimal period that are obtained for low and high stimulation, respectively, for two different strengths of the plasma-membrane Ca^{2+} fluxes ($\varepsilon = 1$ and $\varepsilon = 4$). The positive-feedback model exhibits in both cases a much larger period range than the corresponding model without feedback (Fig. 2.3E). In contrast, the increase of the period range through negative feedback is only seen when the plasma-membrane Ca^{2+} fluxes are comparatively small, $\varepsilon = 1$ (Fig. 2.3F).

In summary, both positive and negative feedbacks of Ca^{2+} on IP_3 may serve a physiological role by greatly enhancing the range of frequency-encoding of the agonist stimulus. The frequency-encoding supported by the positive feedback is more robust against variations in the kinetic parameters of the Ca^{2+} transport processes.

2.2.3 The two feedback-models respond differently to changes in the IP_3 turnover time

In the model simulations, I have noticed that the characteristic time of IP_3 turnover τ_p has a decisive impact on the Ca^{2+}-IP_3 oscillators. The measured IP_3 turnover times span a relatively wide range, from 0.1 to > 10 s depending on cell type and experimental conditions [43, 150]. One finds that fast IP_3 turnover ($\tau_p \approx 0.1$–2 s) is associated with long oscillation periods in the positive-feedback model. Conversely, the negative-feedback model exhibits long-period oscillations when the IP_3 turnover is comparatively slow ($\tau_p \approx 10$–15 s).

Insight into the origin of this difference between the two models can be gained by looking at the time courses of the model variables. In the positive feedback model, fast IP_3 turnover ($\tau_p = 0.1$ s) yields high-amplitude oscillations in $[Ca^{2+}]_c$ and $[IP_3]$ (Fig. 2.4A left panel, solid and dashed lines, respectively). $[Ca^{2+}]_c$ and $[IP_3]$ rise simultaneously, and IP_3-induced Ca^{2+} release and Ca^{2+}-activated IP_3 production coincide. After termination of the $[Ca^{2+}]_c$ spike, $[IP_3]$ returns quickly to a basal level, because Ca^{2+}-activated IP_3 production has ceased and IP_3 degradation is fast. Also, the IP_3R close efficiently after the spike (Fig. 2.4A, dotted line showing the fraction of open IP_3R). For slow IP_3 turnover ($\tau_p = 15$ s) $[IP_3]$ does not sufficiently decline after the $[Ca^{2+}]_c$ spike, leading to an increased basal opening of the IP_3R, lower ER Ca^{2+} store loading and, consequently, much less pronounced $[Ca^{2+}]_c$ spikes (Fig. 2.4A, right panel).

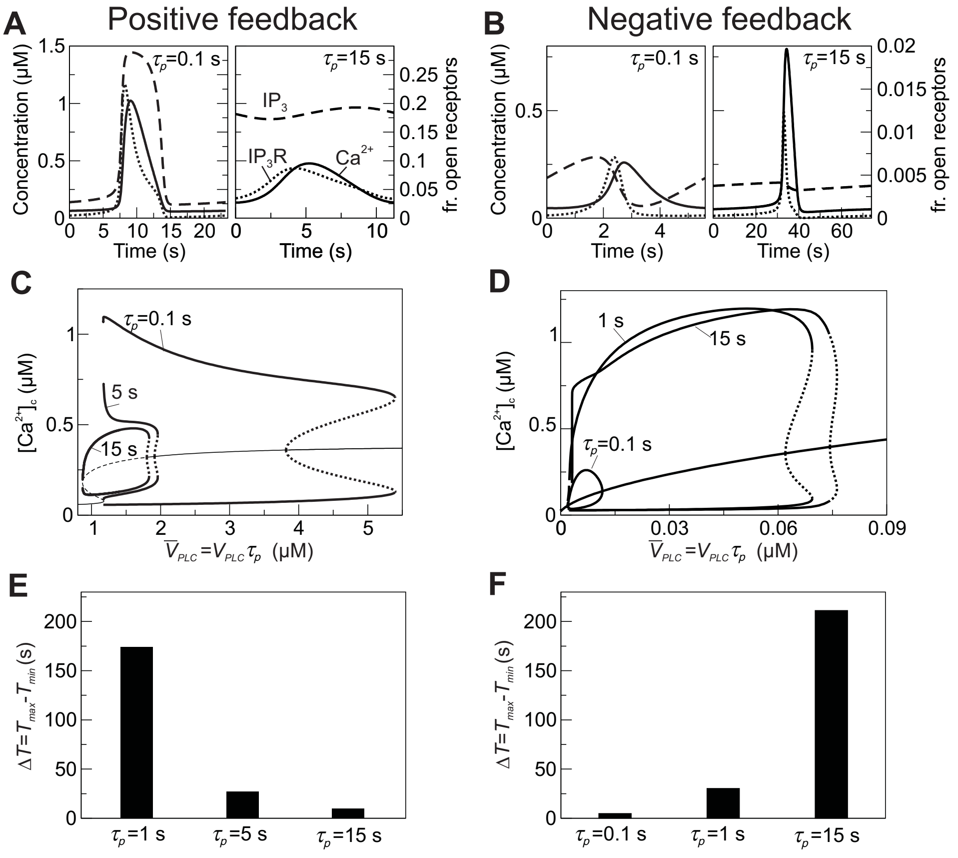

Figure 2.4: IP_3 turnover time controls feedbacks. (A) Positive-feedback model. Dynamics of $[Ca^{2+}]_c$, $[IP_3]$ and the fraction of open IP_3R (solid, dashed and dotted lines, respectively) during an oscillation period; the fraction of open IP_3R is given by $[rcp/((c+K_a)(p+K_p))]^3$ (see Eq. (2.6)). Fast IP_3 turnover yields a pronounced spike (left panel, $\tau_p = 0.1$ s), while slow IP_3 turnover supports only a small-amplitude response (right panel, $\tau_p = 15$ s). (B) The negative-feedback model shows the opposite behavior, a small-amplitude response for fast IP_3 turnover (left panel, $\tau_p = 0.1$ s) and a sharp spike for slow IP_3 turnover (right panel, $\tau_p = 15$ s). (C) Positive-feedback model. Bifurcation diagram showing the maxima and minima of the $[Ca^{2+}]_c$ oscillations as a function of the stimulus for different values of the IP_3 turnover. The bifurcation diagrams for different values of τ_p are compared by plotting them against the product $\overline{V}_{PLC} = V_{PLC}\tau_p$; in this way, the steady-state concentrations of Ca^{2+} and IP_3 are identical for a given $\overline{V}_{PLC}$ (solid and dashed lines indicate stable and unstable states respectively; the stability of the steady state is shown for $\tau_p = 15$ s). Both amplitude and range of stimuli leading to oscillations increase with faster IP_3 turnover. (D) The corresponding bifurcation diagrams for the negative-feedback model show the opposite behavior. The amplitude and range of stimuli leading to oscillations increase with slow IP_3 turnover. (E, F) Dependence of frequency encoding on IP_3 turnover in the positive- and negative-feedback models, respectively. T_{max} and T_{min} are the largest (for low stimulation) and smallest (for high stimulation) oscillation period.

Not only the spike characteristics but also the oscillation period and the range of agonist stimuli that give oscillations are affected by the IP_3 half-life. For fast IP_3 turnover, oscillations in the positive-feedback model are observed over a wide range of stimuli (Fig. 2.4C, $\tau_p = 0.1$ s). Slower IP_3 turnover leads to reduced oscillation ranges and also much smaller amplitudes (Fig. 2.4C, $\tau_p = 5$ and 15 s). Importantly, also the capacity for frequency encoding of the stimulus, as measured by the period range of oscillations, is high when the IP_3 turnover is fast (Fig. 2.4E).

In the negative-feedback model, changing the time scale of IP_3 turnover has the opposite effect. When IP_3 turnover is fast ($\tau_p = 0.1$ s), a rise in $[Ca^{2+}]_c$ triggers, via activation of $IP_3$3K, a pronounced decrease in $[IP_3]$, which in turn limits further Ca^{2+} release (Fig. 2.4B, left panel). Therefore, the $[Ca^{2+}]_c$ spikes are relatively small and $[IP_3]$ shows strong variations (solid and dashed lines, respectively). When the IP_3 lifetime is larger ($\tau_p = 15$ s), $[IP_3]$ remains at a relatively high level throughout and the $[Ca^{2+}]_c$ spikes are accordingly more pronounced (Fig. 2.4B, right panel). Moreover, for slow IP_3 degradation, the range of stimuli where oscillations occur is larger (Fig. 2.4D). The capacity for frequency encoding as measured by the range of oscillation periods, ΔT, strongly increases with the IP_3 half-life (Fig. 2.4F). This finding agrees with the frequent observation that negative feedback is more prone to oscillate when the controlled variable (here IP_3) responds slowly.

To summarize, frequency encoding in the two feedback models poses opposite requirements on IP_3 turnover: positive and negative feedbacks are efficient frequency modulators when the IP_3 turnover is fast and slow, respectively. The critical IP_3 lifetimes estimated in the model indicate that both cases could be realized physiologically.

2.2.4 Period control is shared by all processes

The calculations have shown that the inclusion of IP_3 dynamics strongly alters the frequency properties of the oscillator and, particularly, leads to long-period oscillations. I have therefore quantified the control of the IP_3 dynamics and the other processes present in the model on the oscillation period. To this end, the following sensitivity measure has been used

$$C_i = \frac{\tau_i}{T}\frac{\partial T}{\partial \tau_i} \quad \text{for } i = er,\, pm,\, p,\, r \tag{2.10}$$

which is referred to as period control coefficients (see also [192]). The C_i set the change of the oscillation period T in proportion to the change in the characteristic time τ_i of an individual process i. I analyzed the control of the following processes: IP_3 metabolism (with τ_p as defined in Eq. (2.4)), the IP_3R dynamics (with τ_r as defined in Eq. (2.7)), Ca^{2+} transport across the ER membrane (achieved by scaling $v_{rel} - v_{serca}$ with $1/\tau_{er} = V_{serca}/K_{serca}$ in Eqs. (2.8) and (2.9)), and Ca^{2+} transport across the plasma membrane (achieved by scaling $v_{in} - v_{out}$ with $1/\tau_{pm} = \varepsilon V_{pm}/K_{pm}$ in Eq. (2.8)). A positive period control coefficient implies that a slowing of the respective process (i.e. increase in τ_i) raises the period. At any point, the period control coefficients sum up to unity, $C_p + C_r + C_{er} + C_{pm} = 1$, so that each coefficient quantifies the relative contribution of a single process to the oscillation period [57].

The control coefficients were calculated for various levels of stimulation in the positive and negative feedback models. Because these levels correspond to different oscillation periods, we can plot the C_i against the period. Fig. 2.5A, B depict the result for the model without plasma-membrane fluxes of Ca^{2+} ($\varepsilon = 0$). The two feedback models yield a similar picture. The control is distributed between the dynamics of IP_3, Ca^{2+} and IP_3R. In long-period oscillations, the IP_3 turnover has the leading control (dot-dashed lines). The IP_3R dynamics contributes more significantly to setting the period of fast oscillations, especially in the positive-feedback model (dotted lines).

The distribution of control becomes more complex when the plasma-membrane fluxes of Ca^{2+} are included (Fig. 2.5C, D; $\varepsilon = 1$), although, interestingly, the plasma-membrane fluxes exert very little period control themselves (dashed lines). There are several notable features. First, the fast oscillations in the positive-feedback model are no longer dominated by the IP_3R dynamics. There is even a rather counter-intuitive behavior at intermediate periods where acceleration of the IP_3R dynamics would result in a slowing of the oscillations ($C_r < 0$). Second, the overall tendency that the IP_3 dynamics are more relevant for slow oscillations is preserved. However, the dynamics of ER Ca^{2+} release and refilling now play a more pronounced role in setting the period (solid lines).

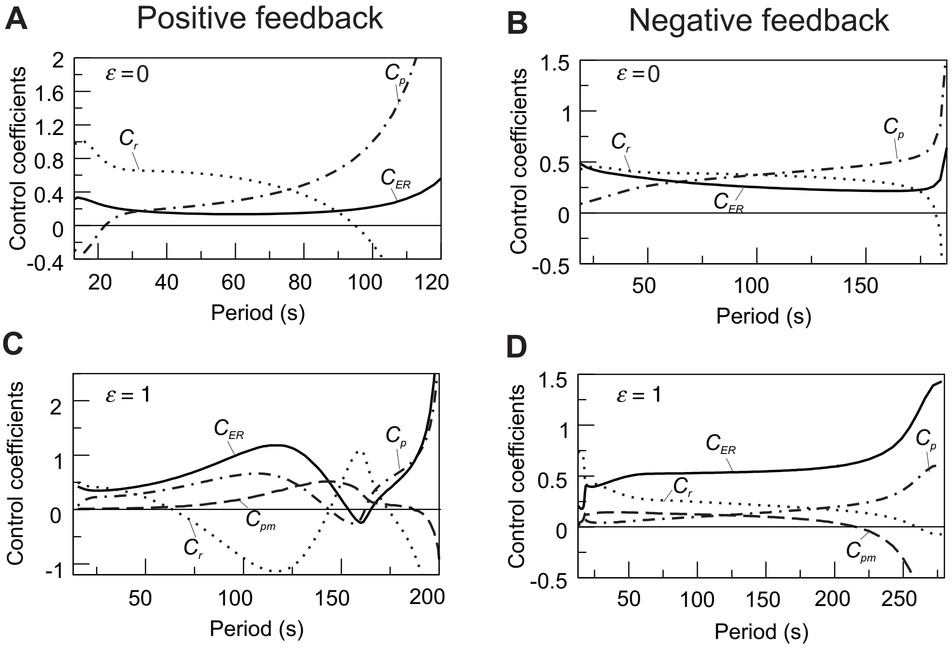

Figure 2.5: Control coefficients for the oscillation period. (A, B) Positive- and negative-feedback models, respectively, in the absence of Ca^{2+} fluxes across the plasma membrane ($\varepsilon = 0$); control coefficients of Ca^{2+} exchange across the ER membrane (C_{er}, solid line), IP_3 metabolism (C_p, dash-dotted line) and IP_3R dynamics (C_r, dotted line) as function of the period of the oscillations. A positive period control coefficient signifies that a slowing of the corresponding process increases the oscillation period. (C, D) show the period control coefficients in the positive- and negative-feedback models, respectively, in the presence of plasma-membrane fluxes of Ca^{2+} ($\varepsilon = 1$). The dashed line indicates the control exerted by Ca^{2+} exchange across the plasma membrane (C_{pm}).

This quantification of period control reveals that no process can be singled out as a unique period controlling factor. Depending on the oscillation mechanism and the reference period, the IP_3 turnover, the ER Ca^{2+} fluxes and the IP_3R dynamics can all exert strong control.

Chapter 3

How to distinguish Ca^{2+} feedbacks on IP_3 metabolism

The previous analysis has shown that oscillation mechanisms involving Ca^{2+}-activated PLC or $IP_3$3K are sensitive to the time scale of IP_3 turnover. This offers the possibility to experimentally interfere with the oscillation mechanism by perturbing the IP_3 turnover. First, I will present the predictions obtained from the mathematical models and then compare them to experiments where an IP_3 binding molecule has been overexpressed in a mammalian cell line.

3.1 Model predictions

3.1.1 Accelerating IP_3 turnover by overexpressing IP_3 metabolizing enzymes

The overexpression of IP_3 metabolizing enzymes would accelerate the IP_3 turnover and also decrease the $[IP_3]$ (see Eqs. (2.3)–(2.5)). The decrease in the concentration of IP_3 can then be compensated for by an increase in the agonist dose. I first tested whether an increase in the Ca^{2+}-insensitive IP_3-metabolizing enzyme, IP_3 5-phosphatase ($IP_3$5P), would interfere with oscillation mechanisms (*i*) without Ca^{2+} feedback on IP_3, (*ii*) with positive feedback, or (*iii*) with negative feedback. In the absence Ca^{2+} feedbacks, implying constant $[IP_3]$, oscillations can be abolished by elevating $IP_3$5P levels and recovered by an increase in V_{PLC} (agonist dose). I found that the same holds in the presence of Ca^{2+} activated PLC (results not shown). This is in line with the observation that the positive-feedback model functions with fast IP_3 dynamics. A similar behavior is predicted by the negative-feedback model. As shown in Fig. 3.1A, B for two increasing stimulation levels (indicated by arrows), Ca^{2+} oscillations in the presence of IP_35P are lost for low stimulation and recovered for high stimulation. By simulating a large number of such cases, one finds that the oscillations are generally faster after introducing IP_35P into the model. This is mainly due to the diminished role of IP_33K, which was crucial in setting the long periods, compared to IP_35P (corresponding to a decrease in η, Eq. (2.5), see Fig. 2.3). However, this predicted acceleration of the oscillations by IP_35P would be difficult to identify experimentally.

Next I tested the effect of increasing the concentration of IP_33K, which introduces or enhances the negative feedback of Ca^{2+} on IP_3. Fig. 3.1C depicts typical $[IP_3]$ and $[Ca^{2+}]_c$ oscillations observed before and after introducing IP_33K in the positive-feedback model (solid and dashed lines, respectively). The amplitude of the oscillations with IP_33K is substantially reduced. Interestingly, although the average IP_3 concentration is lower after introduction of IP_33K the frequency of the oscillations is increased. This effect is observed throughout the stimulation range and is summarized in Fig. 3.1D. Here the longest and shortest periods of the oscillations (obtained at low and high stimulation, respectively) are plotted against the rate constant of IP_33K (k_{3K}). In particular, the long period oscillations progressively disappear as the concentration of IP_33K increases. Very high levels of IP_33K are predicted to abolish the $[Ca^{2+}]_c$ oscillations completely (indicated by the dotted line in Fig. 3.1D). Within this parameter range, the oscillations cannot be recovered by increasing the stimulus. A qualitatively very similar behavior was observed in the absence of Ca^{2+} activated PLC and in the negative-feedback model (results not shown).

The diminished amplitude of the oscillations and the eventual loss of oscillations are specifically obtained by increasing the IP_33K concentration and are not found with an increase in IP_35P. However, in both cases the predicted experimental observations do not depend strongly on whether any feedback mechanism, negative or positive, was present prior to the perturbation. Thus, accelerating IP_3 turnover by overexpressing IP_3 metabolizing enzymes is a poor strategy to verify the existence of Ca^{2+}-dependent feedback mechanisms.

The effects of overexpressing the Ca^{2+}-insensitive IP_35P can always be compensated by raising the agonist stimulus to keep the IP_3 level high. Overexpression of IP_33K is predicted to lead to small-amplitude Ca^{2+} spikes and, at high concentration, abolish the oscillations completely. This scenario is independent of whether (positive or negative) IP_3 feedbacks were present before the overexpression. Therefore, these experiments do not allow one to draw conclusions on the state of the system prior to perturbation.

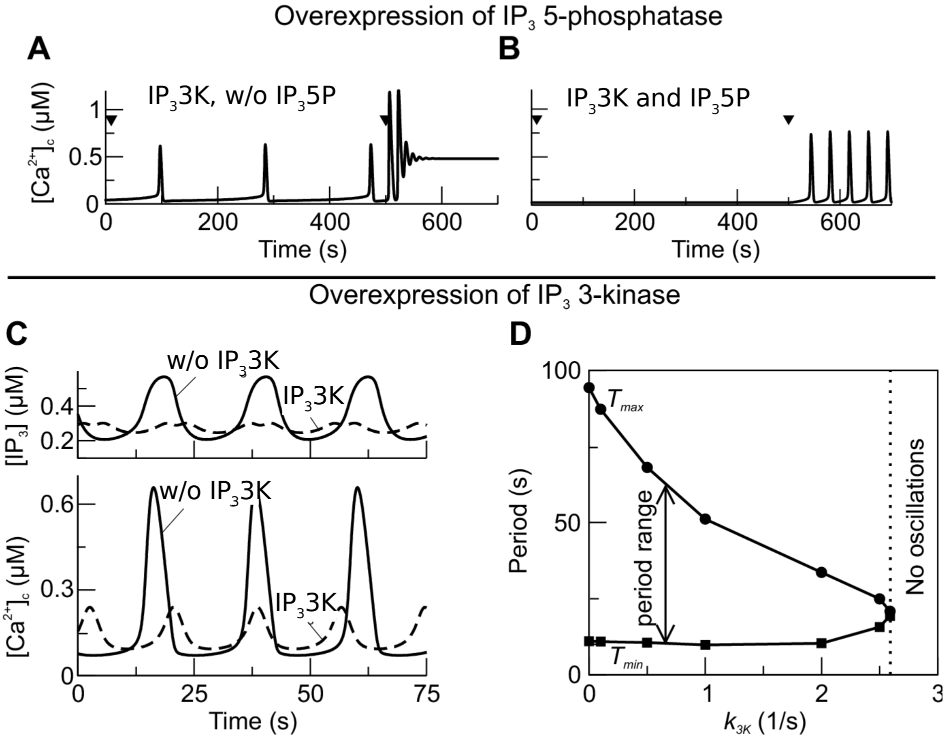

Figure 3.1: Acceleration of IP$_3$ turnover by overexpressing IP$_3$-metabolizing enzymes. (A) Negative-feedback model without IP$_3$ 5-phosphatase ($k_{5P} = 0$, $\eta = 1$). At 10 sec and 500 sec V_{PLC} is increased from 0 to 0.3 and 11 nM/s, respectively (arrowheads). (B) Same model with overexpressed IP$_3$5P, modeled as an increase in the IP$_3$ dephosphorylation rate constant $k_{5P} = 0.1$/s ($\eta = 0.5$). The oscillations are abolished for low stimulation but reappear at high stimulation. (C) Effect of expressing the Ca^{2+} dependent IP$_3$ 3-kinase in the positive-feedback model. [IP$_3$] and [Ca^{2+}]$_c$ oscillations are shown in the absence ($k_{3K} = 0$, solid lines) and presence of IP$_3$3K ($k_{3K} = 2$/s, dashed lines) for $V_{PLC} = 0.4$ μM/s. The amplitude of the oscillations and the period decrease after introduction of IP$_3$3K. (D) Frequency encoding in the positive-feedback model decreases as the concentration of IP$_3$3K increases (increase in k_{3K}). Plotted are the longest (T_{max}, circles) and shortest (T_{min}, squares) oscillation periods, obtained for low and high stimulation, respectively. For high levels of IP$_3$3K, no oscillations are found ($k_{3K} > 2.593$/s, dotted vertical line). Parameters as in Tab. 2.1, except in C and D $K_{PLC} = 0.1$ μM.

3.1.2 Slowing IP$_3$ turnover with an IP$_3$ buffer

A stronger result is obtained if the IP$_3$ turnover is slowed by introducing IP$_3$-binding proteins (IP$_3$ buffers) into the cell. To be specific, I assume a monovalent IP$_3$ buffer with on and off rate constants k_{on} and k_{off}, respectively. The IP$_3$ balance equation

(Eq. (2.3)) is then modified to

$$\frac{dp}{dt} = v_{PLC} - v_{deg} - k_{on}(B - C)p + k_{off}C \tag{3.1}$$

$$\frac{dC}{dt} = k_{on}(B - C)p - k_{off}C, \tag{3.2}$$

where p as before stands for [IP_3], B denotes the total concentration of the introduced IP_3 buffer, and C is the concentration of occupied IP_3 buffer. If the binding of IP_3 to the buffer is fast compared to the IP_3 degradation rate, the amount of occupied buffer will be in equilibrium with [IP_3]. This implies $C = Bp/(K_B + p)$, where $K_B = k_{off}/k_{on}$ is the dissociation constant. Summing Eqs. (3.1)–(3.2) and using the equilibrium relation for C, one obtains for the dynamics of unbound IP_3

$$\frac{dp}{dt} = \frac{1}{\tau_p'}\left[\overline{V}_{PLC}\frac{c^2}{K_{PLC}^2 + c^2} - \left(\eta\frac{c^2}{K_{3K}^2 + c^2} + (1 - \eta)\right)p\right] \tag{3.3}$$

with the modified characteristic time of IP_3 turnover

$$\tau_p' = \tau_p\left(1 + \frac{BK_B}{(K_B + p)^2}\right). \tag{3.4}$$

The IP_3 buffer creates an additional bound pool of IP_3 that is assumed to be protected from degradation. Then the build-up of free IP_3 after PLC activation is delayed, because the buffer binding sites also need to be filled. Similarly, the decay of free [IP_3] is slowed, because IP_3 molecules dissociate from the buffer as cellular [IP_3] decreases. Precisely these two effects are accounted for by the modified time constant τ_p', which increases with the buffer concentration (Eq. (3.4)). Note that the balance between the rates of IP_3 production and degradation is unaffected by the buffer. In particular, the IP_3 buffer would not change the steady-state concentration of free IP_3 attained when $v_{PLC} = v_{deg}$[1]. This remains true also with more detailed models for the IP_3 metabolism, where the dynamics of its precursor PIP_2 has been taken into account. Only when the intracellular total inositol is conserved does one observe a small decrease in the steady-state [IP_3] in the presence of IP_3 buffer (see Section 4.4). However, in experiments inositol is present in the culture medium so that the intracellular inositol pool is probably continously refilled.

Introducing an exogenous IP_3 buffer into a core Ca^{2+} oscillator model operating with constant PLC activity and Ca^{2+}-insensitive degradation (such as the models discussed

---

[1] The cell contains endogenous IP_3 binding sites, such as the IP_3R. They have already been accounted for by the characteristic time of IP_3 turnover, τ_p, defined in the absence of the exogenous IP_3 buffer.

above in the absence of Ca^{2+} feedbacks on IP_3), will delay the rise in $[IP_3]$ after PLC activation. However, eventually the same steady-state concentration of free $[IP_3]$ would be reached as without buffer. Therefore, Ca^{2+} oscillations may set in with an increased latency, while spike shape and period would be unaffected by the presence of the IP_3 buffer.

When introducing the IP_3 buffer into the positive- and negative-feedback models, one finds that for low concentrations of IP_3 buffer ($0 < B < 10$ μM for $K_B = 0.13$ μM) the oscillations persist in both models. However, depending on which type of Ca^{2+} feedback is present, IP_3 buffer affects the kinetic properties of the $[Ca^{2+}]_c$ oscillations in very different ways. In the positive-feedback model, the IP_3 buffer slows the Ca^{2+} responses. The rate of $[Ca^{2+}]_c$ rise in an individual spike is predicted to be decreased by the buffer in a dose-dependent manner (Fig. 3.2A, solid line). Another characteristic property of $[Ca^{2+}]_c$ oscillations is the wave speed, that is, the velocity at which a calcium spike propagates through the cell. To evaluate the effect of an IP_3 buffer on wave propagation, diffusion of Ca^{2+} and IP_3 in the cytoplasm was added to the model. The resulting reaction-diffusion equations were solved numerically on a one-dimensional domain. The propagation speed of a Ca^{2+} spike shows a very similar behavior as the rate of $[Ca^{2+}]_c$ rise: it decreases strongly as a function of IP_3 buffer concentration in the positive-feedback model (Fig. 3.2B, solid line). In contrast, in the negative-feedback model, the IP_3 buffer will cause hardly perceptible increases in the rate of Ca^{2+} rise (Fig. 3.2A, dashed line) and the wave speed (Fig. 3.2B, dashed line). These two properties are well suited for experimental measurements, because they have been found to be remarkably constant in cells not perturbed by IP_3 buffer [137, 169].

For higher concentrations of IP_3 buffer ($B > 20$ μM), the differences between the positive- and negative-feedback models are even more pronounced. In the positive-feedback model, the IP_3 buffer completely abolishes the $[Ca^{2+}]_c$ oscillations, and instead a single slow $[Ca^{2+}]_c$ transient is observed (Fig. 3.2C). In the negative-feedback model, the $[Ca^{2+}]_c$ oscillations persist even for very high concentrations of IP_3 buffer, although the oscillation period is increased (Fig. 3.2D).

Because IP_3 buffering causes the strongest effects in the positive-feedback model, this case will be analyzed in more detail. Fig. 3.3A summarizes the results by showing the regions of oscillatory behavior as a function of the stimulus (V_{PLC}) and the concentration of exogenous IP_3 buffer. Four different regions can be distinguished. In region **I**, the IP_3 buffer slows the oscillations with respect to the rise time and propagation speed (see solid lines in Fig. 3.2A, B). In region **II**, high enough IP_3 buffer concentrations abolish the oscillations (shown in Fig. 3.2C). In region **III**, IP_3 buffer can cause more

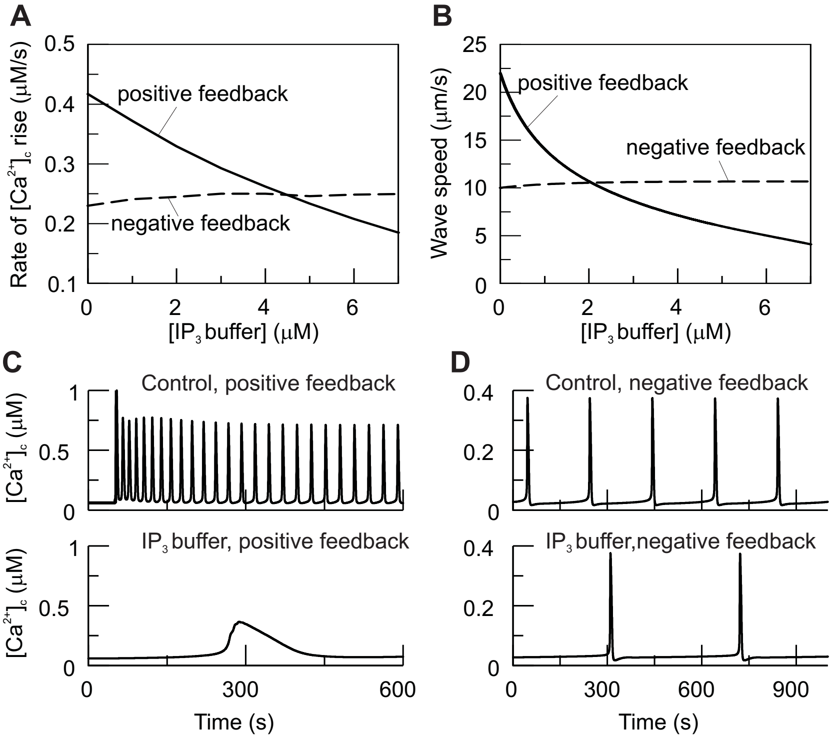

Figure 3.2: Slowing of the IP_3 turnover with an IP_3 buffer. (A) The maximal rate of $[Ca^{2+}]_c$ rise during a Ca^{2+} spike decreases as a function of IP_3 buffer concentration in the positive-feedback model (solid line), while it is barely affected in the negative-feedback model (dashed line). The results are shown for $V_{PLC} = 3$ μM/s (positive feedback) and 0.4 nM/s (negative feedback); similar results are obtained for other values. (B) The intracellular wave speed decreases as a function of IP_3 buffer concentration in the positive-feedback model (solid line), while it is barely affected in the negative-feedback model (dashed line). A solitary Ca^{2+} wave is initiated by a local increase in $[IP_3]$; Ca^{2+} and IP_3 diffuse in the cytoplasm with diffusion constants of 20 and 280 $\mu m^2/s$, respectively [4]; $V_{PLC} = 0.976$ μM/s, (positive feedback) and 0.217 nM/s (negative feedback). (C) High IP_3 buffer concentration abolishes oscillations in the positive-feedback model ($B = 50$ μM, $V_{PLC} = 1.6$ μM/s). (D) Oscillations persist in the presence of IP_3 buffer in the negative-feedback model ($B = 50$ μM, $V_{PLC} = 0.6$ nM/s). In all panels the IP_3 buffer dissociation constant is $K_B = K_p = 0.13$ μM. For the positive-feedback model $\varepsilon = 2$, $\tau_p = 1$ s, $\tau_r = 6$ s, $v_0 = 0.002$ μM/s, $\phi = 0.001$/s. For the negative-feedback model $\varepsilon = 0.1$. Other parameters are listed in Tab. 2.1.

complex oscillations, such as the bursting oscillations shown in Fig. 3.3B. For a large range of stimuli, the oscillations disappear when sufficiently high amounts of IP_3 buffer are added (transition into region **II**). However, for strong stimulation, there can be an additional domain, region **IV** (Fig. 3.3A). Here, the oscillations persist even at very high

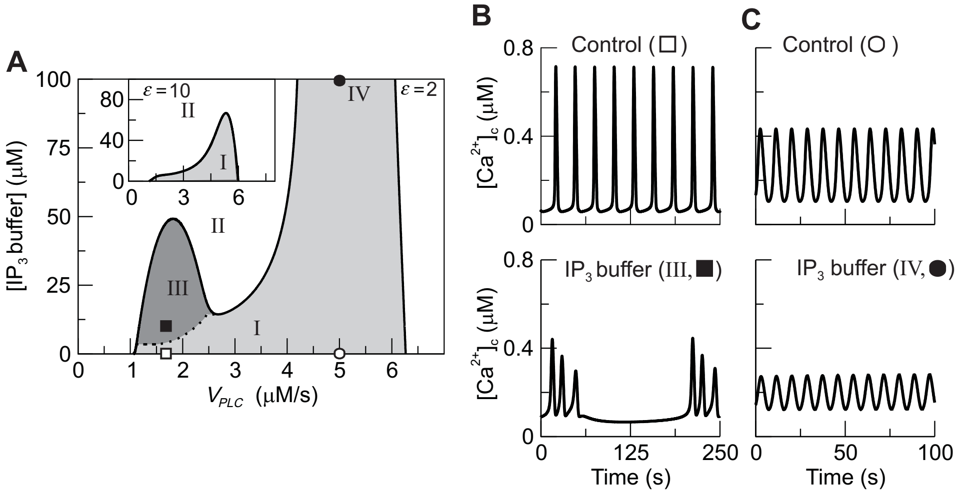

Figure 3.3: Complex responses to an IP_3 buffer in the positive-feedback model. (A) Bifurcation diagram showing the region of oscillations as function of stimulus (V_{PLC}) and IP_3 buffer concentration (gray-shaded area; the solid lines indicate the locus where the steady state becomes unstable via a Hopf bifurcation). In region I, regular oscillations have a decreased rate of $[Ca^{2+}]_c$ rise with increased [IP_3 buffer] as shown in Fig. 3.2A. In region II, the IP_3 buffer abolishes the Ca^{2+} oscillations completely, as shown in Fig. 3.2C. In region III, bursting $[Ca^{2+}]_c$ oscillations are observed (the lower boundary of this region is determined by a period doubling bifurcation, dotted line). An additional region IV is indicated. It is characterized by oscillations persisting even at high [IP_3 buffer]. The parameters are as in Fig. 3.2, with $\varepsilon = 2$. When the strength of the Ca^{2+} plasma-membrane fluxes is increased ($\varepsilon = 10$), regions III and IV disappear (inset). (B) Example of bursting oscillations observed in region III (top panel, control without IP_3 buffer; bottom panel, [IP_3 buffer] = 10 μM; V_{PLC} = 1.6 μM/s). (C) Example of oscillations in region IV ([IP_3 buffer] = 100 μM; V_{PLC} = 5 μM/s), which are characterized by high frequency and low amplitude.

IP_3 buffer concentration but have strongly diminished amplitude (Fig. 3.3C). Note that in the presence of sufficiently high IP_3 buffer, only fast oscillations (at high stimulation) can be retained. The long-period oscillations, which depend on Ca^{2+} feedback on PLC are invariably abolished by the IP_3 buffer.

Whether regions **III** and **IV** exist, depends on the kinetic parameters of the Ca^{2+} fluxes. The inset in Fig. 3.3A shows a situation where the Ca^{2+} fluxes across the plasma membrane are increased 5-fold. Then only regions **I** and **II** remain, and sufficiently high buffering of IP_3 always suppresses oscillations. Closer analysis revealed that if the system can oscillate for constant [IP_3] then IP_3 buffer never completely abolish the oscillations and a region **IV** exists (see also below).

3.1.3 A general property for systems with feedbacks on IP_3 metabolism

The model predictions described in the previous sections do not appear to be crucially dependent on the specific choice for the mathematical model. I tested four different models and obtained qualitatively similar results [25, 69, 147, 151] (see Appendix A). This indicates that there is a general property behind our observations. Here I will show, using a simple and analytical approach, how slowing or accelerating the IP_3 turnover affect differently systems with positive or negative feedback of Ca^{2+} on IP_3 metabolism.

A simplified model for coupled Ca^{2+}-IP_3 oscillations contains three variables (see Fig. 2.1): cytoplasmic and total calcium concentration c and z (c_{tot} in the previous model), and the IP_3 concentration p. For presentation purposes, I assume that the (in)activation of the IP_3R by Ca^{2+} and IP_3 is fast compared to other processes. The higher dimensional model can be treated in an analogous way. The Ca^{2+} concentration in the ER is related to the total concentration by $s = (z - c)/\beta$. The time changes of the three variables are described by

$$\frac{dc}{dt} = f(c, z, p); \; \frac{dz}{dt} = g(c); \; \text{and} \; \frac{dp}{dt} = w(c, p). \tag{3.5}$$

The functions $f(c, z, p)$ and $g(c)$ describe the transport fluxes of cytoplasmic Ca^{2+} across the ER and plasma membrane, $w(c, p)$ the production and degradation of IP_3. For realistic functions f, g and w the existence of a limit cycle must generally be shown numerically. However, the local stability properties of the steady state give us a hint. One can show that, due to the Ca^{2+} transport across the plasma membrane, there is a unique steady state $(\bar{c}, \bar{z}, \bar{p})$ [144]. Therefore, changes in stability of this steady state are likely to be connected with a Hopf bifurcation and the birth/death of a limit cycle. Generally, if the steady state is unstable, it is to be expected that the trajectories move toward a stable limit cycle. Note that a stable limit cycle and a stable steady state can coexist. The following analysis can make no predictions in this regard.

I will focus on how the IP_3 dynamics can contribute in destabilizing or stabilizing the steady state and so possibly generate or abolish Ca^{2+} oscillations. The local stability of the steady state is determined by the Jacobian:

$$J = \begin{pmatrix} f_c & f_z & f_p \\ g_c & 0 & 0 \\ w_c & 0 & w_p \end{pmatrix}. \tag{3.6}$$

The subscripts denote the partial derivatives at the steady state, e.g. $f_c = \frac{\partial f}{\partial c}\Big|_{(\bar{c},\bar{z},\bar{p})}$.

The gating properties of the IP_3R and the properties of the Ca^{2+} transport processes allow to fix the signs of some of the terms in the Jacobian

- $f_z > 0$, the Ca^{2+} concentration in the cytoplasm increases when the total concentration increases.
- $f_p > 0$, an increase in IP_3 causes the opening of the IP_3R and outflow of Ca^{2+} from the ER into the cytoplasm.
- $g_c < 0$, a high Ca^{2+} concentration in the cytoplasm favors the transport of Ca^{2+} outside the cell.
- $w_p < 0$, IP_3 is degraded proportional to its concentration.

The sign of w_c is positive when Ca^{2+} activates the IP_3 production (positive feedback), negative in the presence of Ca^{2+} dependent degradation of IP_3 (negative feedback), and vanishes in the absence of feedbacks of Ca^{2+} on IP_3. When accelerating the IP_3 dynamics, e.g. by overexpressing IP_3 metabolizing enzymes, w_c and w_p increase in magnitude without changing sign. Conversely, slowing the IP_3 dynamics, e.g. by expressing an IP_3 binding protein, decreases w_c and w_p.

The stability of the steady state is determined using the Routh-Hurwitz criterion, which states that all Eigenvalues of the Jacobian have negative real parts when

$$\begin{aligned} a_0 &= f_z g_c w_p \\ a_1 &= -f_z g_c - f_p w_c + f_c w_p \\ a_2 &= -f_c - w_p \\ a_3 &= a_2 a_1 - a_0 \end{aligned}$$

are all positive. Due to the previous assumptions, $a_0 > 0$. The other terms simplify when the IP_3 dynamics is fast compared to the other processes $w_p, w_c \gg 1$, then $a_1 \approx -f_p w_c + f_c w_p$ and $a_2 \approx -w_p$. When the IP_3 dynamics is slow $w_p, w_c \ll 1$, then $a_1 \approx -f_z g_c$ and $a_2 \approx -f_c$.

I compare the behavior of a positive-feedback model ($w_c > 0$), a negative-feedback model ($w_c < 0$), and a model without feedback of Ca^{2+} on IP_3 ($w_c = 0$) when the steady-state is identical in all three models. Equal $[IP_3]$ can be obtained by adjusting e.g. the stimulus dependent IP_3 production. Compared to the case without feedback, the IP_3 production should be higher with positive feedback model and lower with negative feedback (see also the detailed model). The cytoplasmic and total Ca^{2+} concentrations are identical in all three models when the plasma membrane fluxes are unaffected by

If $f_c > 0$

IP_3 dynamics	a_0	a_1	a_2	a_3	**stability**
no feedback, $w_c = 0$	+	±	±	−	unstable
positive feedback, $w_c > 0$					
slow dynamics	+	+	−	−	unstable
fast dynamics	+	−	+	−	unstable
negative feedback, $w_c < 0$					
slow dynamics	+	−	−	−	unstable
fast dynamics	+	±	+	±	stable/unstable

Table 3.1: Stability properties of the steady state when $f_c > 0$ in a model without feedbacks, positive or negative feedback of Ca^{2+} on IP_3. Shown are also the signs of the Routh-Hurwitz coefficients. In the negative feedback model, for fast IP_3 dynamics, the steady state is stable when $f_p w_c - f_c w_p < 0$.

the stimulus. An equal steady state allows to easily compare the three models. Then the partial derivatives, except of course w_c and w_p, are identical for the three cases considered.

Depending on the magnitude of the positive feedback of Ca^{2+} on the IP_3R and on the transport processes that remove Ca^{2+}, f_c can be either positive or negative; both cases will be discussed. The stability properties of the steady state for $f_c > 0$ are summarized in Tab. 3.1. If the system can oscillate in the absence of Ca^{2+} feedbacks on the IP_3 metabolism, i.e. the steady state is unstable, slowing the IP_3 dynamics does not stabilize the system, i.e. abolish the oscillations, in either positive- or negative-feedback models. Overexpressing the enzyme $IP_3$3K which corresponds to accelerating the IP_3 dynamics in the negative-feedback model, can stabilize the steady state and so may suppress the oscillations.

The stability properties of the steady state for $f_c < 0$ are summarized in Tab. 3.2. When the steady state is stable in the absence of feedbacks, the presence of a positive feedback of Ca^{2+} on IP_3 can destabilize the system and so generate oscillations. The conditions that must be fulfilled is a sufficiently fast IP_3 dynamics and $f_p w_c - f_c w_p > 0$. In the last formula one recognizes that the mutual activation of IP_3 and Ca^{2+}, $f_p w_c$, needs to be strong compared to processes responsible for the clearance of Ca^{2+} and the degradation of IP_3, which enter $f_c w_p$. Slowing of the IP_3 dynamics stabilizes the system,

If $f_c < 0$					
IP$_3$ dynamics	a_0	a_1	a_2	a_3	**stability**
no feedback, $w_c = 0$	$+$	$+$	$+$	$+$	stable
positive feedback, $w_c > 0$					
slow dynamics	$+$	$+$	$+$	$+$	stable
fast dynamics	$+$	$\pm$	$+$	$\pm$	stable/unstable
negative feedback, $w_c < 0$					
any dynamics	$+$	$+$	$+$	$+$	stable

Table 3.2: Stability properties of the steady state when $f_c < 0$. Shown are also the signs of the Routh-Hurwitz coefficients. For fast IP$_3$ dynamics and in the presence of Ca^{2+} activation of IP$_3$ production the steady state is unstable when $f_p w_c - f_c w_p > 0$.

and so abolishes the oscillations. The presence of a negative feedback does not affect the stability of the steady state and so may not give rise to Ca^{2+} oscillations.

These conclusions are independent of specific expressions for the rates f, g and w. In particular, slowing of the IP$_3$ dynamics may unmask a critical role of positive feedback of Ca^{2+} on IP$_3$ in the oscillatory mechanism, and is predicted to cause a transition from oscillatory to non-oscillatory behavior.

3.2 Expression of an IP_3 buffer suppresses Ca^{2+} oscillations

The analytical and numerical results obtained so far indicate that the expression of an IP_3 buffer can be used to identify the dominating Ca^{2+} feedback on $IP_3\dot{T}$he most significant difference in the responses of a system with positive feedback and a system negative feedback is that agonist-induced oscillations always persist in the latter case whereas they can be abolished in the former.

To examine the model predictions experimentally, a molecular IP_3 buffer developed in the laboratory of A.P. Thomas (Newark, USA) has been used. It consists of the N-terminal ligand binding domain of rat type 1 IP_3R linked to enhanced green fluorescent protein (EGFP-LBD; [46], Gaspers et al. in preparation). Chinese hamster ovary (CHO) cells were transiently transfected with EGFP or EGFP-LBD, then challenged with submaximal and maximal ATP concentrations. The subsequent $[Ca^{2+}]_c$ responses were monitored via changes in the fura-2 fluorescence ratio. EGFP fluorescence was utilized to distinguish transfected from non-transfected cells in a given field of view and to estimate the intracellular concentration of the transgene (see materials and methods, Section 2.1).

The addition of low ATP concentrations elicited periodic $[Ca^{2+}]_c$ spikes in $> 85\%$ of the CHO cells expressing EGFP (Fig. 3.4A, B) or non-expressing cells from cultures transfected with EGFP-LBD (not shown). Agonist-evoked $[Ca^{2+}]_c$ oscillations required functional ER Ca^{2+} stores (i.e. thapsigargin-sensitive), but ceased abruptly upon removing extracellular Ca^{2+} suggesting that plasma membrane Ca^{2+} fluxes are relatively strong in this cell type (not shown). In both EGFP-expressing and non-expressing cells, the $[Ca^{2+}]_c$ increase immediately following agonist challenge was more prolonged and the rate of Ca^{2+} rise faster than subsequent $[Ca^{2+}]_c$ oscillations (Fig. 3.4A, C). No systematic differences were evident in agonist sensitivity or the pattern of the $[Ca^{2+}]_c$ spiking between EGFP expressing and non-expressing cells suggesting that neither EGFP nor the transfection reagents *per se* had significant effects on Ca^{2+} signaling. By contrast, the presence of EGFP-LBD had a dose-dependent effect on the agonist dependent Ca^{2+} oscillations in CHO cells (Fig. 3.4A). High levels of EGFP-LBD expression correlated with a loss of repetitive $[Ca^{2+}]_c$ spiking and the appearance of low amplitude $[Ca^{2+}]_c$ increases (Fig. 3.4A, B). Moreover, EGFP-LBD expression significantly slowed the rate of $[Ca^{2+}]_c$ rise (Fig. 3.4C; $p < 0.01$) and significantly broadened the width of the $[Ca^{2+}]_c$ spike (Fig. 3.4D; $p < 0.05$) compared to EGFP expressing cells.

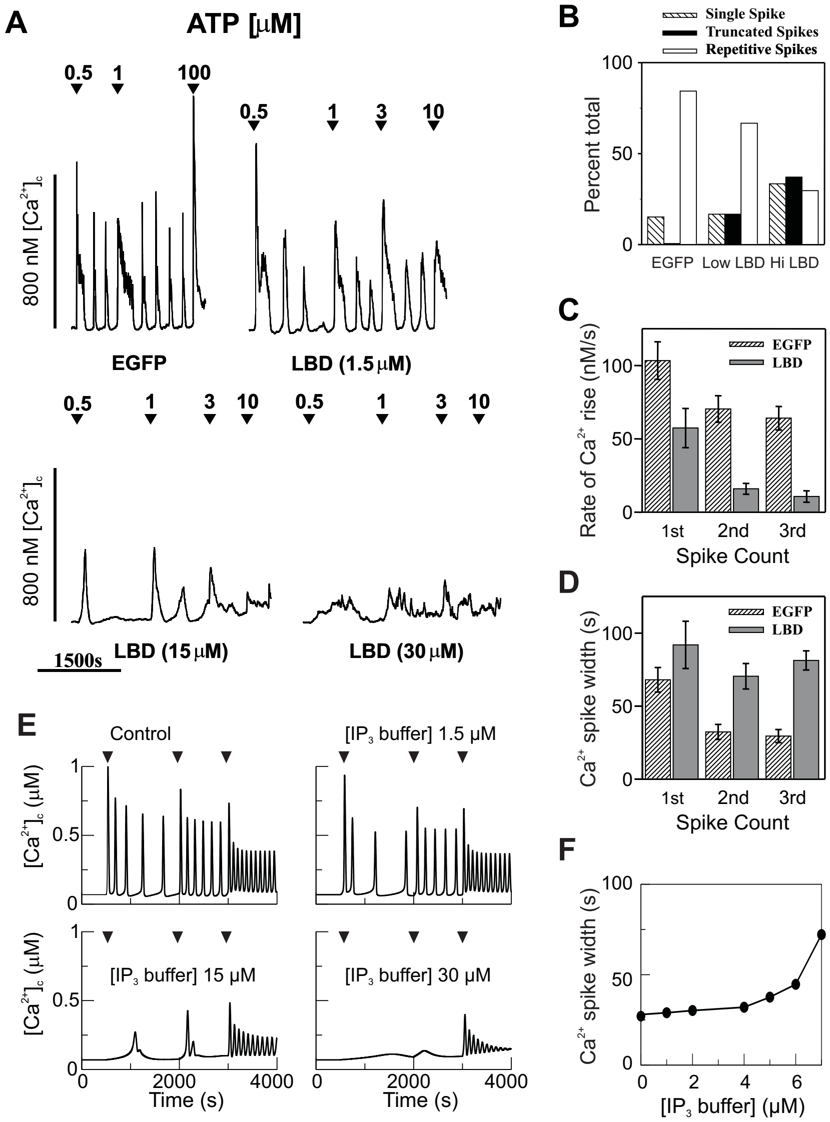

Figure 3.4: Effects of an IP$_3$ buffer on ATP-evoked [Ca^{2+}]$_c$ oscillations in CHO cells. Cells ($n = 5$ independent cultures) were transiently transfected with pEGFP-LBD (EGFP-LBD) or pEGFP-C1 (EGFP) and imaged as described in Section 2.1. (A) Typical ATP-evoked [Ca^{2+}]$_c$ spikes in CHO cells expressing EGFP or different levels of EGFP-LBD. (B) Cells expressing EGFP-LBD were arbitrarily divided into low (489 ± 66 units; $n = 18$ cells) or high (3170 ± 480 units; $n = 27$ cells) categories using a cutoff of 1000 fluorescence intensity units. The estimated mean EGFP-LBD concentration was 6 ± 0.8 or 38 ± 6 μM, respectively. Truncated spikes are low amplitude [Ca^{2+}]$_c$ oscillations similar to those shown in the bottom traces of panel A. (C) Initial rates of [Ca^{2+}]$_c$ rise.

For these data, only EGFP ($n = 52$ cells) or EGFP-LBD ($n = 20$ cells) expressing cells, where low ATP challenge (0.5 or 1 μM) evoked at least 3 sequential baseline-separated Ca^{2+} spikes, have been analyzed. This was observed predominately in cells expressing low levels of EGFP-LBD and, thus, probably the actions of IP_3 buffering on the kinetics of $[Ca^{2+}]_c$ oscillations is underestimated.

According to the theoretical results, the disappearance of the oscillations and a slowing of the Ca^{2+} rise suggests that IP_3 oscillations driven by positive feedback of Ca^{2+} on IP_3 production are involved in this system. We have simulated the positive-feedback model with relatively strong plasma-membrane Ca^{2+} fluxes as observed in CHO cells. At high concentrations of IP_3 buffer (Fig. 3.4E), the model exhibits single transients (for lower agonist dose) and repetitive truncated spikes (for high agonist dose). Both responses closely resemble the experimentally observed patterns in cells expressing high amounts of EGFP-LBD. The Ca^{2+} oscillations at lower concentrations of IP_3 buffer (Fig. 3.4F) exhibit a broadening of the individual spikes, which is very similar to the experimental observation in cells expressing low amounts of EGFP-LBD. Also the observed decrease in the rate of Ca^{2+} rise is reproduced by the model (data similar to Fig. 3.2A). A model with negative feedback could account for none of the experimental findings (see Fig. 3.2).

Figure 3.4 (continued): (D) The width of the $[Ca^{2+}]_c$ spike were determined at half peak height. (E,F) Positive-feedback model, Ca^{2+} activation of PLC. (E) Simulations with different IP_3 buffer concentrations (as indicated) show a good agreement with the EGFP-LBD experimental data in A. An increase in ATP is simulated by an increase in the maximal activity of PLC (arrowheads). (F) One also observes a significant increase in spike width. To match the Ca^{2+} oscillations in CHO cells, all variables have been slowed by a factor 10, reference parameter set as in Fig. 3.2. In (E) $V_{PLC} = 0.125$, 0.2, 0.4 μM/s. Initial condition at $V_{PLC} = 0.05$ μM/s. In (F) $V_{PLC} = 0.2$ μM/s.

Chapter 4

Towards an integrative model for the phosphoinositide metabolism

In the previous chapters, I was able to show how the dynamics of inositol 1,4,5-trisphosphate (IP_3) plays a central role in modulating Ca^{2+} signals. The models for the Ca^{2+} dynamics used here, and most of published models (see reviews [144, 152]), consider production and degradation of IP_3 but neglect the reactions leading to its precursor phosphatidylinositol-4,5-bisphosphate (PIP_2). The mathematical models tacitly assume that the PIP_2 level remains constant during stimulation. However, this is in contradiction to experimental evidence in several cell lines where PIP_2 and its precursor phosphatidylinositol-4-phosphate (PIP) clearly decrease upon stimulation with hormones [116, 167, 189, 197]. This raises the question on how production and degradation of PIP_2 are balanced in order to maintain, during stimulation, the observed elevated cytoplasmic IP_3 concentration. A long-lasting IP_3 signal is the *conditio sine qua non* for long-lasting $[Ca^{2+}]_c$ oscillations measured in cells such as hepatocytes.

After shortly reviewing the reactions involved in the phosphoinositide pathway and the available data, I will discuss several alternative mathematical models. The experimental data allow to estimate kinetic parameters and so to make predictions on duration and amplitude of IP_3 signals, and on the contribution of the different reactions. If the PIP_2 production flux is independent of PIP_2 and stimulus, an increase in phospholipase C (PLC) activity can only lead to a transient increase in IP_3. The estimated maximal duration of this transient is far below the duration of agonist dependent Ca^{2+} signals. To generate a long-lasting increase in IP_3 concentration the PIP and PIP_2 phosphatase, two enzymes, which counteract phosphatidylinositol (PI) 4-kinase and PIP 5-kinase, are required. This regulatory advantage is gained at the cost of higher energy consumption, necessary to maintain the futile phosphorylation-dephosphorylation cycles. I finally show, by coupling the Ca^{2+} and IP_3 metabolism models, how Ca^{2+} feedbacks on the IP_3/phosphoinositide metabolism can give long-lasting oscillating Ca^{2+} signals without the requirement of futile cycles.

4.1 The phosphoinositide pathway

4.1.1 Structure

Phosphatidylinositol phosphates are composed of a membrane-associated phosphatidic acid group and a glycerol moiety that is linked to a phosphorylated inositol head group (Fig. 4.1A). The main pathway for their production and degradation is shown in Fig. 4.1B. In this pathway one can differentiate between metabolites bound to cellular membranes and freely diffusing.

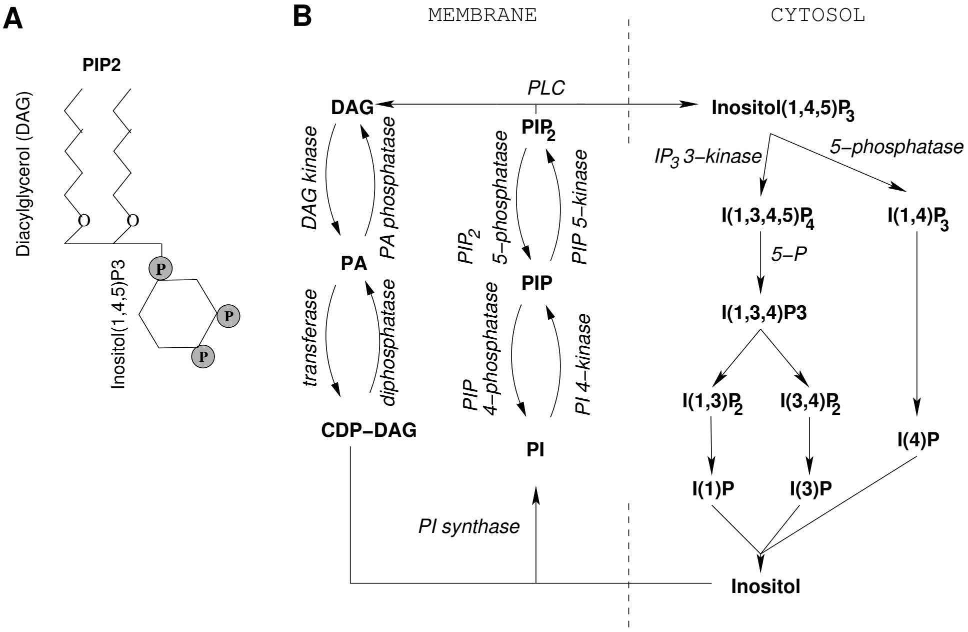

Figure 4.1: (A) Scheme of PIP_2 which can be hydrolyzed by phospholipase C to IP_3 and DAG. (B) Main pathway of phosphoinositides synthesis and degradation. Inositol is phosphorylated/dephosphorylated at different positions (indicated by the number in brackets). DAG is first phosphorylated to phosphatidic acid (PA) before binding to CTP to form CDP-DAG.

Several isoforms of phospholipase C (PLC) are activated by external stimulation [135], they catalyze hydrolysis of phosphatidylinositol-4,5-bisphosphate (PIP_2) to diacylglycerol (DAG) and the freely diffusing inositol 1,4,5-trisphosphate IP_3. In a series of phosphorylation and dephosphorylation reactions IP_3 is freed of all its phosphates to finally obtain inositol. On the other branch of the pathway, DAG is activated by covalent binding to the nucleotide CTP. Under action of PI synthase CDP-DAG and inositol are consumed to form phosphatidylinositol. The phosphorylation of its inositol moiety by PI 4-kinase generates PIP, which is further phosphorylated by PIP 5-kinase to PIP_2. Phosphorylation of PIP and PI is counteracted by PIP_2 5-phosphatase and PIP 4-phosphatase, respectively. The production of CDP-DAG is also opposed by two phosphatases.

The pathway depicted in Fig. 4.1B is the main synthesis and degradation pathway, however one should keep in mind that there are side branches which can be regulated by external stimuli [18, 53, 178]. For instance, it has been reported that PIP_2 can be produced by 5-phosphorylation of PI and subsequent 4-phosphorylation of PI-5-phosphate [18, 128]. PIP_2 can be further phosphorylated to PI (3,4,5) trisphosphate by the phosphatidylinositol 3-kinase (cf. [178]). The substrates necessary for the synthesis of PI, inositol and DAG, can also come from side branches of the metabolism. For instance inositol can be synthesized from different sugars (e.g. glucose-6-phosphate), DAG can be obtained from the hydrolysis of other phosphoinositides, e.g. phosphatidylcholine or phosphatidylethanolamine (see also the KEGG database http://www.genome.jp/kegg/pathway.html [78]). The contribution of these different branches to the homeostasis of the phosphoinositides has not been quantified in detail. Therefore, for the modeling I will not take them into account.

4.1.2 Quantitative data

Measurements of pathway metabolites were done principally in rat hepatocytes and mouse neuroblastoma cell lines with radioactively labeled PI, PIP, PIP_2 and inositol phosphates. A detailed summary of experimental results is given in Tab. 4.1. The relative amounts of the three phosphoinositides are consistent in the different cell lines and experiments. The plasma membrane density of PI ([PI]) is much higher than PIP density ([PIP]) and PIP_2 density ($[PIP_2]$), [PIP] is slightly lower than $[PIP_2]$. The fractional changes after stimulation are also similar in the different experiments. [PI] remains nearly constant, whereas [PIP] and $[PIP_2]$ decrease by a factor of ~ 2. In contrast the absolute values often differ by one order of magnitude. For IP_3 a similar trend is observed. The reported absolute concentrations in the unstimulated cells strongly varies between cell lines and experiment, but the increase observed after stimulation is about 10 fold. The changes in phosphoinositides concentrations last for the total duration of

	Unstimulated cells					Hormone stimulated cells		
	Relative amount (%)		Density (molecules/μm^2)			Fractional changes		
	Hepatocyte [167]	Neuroblastoma [189, 197]	Hepatocyte [167]	Neuroblastoma [189, 197]	Other	Hepatocyte [167]	Neuroblastoma [189]	Other
PI	96.5	94.32; 95.05	110225	913162; 142857	–	0.92	0.86	–
PIP	1.33	2.53; 2.28	1,526	24494; 3428	–	0.7	0.32-0.4	–
PIP_2	2.08	3.14; 2.66	2,370; 14845 [116]	30400; 4000	–	0.65; 0.51 [116]	0.28-0.35; $0.35^{\dagger}$ [197]	–
DAG	–	–	212077 [116]	–	–	2-4 [116]	–	–
			Concentration (μM)					
IP_3	–	–	$0.1^{\ddagger}$; 1 [51, 116]	0.01; 0.16; 1 [43, 186, 189]	$0.01^{\ddagger}$; 0.04 [42, 95]	3-4; 6 [116, 168]	4; $6\text{-}12^{\dagger}$; 8-12 [43, 186, 189]	15 [95]
IP_x	–	–	–	16.7 [189]	–	–	3 [189]	–

† In [43, 197] effect of hormone is transient (<150 s).

‡ In [42, 51] IP_3 is directly increased. Given is the lowest IP_3 concentration leading to a Ca^{2+} signal.

Table 4.1: Concentrations of phosphoinositides, DAG, IP_3 and IP_3 products in unstimulated and stimulated cells. The other cells studied are smooth muscle cells, and Xenopus Oocytes [42, 95]. IP_x represents the sum of different inositol-phosphates (IP_1, IP_2, IP_3, ...). In part of the literature phosphoinositides quantities are given in amount/mg cell protein. These values are converted into densities or concentrations by taking $2*10^6$ cells/mg cell protein [189], 3550 μm^2 plasma membrane surface, and 2.5 pl cytoplasmic volume [81].

	Half-lifes (s)		
	Hepatocyte	Neuroblastoma	Xenopus oocyte
IP_3	30 [116]	6.2; 9; 12.5 [43, 186, 197]	60-500† [150]
IP_4	–	–	1800 [150]
IP_x	–	200 [189]	–
DAG	600 [116]	–	–

† for high and low $[Ca^{2+}]_c$, respectively.

Table 4.2: Half-lifes of the PLC reaction products. IP_x stands for the sum of inositol phosphates (i.e. IP_3, IP_4, IP_2 ...). Half-life is determined after $1/e$ decay.

	Concentrations		**Half-lifes**
	Unstimulated	Stimulated	
IP_3	0.15 μM, $\overline{Y}_1$	1.5 μM, $\overline{Y}_1^*$	6.66 s, $1/k_4$
IP_3 products	–	–	66.6 s, $1/k_6$
PI molecules/μm^2	12015, $\overline{X}_1$	10093, $\overline{X}_1^*$	–
PIP molecules/μm^2	3223, $\overline{X}_2$	1289, $\overline{X}_2^*$	–
PIP_2 molecules/μm^2	4000, $\overline{X}_3$	1440, $\overline{X}_3^*$	–

Table 4.3: Reference concentrations and half-lifes in unstimulated and stimulated cells used for the modeling. Shown are also the notations used in the mathematical models.

stimulation (>15 min [189], >30 min [168], >60 min [116]). In some cases, one observes for $[PIP_2]$ and [PIP] a slow (>30 min) recovery to basal levels [116]. Only in bradykinin stimulated neuroblastoma cells do the $[IP_3]$ and $[PIP_2]$ changes last for less than 120 s [43, 197]. The metabolites half-lifes are also a source of valuable informations (Tab. 4.2). There is strong variation between cell types, but for one cell type the experimental values are similar. Typically, the half-life of DAG and IP_3 products is about 10–20 times longer than that of IP_3.

Reference values which are used for estimating the model parameters are listed in

Tab. 4.3. The differences pointed previously may be accounted for by (*i*) increasing all concentrations by the same factor, and by (*ii*) changing the life time of IP_3. In (*i*) the values of most of the parameters remain unchanged as these are determined by the density ratios and the degradation rate constant of IP_3 (see below). In (*ii*) all parameters are rescaled by the same factor.

4.2 The phosphoinositide pathway as a linear chain

Phosphorylation of PI and PIP is counteracted by the PIP phosphatase and the PIP_2 phosphatase, respectively (Fig. 4.1B). These phosphorylation-dephosphorylation cycles are so called futile cycles. Futile because the ATP consumed to maintain a certain net production rate of IP_3 is higher in their presence. I will show how this apparently unfavorable property allows for a flexible control of cytosolic IP_3 concentration.

4.2.1 The model

The mathematical treatment of the phosphoinositide pathway is simplified by following assumptions:

- Inositol and CDP-DAG do not change during stimulation so that phosphatidylinositol is produced by the PI synthase at a constant rate. PI is removed by PI 4-kinase mediated phosphorylation and by an additional path. This additional degradation path reveals essential for controlling $[IP_3]$. It can be equated with 5- and/or 3-phosphorylation by PI 5-kinase and 3-kinase, respectively [6, 128].

- Degradation of IP_3 is described by one reaction, the fate of IP_3 products is not specifically modeled.

- Reaction rates depend linearly on the concentrations. Thus, the enzymes are assumed to be unsaturated with substrate.

The first two points lead to the linear chain depicted in Fig. 4.2. The latter one allows for a precise estimation of kinetic parameters. Further in the text some of these assumptions will be relieved, and their role in IP_3 homeostasis will be discussed.

The system of equations governing the time evolution of PI, PIP and PIP_2 plasma membrane densities is

$$\frac{dX_1}{dt} = v - \kappa X_1 - k_1 X_1 + k_{-1} X_2 \tag{4.1}$$

$$\frac{dX_2}{dt} = k_1 X_1 - k_{-1} X_2 - k_2 X_2 + k_{-2} X_3 \tag{4.2}$$

$$\frac{dX_3}{dt} = k_2 X_2 - k_{-2} X_3 - k_3 X_3. \tag{4.3}$$

For the cytosolic IP_3 concentration one has

$$\frac{dY_1}{dt} = k_3 f X_3 - k_4 Y_1. \tag{4.4}$$

X_1, X_2, X_3 are the plasma membrane densities of PI, PIP, and PIP_2, respectively, Y_1 is the cytosolic concentration of IP_3. v is the PI synthase rate, κ the rate constant of the additional PI degradation path. k_1 and k_2 are phosphorylation rate constants characterizing respectively PI 4-kinase and PIP 5-kinase. k_3 characterizes the activity of PLC, k_4 the degradation of IP_3. The rate constants of PIP and PIP_2 dephosphorylation are k_{-1} and k_{-2}, respectively. The factor $f = A_{pm}/(V_{cyt} N_A)$ in Eq. (4.4) (membrane surface A_{pm} to cytoplasmic volume V_{cyt} and Avogadro constant N_A) accounts for a reaction occurring at the plasma membrane, but which releases its product in the cytosol.

In steady state ($dX_i/dt = 0$, $i = 1, \cdots, 3$; $dY_1/dt = 0$) the concentrations are given by

$$Y_1 = \frac{V_m f}{k_4} \frac{k_3}{k_3 + K_d} \tag{4.5}$$

$$X_3 = V_m \frac{1}{k_3 + K_d} \tag{4.6}$$

$$X_2 = \frac{V_m}{k_2} \frac{k_{-2} + k_3}{k_3 + K_d} \tag{4.7}$$

$$X_1 = \frac{V_m (k_{-1} + k_2)}{k_1 k_2} \frac{k_3 + \frac{k_{-1} k_{-2}}{k_{-1} + k_2}}{k_3 + K_d}. \tag{4.8}$$

I introduced the maximal production rate through the linear chain V_m and the half-saturation rate constant K_d

$$\text{a) } V_m = \frac{v k_1 k_2}{k_1 k_2 + \kappa (k_{-1} + k_2)}, \text{ and b) } K_d = \frac{\kappa k_{-1} k_{-2}}{k_1 k_2 + \kappa (k_{-1} + k_2)}. \tag{4.9}$$

Using the previous relations some of the parameters can be expressed as function of the known metabolite concentrations when the cell is unstimulated. These are denoted

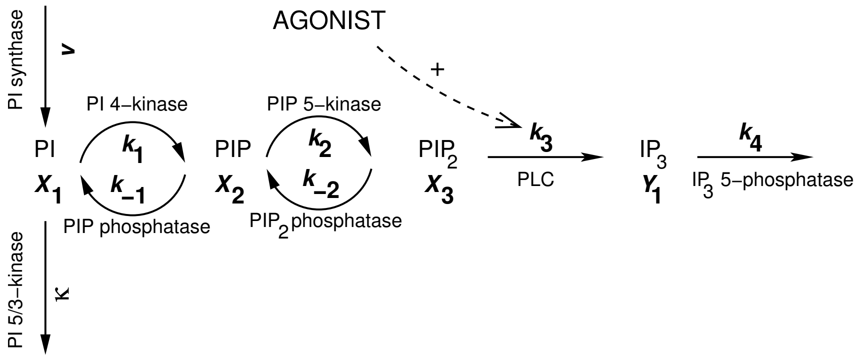

Figure 4.2: Scheme of the linear chain model for the phosphoinositide pathway. In boldfaced are the variable and parameter names used in the model

by $\overline{X}_1$, $\overline{X}_2$, $\overline{X}_3$, and $\overline{Y}_1$ (see Tab. 4.3). One obtains for the PI synthase rate

$$v = \kappa \overline{X}_1 + \frac{\overline{Y}_1 k_4}{\overline{X}_1 f}, \tag{4.10}$$

for the phosphorylation rate constants

$$k_1 = k_{-1}\frac{\overline{X}_2}{\overline{X}_1} + \frac{\overline{Y}_1 k_4}{\overline{X}_1 f} \tag{4.11}$$

$$k_2 = k_{-2}\frac{\overline{X}_3}{\overline{X}_2} + \frac{\overline{Y}_1 k_4}{\overline{X}_2 f}, \tag{4.12}$$

and for the basal PLC activity

$$k_3 = k_4 \frac{\overline{Y}_1}{f\overline{X}_3}. \tag{4.13}$$

If the phosphoinositides distribution during stimulation is known, the dephosphorylation rate constants can be determined from

$$k_{-1} = f_c \frac{k_4(\overline{Y}_1^*\overline{X}_1 - \overline{Y}_1\overline{X}_1^*)}{f(\overline{X}_2\overline{X}_1^* - \overline{X}_2^*\overline{X}_1)} \tag{4.14}$$

$$k_{-2} = f_c \frac{k_4(\overline{Y}_1^*\overline{X}_2 - \overline{Y}_1\overline{X}_2^*)}{f(\overline{X}_3\overline{X}_2^* - \overline{X}_3^*\overline{X}_2)}. \tag{4.15}$$

Where * denotes the steady state concentrations during stimulation, which is at a PLC rate constant of $k_3 = \overline{Y}_1^* k_4/(f\overline{X}_3^*)$. Similarly for the 3/5 phosphorylation of PI one has

$$\kappa = f_c \frac{k_4(\overline{Y}_1^* - \overline{Y}_1)}{f(\overline{X}_1 - \overline{X}_1^*)}. \tag{4.16}$$

The parameter f_c is introduced to tune the contribution of futile cycling to the pathway. By changing f_c, the reference unstimulated steady state remains unaffected (see Section 4.6).

Reaction	**Parameter values** Without phosphatases	 With phosphatases
PLC, k_3	2.38×10^{-3}/s	
PI 4-kinase, k_1	0.794×10^{-3}/s	0.0173/s
PIP 5-kinase, k_2	2.96×10^{-3}/s	0.7135/s
PIP phosphatase, k_{-1}	0	0.0616/s
PIP_2 phosphatase, k_{-2}	0	0.5725/s
IP_3 degradation, k_4	0.15/s	
PI synthase rate, v	546.28 molecules/μm^2/s	
PI 5/3-kinase, κ	0.04467/s	
†Inositol phosphates degradation, k_5	0.015/s	
†PI synthase rate constant, k_6	0.725/s	
†Total inositol, Y_t	70.8×10^6 molecules	
$f = A_{pm}/(V_{cyt}N_A)$	2.358×10^{-3} μMμm^2	

† The parameters k_5 and k_6, and total inositol amount are used in Section 4.3.

Table 4.4: Second column: Parameters are determined from the unstimulated reference state (Tab. 4.3) and Eqs. (4.10)–(4.13). Third column: Parameters are determined from the steady state in unstimulated and stimulated cells and Eqs. (4.10)–(4.13), (4.14)–(4.15). Agonist increases the PLC rate constant k_3, the reference stimulated steady state is obtained for $k_3 = 0.0662/s$. The half-life of IP_3 and inositol phosphates gives k_4 and k_5, respectively (see Tab. 4.3). From [81] $A_{pm} = 3550$ μm^2 and $V_{cyt} = 2.5$ pl which yields the coefficient f.

4.2.2 Transient [IP_3] increase

External stimulation is known to activate PLC and so to increase the rate of PIP_2 hydrolysis, k_3. According to Eqs. (4.5) and (4.9) this may lead to a prolonged increase in [IP_3] if and only if the two phosphatases and the additional PI degradation path are active. Given that any of these processes is missing, that is either k_{-1}, k_{-2} or κ are zero (Figs 4.3A, 4.4A, D), the steady-state [IP_3] does not change with an increase in PLC activity (half-saturation rate constant K_d vanishes, Eq. (4.9b)). It holds

$$\begin{aligned} Y_1 &= \frac{V_m f}{k_4} \\ &= \frac{v k_1 k_2 f}{k_4 \left[k_1 k_2 + \kappa(k_{-1} + k_2)\right]} = \overline{Y}_1. \end{aligned} \tag{4.17}$$

Accordingly, the stationary [IP$_3$] is controlled by processes which are not supposed to be activated during stimulation. An increase in PLC rate constant produces a transient elevation in [IP$_3$], which will inevitably return to its basal level (Fig. 4.3B). On the other hand [PIP$_2$] decreases and reaches a lower steady state during stimulation (Eq. (4.6) and Fig. 4.3C). Also [PIP] sinks if [PIP$_2$] phosphatase is active (Eq. (4.7), Fig. 4.4C), whereas [PI] decreases only when both phosphatases are present (Eq. (4.8), Fig. 4.4F).

The transient in [IP$_3$] is accompanied by few [Ca^{2+}]$_c$ spikes (Fig. 4.3D). These signals are often ascribed to desensitization of agonist receptors, by e.g. internalization or covalent modifications [26, 75]. In the light of IP$_3$ metabolism, the depletion of PIP$_2$ is intrinsically a desensitization mechanism. Indeed, increasing the activity of PLC transiently "resensitizes" the system and produces additional spikes (Fig. 4.3D, arrows). Information on which type of cells show transient signals of this type can be gained when the duration of these is compared to the duration of Ca^{2+}/IP$_3$ signals observed in experiments. The definitions proposed by Heinrich et al. (2002) [58] prove useful for this comparison. The mean signal duration is defined by

$$\theta = 2\sqrt{\frac{\int_0^\infty t^2 \Delta Y_1(t) dt}{\int_0^\infty \Delta Y_1(t) dt} - \left(\frac{\int_0^\infty t \Delta Y_1(t) dt}{\int_0^\infty \Delta Y_1(t) dt}\right)^2}, \tag{4.18}$$

where $\Delta Y_1(t) = Y_1(t) - \overline{Y}_1$. Only high enough IP$_3$ concentrations sensitize the IP$_3$-receptors and generate [Ca^{2+}]$_c$ signals, thus the second important quantity is the mean amplitude which is defined by

$$\alpha = \frac{\int_0^\infty \Delta Y_1(t)}{\theta}. \tag{4.19}$$

A graphical representation of these two measures is shown in Fig. 4.3B.

I calculated the duration and amplitude of the signal when the system is in the reference unstimulated state, that is Eqs. (4.10)–(4.13) must be fulfilled. As described in Appendix B.1 when PIP$_2$ phosphatase is inactive ($k_{-2} = 0$) one derives for the signal duration

$$\theta = 2\sqrt{\frac{1}{k_3^{*2}} + \frac{1}{{k_4}^2}}, \tag{4.20}$$

and for the IP$_3$ signal amplitude

$$\alpha = \frac{\overline{Y}_1 \left(\frac{1}{k_3} - \frac{1}{k_3^*}\right)}{\theta} \tag{4.21}$$

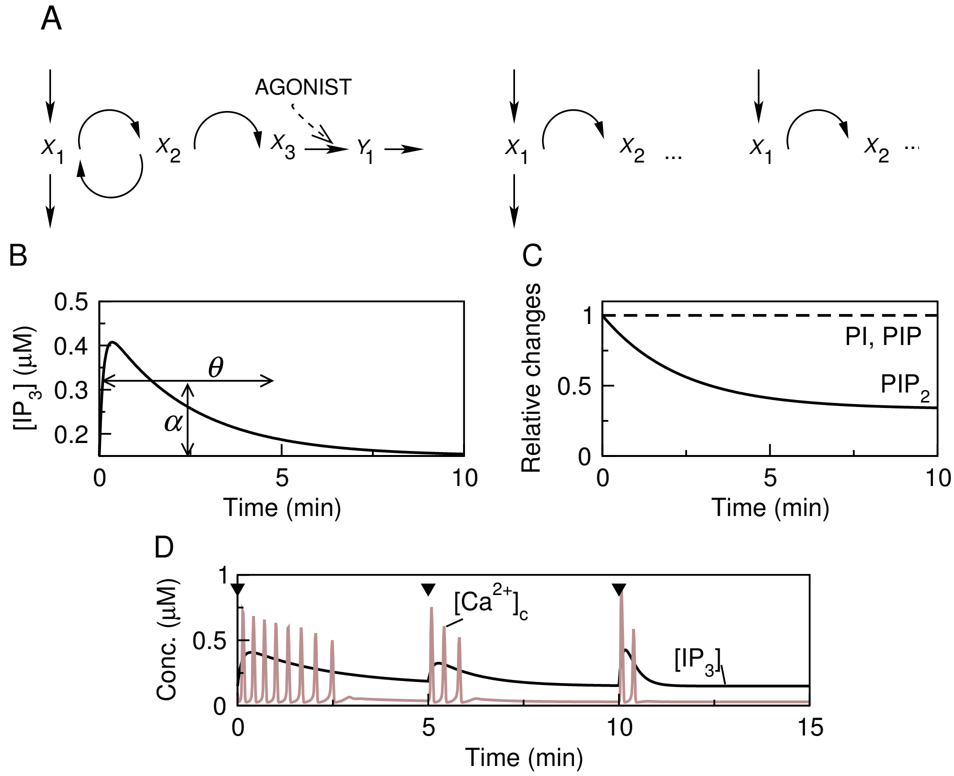

Figure 4.3: Transient increase in [IP$_3$]. (A) The three depicted pathways do not have the PIP$_2$ phosphatase. They all exhibit the same phosphoinositide kinetics (see B and C) after stimulation of PLC. (B) Changes in [IP$_3$] after agonist mediated activation of PLC. Shown are the signaling length θ and amplitude α (Eqs. (4.18)–(4.19)). (C) PIP$_2$ density (solid line) decreases during stimulation, whereas PI and PIP densities (dashed lines) remain constant. Changes are relative to the unstimulated state. (D) [Ca^{2+}]$_c$ oscillations, grey line, cease when the [IP$_3$], black line, falls below a threshold value. Increasing the stimulus transiently resensitizes the system to agonist. Parameters listed in Tab. 4.4, (B), (C) PLC rate constant k_3 is set to 0.007/s, in (D) at time indicated by arrows $k_3 = 0.007$, 0.014 and 0.062/s. Model for the Ca^{2+} dynamics given by Eqs. (2.7)–(2.9). Parameter listed in Tab. 2.1 left column, no positive feedback ($K_{PLC} = 0$).

where $k_3^* \geq k_3$ is the rate constant of stimulated G-protein bound PLC and $\overline{Y}_1$ is the steady state unstimulated [IP$_3$].

The above formulas demonstrate that only processes which are directly connected to IP$_3$, that is PLC and IP$_3$ degradation, govern its time evolution. In particular, PIP phosphatase alone does not affect the kinetics of IP$_3$ (see Fig. 4.3A). Stronger stimulation has opposing effects on amplitude and duration of the IP$_3$ signal. For a high activity of the PLC ($k_3^* \gg k_3, k_4$), the IP$_3$ transient has the shortest duration and the largest amplitude

$$\begin{aligned}\theta(k_3^* \gg k_3, k_4) &= \frac{2}{k_4}\\ \alpha(k_3^* \gg k_3, k_4) &= \frac{\overline{Y}_1\, k_4}{2k_3},\end{aligned}$$

whereas for weak stimulation, $k_3^* \approx k_3$, the signal has a maximal duration, but vanishing amplitude

$$\begin{aligned}\theta(k_3^* \approx k_3) &= 2\sqrt{\frac{1}{{k_3}^2} + \frac{1}{{k_4}^2}} \qquad (4.22)\\ \alpha(k_3^* \approx k_3) &= 0.\end{aligned}$$

With the parameter values from Tab. 4.4 one obtains an IP_3 signal duration which does not exceed 14 min (Eq. (4.22)). This value represents the upper limit for the IP_3 signal duration. To generate a $[Ca^{2+}]_c$ signal, $[IP_3]$ should be high enough to activate the IP_3R leading inevitably to shorter signals. For example, with an IP_3 signal amplitude of 0.15 μM the signal is not longer than 5 min. The presence of PIP_2 phosphatase alone does not allow for a steady increase in $[IP_3]$ after PLC activation, however, it changes the signal duration and amplitude. One can show that in the presence of PIP_2 phosphatase ($k_{-2} \neq 0$, $k_{-1} = 0$ and $\kappa = 0$) the signal duration increases, whereas the signal amplitude is only slightly modified (see Appendix B.1). For $k_3^* \to k_3$ and large k_{-2} the signal duration is maximized and reaches 25 min. With a signal amplitude of 0.15 μM the duration does not exceed 15 min[1]. Thus, the presence of PIP_2 phosphatase makes the phosphoinositide pathway more efficient by prolongating the IP_3 signal. The signal duration further increases when both phosphatases are active and the additional PI degradation path is absent ($k_{-1}, k_{-2} \neq 0$ and $\kappa = 0$). One obtains a maximal duration of $\sim$ 1 hour, and $\sim$ 20 min with a signal amplitude of 0.15 μM. To illustrate these properties, I plotted in Fig. 4.4E the transients obtained in the three cases discussed above for an amplitude of 0.15 μM.

To summarize, the phosphoinositide pathway shown in Fig. 4.2 without one of the phosphatases or without the additional PI degradation pathway can only give rise to transient IP_3 signals. This may underly the $[Ca^{2+}]_c$ dynamics in cells with short-lasting $[Ca^{2+}]_c$ signals. For all cases discussed, the estimated duration of IP_3 transients with non vanishing amplitude does not exceed 30 minutes. In hepatocytes, $[Ca^{2+}]_c$ oscillations can last for more than 90 min, indicating long-lasting IP_3 signals ([138], L.D. Gaspers,

---

[1] The signal duration is maximized by varying the stimulated PLC rate constant k_3^* with the constraint of fixed signal amplitude. This problem is solved using the method of *Lagrange*-multipliers.

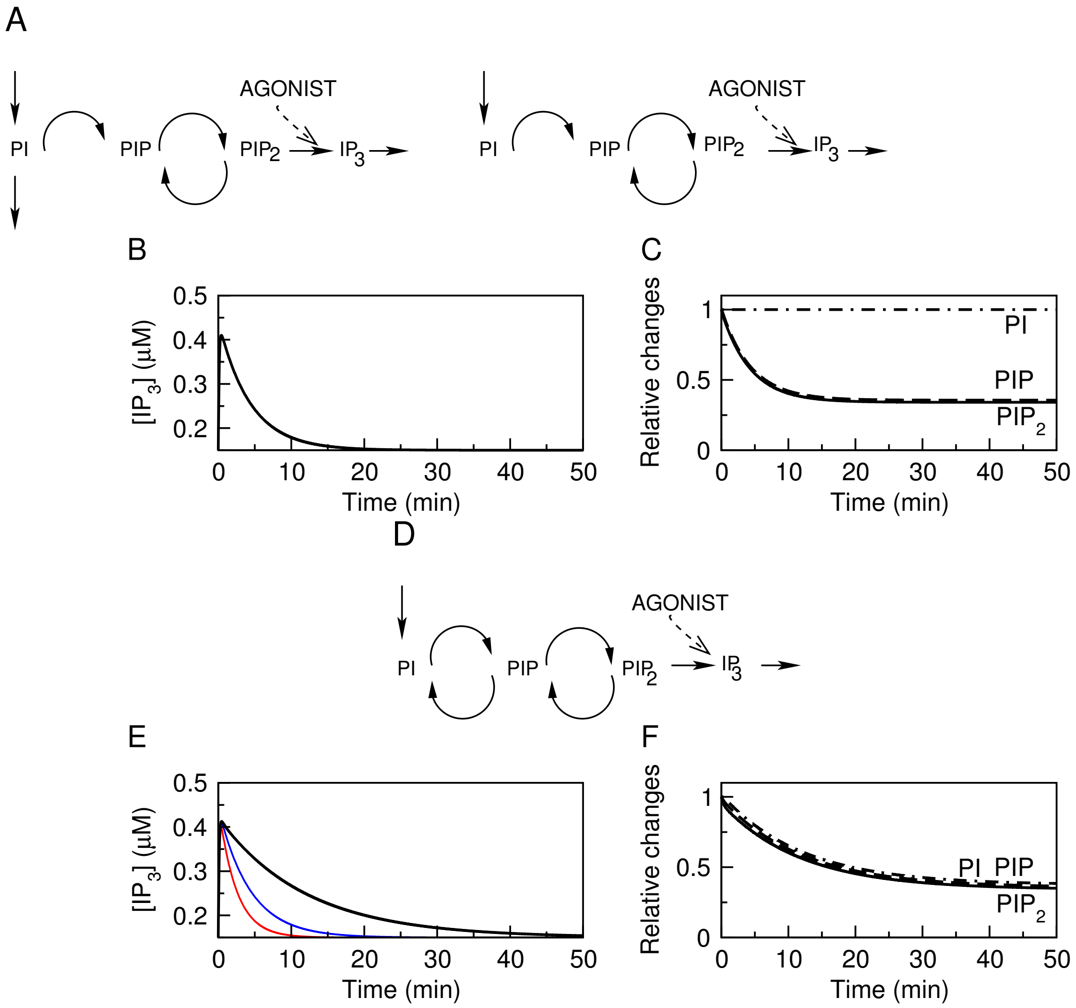

Figure 4.4: The transient IP_3 signal lasts longer when PIP_2 phosphatase is active. (A) The two pathways show identical kinetics (same reference unstimulated state). (B) $[IP_3]$ after agonist mediated activation of PLC. (C) $[PIP_2]$ (solid line) and [PIP] (dashed line) decrease, whereas [PI] (dot-dashed line) remains constant. (D) Both phosphatases are active, but PI is degraded by PI 4-kinase only. (E) $[IP_3]$ after activation of PLC (solid black line). For comparison the shorter lasting IP_3 transients in the absence of PIP_2 phosphatase (blue line, same as B) or PIP phosphatase (red line, same as Fig. 4.3). (F) All three phosphoinositides decrease. Parameters given in Tab. 4.4, $k_3 = 0.007/\mathrm{s}$; in (B),(C) $k_{-1} = 0$, $k_{-2} = 0.1/\mathrm{s}$, $k_2 = 0.127/\mathrm{s}$; in (E), (F) $\kappa = 0$, $v = 9.5$ molecules/$\mu\mathrm{m}^2$/s, $k_{-1} = 0.1/\mathrm{s}$, $k_{-2} = 0.1/\mathrm{s}$, $k_1 = 0.0276/\mathrm{s}$, $k_2 = 0.127/\mathrm{s}$.

personal communication). The observed $[IP_3]$ increase in hepatocytes lasts for more than 60 min [116]. These results indicate that at least in such cell type all processes depicted in Fig. 4.2 must be active. The phosphatases play a determinant role in controlling the $[IP_3]$ dynamics (see Section 4.5). Alternatively, as suggested by Xu and coworkers [197], the kinases themselves could be activated during stimulation (see discussion in Chapter 5).

4.2.3 Steady increase in [IP$_3$] obtained with futile cycling

As pointed out in the previous section, activation of PLC leads to a long-lasting increase in [IP$_3$] when the two phosphatases and the PI 3/5-kinases are active (Eq. (4.5) and (4.9)). The rise in [IP$_3$] is accompanied by a decrease in the plasma membrane density of the three phosphoinositides (Fig. 4.5B). The depicted curves closely match the experimental measurements from Willars and coworkers [189]. Also the kinetics are in agreement with the experimental data (Fig. 4.5C, D). One notices that the initial inflection observed in the data is not reproduced by the model. Willars and coworkers suggested that this inflection is due to agonist receptor desensitization. The insets of Fig. 4.5C and D show that implementing this hypothesis, by assuming a PLC rate constant which relaxes in time to a lower value (see Figure 4.5 legend), improves the accordance between data and model.

For strong stimulation, $k_3 \gg K_d$, the [IP$_3$] reaches a maximal value Y_1^m, which represents the upper limit in [IP$_3$] attained with the phosphoinositide pathway. Using Eq. (4.5) and Eqs. (4.10)–(4.12) one obtains

$$Y_1^m = \overline{Y}_1 + \frac{f\overline{X}_3\kappa k_{-1}k_{-2}}{k_4\left[k_{-1}\left(\kappa + \frac{k_4\overline{Y}_1}{f\overline{X}_1}\right) + k_{-2}\left(\frac{\kappa\overline{X}_3}{\overline{X}_2} + \frac{k_4\overline{X}_3\overline{Y}_1}{f\overline{X}_1\overline{X}_2}\right) + \frac{k_{-1}k_{-2}\overline{X}_3}{\overline{X}_1} + \frac{\kappa k_4\overline{Y}_1}{f\overline{X}_2} + \frac{k_4^2\overline{Y}_1^2}{f^2\overline{X}_1\overline{X}_2}\right]}. \tag{4.23}$$

Accordingly, any [IP$_3$] can be reached provided that the activity of both phosphatases and PI 3/5-kinases are sufficiently high (large k_{-1}, k_{-2}, and κ). This implies increased phosphorylation of phosphoinositides and so additional energy consumption. The ATP hydrolysis rate is obtained straightforward from

$$v_{ATP} = f\left[(\kappa + k_1)X_1 + k_2X_2\right]. \tag{4.24}$$

For example, in the unstimulated state the phosphoinositide pathway uses 7.18 μM/s ATP. With a cytosolic ATP concentration of $\sim$ 1 mM [3], the total pool of ATP cycles in approx. 2.5 min only to maintain the phosphoinositide pathway.

4.3 Conserved inositol/DAG moieties

One of the assumptions in the previous models was that the concentrations of the PI precursors inositol and CDP-DAG remain constant. However, closer inspection of

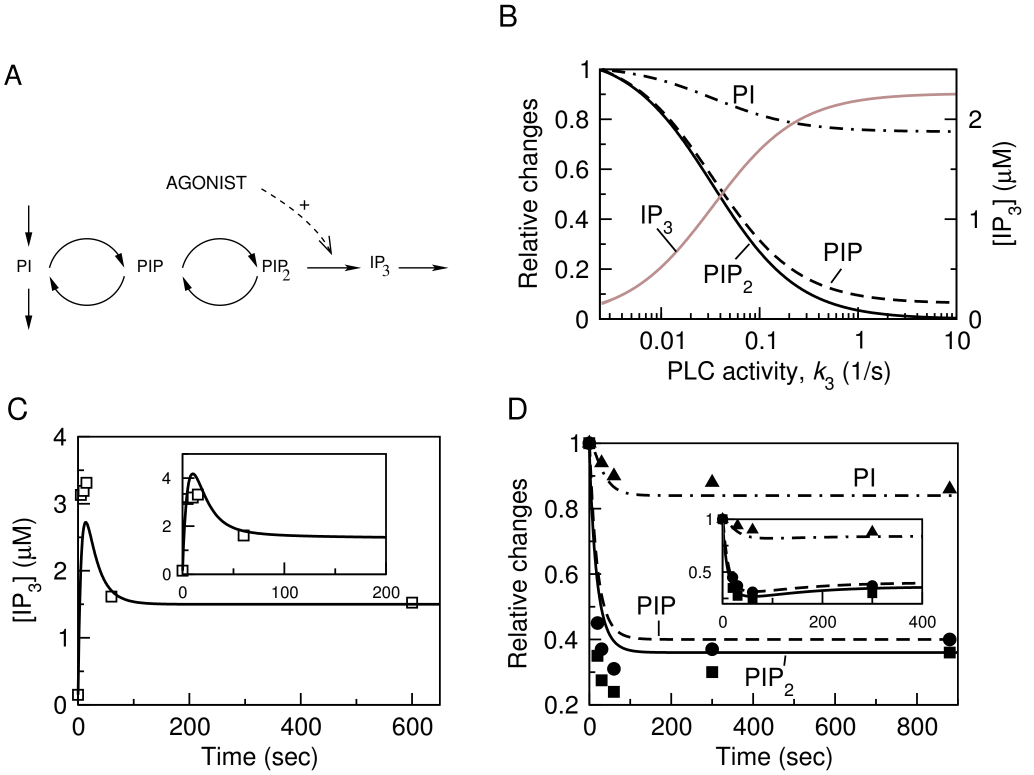

Figure 4.5: Steady increase in [IP_3]. (A) Reaction scheme. (B) Steady state [PI] (dot-dashed line), [PIP] (dashed line), [PIP_2] (solid line), and [IP_3] (grey line) as function of agonist stimulus (k_3, Eqs. (4.5)–(4.7)). Changes are relative to the unstimulated state. (C) Kinetics of [IP_3] in model and experiment (squares). (D) Kinetics of [PI], [PIP], [PIP_2] in model and experiments (triangles, squares, circles, respectively). Experimental data are from [189]. At time $t = 0$, the PLC rate constant is set to $k_3 = 0.0662$/s. Better agreement with the data is obtained by assuming partial desensitization of the agonist receptor (insets in C and D). This is modeled by taking a time dependent PLC activity $k_3 = 0.0662(1 + e^{-t/\tau})$/s where $\tau = 100$ s is the characteristic time of receptor desensitization [75]. The PLC rate constant decreases exponentially from 0.1324/s to 0.0662/s. Parameters listed in Tab. 4.4, right column.

Fig. 4.1B indicates that during stimulation their production rate may change due to accumulation of IP_3 and DAG. I will show here how this may feeds forward and regulate the [IP_3].

If there are no additional production and degradation pathways for inositol and DAG, as shown in Fig. 4.1, or if these are slow compared to the depicted processes, then the total amount of inositol and DAG can be considered constant during stimulation. For example, total inositol consists of free inositol plus PI, PIP, PIP_2, IP_3, and the IP_3 products. For clarity, the mathematical model is posed in terms of a conserved total

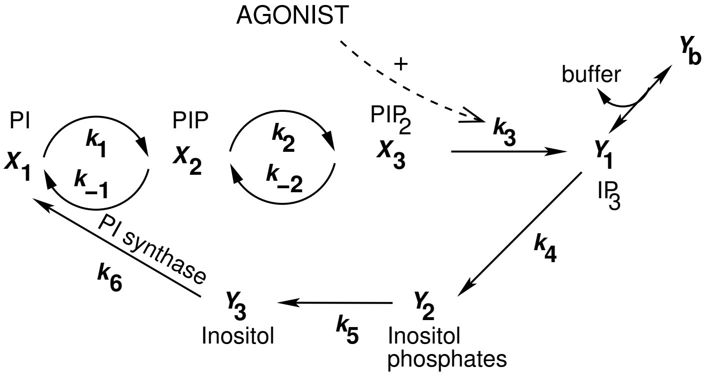

Figure 4.6: Total amount of inositol is conserved. The above reactions are included in the model. An IP$_3$ buffer can bind reversibly to IP$_3$ and form the complex Y_b (see Section 4.4).

inositol concentration. CDP-DAG is assumed, as before, to remain constant during stimulation. In the scheme of Fig. 4.6, the IP$_3$ degradation reactions are lumped into one reaction which leads to an intermediary inositol phosphate pool with concentration Y_2. A second reaction produces inositol, with concentration Y_3, which is used to synthesize PI. The time changes in X_1, Y_2 and Y_3 are given by

$$\frac{dX_1}{dt} = \frac{k_6 Y_3}{f} - k_1 X_1 + k_{-1} X_2$$

$$\frac{dY_2}{dt} = k_4 Y_1 - k_5 Y_2, \qquad \frac{dY_3}{dt} = k_5 Y_2 - k_6 Y_3$$

The model equations for the other metabolites remain unchanged (Eqs. (4.1)–(4.4)).

The conservation relation for the inositol moiety, given as the number of molecules per cell, reads

$$Y_t = A_{pm}(X_1 + X_2 + X_3) + V_{cyt} N_A (Y_1 + Y_2 + Y_3), \tag{4.25}$$

where A_{pm} and V_{cyt} are the plasma membrane area and the cytosolic volume, respectively. One obtains for the steady state [IP$_3$]

$$Y_1 = \frac{Y_t}{V_{cyt} N_A} \frac{1}{k_4 Q}, \tag{4.26}$$

with the following denominator

$$Q = \sum_{i=1}^{6} \frac{1}{k_i} + \frac{k_{-1}}{k_1 k_2} + \frac{k_{-2}}{k_2 k_3} + \frac{k_{-1} k_{-2}}{k_1 k_2 k_3}. \tag{4.27}$$

For the steady state of the other metabolites one has

$$X_1 = \frac{Y_t}{A_{pm}} \left(\frac{1}{k_1} + \frac{k_{-1}}{k_1 k_2} + \frac{k_{-1} k_{-2}}{k_1 k_2 k_3} \right) \frac{1}{Q}, \tag{4.28}$$

$$X_2 = \frac{Y_t}{A_{pm}} \left(\frac{1}{k_2} + \frac{k_{-2}}{k_2 k_3} \right) \frac{1}{Q}, \quad X_3 = \frac{Y_t}{A_{pm}} \frac{1}{k_3 Q} \tag{4.29}$$

$$Y_2 = \frac{Y_t}{V_{cyt} N_A} \frac{1}{k_5 Q}, \quad Y_3 = \frac{Y_t}{V_{cyt} N_A} \frac{1}{k_6 Q}. \tag{4.30}$$

The steady state expression Eq. (4.26) points to a general property of the phosphoinositide pathway with conservation relation, namely that upregulation of processes driving inositol cycling, except IP_3 degradation, leads to an increase in $[IP_3]$ ($k_4 Q$ diminishes when the k_i's, $i \neq 4$, increase Eq. (4.27)). The sustained $[IP_3]$ is maintained by a higher rate of PI production arising from accumulation of free inositol. Thus, different from the case without conservation relation, activation of PLC produces a steady elevation in $[IP_3]$ even in the absence of phosphatases, and the additional degradation path for PI ($k_{-1} = k_{-2} = \kappa = 0$). The increment in $[IP_3]$ after PLC activation depends on which process was the rate limiting prior the stimulation. When no phosphatases are present, the distribution of phosphoinositides in the unstimulated state indicate that the PI 4-kinase reaction is rate limiting (Tab. 4.4, second column). The PLC reaction is not the rate limiting process and therefore its up regulation only minimally changes the $[IP_3]$. Using the values of Tab. 4.4, one obtains an increase from 0.15 to 0.187 μM after activation of PLC. An additional general property of this pathway without phosphatases is that PI, PIP and PIP_2 plasma membrane densities increase with activation of PLC due to accumulation of their precursor inositol (Eqs. (4.28)–(4.30)). This has not been observed in experiments.

Conservation of the inositol moiety obviates for additional degradation paths for PI (3/5 phosphorylation), making the system more energy efficient. Although PLC activation can always produce an increase in $[IP_3]$, the experimental data suggests futile phosphorylation cycles in order to explain (*i*) the strong increase in $[IP_3]$, and (*ii*) the decrease in PI, PIP, and PIP_2 densities during stimulation. Indeed, after introducing the two phosphatases according to Eqs. (4.14)–(4.15) the model reproduces these experimental facts. The model simulations are nearly indistinguishable from the simulations shown in Fig. 4.5. Using a similar mathematical treatment, the same conclusions are derived when the DAG moiety is conserved or both total DAG and inositol are conserved (not shown).

4.4 Effect of an IP_3 buffer on the $[\mathrm{IP}_3]$ in the absence of Ca^{2+} feedbacks

The derived phosphoinositide pathway models allow to answer whether the effects of the IP_3 buffer on the Ca^{2+} signals, in particular abolishment of $[\mathrm{Ca}^{2+}]_c$ oscillations (see section 3.2), could be ascribed to depletion of IP_3?

I have shown that this is not the case when the phosphoinositide metabolism is reduced to IP_3 production and degradation. The IP_3 buffer slows the kinetics of IP_3, but does not change its steady state. The same result is obtained with the more detailed linear chain model, which accounts for the synthesis of the IP_3 precursor PIP_2 (Section 4.2). Only if the inositol moiety is conserved an IP_3 buffer modifies the steady state $[\mathrm{IP}_3]$. This is because sequestration of IP_3 in a non-metabolizable pool effectively decreases the total amount of available inositol.

To assess the magnitude of such an effect, I rewrite the conservation relation for the inositol moiety in the presence of the IP_3 buffer (see Fig. 4.6)

$$Y_t = A_{pm}(X_1 + X_2 + X_3) + V_{cyt}N_A(Y_1 + Y_2 + Y_3 + Y_b). \tag{4.31}$$

In steady state the concentration of IP_3 bound to buffer is given by $Y_b = B_t Y_1/(Y_1 + K_B)$ where B_t is the total concentration of IP_3 buffer and K_B its dissociation constant. One derives the implicit relation

$$Y_1(B_t) = \frac{Y_t}{V_{cyt}N_A}\frac{1}{k_4 Q} - \frac{B_t Y_1(B_t)}{Y_1(B_t) + K_B}\frac{1}{k_4 Q}. \tag{4.32}$$

It is straightforward to solve the corresponding quadratic equation and obtain the IP_3 concentration. One finds that the $[\mathrm{IP}_3]$ monotonically decreases with the IP_3 buffer dissociation constant K_B and reaches a minimum for $K_B = 0$ (Fig. 4.7). Therefore, following inequality for the ratio of $[\mathrm{IP}_3]$ with and without IP_3 buffer holds

$$1 \geq \frac{Y_1(B_t \geq 0)}{Y_1(B_t = 0)} \geq 1 - V_{cyt}N_A\frac{B_t}{Y_t}. \tag{4.33}$$

The above formula shows that the decrease in $[\mathrm{IP}_3]$ due to buffering crucially depends on the total amount of cellular inositol Y_t. The reported phosphoinositides concentrations varied by a factor of 10 (see Section 4.1.2), thus the total inositol Y_t can be estimated to lie between 70 and 700 million molecules/cell. With the maximal IP_3 buffer concentration used in experiments of about 30 μM one obtains

$$1 > \frac{Y_1(B_t = 30)}{Y_1(B_t = 0)} \geq 0.36 \text{ to } 0.93. \tag{4.34}$$

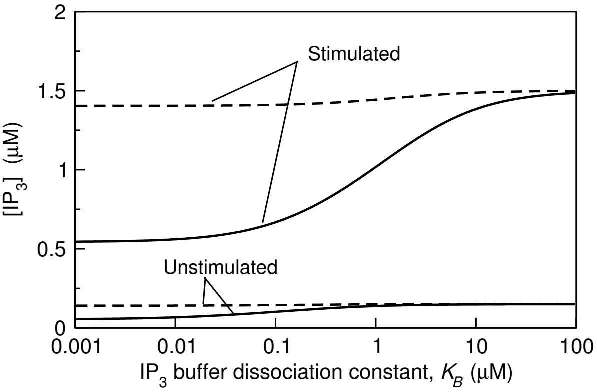

Figure 4.7: Changes in steady state [IP$_3$] as function of buffer dissociation constant K_B. Shown is [IP$_3$] in resting and stimulated cells when total inositol Y_t is 70 (solid line) or 700 (dashed line) million molecules. The decrease in [IP$_3$] due to IP$_3$-buffering is more pronounced at low total inositol (solid line).

Therefore, for strong stimulation, the [IP$_3$] reaches 0.54–1.39 μM. It has been shown that in this range the [IP$_3$] is high enough to induce [Ca^{2+}]$_c$ oscillations [51]. Thus, even for this extreme case, where conservation of inositol and strong binding of the buffer to IP$_3$ are assumed, the effect of IP$_3$ buffering on the [Ca^{2+}]$_c$ dynamics cannot be ascribed to depletion of IP$_3$.

4.5 Perturbing the phosphoinositide pathway

To verify the model predictions, with respect to the contribution of the different enzymes to the IP$_3$ dynamics, one could inhibit or activate some of the kinases and phosphatases (with RNAi for instance cf. [98]). The effect of such perturbations can be analyzed using the metabolic control analysis. I focus on the control exerted by the different reactions on the [IP$_3$]. The unstimulated state is used as reference state. For example, the control coefficient of PLC on the [IP$_3$] is defined by

$$C_{k_3} = \frac{k_3}{\overline{Y}_1}\frac{\partial Y_1}{\partial k_3}, .$$

where the overline indicates the unstimulated steady state. This coefficient, gives the fractional changes in [IP$_3$] after an increase in the rate constant of the PLC mediated reaction, k_3. A positive (negative) control coefficient implies an increase (decrease) in [IP$_3$].

For the linear chain model one obtains

$$C_{k_3} = \frac{K_d}{k_3 + K_d}, \tag{4.35}$$

indicating that PLC exerts no control on the [IP$_3$] if K_d vanishes. This occurs when the activities of the phosphatases and/or the PI 3/5-kinases are weak (Eq. (4.9)). Con-

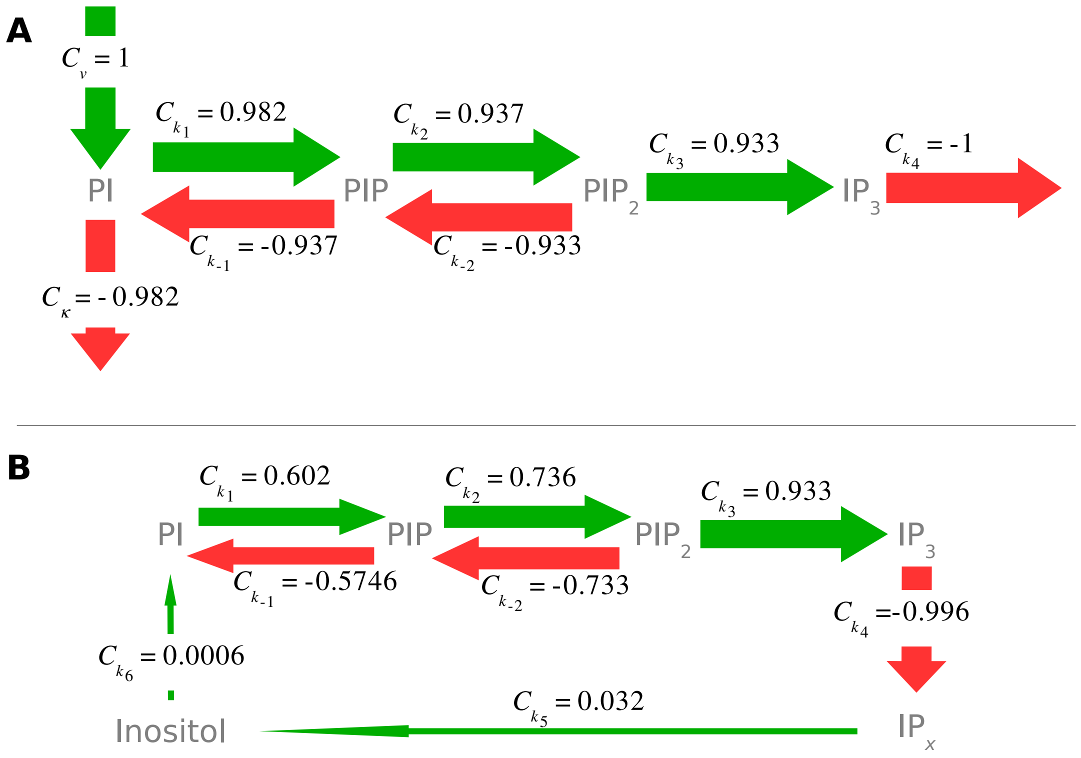

Figure 4.8: Control coefficients of the indicated reactions on the [IP_3] in the linear chain model (A) and in the model with conservation of the inositol moiety (B).

versely, when these enzymes are highly active K_d is large and the control exerted by PLC is maximized. The expressions for the other control coefficients are listed in Tab. 4.5 left column. PLC, PI 4-kinase, PIP 5-kinase, and PI synthase have always positive control on [IP_3], indicating that activation of these enzymes increases the [IP_3]. On the other hand, phosphatases and the PI 3/5-kinases have negative control. The expressions in Tab. 4.5, yield a ranking in the control, which is valid for any parameter values

$$|C_v| = |C_{k_4}| > |C_{k_1}| = |C_\kappa| > |C_{k_2}| = |C_{k_{-1}}| > |C_{k_3}| = |C_{k_{-2}}|. \tag{4.36}$$

Accordingly, PLC exerts the weakest control on the [IP_3] and the IP_3 degradation the strongest. For the estimated parameters the control appears, however, to be evenly distributed between all processes and the differences between absolute control coefficients are small (Fig. 4.8A).

Control can distribute differently when the total amount of inositol is conserved. For the PLC reaction one has

$$C_{k_3} = \frac{\overline{X}_3 A_{pm}}{Y_t} \left(1 + \frac{k_{-2}}{k_2} + \frac{k_{-1}k_{-2}}{k_1 k_2}\right). \tag{4.37}$$

The control of PLC on the [IP$_3$] is proportional to the relative amount of PIP$_2$, $\overline{X}_3/Y_t$, and increases in the presence of phosphatases. If PLC is the bottleneck reaction in the phosphoinositide pathway, because of a low rate constant, the inositol moiety accumulates in form of PIP$_2$ ($\overline{X}_3 \rightarrow Y_t/A_{pm}$). Then, even in the absence of phosphatases, the control exerted by the PLC can be large and an increase in k_3 produces significant changes in the [IP$_3$]. The control coefficient of the other reactions also increases when the inositol moiety accumulates in form the reaction substrate (Tab. 4.5, right column). An exception is made by the IP$_3$ degradation. The control exerted by its rate constant k_4 is negative and approaches zero with accumulation of its substrate IP$_3$. Using the formulas given in Tab. 4.5 one derives following relations, which hold independently of the parameter choice,

$$|C_{k_2}| > |C_{k_{-1}}| \text{ and } C_{k_2} + C_{k_{-1}} = 1 \tag{4.38}$$

$$|C_{k_3}| > |C_{k_{-2}}| \text{ and } C_{k_3} + C_{k_{-2}} = 1. \tag{4.39}$$

Which reaction has the strongest control depends on the distribution of phosphoinositides in the resting state. According to the reported distribution, inositol accumulates primarily as PI, so that inositol phosphates degradation and the PI synthase have practically no control on the [IP$_3$]. The highest absolute control is exerted by the IP$_3$ degradation, followed by the PLC reaction (Fig. 4.8B). Note that due to the low levels of PIP$_2$, the control exerted by the PLC in the absence of phosphatases is low ($C_{k_3} = 0.2$, compared to 0.933 with phosphatases)

In both the linear model and the model with conservation of inositol, inhibition of the phosphatases should produce a significant increase in the IP$_3$ concentration. The changes in the [IP$_3$] are predicted to be similar to changes obtained after hormone addition (i.e. activation of PLC).

Process	Control coefficients Linear model	 Conservation of inositol
C_{k_3} PLC	$\frac{K_d}{k_3+K_d}$	$\frac{\overline{X}_3 A_{pm}}{Y_t}\left(1+\frac{k_{-2}}{k_2}+\frac{k_{-1}k_{-2}}{k_1k_2}\right)$
C_{k_4} IP$_3$ degradation	-1	$-1+\frac{\overline{Y}_1 V_{cyt} N_A}{Y_t}$
C_{k_1} PI 4-kinase	$1-\frac{V_m}{v}\frac{k_3}{k_3+K_d}$	$\frac{\overline{X}_1 A_{pm}}{Y_t}\frac{k_2k_3+k_{-1}(k_3+k_{-2})}{k_2k_3+k_{-1}(k_3+k_1k_{-2})}$
$C_{k_{-1}}$ PIP phosphatase	$-\frac{K_d(1+k_3/k_{-2})}{k_3+K_d}$	$-\frac{\overline{X}_2 A_{pm}}{Y_t}\frac{k_{-1}}{k_1}$
C_{k_2} PIP 5-kinase	$\frac{K_d\,(1+k_3/k_{-2})}{k_3+K_d}$	$\frac{\overline{X}_2 A_{pm}}{Y_t}\left(1+\frac{k_{-1}}{k_1}\right)$
$C_{k_{-2}}$ PIP phosphatase	$-\frac{Kd}{k_3+K_d}$	$-\frac{\overline{X}_3 A_{pm}}{Y_t}\left(\frac{k_{-2}}{k_2}+\frac{k_{-1}k_{-2}}{k_1k_2}\right)$
C_{k_5} inositol phosphates deg.	0	$\frac{\overline{Y}_2 V_{cyt} N_A}{Y_t}$
C_v, C_{k_6} PI synthase	1	$\frac{\overline{Y}_3 V_{cyt} N_A}{Y_t}$
C_κ PI 3/5-kinase	$-1+\frac{V_m}{v}\frac{k_3}{k_3+K_d}$	0

Table 4.5: Control of the different enzymatic reactions on the IP$_3$ concentration. Control coefficients are calculated for the linear model (Eq. (4.5)) and the model with conservation of the inositol moiety (Eq. (4.26)).

4.6 Positive feedback of Ca^{2+} on IP_3 obviates for futile cycling

The mathematical modeling of the phosphoinositide pathway indicates that long-lasting non-oscillating IP_3 signals are obtained in the presence of phosphatases, and such futile cycles demand increased energy (Eq. (4.24)). However, we learned that to induce $[\mathrm{Ca}^{2+}]_c$ oscillations the $[\mathrm{IP}_3]$ must not remain constant. In Chapter 2, I demonstrated how the mutual interaction of oscillating $[\mathrm{Ca}^{2+}]_c$ and $[\mathrm{IP}_3]$ brings about a variety of dynamic behaviors and how several experimental facts could be explained by this interaction. The theoretical results put forward a possible physiological role for $[\mathrm{IP}_3]$ oscillations namely a better frequency encoding of the external stimulus. In this last section, I will show how Ca^{2+} feedbacks on IP_3 metabolism relax the necessity for futile cycling and allow to economize cellular energy.

For the mathematical treatment, I will use the linear chain phosphoinositide metabolism model (Section 4.2). Ca^{2+} feedback on IP_3 production mediated by activation of PLC is taken into account by modifying the equation for the $[\mathrm{IP}_3]$

$$\frac{dY_1}{dt} = k_3 \left(\mu \frac{c^2}{K_{PLC}^2 + c^2} + 1 - \mu \right) f X_3 - k_4 Y_1. \tag{4.40}$$

Here μ is the fraction of Ca^{2+} activated to Ca^{2+} insensitive PLC and c the $[\mathrm{Ca}^{2+}]_c$. For the $[\mathrm{Ca}^{2+}]_c$ dynamics, the model with delayed $\mathrm{IP}_3\mathrm{R}$ receptor inactivation is used (Eqs. (2.7)–(2.9)).

In the absence of phosphatases and PI 3/5-kinase, activation of the Ca^{2+} insensitive PLC induces only a few transients in $[\mathrm{Ca}^{2+}]_c$ and $[\mathrm{IP}_3]$ because $[\mathrm{PIP}_2]$ depletes (Fig. 4.9A). On the contrary, activation of the Ca^{2+} sensitive PLC gives rise to sustained $[\mathrm{Ca}^{2+}]_c$ oscillations (Fig. 4.9B). The rationale for this is that during the interspike interval, characterized by low $[\mathrm{Ca}^{2+}]_c$, PLC is less active so that the PIP_2 hydrolysis rate is low and PIP_2 can regenerate. Mutual activation of IP_3 production and Ca^{2+} release brings the $[\mathrm{Ca}^{2+}]_c$ to the threshold for calcium induced calcium release. The IP_3 necessary to sensitize the $\mathrm{IP}_3\mathrm{R}$ towards Ca^{2+} is supplied by the newly regenerated pool of PIP_2. The explosive increase in $[\mathrm{Ca}^{2+}]_c$ is accompanied by PLC activation which causes concomitant $[\mathrm{IP}_3]$ increase and $[\mathrm{PIP}_2]$ decrease. Thereafter, the $[\mathrm{Ca}^{2+}]_c$ spike is brought to an end by several complementary processes such as $\mathrm{IP}_3\mathrm{R}$ inactivation, depletion of PIP_2, depletion of the ER Ca^{2+} store. The cycle begins anew with regeneration of the PIP_2 pool. The resulting oscillations have the typical properties for an oscillation mechanisms that include positive feedback of Ca^{2+} on IP_3, namely long-period oscillations

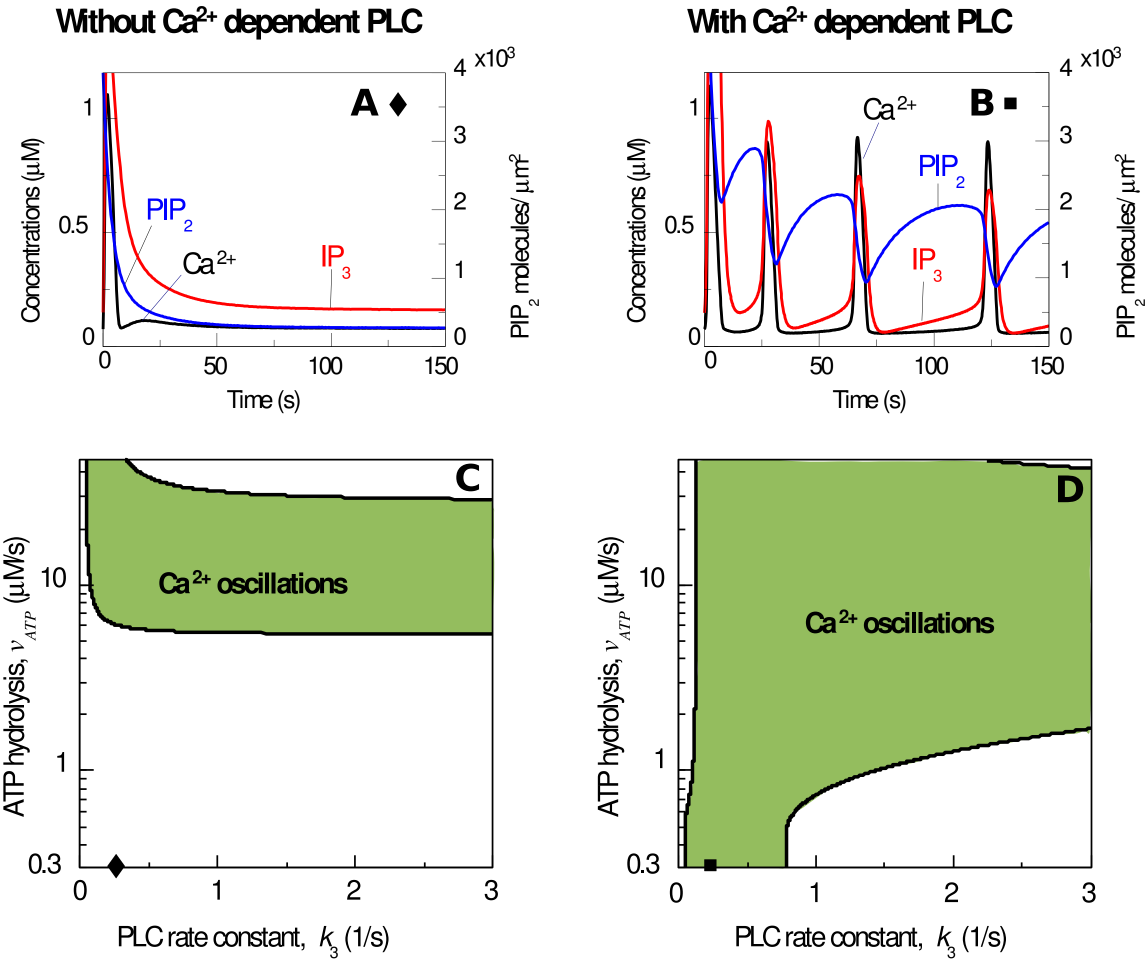

Figure 4.9: (A) In the absence of futile cycling and Ca^{2+} activated PLC, increase in the PLC rate constant k_3 produces a [Ca^{2+}]$_c$ transient and PIP$_2$ depletion (black and blue line, respectively). However, with Ca^{2+} activated PLC (B), [Ca^{2+}]$_c$ oscillates due to transient regeneration of the PIP$_2$ pool. (C) Oscillatory domain (shadowed region) in the absence of Ca^{2+}-feedback on PLC. The ATP-hydrolysis rate increases when the kinase rate constants are increased due to higher phosphatases activity (futile cycling). (D) The oscillatory region is considerably enlarged when Ca^{2+} activation of PLC is present. Diamond and square in C and D indicate parameters for panel A and B, respectively. The linear model without conservation of inositol is used, similar results are obtained with conservation of inositol (not shown). PIP and PIP$_2$ phosphatase as well as PI 3/5-kinases are gradually introduced by increasing f_c in Eqs. (4.14)–(4.16) from 0 to 1. The ATP hydrolysis rate v_{ATP} is determined from Eq. (4.24). Parameters: (A) $f_c = 0$, $\mu = 0$, $k_3 = 0.25/s$; (B) $f_c = 0$, $\mu = 1$, $k_3 = 0.25/s$; (C) $\mu = 0$, (D) $\mu = 1$. In all simulations $k_4 = 1/s$, all rate constants are determined from Eqs. (4.11)–(4.16) and are accordingly higher than listed in Tab. 4.4. Parameters for the Ca^{2+} dynamics as given in Tab. 2.1, positive feedback.

and a marked frequency encoding of the stimulus (data not shown, see examples in Chapter 2).

Introducing phosphatases and the PI 3/5-kinase, rescues the pathway with Ca^{2+} insensitive PLC with respect to stimulus induced $[Ca^{2+}]_c$ oscillations. This leads to a higher ATP consumption, because the phosphoinositide concentrations must be maintained by increasing the phosphorylation rates. I recall that the rate of ATP hydrolysis in the phosphoinositide pathway is given by

$$v_{ATP} = f\left[(\kappa + k_1)X_1 + k_2X_2\right]. \tag{4.41}$$

In Fig. 4.9 I plotted the oscillatory region as function of v_{ATP} and of the stimulus dependent PLC rate constant k_3 (shadowed region). When futile cycling is strong enough, so that the $[IP_3]$ attains the threshold for activating the IP_3R, $[Ca^{2+}]_c$ oscillations are observed also in the system without Ca^{2+} feedback on PLC. However, as shown in chapter 2, such a pure Ca^{2+}/IP_3R oscillator has fast $[Ca^{2+}]_c$ oscillation which only poorly frequency-encode the stimulus. Positive feedback of Ca^{2+} on IP_3 production, in addition of enhancing the ability to frequency encode the stimulus, allows for $[Ca^{2+}]_c$ oscillations in the complete absence of futile cycling and so economizes cellular energy, and greatly expands the parameter domain where $[Ca^{2+}]_c$ oscillations are observed (Fig. 4.9D compare to C).

In both systems, one notices that for intermediary ATP hydrolysis rates $[Ca^{2+}]_c$, oscillations persist for high PLC rate constants (Fig. 4.9C, D). In experiments, the typical hallmark of high agonist dose is the elevated steady cytoplasmic Ca^{2+} concentration at high agonist dose [170]. This difference between model and experiment is readily explained by the fact that the maximal $[IP_3]$ reached within this parameter region, is below the threshold value where the IP_3R are continuously open and the elevated $[Ca^{2+}]_c$ steady state is stable (Eq. (4.23)). In principle, for strong stimulation, processes other than high $[IP_3]$ may bring the oscillations to an end. These are, for example, stimulus dependent Ca^{2+} entry from the external medium or agonist receptor desensitization [26, 75, 149], both processes can be easily taken into account in the model (see e.g. Chapter 2).

From the different isoforms of PLC, some are activated at physiological $[Ca^{2+}]_c$, whereas some are activated at much lower concentrations than basal $[Ca^{2+}]_c$ and so are insensitive to $[Ca^{2+}]_c$ changes [135]. To evaluate their contribution, the strength of the positive feedback is tuned by varying the fraction μ of Ca^{2+} sensitive to Ca^{2+} insensitive PLC (see Eq. 4.40), then, the ATP hydrolysis rate over which activation of PLC induces long-lasting $[Ca^{2+}]_c$ oscillations is computed. The results are summarized in Fig. 4.10.

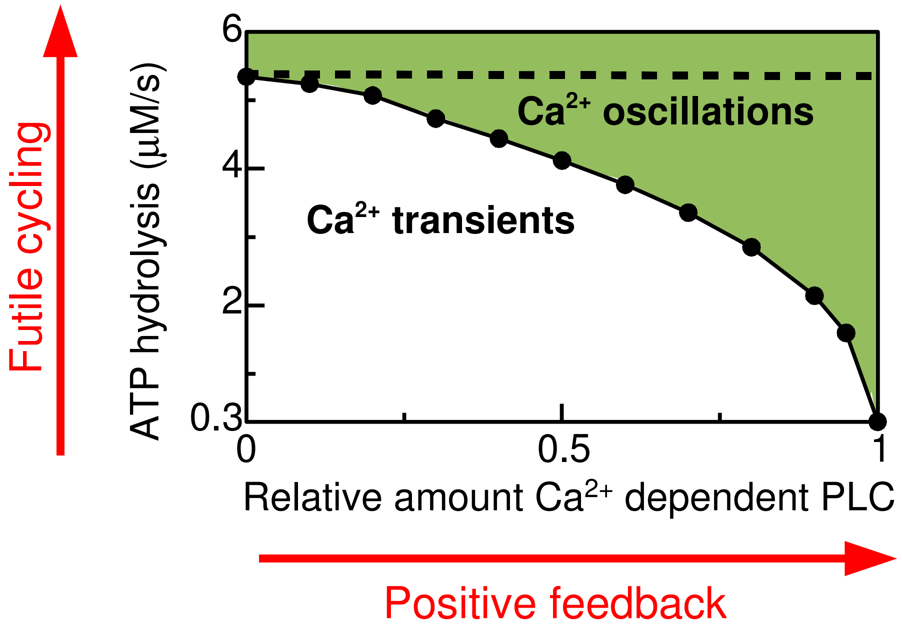

Figure 4.10: Presence of positive feedback of Ca^{2+} on IP_3 production improves energy efficiency. In the shadowed region activation of PLC (k_3 increase) induces $[Ca^{2+}]_c$ oscillations. The more Ca^{2+} activated PLC the less futile (de)phosphorylation cycling is needed. When only Ca^{2+} dependent PLC is present futile cycling is not necessary for an oscillating $[Ca^{2+}]_c$ signal. For parameters below the dashed line introducing an IP_3 buffer quenches the oscillations completely.

The solid line divides the parameter space into two regions: in the shadowed region, feedback strength and futile cycling are high enough, so that activation of PLC brings the $[IP_3]$ above the threshold to sensitize the IP_3R and so generates $[Ca^{2+}]_c$ oscillations; below the black solid line, activation of PLC induces only a few $[Ca^{2+}]_c$ transients.

These results give an appealing interpretation for the experiments performed with an $[IP_3]$ clamped at a fixed value. In some cell types, including hepatocytes, one observes $[Ca^{2+}]_c$ oscillations during such experimental protocol [16, 51, 164, 204]. This suggests that $[Ca^{2+}]_c$ oscillations can occur at a constant $[IP_3]$. On the other hand, the experiments with the IP_3 buffer ascribe a central role to IP_3 oscillations in controlling $[Ca^{2+}]_c$ oscillations. According to the theoretical results, Ca^{2+} feedback on PLC may be essential to regenerate the PIP_2 pool, and this positive feedback is impaired when the IP_3 dynamics is slowed after expressing an IP_3 buffer. Therefore, if futile cycling is weak, below the dashed line in Fig. 4.10, the IP_3 buffer quenches agonist induced oscillations because the PIP_2 pool depletes. However, if PIP_2 hydrolysis is bypassed, by supplying IP_3 externally, the cell regains the ability to generate $[Ca^{2+}]_c$ oscillations. This shows that the necessity for $[IP_3]$ oscillations in agonist mediated $[Ca^{2+}]_c$ signaling and the ability to oscillate for clamped $[IP_3]$ are not mutually exclusive.

Chapter 5

Discussion part I: Calcium and IP$_3$ dynamics

This work represents a contribution for the understanding of the phosphoinositide metabolism in general and the IP$_3$ mediated Ca^{2+} signals in particular. The increasing evidence that hormone evoked periodic Ca^{2+} spiking can be accompanied by oscillations of the Ca^{2+}-releasing second messenger IP$_3$ [61, 112, 161, 171, 201], raises the questions of (*i*) the underlying mechanisms of IP$_3$ oscillations, (*ii*) their potential functional role, and (*iii*) the prerequisites of the phosphoinositide metabolism for generating long-lasting IP$_3$ signals and oscillations. The theoretical analysis and experiments presented here provide insight in all three issues.

Several processes could be involved in the generation of IP$_3$ oscillations. Feedbacks of IP$_3$ and the second product of the PLC reaction, diacylglycerol, on PLC and upstream agonist receptor/G-protein could produce IP$_3$ oscillations without involvement of Ca^{2+} [25, 62]. Alternatively, feedbacks on IP$_3$ metabolism may be mediated by Ca^{2+}, resulting in coupled IP$_3$–Ca^{2+} oscillators [28, 34, 83, 104]. In this work, the focus was put on the latter type of feedback oscillators because they can naturally account for the experimental observations of (*i*) Ca^{2+} oscillations at clamped IP$_3$ concentration and (*ii*) coupled IP$_3$ and Ca^{2+} oscillations. I considered prototypical positive and negative feedbacks of Ca^{2+} ions on IP$_3$ metabolism: Ca^{2+} activation of PLC and Ca^{2+} activation of IP$_3$ 3-kinase, respectively.

Physiological role of IP_3 oscillations

Frequency encoding

The incorporation of feedbacks of Ca^{2+} on IP_3 into a core Ca^{2+} oscillator model based on the regulatory properties of the IP_3 receptor can greatly expand the sensitivity of signal transduction to the hormonal stimulus. The presence of either feedback increases the range of agonist concentrations where one observes Ca^{2+} oscillations and enhances the ability to frequency-encode the agonist dose. Mathematical models indicate that a large range in stimulus dependent frequencies permits a more precise and selective decoding of the Ca^{2+} oscillations by Ca^{2+}-regulated processes (Salazar et al., submitted; [37, 145]). The Ca^{2+} feedbacks on the IP_3 metabolism represent a possible mechanism for the generation of robust long-period oscillations. This is likely to be an important component of frequency-modulated Ca^{2+} signals, since physiological responses are controlled in this lower frequency range [30, 52].

Energy efficiency

I was able to show, that coupling the phosphoinositide metabolism to the Ca^{2+} dynamics using the positive feedback of Ca^{2+} on the IP_3 production, greatly enhances the energy efficiency of the Ca^{2+}/IP_3 signaling pathway (Section 4.6). This is because such a feedback allows the regeneration the PIP_2 pool in the interspike intervals, and so reduces the necessity of futile phosphorylation/dephosphorylation cycles in the phosphoinositide metabolism. One of the interesting results was that IP_3 oscillations may be the only way for generating long-lasting Ca^{2+} oscillations *in vivo*. This occurs if the activities of the PIP 4-phosphatase and the PIP_2 5-phosphatase are not strong enough, so that activation of PLC does not lead to the $[IP_3]$ necessary to sensitize the IP_3R. In this case, an IP_3 buffer will inevitably abolish the $[Ca^{2+}]_c$ oscillations. The necessity for PIP_2 regeneration and IP_3 oscillations can be bypassed by supplying IP_3 externally. The $[Ca^{2+}]_c$ can then oscillate at clamped $[IP_3]$ as observed in experiments.

These properties do not appear to rely on the precise choice of the model for the Ca^{2+}/IP_3R dynamics. Indeed, the models by Sneyd et al. (2004) [154], Tang and Othmer (1992) [163], or Dupont and Goldbeter (1993) [35], implemented with Ca^{2+} activation of PLC and the phosphoinositide metabolism, gave qualitatively similar results (results not shown). The essential component is the positive feedback of Ca^{2+} on the IP_3 production. With the negative feedback model, which describes the Ca^{2+} dependent IP_3 degradation, the PIP_2 pool does not regenerate in the interspike intervals. Therefore, in the negative feedback model, I could not find sustained Ca^{2+} oscillations when futile cycling is weak (not shown).

Coordination of intercellular Ca^{2+} signals

An additional possible role for IP_3 oscillations is to facilitate the coordination of intercellular Ca^{2+} signals. In the intact liver, cells can communicate with their neighbors by diffusion of small molecules through intercellular channels (gap junctions). This is a premise for a coordinated response to the external hormonal stimulation, where one observes repetitive Ca^{2+}-waves propagating through a large number of cells [113, 137]. If the gap-junctional coupling is disrupted, the coordinated intercellular waves are abolished and the cells oscillate independently with different oscillation frequencies. This heterogeneity between cells is supposed to arise from intercellular variations in the number of agonist-receptors, and so in the amount of produced IP_3 [20, 172].

In models without feedbacks of Ca^{2+} on IP_3, intercellular diffusion of Ca^{2+} alone is sufficient to account for the coordinated response observed in an heterogeneous population of cells coupled by gap junctions [63, 64]. For this, the gap-junctional Ca^{2+} permeability must be higher than a critical value. When IP_3 does not oscillate its intercellular diffusion smooths out the differences between cells, and so decreases the value of the critical Ca^{2+} gap-junctional permeability. I have previously shown together with T. Höfer that the intercellular diffusion of IP_3 alone cannot actively couple cells [123]. In fact, if the Ca^{2+} permeability is to low, one observes a coordinated response which lasts only for a limited number of spikes [36].

In vivo, the theoretically estimated gap-junctional permeability of Ca^{2+}, necessary for the intercellular coordination, may not be attained because Ca^{2+} is strongly buffered in the cytoplasm [187]. The fact that, due to Ca^{2+} feedbacks, IP_3 oscillates, and that IP_3 is only weakly buffered (its diffusion is 10-20 times faster than the diffusion of Ca^{2+} [4]), now makes IP_3 a promising candidate for the active synchronization of Ca^{2+} oscillations in coupled cells. This notion is supported by recent theoretical results (Politi et al., in press; [196]).

Properties of Ca^{2+}/IP_3 oscillators

For the positive feedback to modulate the oscillation properties, the Ca^{2+} sensitivity of PLC needs to be only somewhat above basal $[Ca^{2+}]_c$ (K_{PLC} = 0.1–0.2 μM). Such values are in agreement with experimental data [11]. This feedback delays the onset of the Ca^{2+} spike, because both $[IP_3]$ and $[Ca^{2+}]_c$ must rise to a certain level for triggering explosive opening of the IP_3R. In this way, long oscillation periods arise for low levels of stimulation, while for strong stimuli the high IP_3 level obviates the need for additional Ca^{2+} activation of PLC. I have here specifically assumed that Ca^{2+} and agonist act on the same isoform of PLC (e.g. PLCβ). However, similar results were obtained in a model variant where the isoform PLCδ, which is a Ca^{2+}-sensitive but agonist-insensitive PLC isoform, is also included (data not shown).

Negative feedback exerts control on the Ca^{2+} oscillations when IP_3 removal takes place predominantly via $IP_3$3K rather than by the $IP_3$5P ($> 60\%$ of the removal flux at high $[Ca^{2+}]_c$ carried by $IP_3$3K). Long oscillation periods are generated when the $[IP_3]$ drops during the Ca^{2+} spike due to $IP_3$3K activation and subsequently recovers slowly to the level needed to activate the IP_3R. I have found that this mechanism requires a finely tuned interplay between IP_3 metabolism and Ca^{2+} fluxes. This sensitivity may explain the discrepancy to the work of Dupont and Erneux [34], who reported only small effects of $IP_3$3K on $[Ca^{2+}]_c$ oscillation periods. In contrast, the effects of the positive feedback were found to be very robust with respect to the properties of the core Ca^{2+} oscillator.

The different modes of action of positive and negative feedbacks are reflected by opposing requirements on the lifetime of IP_3. In the case of positive feedback, IP_3 turnover must be fast to support long-period oscillations, allowing (*i*) for coincidence of Ca^{2+} and IP_3 spikes and (*ii*) for the rapid removal of IP_3 in the wake of a spike. In the case of negative feedback, slow IP_3 turnover is required for the slow recovery of IP_3 levels in between spikes. In different cellular systems, either one of the IP_3 feedbacks could play a significant role in controlling Ca^{2+} oscillations, depending primarily on the underlying turnover rate of IP_3. However, they cannot be expected to act synergistically.

The theory can be used to estimate, whether IP_3 oscillations, generated by positive feedback of Ca^{2+} on IP_3, can play a significant role in modulating Ca^{2+} oscillations. If the Ca^{2+} oscillations have a high frequency and the IP_3 turnover time is below the time in between spikes, one expects the amplitude of the IP_3 oscillations to be very small. These small amplitude IP_3 oscillations will not modulate the $[Ca^{2+}]_c$ oscillations. Thus, a system with fast Ca^{2+} oscillations and positive feedback behaves as it would have a constant $[IP_3]$. This is in agreement with recent experimental and theoretical results. The results by Sneyd and coworkers indicate that in airway smooth muscle cells, a cell type which show comparatively fast oscillations, the Ca^{2+} oscillations do not depend on IP_3 oscillations (frequencies of 0.2–0.5 spikes/s). On the contrary, in the slower oscillating pancreatic acinar cells the authors found that IP_3 oscillations affect the Ca^{2+} oscillations (frequencies 0.03–0.04 spikes/s) [155].

Identification of Ca^{2+} feedbacks on IP_3

A critical question is the experimental identification of the mechanisms that drive IP_3 oscillations. The theoretical analysis showed that slowing the IP_3 turnover by means of an IP_3 buffer can be used to distinguish between the two feedback mechanisms. I demonstrated that in models without Ca^{2+} feedbacks on IP_3, an IP_3 buffer will have practically no effect on the steady state IP_3 concentration and so on the Ca^{2+} oscillations. An IP_3 buffer can quench the oscillations generated by an IP_3–Ca^{2+} oscillator based on positive feedback of Ca^{2+} on IP_3, but not by one based on negative feedback. The analytical results indicate that the weak response of the negative-feedback oscillator to IP_3 buffering could be a general property not limited to a mechanism operating through IP_3 3-kinase. Indeed, very similar results are obtained with an alternative mechanism acting through PKC-dependent inactivation of the agonist receptors (Gaspers et al., submitted).

To test this theoretical prediction, the ligand binding domain of the type 1 IP_3R has been expressed in a mammalian cell line. This construct acts as an IP_3 buffer. The observed dose-dependent suppression of Ca^{2+} oscillations demonstrates that the IP_3 dynamics play a critical role in the oscillator mechanism. Moreover, the detailed agreement between the experimental data and the simulations of the positive-feedback model is consistent with a coupled IP_3–Ca^{2+} oscillator based on Ca^{2+} activation of PLC.

The model suggests a further experiment to strengthen the theoretical and experimental results. The Ca^{2+} oscillations, which have been suppressed by slowing the IP_3 dynamics with an IP_3 buffer, should be rescued by injecting the IP_3 metabolizing enzyme IP_3 5-phosphatase and stimulating with higher agonist doses. The rationale for this is that the IP_3 5-phosphatase will fasten the IP_3 turnover, and so allow for the $[IP_3]$ to decrease in the wake of a Ca^{2+} spike.

Key features of the phosphoinositide metabolism

In this work, I developed one of the first detailed mathematical models for the phosphoinositide pathway. The model was a compromise between completeness and experimentally available data for the different reactions and metabolites. These data were used to estimate the kinetic parameters and to assess the contribution of the different reactions to the IP_3 homeostasis.

To generate, after PLC activation, a sustained increase in [IP_3], the PIP 4-phosphatase and PIP_2 5-phosphatase are essential. Furthermore, PI must be metabolized at least by two different enzymes (the PI 4-kinase and e.g. the PI 3-kinase). In the absence of one of these enzymes, the increase in [IP_3] is transient and lasts not longer than 30 minutes. To account for the experimental data, the two phosphatases must have similar activities as their opposing kinases (PI 4-kinase and PIP 5-kinase, respectively). This is reflected in the strong control the phosphatases exert on the [IP_3] and the elevated energy consumption. These results do not depend on the assumed linear reaction rate laws. The description of the enzyme activities with more realistic reversible Michaelis-Menten rate laws led to similar conclusions (see Appendix B.3).

I already discussed how the presence of Ca^{2+} activated PLC can rescue Ca^{2+} signaling when the dephosphorylation rates are low. A second and simple way to obtain a long-lasting IP_3 signal is the upregulation of the producing enzymes. The model predicts that, in order to supply PIP_2 for maintaining an elevated IP_3 flux, a stimulus dependent increase in the synthesis rate of PI is required. Furthermore, the PI 4-kinase and PIP 5-kinase rates must also be stimulus dependent, in order to reproduce the experimental data (see Appendix B.2). There are indications that this could be the case. PIP 5-kinase and PI 4-kinase have been shown to be activated after binding of ligand to tyrosine kinase receptors or G-protein coupled receptors (see review [188] and [21, 143, 173, 197]). The PI-transfer protein, a protein responsible for the transfer of PI from the ER membrane to the plasma membrane, has been shown to be activated by GTP binding proteins, and is required for the epidermal growth factor dependent signaling (see review by [72] and [24, 79]).

In the last years, the increased attention devoted to the phosphoinositide metabolism, revealed how complex and intricated can be the regulation and signaling of such a pathway. The quantitative data that will soon be available for the other metabolites will allow to develop more detailed models and make predictions on how the different signaling pathways controlled by the phosphoinositides interact.

Part II

DNA Repair: a Paradigm for Nuclear Processes

Chapter 6

Introduction to DNA repair and experimental methods

The DNA is continuously damaged by different endogenous and exogenous agents. Thermal fluctuations break about 5000 purine bases per day (spontaneous *depurination*), similarly spontaneous *deamination* of cytosine to uracyl occurs at a frequency of 100 bases/cell/day [3]. Reactive oxygen species and radiation alter the base pairing ability of the DNA and produce double strand-breaks at a frequency of ~ 1 million bases/cell/day [49]. These high mutational rates would be disastrous in the absence of DNA repair.

There are several DNA repair mechanisms that reduce the mutations per cell generation below 1 base pair change per 10^9 base pairs [3]. One distinguishes five main repair pathways:

1. *Direct reversal* converts modified nucleotides back to their original structure without removing them from the sugar-phosphate backbone. This repair mechanism often uses only one protein to perform repair. For example, in many species, except placental mammal, UV-light induced damages are removed by a photolyase (cf. [3]).

2. *Recombinational repair* uses the recombination machinery and the information of the sister chromatin to repair double-strand breaks generated by high-energy radiation or during mitotic recombination (cf. [82]).

3. *Mismatch repair* removes replication errors (cf. [84]).

4. *Base excision repair* removes spontaneous deaminations, oxidative and alkylation damages (cf. [7]).

5. *Nucleotide excision repair* (NER) removes helix-distorting lesions such as bulky adducts, cisplatin and UV-light induced damages (cf. [27]).

Repair in the four latter pathways is a multiprotein process. The involved proteins are thought to assemble at the site of damage and perform the basic tasks of recognition and excision of the damage, synthesis of the correct nucleotide sequence and ligation of the nick.

DNA damage and repair are interconnected with several other processes. When DNA lesions occur at cell cycle checkpoints the *cell cycle* is arrested to prevent cells from replicating damaged DNA. If repair is completed the cell cycle may resume, otherwise when the DNA is damaged beyond repair cells may initiate the signaling cascade which leads to regulated cell death, that is *apoptosis*. *Transcription* is blocked after DNA damage and there is a specific repair pathway for removing lesions on transcribed genes. Furthermore, some of the proteins used for repair can be engaged in other processes in the absence of damage (e.g. transcription, replication, cell cycle regulation [27]). Mutations in enzymes involved in repair can lead to severe disorders. For example Xeroderma Pigmentosum (XP) is a disease related to NER. The patients suffer from extreme sun-sensitivity and an increased incidence of skin cancer.

The specific role of DNA repair as a junction of replication, recombination, and transcription, and the shared mechanisms to these DNA related processes makes it an ideal starting point for their comprehension.

6.1 Nucleotide Excision Repair

Nucleotide excision repair (NER) is a versatile DNA repair mechanism for eliminating helix-distorting lesions throughout the genome. Its most abundant substrates are UV-induced photoproducts, mainly cyclobutane pyrimidine dimers (CPDs) and 6-4 photoproducts (6-4PPs) (see Fig. 6.1). For their removal, placental mammals are fully dependent on functional NER [45]. NER eliminates DNA injuries employing a multi-step strategy that requires the combined action of at least 25 different polypeptides that detect the lesion and excise a 24-32 residue oligonucleotide from the damaged strand, after which the replication machinery fills in the gap [27].

There are two distinct NER pathways: transcription-coupled NER (TC-NER) and global genome NER (GG-NER). TC-NER removes lesions from the transcribed strand of active genes. Damage recognition occurs at RNA polymerases that are blocked at DNA lesions, and is mediated by the TC-NER-specific protein cokayne syndrome group A

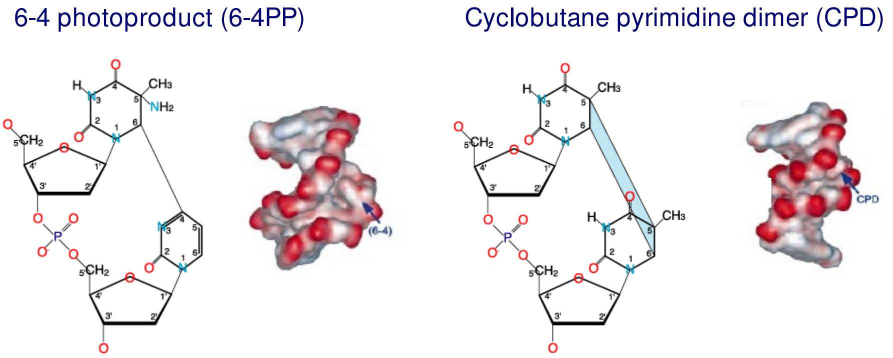

6-4 photoproduct (6-4PP)

Cyclobutane pyrimidine dimer (CPD)

Figure 6.1: UV-light induces dimerization of pyrimidine nucleotides (thymine and cytosine) and produces 6-4 photoproducts (6-4PPs) and cyclobutane pyrimidine dimers (CPDs). The helix distortion caused by a 6-4PP is more pronounced then the distortion caused by a CPD.

and B, and XPA binding protein 2 proteins [54, 110]. After recognition, the subsequent steps in TC-NER are thought to be the same as for GG-NER. TC-NER is crucial for cell survival after DNA damage, but the vast majority of genomic lesions are eliminated by GG-NER.

Seven protein complexes are found to be important for functional GG-NER. Below, I summerize briefly the known function of the different protein complexes.

XPC-HR23B

There is increasing evidence that the heterodimer XPC-HR23B (183 kDa) plays a central role in damage recognition [158]. Its binding to DNA causes a slightly opening of the DNA helix and appears to be sufficient for the recruitment of transcription factor II H (TFIIH) [40, 76, 165, 180, 199]. The XPC subunit is thought to play the active part in NER [133, 199], whereas the HR23B subunit is involved in protecting XPC from proteosomal degradation [114]. XPC-HR23B has a high affinity for a broad spectrum of DNA lesions such as UV-light induced lesions (6-4 PP and CPD) and cisplatinum adducts. To a lower extent it binds to small bubbles on the DNA devoid of lesions and to non-damaged DNA. This has lead to the hypothesis that XPC-HR23B continuously probes the DNA for lesions.

UV-DDB

The role of the UV-damaged DNA binding factor (UV-DDB, 176 kDa) is still controversial. UV-DDB has a high affinity for both 6-4PP and CPD and has been suggested to be the recognition factor. However, it is essential for repairing CPD but not for repairing 6-4PP [73]. Recent studies indicate that UV-DDB assists XPC in repair by monoubiquitinating it. In this case, it is not a signal for targeting XPC to the proteasome but on the contrary reduces XPC degradation rate by increasing its affinity for HR23B [114]. Furthermore, ubiquitination leads to an increased affinity of XPC for damaged and non-damaged DNA [159]. This increased affinity may be needed to recognize CPDs.

TFIIH

Transcription factor II H (TFIIH) is a holocomplex of considerable size (450 kDa) containing up to nine subunits. As its name indicates TFIIH is also involved in transcription with RNA polymerase I and II [44, 74]. TFIIH is recruited at the site of damage after binding of XPC-HR23B and is responsible for strand separation 10-12 nucleotides around the lesion [40]. This is mediated by its bidirectional ATP-dependent helicase activities [141, 142]. TFIIH bound to DNA may serve as the platform for recruiting the other repair factors which interact with TFIIH [5].

XPA

Xeroderma Pigmentosum group A protein (XPA) (30 kDa) has also been suggested to be involved in the first step of NER [92], possibly in combination with RPA [131] (see below). Although XPA shows high affinity for damaged DNA *in vitro* [183], *in vivo* experiments indicate that recruitment of XPA needs functional XPC-HR23B [180]. Because a DNA-XPC-HR23B-TFIIH complex may form on undamaged DNA, due to the affinity of XPC-HR23B to this substrate, the role of XPA is thought to be that of a “damage verificator” which prevents erroneous repair of undamaged DNA (cf. review by [166]). The binding of XPA may stabilize the DNA-XPC-HR23B-TFIIH complex, induce further opening of the DNA by stimulating the helicase activity of TFIIH [190], and allow for the recruitment of other repair factors. Indeed, the 5’ endonuclease ERCC1-XPF can only be recruited to the damage in the presence of XPA [180].

RPA

Replication protein A (RPA, 121 kDa) has a very high affinity for single stranded DNA (ssDNA) and protects it from misfolding and unwanted endonucleases. For the NER process it has been suggested that RPA acts as damage detector [131]. However, RPA most probably binds after TFIIH when the two ssDNA have been formed by the helicases of TFIIH. RPA appears to be necessary for the correct positioning of the two endonucleases XPG and ERCC1-XPF and is an essential component for the resynthesis of the DNA after incision. Initially XPA and RPA were supposed to exist as a dimer in the absence of damage [56]. However, recent experiments indicate that RPA can bind to damaged DNA in the absence of XPA [127, 179]. Besides being involved in NER the RPA is used in many processes that have ssDNA as intermediates (replication, recombination, and other repair pathways).

XPG

The 133 kDa XPG is a 3' endonuclease which shows interactions with TFIIH *in vitro* [5]. The presence of XPG in the dual-incision comples is necessary for ERCC1-XPF to bind and cleave the 5' ssDNA [184].

ERCC1-XPF

The heterodimer ERCC1-XPF (136 kDa) is a 5' endonuclease. Several reports suggest that this factor is probably the last factor recruited for completing the dual-incision complex [40, 180].

Resynthesis and ligation

After dual incision the DNA must be synthesized and ligated. The proteins involved are PCNA, which acts as a loading platform for DNA polymerases δ and ϵ. After resynthesis DNA ligase I is thought to ligate the nick. Most of the proteins involved in this process are the same as for replication.

6.2 Experimental methods used to study NER

To facilitate the understanding of my work I give a short overview of the experimental methods used to investigate NER. NER is initiated by irradiating cell nuclei with UV-

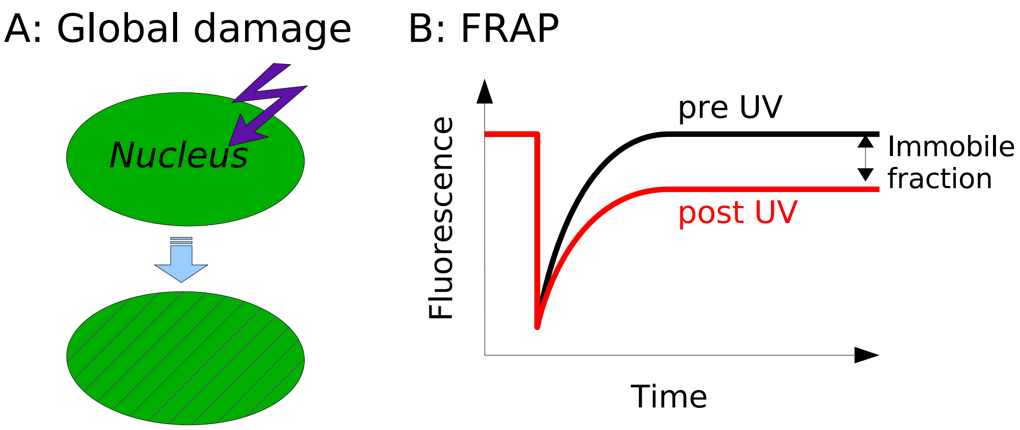

Figure 6.2: Global damage experiments. (A) The whole nucleus is damaged at once. (B) Fluorescence recovery after photobleaching (FRAP) is used to estimate immobile fractions and diffusion coefficients.

light. One differs between global damage, where the whole nucleus is irradiated, and local damage, where only part of the nucleus is irradiated. Generally, one takes cells where a repair factor is completely absent or malfunctioning (e.g. XP-cells), this mutation is then rescued with a fluorescent protein tagged version of the missing repair factor (e.g. XPC-GFP). The survival of the recombinant cells after UV-irradiation show that they have a functioning NER similar to wild-type cells (i.e. cells with no mutations in NER). Cells with the fluorescent construct are used for life-cell imaging. Alternatively, antibodies specific for the repair factors specific are used.

6.2.1 Global damage experiments

In global damage experiments the whole nucleus is irradiated with UV-C light (Fig. 6.2A). Typical doses to observe saturation are around 8 J/m^2. At these doses 1.3-8$\times10^5$ CPDs and 0.38-1.8$\times10^5$ 6-4PP are generated [120, 175, 198]. With fluorescently labeled proteins and photobleaching methods the diffusional properties of the repair factors prior and after irradiation are measured (see below). Furthermore, the fraction of proteins immobilized on the DNA after damage induction can be obtained, this is the fraction of proteins involved in repair. A summary of the experimental data is given in Tab. 6.1. The listed values for the immobile fractions are for saturating doses of UV light (8-10 J/m^2). Experiments show that a further rise in the UV dose did not produce measurable increases in the immobile fractions.

	Global damage experiments	
Factor	Immobile fraction	Diffusion coefficient
XPC-HR23B [66]	40%	1 μm^2/s
TFIIH [67]	40%	6±0.2 μm^2/s
XPA [127]	35%	13±2 μm^2/s
ERCC1-XPF [71]	35%	15±5 μm^2/s

Table 6.1: Fraction of repair factors involved in repair after global irradiation of cell nuclei (saturating dose) and diffusion coefficients. The diffusion coefficients are determined in non-irradiated cells using FRAP (see below).

6.2.2 Local damage experiments

In these experiments, only a small part ($\sim$ 1/7-1/10 of the nuclear volume) of the nucleus is irradiated. The typical dose of UV-C light used is much higher than for global damage experiments ($\sim$ 100 J/m^2 inducing 1.6-3.2$\times 10^5$ CPDs and 4.8-1.3$\times 10^5$6-4PP [120, 175, 198]). Starting, prior to damage, with an homogeneous distribution of fluorescently labeled repair protein, the fluorescence in the local damaged area increases over time (Fig. 6.3A). This is an hallmark that a repair factor binds to damaged DNA. To quantify the fraction of proteins involved in repair, one takes the difference between fluorescence in the local damaged area and in a control region of equal size (area 1 and 2 in Fig. 6.3A), and normalizes this value with the total fluorescence of the nucleus. This procedure is necessary as it is not possible to distinguish between fluorescence emitted from freely diffusing and DNA bound factors. The recruitment process as a whole can then be characterized by the accumulation time (see Tab. 6.2).

The mean time a repair factor resides in the locally damaged area is monitored using photobleaching methods, this time is a measure on how long a protein resides in the repair complex (see below and Fig. 6.4). A summary of the residence time experiments is given in Tab. 6.2. The listed values are for a saturating dose. Experiments show that a further increase in UV dose, e.g. from 100 to 200 J/m^2, does not produce faster accumulation nor an increase in immobile fractions (M. Luijsterburg and M. Moné, unpublished data). Local damage experiments combined with immunofluorescence techniques can be used to study if a factor binds when one of the other factors is absent (due to a mutation). This gives a hint on the mutual dependencies between factors. The results are summarized in Tab. 6.3.

Although measurements used in this work are performed in different cell lines (ham-

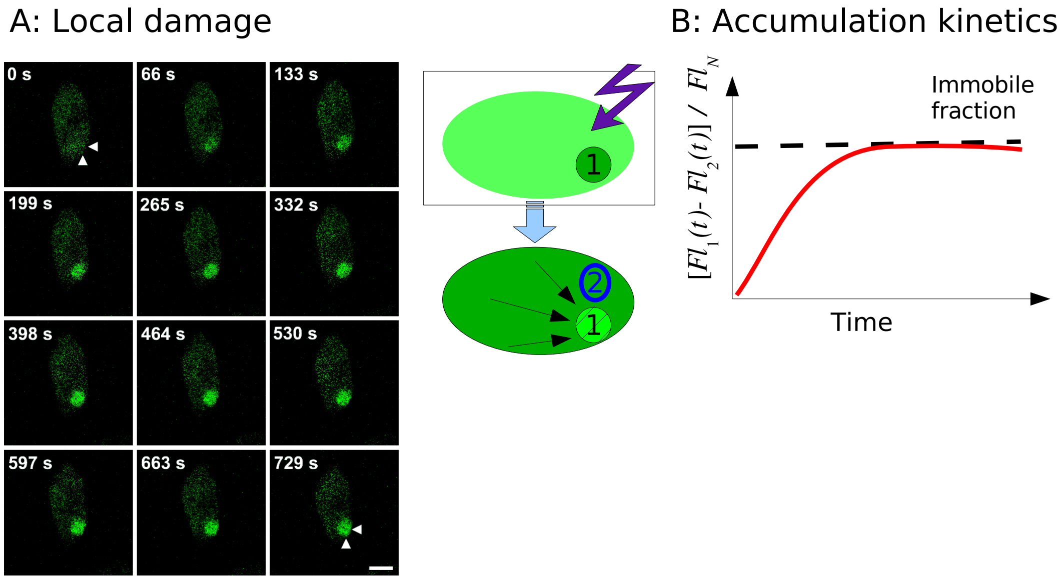

Figure 6.3: Local damage experiments (A) Only a small part of the nucleus is damaged. The right panel shows the accumulation of XPC-GFP in the local damaged area (arrows). Bar represents 10 μm. (B) The recruitment of repair factors leads to an increase in fluorescence in the damaged area. Shown is $(Fl_1(t) - Fl_2(t))/Fl_N(t)$, the difference between fluorescence in the local damaged area 1 $Fl_1(t)$ and in a control region 2 $Fl_2(t)$ normalized with the total fluorescence in the nucleus $Fl_N(t)$ (solid line). The maximal immobile fraction is indicated by the dashed line.

ster and human cell lines), one can assume that they represent the same process. That is, if one could measure simultaneously all factors in one cell, the data should be similar as the data obtained from the independent measurements in different cell lines. This is justified by two observations: (*i*) Survival after UV irradiation is the same in all transfected cells and in wild-type cells [67, 71, 127]; (*ii*) The accumulation kinetics appear to be surprisingly similar between hamster and human. The dynamics of XPG recruitment was found to be the same in both cell types (M. Luijsterburg and R. van Driel, unpublished data).

6.2.3 Photobleaching methods

Fluorescence recovery after photobleaching (FRAP) and fluorescence loss in photobleaching (FLIP) are reviewed in Houtsmuller and Vermeulen [70]. Their applications to the repair process are described by Hoogstraten et al. (2002) and Rademakers et al. (2003) [67, 127]. Here I give a brief overview.

	Local damage experiments		
Factor	Accumulation time ($t_{1/2}$)	Immobile fraction	Residence time
XPC-HR23B [1] [66, 124]	195 (150) sec	$13 \pm 3.3\%$	44 ± 10 sec
TFIIH [67, 107]	140 (115) sec	$14.8 \pm 1.1\%$	102 ± 5 sec
XPG[1]	200 (200) sec	$9.1 \pm 1.8\%$	–
XPA[1] [127]	810 (600) sec	7.4%	160 ± 22 sec
ERCC1-XPF [107]	75 (65) sec	$13.4 \pm 1.7\%$	144 ± 27 sec (g.d.)

[1] Luijsterburg et al. in preparation.

g.d.: data from global damage experiments.

Table 6.2: The accumulation kinetics from local damage experiments can be summarized using the accumulation times, second column, defined in 7.2.2. In brackets is the $t_{1/2}$ time to attain half the plateau. Third column gives the fraction of repair factors in the local damaged area, i.e. factors involved in repair. The fourth column gives the mean time a factor is involved in repair, the residence time, as defined in Appendix D.1 (see also Fig. 6.4).

	Immunolabeling					
	XPC-HR23B	TFIIH(XPB)	XPA	RPA	XPG	ERCC1-XPF
ΔXPC	n.b.	n.b.	n.b.	n.b.	n.b.	n.b.
ΔXPA	b.	b.	n.b.	b.	b.	n.b.
ΔXPF	–	–	b.	–	b.	n.b.
ΔXPG	–	–	b.	b.	n.b.	b.

Table 6.3: Summary of the results from immunolabeling experiments [127, 179, 180]. A mutant Δ has a malfunction/absence in one of the repair factors (first column). In this mutant background one repair factor is immunolabeled (first rows). b.: Binding of a labeled factor in a specific mutant background. n.b.: no binding is observed. A minus (–) is used when no experimental data were available in that combination.

In FRAP a small area of the nucleus is bleached and the recovery to steady state is monitored (Fig. 6.2B). The time needed for recovering depends on the diffusion properties of the fluorescently labeled repair factor. Using computational methods one can estimate the diffusion coefficient [157]. If part of the repair factors are bound to DNA, because they are involved in repair, then the FRAP curve does not fully recover. The difference between the FRAP curve prior and post UV irradiation gives the fraction of

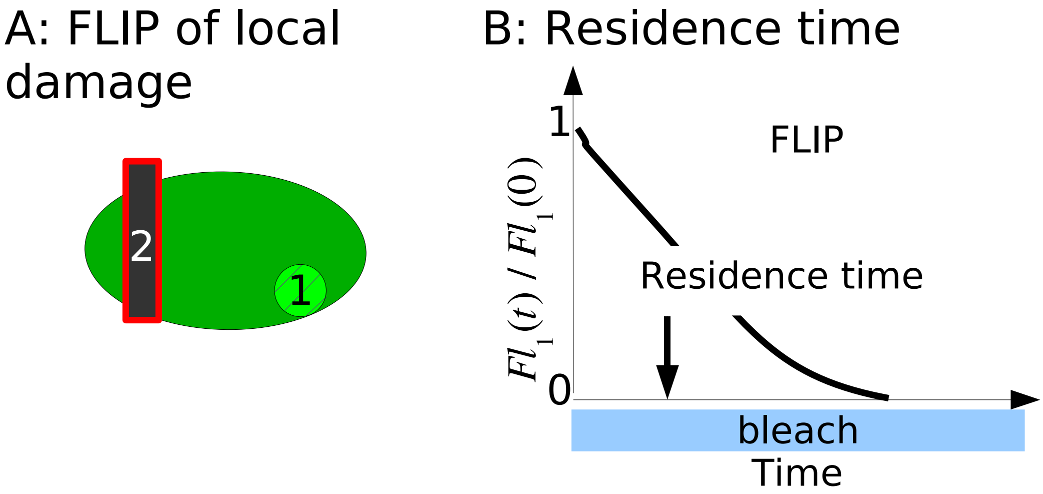

Figure 6.4: Fluorescence loss after photobleaching. (A) Area 2 is continously bleached. (F) The residence curve is $R(t) = Fl_1(t)/Fl_1(0)$. The residence time is given e.g. by the time at $1/e$ decay of $R(t)$ or using an integral definition (see Appendix D.2.4).

proteins involved in repair.

In FLIP a small strip at the opposite pole of the nucleus from the local damage is continously bleached (Fig. 6.4A, region 2). After few seconds there no more fluorescence is emitted outside the local damaged area. When a factor dissociates from the repair complex it can freely diffuse in the nucleus and eventually becomes bleached in region 2. Thus, the mean time to completely lose fluorescence in the local damaged area quantifies the mean time a protein is involved in repair, this time is referred to as the *residence time* (Fig. 6.4B). To minimize the contribution of diffusion to the residence time a combination of FRAP and FLIP has been developed [70]. In combined FRAP-FLIP experiments the bleaching occurs only for a few seconds. The time to reestablish the initial fluorescence difference between the local damaged area and a control region is the residence time.

6.3 Research objectives

Although many details on the biochemistry of NER are known, there are several questions that are not completely resolved:

(*i*) How do the repair factors assemble? Do they assemble sequentially or randomly at the site of damage, or does a fully pre-assembled holocomplex perform repair?

(*ii*) Which are the processes that limit repair? Can we assess the efficiency of NER in removing lesions?

(*iii*) How are the factor released after repair? Do they leave the DNA simultaneously or sequentially?

Mathematical models can help in address these questions and first attempts to quantitatively model DNA repair have bean done for another repair pathway (base excision repair [156]). I developed a mathematical model for NER that accounts for the sequential assembly of NER proteins at the sites of DNA damage, their release, and the removal of the lesions as proposed by recent experiments [1, 67, 127, 180]. I explored the general characteristics of the sequential assembly mechanism and derived analytical expressions, which describe repair factors recruitment and release kinetics at the damaged sites. These expressions have been used to draw general conclusions on how the structural properties of NER, i.e. assumed binding and release order, determines the repair factor kinetics (Chapter 7). For the identification of the model parameters, I used the assembly kinetics of XPC-HR23B, TFIIH, and ERCC1-XPF at the local damaged nuclear area [107, 124]. The direct comparison of model and data revealed to what extent the model assumptions, deduced from several experimental facts, are in agreement with the observed kinetic data (Section 7.3). The developed model is used to assess the efficiency and specificity of repair in relation to the system parameters, i.e. reaction rates, concentrations, and number of repair factors (Chapter 8). For this, measures that quantifies these two properties have been defined and applied to the model. In the literature, beside sequential assembly, other mechanisms have been proposed for assembling the repairosome. The efficiency of the alternative pathways are compared to the efficiency of the sequential pathway. The critical reviewing of the theoretical and experimental results (Chapter 9) suggested several experiments to better understand the initial and final steps in NER (Chapter 10)

This theoretical work has been done in close collaboration with the group of Prof. Roel van Driel, University of Amsterdam, The Netherlands. Within this group, most of the experiments presented in this work have been done by Dr. Martijn Moné.

Chapter 7

A sequential assembly strategy in NER

7.1 The mathematical model

7.1.1 Model description

The mathematical model takes into account six separate events: a recognition binding step, four intermediate binding steps, and a DNA repair plus dissociation step (Fig. 7.1). It assumes a strict sequential, reversible binding of NER factors to a damaged DNA site and their subsequent simultaneous release after a successful repair event. Repair is initiated by the recognition of the damage by XPC-HR23B, its binding leads to the intermediary complex S_1 (DNA/XPC-HR23B). The binding of the other four repair factors occurs sequentially in the order as shown in Fig. 7.1 (according to [180]). The binding of ERCC1-XPF to the intermediary complex S_4 completes the assembly process, generating the full pre-incision complex (PC). Subsequent dual endonuclease incision of the damaged strand, dissociation of the DNA damage and of the protein factors, and the filling of the gap by the replication machinery are treated as a single reaction: the repair step.

The concentrations of the free damage S_0 and the intermediary complexes S_i are governed by

$$\frac{dS_0}{dt} = V_{dam} - \tilde{k}_1 S_0 F_1 + k_{-1} S_1 \tag{7.1}$$

$$\frac{dS_i}{dt} = \tilde{k}_i S_{i-1} F_i - k_{-i} S_i - \tilde{k}_{i+1} S_i F_{i+1} + k_{-(i+1)} S_{i+1} \tag{7.2}$$

$$\frac{dS_n}{dt} = \tilde{k}_n S_{n-1} F_n - k_{-n} S_n - k_R S_n \tag{7.3}$$

Equation (7.2) applies for $i = 1, \cdots, n-1$, where n is the number of different repair factors. The F_i's are the concentrations of the free factors, $\tilde{k}_i$ and k_R denote the binding rate constant and the rate constant of the repair step, respectively, k_{-i} is the dissociation rate constant of the ith repair factor from its corresponding substrate. V_{dam} denotes the rate at which lesions are formed.

For the analysis of NER efficiency it is useful to define the total concentration of DNA lesions

$$D_T = \sum_{i=0}^{n} S_i \tag{7.4}$$

From Eqs. (7.1)–(7.3) it follows that

$$\frac{dD_T}{dt} = V_{dam} - V_R. \tag{7.5}$$

Here, I introduced the rate at which damaged sites are removed $V_R = k_R S_n$.

The total concentrations T_i of the factors are

$$T_i = F_i + I_i \tag{7.6}$$

where

$$I_i = \sum_{j=i}^{n} S_j. \tag{7.7}$$

is the concentration of the ith factor engaged in repair, and therefore immobilized on the DNA. From the previous formula follows that the more upstream in the chain a factor is recruited, the higher its immobilized concentration

$$I_i > I_j, \text{ for } j > i \tag{7.8}$$

During the times pan of the experiments ($\sim$ 10 min), the total concentration of XPC-HR23B, and probably of the other repair proteins, remains constant [2, 114]. Thus, the repair system is fully described by Eqs. (7.1)–(7.3) where $F_i = T_i - I_i$.

NER proteins also have an affinity for undamaged DNA (e.g. XPC-HR23B) and several repair factors are involved in processes besides repair (e.g. TFIIH in transcription)

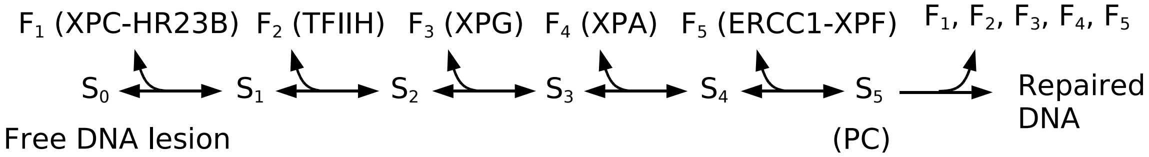

Figure 7.1: Scheme of the basic model showing the sequential binding of five different protein factors to a damaged DNA site and their simultaneous release after repair.

[3, 60, 67, 133]. As illustrated in Appendix C.1 the presence of undamaged binding sites reduces the free factor concentrations available for repair. One can show that $F_i = (T_i - I_i)/\beta_i$, where the coefficients β_i are referred to as buffering coefficients. Their values are directly proportional to the amount of undamaged binding sites ($\beta_i = 1$ without undamaged binding sites; $\beta_i > 1$ otherwise). The model equations that account for the presence of undamaged binding sites read

$$\frac{dS_i}{dt} = k_i S_{i-1}(T_i - I_i) - k_{-i} S_i - k_{i+1} S_i (T_{i+1} - I_{i+1}) + k_{-(i+1)} S_{i+1}. \tag{7.9}$$

The effective binding rate constants are defined by $k_i = \tilde{k}_i/\beta_i$. The above formula shows that the presence of undamaged binding sites slows the formation of intermediary complexes and thus of the PC.

The model accounts for a situation where DNA damage is evenly distributed throughout the nucleus. In this case, there are no spatial gradients in the factor concentrations. If a high concentration of damage sites is induced locally, it may be necessary to include the nuclear diffusion of the factors. This is taken into account when directly comparing the model simulations with the data from local damage experiments (Section 7.3, page 96).

7.1.2 Damage generation

At low UV light intensities the amount of damages increases linearly with the UV dose. I will assume that the linear dependency remains valid for the high UV doses (>30 J/m^2) used in local damage experiments. From [175, 198] one obtains[1]

$$\text{Concentration of 6-4PP } [\mu\text{M}] = \frac{57218 \times UV \times f}{V_d N_A} = 0.3166 \times UV \tag{7.10}$$

---

[1] In the initial phase of repair, mainly 6-4PPs are recognized and removed by NER, therefore, the other type of damage induced with UV (CPD) is not considered at this stage.

The UV light intensity is given in $\mathrm{J/m^2}$. f is the fraction of damaged nucleus ($\approx 1/7$), $V_d = fV_n$ is the volume of the local damaged area, with a nuclear volume $V_n = 0.3$ pl, N_A is the Avogadro's constant. The linear dependency of the number of damaged sites on the UV light intensity has several implications for the interpretation of the data and for the model predictions. This caveat will be discussed in more detail in Chapter 10.

7.2 General properties of the sequential model

7.2.1 Saturation and maximal repair rate

In experiments, the amount of factors involved in repair saturates with increasing UV light intensity. Also, the kinetics of accumulation in the local damaged area does not become faster for increasing dose (cf. Section 6.2, page 79). These two facts indicate that NER is saturated. With the model one can try to provide a mechanistic explanation. For example, saturation can merely be due to the fact that not enough damages have been induced. However, this option will be neglected for the moment, because I assumed that the number of damages increases with the UV light Eq. (7.10) (see Chapter 10, where alternatives have been modeled).

The second possibility is that the recognition factor becomes fully involved in repair. In the model, increasing the initial damage concentration causes additional involvement of factors in repair as long as repair complexes can be initiated. How many repair complexes can be initiated depends on the available free diffusing molecules of the first factor. Saturation at high UV light doses can be identified with depletion of the free diffusing pool of the first factor ($F_1 \approx 0$); in this situation, damages are removed with a maximal rate $V_R = V_{max}$ (see Appendix C.4). This result is comparable to enzyme kinetics, where at high substrate concentrations the enzyme reaches its maximal rate because all the catalytic sites are occupied by substrate.

7.2.2 Time hierarchy of binding and release: analytical results

Before proceeding with the direct comparison of model and data (as done in Section 7.3, page 96), I will derive analytical expressions, which relate the structure of the model to the kinetics of the repair proteins. I will present two measures, the accumulation and the residence time, that characterize the factor kinetics at the local damage.

For better illustrating these two measures, I plotted, qualitatively, the type of experimental data obtained from local damage experiments (Fig. 7.2A). At $t = 0$ the

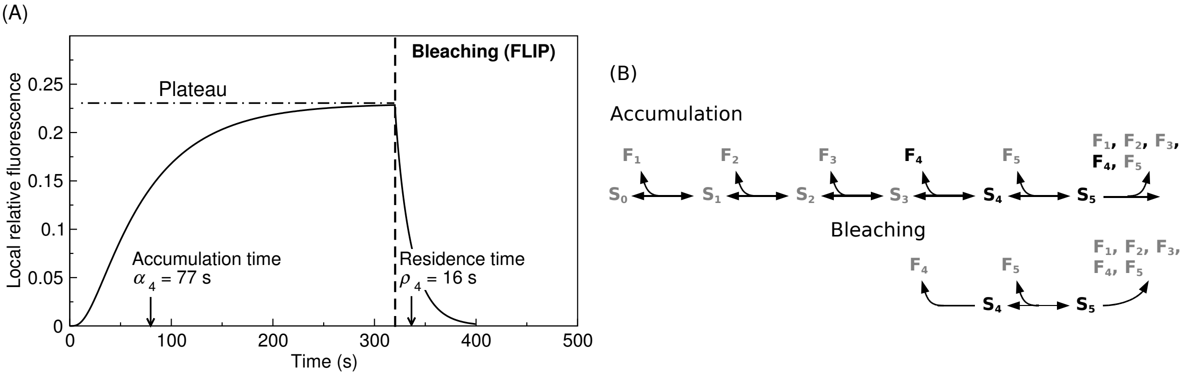

Figure 7.2: Accumulation and residence times. (A) Qualitative data as would be obtained from local damage experiments (simulation). After damage, at $t = 0$, one observe accumulation of the repair factor in the locally damaged area. The accumulation time α_4 characterizes its recruitment kinetics. As soon as a plateau is reached, bleaching outside the local damaged area is initiated (FLIP). The residence time ρ_4 quantifies the dissociation kinetics from the repairosome. (B) During accumulation, all reactions before and after binding of a factor (bold faced) contribute to its recruitment kinetics. In FLIP experiments, the observed loss in fluorescence is proportional to the dissociation rate from the repairosome. This is because, the fluorescence of the free diffusing molecules is continuously quenched.

nucleus is damaged locally, this initiates an increase in fluorescence in the local area (the concentration of proteins involved in repair rises). Within 2–5 min, the fluorescence does not change any further and a plateau is attained. This marks the end of a factor accumulation/recruitment phase, whereof the kinetics is characterized by the *accumulation time* α_i (Fig. 7.2A). During the plateau phase, where the release of factors is balanced by new factors entering repair, bleaching of an area outside the local damage is initiated (FLIP). First all the free diffusible factors are bleached, so that only factors bound to damage are visible. Then, as soon as a factor leaves the repairosome, it diffuses away from the local damaged area and eventually becomes bleached to. Because new proteins entering repair are not fluorescent, one observes a continuous decrease of the fluorescence intensity in the local damaged area. This kinetics is directly proportional to repair factors leaving the repairosome and is characterized by the mean *residence time* ρ_i (Fig. 7.2A).

In the model, when the spatial gradients are neglected, the accumulation time of the ith factor simply reads

$$\alpha_i = \frac{\int_0^{t_p} [I_i(t_p) - I_i(t)]dt}{I_i(t_p) - I_i(0)}, \tag{7.11}$$

where t_p is the time point when the plateau is reached. A similar definition is used for the mean residence time

$$\rho_i = \frac{\int_0^\infty [I_i(t) - I_i(\infty)]\, dt}{I_i(0) - I_i(\infty)}. \tag{7.12}$$

Note that in the latter equation, the time point $t = 0$ is set when bleaching is initiated (for a general definition see Appendix D.1). Both the accumulation and residence time can be computed from experimental data and allow for a quantitative comparison of model and experiment.

Accumulation time: At low damage, the amount of factors immobilized on the DNA is small compared to their total amount ($T_i - I_i \approx T_i$); therefore, the system of differential equations describing NER can be linearized. Analytical expressions for the accumulation times are derived assuming that the free damage S_0 does not significantly decrease during the recruitment of repair factors (Appendix D.2). When binding is irreversible ($k_{-i} = 0$), the accumulation time of the ith factor reads

$$\alpha_i = \frac{\sum\limits_{j=i+1}^{n+1} \frac{1}{\kappa_j} \left(\sum\limits_{l=2}^{j} \frac{1}{\kappa_l} \right)}{\sum\limits_{j=i+1}^{n+1} \frac{1}{\kappa_j}}, \tag{7.13}$$

where the $\kappa_i = k_i T_i$ are the first order rate constants for the transitions between intermediary complexes. In this compact notation, the repair rate constant k_R is denoted by κ_{n+1}.

For example, the accumulation time of the last factor is ($n = 5$)

$$\alpha_5 = \frac{1}{\kappa_2} + \frac{1}{\kappa_3} + \frac{1}{\kappa_4} + \frac{1}{\kappa_5} + \frac{1}{\kappa_6}. \tag{7.14}$$

One recognizes that not only the binding of the 5th factor itself, but also processes occurring prior and after incorporation of this factor, that is binding of other repair factors and repair/release, respectively, contribute to its accumulation time. An exception is the binding of the first factor, which does not influence the accumulation kinetics (κ_1 does not enter Eq. (7.14)). In fact, due to the approximations made, the binding of the first factor only contributes in setting the immobilized concentrations at the end of the accumulation phase.

The same properties are found for the accumulation time of all other factors. Furthermore, using Eq. (7.13), one can show that the accumulation time of factors that bind later in the pathway is higher than of early binding factors

$$\alpha_j > \alpha_i, \quad \forall j > i. \tag{7.15}$$

Also for reversible binding does relation (7.15) hold true (see Appendix D.2.3). When the initial damage is high one can harness the fact that the first factor is nearly completely immobilized ($T_1 \approx I_1$). Assuming that the other factors are only weakly immobilized ($T_i - I_i \approx T_i$, $i > 1$), allows to compute the accumulation times (see Appendix D.3.2). One can show that, also in this case, relation (7.15) holds true.

Therefore, for these simplified cases with linear rate laws, the recruitment kinetics of a factor reflects its binding position. Early binding factors reach the plateau faster than later binding factors. Deviation from this order, may indicate that (*i*) the binding position of a factor is different, or that (*ii*) the structure of the NER pathway is more complicated than assumed. In particular, release may not occur simultaneously (see Section 10.3, page 134). For the complete model, when free factor concentrations do change in time, general conclusions cannot be derived. As we will see, when customizing the model parameters to the data, the analytical results represent a guideline but not the full answer.

In the expressions derived above, I neglected the diffusion of repair factors from the non-damaged area to the damaged area, which is a valid approximation for most of the factors who diffuse fast compared to the measured accumulation times (see Tables 6.1, 6.2, and Appendix D.1). Diffusion slows down the recruitment of repair factors and this is of particular interest for the first factor. The binding rate of the first factor is proportional to the amount of damages, and, at saturating UV dose, the number of damaged sites is in large excess, therefore, the first factor will quickly bind to the DNA as soon as it reaches the damaged area. Thus, the accumulation time of the first factor at saturating conditions, is predicted to be mainly influenced by its diffusional properties and not by its binding/dissociation characteristics. This point is illustrated in Section 7.3, where the model parameters have been estimated from the experimental data using a NER model that includes repair factor diffusion.

Residence time: As described above, the residence time of a factor i quantifies the mean time it remains at the damaged site. In experiments, this is determined from the kinetics of the local fluorescence intensity loss[2], which is initiated by photobleaching of the free diffusing proteins (FLIP, see Fig. 7.2). In the model, bleaching corresponds to

---

[2] In combined FRAP-FLIP experiments bleaching occurs only for a short time. However, in the framework of the model FRAP-FLIP and FLIP experiments give similar residence times (not shown).

$F_i(t > 0) = 0$, so that only the dissociation of the fluorescent factor from the repair complexes is observed, but not its binding. Because experiments are performed after a plateau in the immobile and free fraction of the factors has been reached, it can be assumed that the free factor concentrations remain constant during bleaching. For irreversible binding ($k_{-i} \approx 0$), one derives following residence times (cf. Appendix D.2.4)

$$\rho_i = \frac{1}{k_R} + \sum_{j=i+1}^{n} \frac{1}{k_j F_j} \left(1 - \frac{I_j(0)}{I_i(0)}\right) \text{ and } \rho_n = \frac{1}{k_R}, \tag{7.16}$$

where $I_j(0)$ is the concentration of the jth factor involved in repair at the beginning of bleaching ($t = 0$).

Equation (7.16), shows that the residence time is determined by the repair step, which is the step where the factor dissociates from the repairosome, and the transition from one intermediary complex to another (Fig. 7.2B, bleaching). Furthermore, due to relation $I_j(0) > I_i(0)$ ($j > i$), valid in a sequential assembly and simultaneous release mechanism (Eq. (7.8)), one obtains

$$\rho_j < \rho_i \text{ for } \forall j > i \tag{7.17}$$

This formula indicates that there is a strict relation between binding position and residence time. Early-binding factors reside longer at the site of damage than later-binding factors. The reason is that they have to pass a larger number of intermediate complexes before being released at the end of the pathway. When factors bind reversibly, the dissociation of a factor from its intermediary complex also influences its residence time. One can show that relation (7.17) holds true if the factors bind equally well to their respective substrate $\kappa_i = \kappa$ and $k_{-i} = k_-$, $i \leq n$ (see Appendix D.2.4).

This hierarchy in the residence times can break when the binding properties of repair factors to their respective substrate differ. Then, an early binding factor may reside for a shorter time in the repair complex than a late binding factor. This occurs, for example, when the intermediary complex formed by the binding of the factor of interest (e.g. complex S_4 in Fig. 7.2B, bottom panel) is unstable, that is the probability to dissociate just after binding is high. Then, the repair factor primarily leaves the damaged site by dissociating from its intermediary complex.

If the residence times of early binding factors is lower than of those which bind later, the presented theoretical analysis indicates that (*i*) factor release is not simultaneous; for example, the early binding factor is not needed for completion of the repair complex and leaves the repairosome at an early stage (see Section 8.3.2). (*ii*) Intermediary complexes containing the early binding factor are unstable, so that the repair factor dissociates before the repair complex is completed (see Appendix D.2.4). A direct comparison between the residence times estimated in the model and the experimental values is presented in Section 7.3.3, page 102.

7.3 Comparison of experimental data and model predictions

7.3.1 Recruitment of repair factors to the damage

Data acquisition and treatment: The data used for the development of the model were the accumulation kinetics in local damaged nuclei of XPC-GFP, XPB-GFP (a subunit of TFIIH), and ERCC1-GFP. These proteins have been expressed respectively in human XPC-deficient, human XPB-deficient, and CHO ERCC1-deficient cells and rescue the defects in NER [107, 124]. The immobile fractions as determined by FRAP in global damage experiments are used to set the plateau values of TFIIH and ERCC1-XPF [67, 71] (cf. Section 6.2). This is because FRAP is presumed to be a more reliable method for measuring immobile fractions, and with large excess of damaged sites, the maximal immobile fractions in local and global damage experiments should be approximately the same (see Chapter 10). To set the plateau level of XPC-HR23B I proceeded differently. According to the model, at saturation, the first factor will be fully engaged in repair (cf. Section 7.2.1). However, with FRAP only a maximum of ∼40% of XPC-HR23B was found to be immobilized at high UV doses [66]. A possible explanation is that only a subpopulation of XPC-HR23B is functional in NER, e.g. because not properly folded. Therefore, in the model, I assume that at the high UV dose used here this subpopulation is ∼100% involved in repair. For a more exhaustive discussion on this point I refer the reader to the Chapter 9 and 10.

Irreversible binding: The experimental data obtained from the local damage experiments are shown in Fig. 7.4A-C. One notices that at the saturating UV dose used (120 J/m^2), the accumulation kinetics of XPC-HR23B is slow. The model presented previously, where diffusion of the factors is not explicitely considered, would predict, at such large damage loads, a much faster accumulation of the first factor (not shown). I postulated that the observed accumulation kinetics of XPC-HR23B may be due to its slow diffusion from the non-damaged to the damaged area. Thus, to simulate the accumulation experiments and account for the spatial gradients arising after local generation of damages, I included nuclear diffusion of the free factors in the NER model; furthermore, the experimental procedure, necessary for the estimation of the immobile fractions, is explicitely modeled (see Appendix E).

The NER model, including diffusion of the repair factors, is fitted to the accumulation data. In a first step, the binding reactions are assumed irreversible (k_{-i}). This

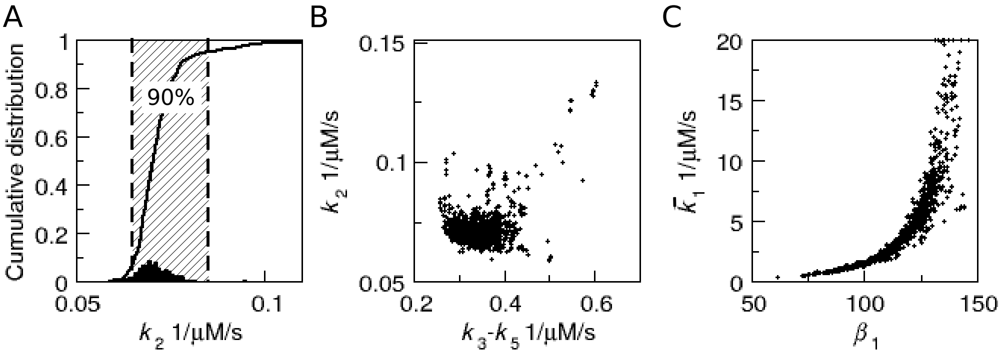

Figure 7.3: Estimation of confidence intervals and parameter dependencies. (A) Parameter distribution of the binding rate constants (shown for TFIIH, k_2) obtained by fitting the model to bootstrapped data (black bars). The 90% confidence interval is calculated by integrating the cumulative distribution (solid line). (B) Most parameters can be estimated independently. (C) The unbuffered binding rate constant for XPC-HR23B $\tilde{k}_1$ has high variance and positively correlates with the buffering coefficient β_1 .

simplification is justified by the fact that XPC-HR23B readily binds to damaged DNA in vitro, with an equilibrium constant of 0.5 to 5 nM [8, 60]. One can estimate that the probability for XPC-HR23B to dissociate from the damaged site before TFIIH binds is very low (< 1%). Thus, XPC-HR23B is committed to repair as soon as it binds to the damage. Assuming similar dissociation constants for the other factors leads to analogous conclusions. Hence, the contribution of the dissociation events to the repair process is expected to be small.

The fitting yields the binding rate constants for all NER factors and an effective diffusion coefficient for XPC-HR23B. The effective diffusion coefficients of the other factors are taken from literature (Tab. 7.2, set 1). I recall that the effective diffusion coefficients account for the impairment in diffusion caused by binding of repair factors to non-damaged sites (see Appendix E). The 90% confidence intervals were estimated using bootstrap [39, 125]. Briefly, I generated synthetic data by drawing for each time point of the original data set so many data points as the original set (drawing with replacement). The model is then fitted to this synthetic data set. The operation is repeated so many times as necessary to obtain a smooth parameter distribution. From this distribution, it is straightforward to calculate the 90% confidence interval (Fig. 7.3A). One can also assess how good the parameters can be determined independently from each other. For nearly all parameters I found no correlation to another parameter, Fig. 7.3B. An exception is the positive correlation observed between the XPC-HR23B unbuffered

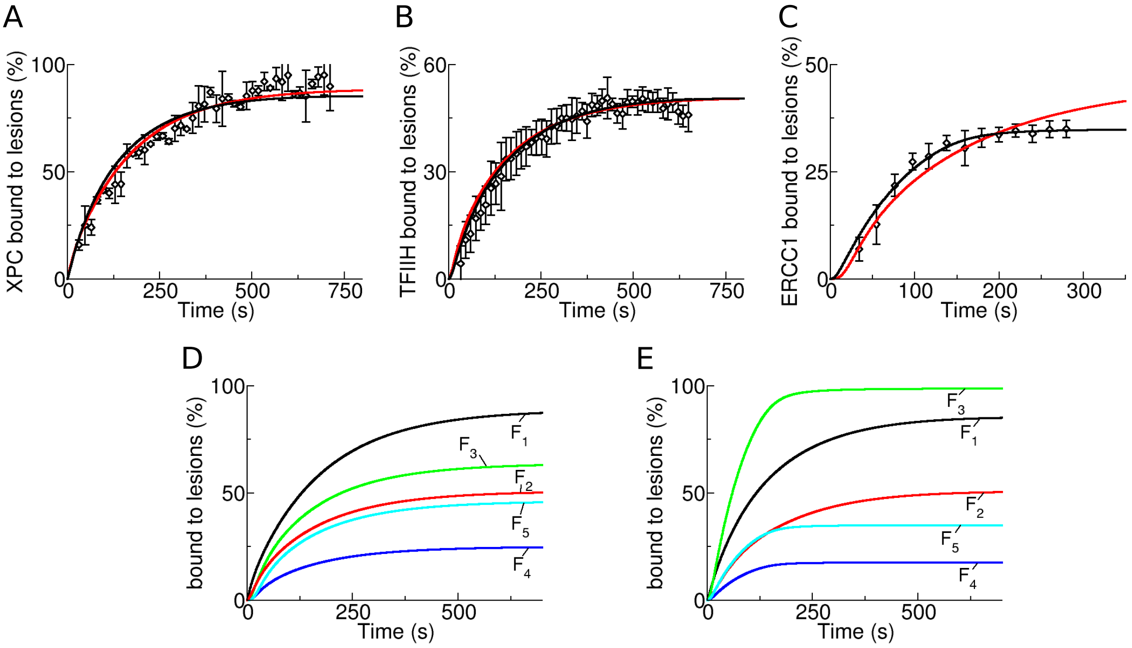

Figure 7.4: (A-C) Accumulation in the UV damaged area of XPC-HR23B, TFIIH and ERCC1-XPF (average of 3, 10 and 9 experiments, respectively). Red and black lines are model predictions using parameter set 1 and 2, irreversible binding Tab. 7.2, respectively (model with free factor diffusion, Appendix E.1). In simulations, DNA repair is initiated by 38 μM damages in one-seventh of the nuclear volume. (D-E) Simulated immobilized fractions using, respectively, set 1 and 2. In (E) kinetics of ERCC1-XPF (F_5) is shorter than of XPC-HR23B (F_1) and TFIIH (F_2). Immobilization of the putative limiting factor F_3 is more rapid and complete than for the other factors. The sum of least squares is 100.7 and 49.73 for set 1 and 2, respectively. According to a χ^2 test, the observed values can be explained by the noise in the data ($p < 0.01$). A likelihood ratio test indicates that parameter set 2 is significantly better in reproducing the data than parameter set 1 [109, 125].

binding rate constant $\tilde{k}_1$ and buffering coefficient β_1, a parameter that is proportional to the amount of non-damaged XPC-HR23B binding sites (Fig. 7.3C). Therefore, with the available data, both parameters can only be poorly determined independently. Nevertheless, the effective rate constant $k_1 = \tilde{k}_1/\beta_1$ shows an acceptable variance (Tab. 7.2).

The model with the estimated parameters properly reproduces the recruitment kinetics for both XPC-HR23B and TFIIH (Figs. 7.4A and B, respectively: red curves). It predicts an effective diffusion coefficient of 0.1–0.3 μm^2/s for XPC-HR23B, which accounts for its slow accumulation in the locally damaged nuclear area. This value is remarkably low, as a diffusion coefficient of $\sim$ 15 μm^2/s is expected based on its molecular size and assuming free diffusion. The low effective diffusion coefficient indicates that a large fraction ($\sim 98\%$) of XPC-HR23B is transiently immobilized (see Appendix C.1 and E.1). This notion is supported by the fact that XPC-HR23B has a significant affinity for undamaged DNA [148], and by recent experimental data on mobility and nuclear distribution of XPC-HR23B *in vivo* [66]. Using the same parameter set that is adequate for XPC-HR23B and TFIIH I found that the predicted accumulation kinetics of ERCC1-XPF is slightly slower compared to its measured behavior (Fig. 7.4C: red line; predicted accumulation time 110 s, compared to a measured value of 75 s). In fact, the binding phases of all NER factors have similar kinetics (Fig. 7.4D). In agreement with the analytical results (Section 7.2.2), the tendency is that early binding factors accumulate faster than late binding factors.

For each repair factor, the experimentally reported concentration values vary by a factor of 2–3 [5, 174, 191] and this may affect the model predictions. Therefore, I tested whether variations in the total concentrations could improve the agreement between the ERCC1-XPF simulated and measured accumulation data. The model predicts that the assembly kinetics of XPC-HR23B, TFIIH, and ERCC1-XPF can all be reproduced faithfully if one of the NER factors that binds after TFIIH, but prior to ERCC1-XPF, is present at a significantly lower concentration than assumed in parameter set 1 (Tab. 7.2). Figures 7.4A–C (black lines) show a model simulation where the total concentration of the third factor (in my model XPG) is estimated numerically to be three to four times lower than the concentration of the other NER factors (Tab. 7.2, set 2). Due to its low concentration, a large fraction of this protein becomes involved in DNA repair (compare the curves for F_3 in Fig. 7.4D and E), and will therefore become "limiting" for the accumulation of ERCC1-XPF. In contrast, the initial accumulation of both XPC-HR23B and TFIIH is unaffected.

Reversible binding: A factor, after binding of TFIIH, that is highly immobilized during repair, has not been yet identified experimentally. It is now important to understand, whether the prediction of a limiting factor is related to the irreversibility assumption, or whether it is a result of the model structure (sequential binding and simultaneous release). I therefore tested the performance of the complete model, with reversible binding of the factors, against the data.

The fitting yields binding and dissociation rate constants of the factors (Tab. 7.3, set 3). There is only a slight improvement in the quality of the fit (Fig. 7.5A-C, red curves), and the obtained results are similar to the irreversible model (Fig. 7.4A-C, red curves). In particular, the fast kinetics of ERCC1-XPF is only partially reproduced. However, if

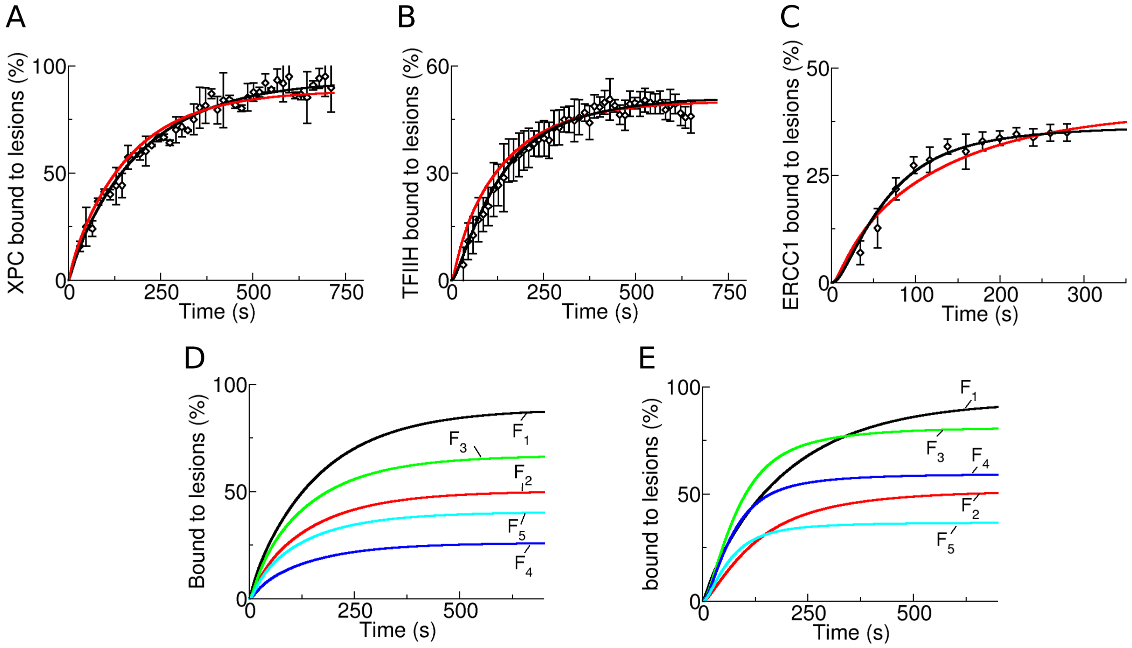

Figure 7.5: (A-C) Red, and black lines are model predictions using parameter set 3 and 4 (Reversible binding, Tab. 7.3), respectively. (D-E) In none of the two parameter sets is there a limiting factor after XPC-HR23B. The sum of least squares is 75.1 and 30.8 for parameter set 3 and 4. A likelihood ratio test indicates that there is no significant difference in the quality of the fit obtained with set 4 and set 2 (limiting factor).

the total factor concentrations are also fitted numerically (Tab. 7.3, set 4), the agreement between model and data considerably increases, and also the accumulation kinetics of ERCC1-XPF is reproduced faithfully (Fig. 7.5A-C, black curves). Interestingly, except for XPC-HR23B, the immobile fractions are all below 80% (Fig. 7.5E). This indicates that when the binding of downstream factors to their intermediary complex is strongly reversible (see Tab. 7.3), the accumulation of XPC-HR23B, TFIIH, and ERCC1-XPF can all be reproduced without invoking the existence of a limiting factor. However, as shown in Section 7.3.3, the presence of dissociation events prior the repair step dramatically modifies how long the factors reside at the damaged site. One obtains large differences in the simulated and experimentally measured residence times.

7.3.2 Long-time behavior

I wanted to test whether the model could correctly reproduce the kinetic behavior over longer time periods. To this end, the ERCC1-XPF immobilization has been measured

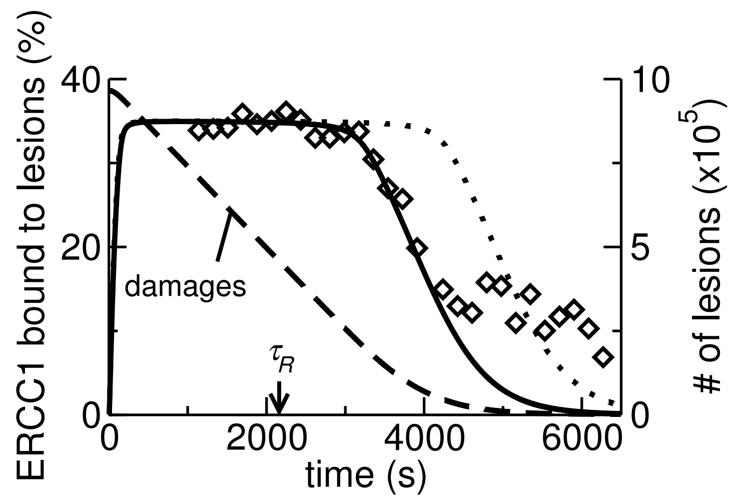

Figure 7.6: Kinetics of ERCC1-XPF after local UV irradiation (dots). The solid line is a model simulation using parameter set 2 (set 1,3 and 4 gave similar results). Shown are also the total number of damaged DNA sites (dashed line) and the release kinetics of ERCC1-XPF for a higher damage dose (dotted line, 48 μM damaged DNA sites) as obtained in the model. The arrow indicates the value of the repair time τ_R obtained from Eq. (8.1).

over several hours. In experiment and model, one can distinguish a long plateau phase during which the amount of immobilized ERCC1-XPF remained approximately constant (Fig. 7.6; diamonds: experimental data; solid line: simulation). The model predicts that during this phase the number of damaged DNA sites decreases with a nearly constant and maximal rate V_{max} (dashed line). Finally, in the model and experiment, one observes a "release" phase where the damage-bound protein fraction gradually decreases[3]. A plateau, followed by a monophasic decrease in the fraction bound to the DNA has been measured for other repair factors (M. Luijsterburg, personal communication).

The time course shown in Fig. 7.6, with its long plateau phase, indicates that the repair system is indeed saturated. The model predicts that: (*i*) a similar time course is expected for the other repair factors, and (*ii*) if the initial damage concentration is increased, the characteristics of both the assembly and the "release" phase remain unaffected; only the duration of the plateau phase changes, proportionally to the amount of initial damage (Fig. 7.6: dotted line).

---

[3] Only in the experiment shown in Fig. 7.6 does one observe a third phase (for $t > 4000$ s). During this phase the bound fraction decreases more slowly. Such a marked biphasic behavior is not observed in the model.

Residence times (in sec)					
Factor	Experiment	Set 1	Set 2	Set 3	Set 4
XPC-HR23B	~ 44	166.6	221.6	222.4	884.3
TFIIH	~ 102	147.1	196.1	153.9	142.9
XPG	–	143.7	142.8	62.4	6.9
XPA	~ 160	143.4	142.8	10.4	3.7
ERCC1-XPF	~ 144	142.8	142.8	2.1	1.1

Table 7.1: Residence times as obtained from experiments and with the mathematical model using the different parameter sets (Tab. 7.2–7.3). In the model the residence times have been calculated for saturating conditions as described in Appendix D.3.3.

7.3.3 Life time of repair factors in the repairosome

The residence times represent a source of independent data against which the developed model can be tested. In Tab. 7.1 I listed the experimental data together with the model results for the four different parameter sets. When binding is irreversible (set 1 and 2), the calculated residence times of TFIIH, XPA, and ERCC1-XPF are in the range of the reported values. This is not the case when binding is reversible (set 3 and 4). One finds, for XPA and ERCC1-XPF, residence times which are far below the measured values. This is due to the fact that, for these factors, it is likely to leave the DNA before finishing repair (large dissociation rate constants k_{-4} and k_{-5}, Tab. 7.3). For example, the residence time of ERCC1-XPF reads

$$\rho_5 = \frac{1}{k_{-5} + k_R}. \tag{7.18}$$

According to the estimated parameters $k_{-5} \gg k_R$, so that the dissociation reaction is the main process which determines the residence time of ERCC1-XPF.

A second feature, observed for all parameter sets, is that the residence time of XPC-HR23B is far above its experimentally obtained residence time. I will show, in Section 8.3.2, how a low residence time of XPC-HR23B may be accounted for by the fact that the last step of repair is performed in the absence of XPC-HR23B. This allows for XPC-HR23B to leave the repairosome at an earlier time point.

7.3.4 Concluding remarks

To summarize, the developed model performs well for most of the experimental data available. The few differences between model predictions and experimental data are not due to the choice of parameters, as different parameter sets and situations have been tested, but rather indicate that some of the assumptions that entered the model may need to be reviewed. In particular, relaxing the assumption of simultaneous release of the factors may bring to the fore other dynamic properties of NER. This will be discussed in detail in Chapter 10.

Model parameter and values: irreversible binding

Parameters	Set 1	Set 2
Total concentrations		
T_1, T_2	0.44, 0.6 μM	0.44, 0.6 μM
T_3	0.44 μM	**0.1959 μM (0.191–0.258)**
T_4, T_5	1.1, 0.55 μM	1.1, 0.55 μM
Effective binding rate constants ($k_i = \tilde{k}_i/\beta_i$)		
k_1	**0.0118/μM/s (0.01-0.088)**	**0.0054/μM/s (0.0046-0.01)**
k_2	**0.0697/μM/s (0.065-0.085)**	**0.0631/μM/s (0.059-0.09)**
k_3, k_4, k_5	**0.373/μM/s (0.282-0.427)**	**5/μM/s (0.85–93.77)**
Repair rate constant		
k_R	0.007/s	0.007/s
Diffusion coefficients		
$\tilde{D}_1$, $\tilde{D}_2$, $\tilde{D}_3$, $\tilde{D}_4$, $\tilde{D}_5$	15, 6, 15, 15, 15 μm^2/s	15, 6, 15, 15, 15 μm^2/s
Buffering coefficients		
β_1	**90 (87.4-136.4)**	**60 (47.53-92.82)**
β_2, β_3, β_4, β_5	1.2, 1, 1, 1	1.2, 1, 1, 1
Effective diffusion coefficients coefficients ($D_i = \tilde{D}_i/\beta_i$)		
D_1	**0.16 μm^2/s (0.11-0.171)**	**0.25 μm^2/s (0.16-0.31)**
D_2, D_3, D_4, D_5	5, 15, 15, 15 μm^2/s	5, 15, 15, 15 μm^2/s

Table 7.2: The nuclear volume is 0.3 pl. In set 1 total concentrations are based on published data [5], whereas in parameter set 2 the concentration of the 3rd factor is estimated numerically. The repair rate constant k_R corresponds to the inverse of the residence time measured for ERCC1-XPF [71]. Due to the lack of kinetic data for the 3rd and 4th factor, I took $k_3 = k_4 = k_5$. The bold faced parameters are estimated by fitting the model depicted in Fig. 7.1 with free factor diffusion (Appendix E) to the accumulation curves shown in Fig. 7.4A–C. Binding is irreversible ($k_{-i} = 0$). Numbers in brackets give the 90% confidence intervals as determined with bootstrapping. The diffusion coefficients of the free TFIIH, XPA, and ERCC1-XPF ($\tilde{D}_2$, $\tilde{D}_4$ and $\tilde{D}_5$ respectively) and their buffering coefficients (β_2, β_4 and β_5 respectively) were taken from literature [67, 71, 127]. The diffusion coefficients of the free XPC-HR23B and XPG proteins ($\tilde{D}_1$ and $\tilde{D}_2$ respectively) were estimated according to their molecular weights. For XPG there are no indications that it binds to undamaged DNA ($\beta_3 = 1$).

Model parameter and values: reversible binding		
Parameters	Set 3	Set 4
Total concentrations		
T_1	0.44 μM	**1.1 μM (0.897-1.1)**
T_2	0.6 μM	**1.07 μM (0.764-1.1)**
T_3, T_4, T_5	0.44, 1.1, 0.6 μM	0.44, 0.44, 0.44 μM
Effective binding rate constants ($k_i = \tilde{k}_i/\beta_i$)		
k_1	**0.0078/μM/s (0.0071-0.0084)**	**0.0043/μM/s (0.0039-0.0046)**
k_2	**0.0783/μM/s (0.062-0.143)**	**0.0155/μM/s (0.0135-0.023)**
k_3, k_4, k_5	**5/μM/s (0.91-9.7)**	**5/μM/s (4.8-5.2)**
Dissociation rate constants		
k_{-1}	**0**	**0**
k_{-2}	**0.0762/s (0.02-0.6513)**	**0.0138/s (0.012-0.036)**
k_{-3}, k_{-4}, k_{-5}	**0.463/s (0.12-0.714)**	**0.85/s (0.66-0.9)**

Table 7.3: NER model with reversible binding and free factor diffusion (Appendix E). Bold faced parameters are fitted to the accumulation curves in Fig. 7.4A-C, number in brackets give the 90% confidence interval. Due to the lack of kinetic data for the 3rd and 4th factor, I assumed binding and dissociation rate constants equal to the rate constants of the 5th factor. Parameters which are not listed are as given in Tab. 7.2, set 1. In parameter set 4 also the total factor concentrations are estimated numerically. The total concentration of the 3rd, 4th, and 5th factor are assumed to be the same.

Chapter 8

Efficiency of sequential NER and pathway alternatives

8.1 Repair efficiency

Repair is considered to be efficient if the DNA damage is rapidly removed. The mean repair time, needed to remove a certain amount of initial damaged DNA sites, is defined by

$$\tau_R = \frac{1}{D_T(0)} \int_0^\infty D_T(t)dt \tag{8.1}$$

where $D_T(t)$ denotes the damage concentration in time. The value of the repair time for the local damage experiments is indicated by an arrow in Fig. 7.6 ($\tau_R = 2161$ s). Efficient repair is characterized by a low τ_R. To assess how the system parameters affect repair efficiency, I define the following control coefficients

$$C_p^{\tau_R} = \frac{p}{\tau_R} \frac{\partial \tau_R}{\partial p}, \tag{8.2}$$

where p denotes one of the rate constants or one of the factor concentrations [57]. Parameters that strongly affect repair efficiency will have high absolute values for their corresponding control coefficients. Two cases can be distinguished, a low and a high initial damage, for which analytical expressions of the repair time are derived.

8.1.1 Low initial damage

In this case, the immobile fraction of the factors is low ($T_i - I_i \approx T_i$). With the so linearized system one can calculate the repair time analytically (Appendix D.2.2). If

Control on the repair time: low damage				
Parameter	Set 1	Set 2	Set 3	Set 4
k_1T_1	**–0.5167**	**–0.7113**	**–0.601**	**–0.4157**
k_2T_2	–0.0642	–0.0447	–0.0472	–0.1331
k_3T_3	–0.0163	–0.0017	–0.005	–0.0322
k_4T_4	–0.0065	–0.0003	–0.0071	–0.0737
k_5T_5	–0.0131	–0.0006	–0.057	–0.1816
k_R	**–0.3832**	**–0.2414**	**–0.3508**	**–0.461**
k_{-1}	0	0	0	0
k_{-2}	0	0	0.0031	0.0146
k_{-3}	0	0	0.0025	0.0305
k_{-4}	0	0	0.0065	0.0722
k_{-5}	0	0	0.0561	0.18
Reference repair time				
τ_R (sec)	372.77	591.71	484.68	508.54

Table 8.1: Control coefficients of the reaction rate constants on the repair time as obtained from the four parameter sets. Note that the repair times (last row) has been calculated for low damage conditions, a case that most likely reproduce the situation in nature (e.g. sun exposure). In experiments a high initial damage has been used.

binding is irreversible, $k_{-i} = 0$, the repair time reads

$$\tau_R = \sum_{i=1}^{n+1} \frac{1}{\kappa_i}, \tag{8.3}$$

where $\kappa_i = k_iT_i$ and $\kappa_{n+1} = k_R$ $(i = 1, \cdots, n)$.

Clearly, all binding reactions and the repair step contribute to the repair time. The control coefficients

$$C^{\tau_R}_{\kappa_i} = -\frac{1}{\tau_R \kappa_i} \tag{8.4}$$

reveal that the strongest influence on the repair time is exerted by the slowest step. For low damage concentrations, the recognition and the repair step, because of their low rate constants, are the principal processes that limit repair (Tab. 8.1, set 1 and 2).

The presence of dissociation events prior to the repair step ($k_{-i} \neq 0$) changes the repair time

$$\tau_R = \sum_{i=1}^{n+1} \frac{1}{\kappa_i} + \sum_{i=0}^{n-1} \sum_{j=1}^{n-i} \frac{\prod_{l=j}^{i+j} k_{-l}/\kappa_l}{\kappa_{i+j+1}}. \tag{8.5}$$

If the stability of the intermediary complexes is decreased by increasing the dissociation rate constants, the repair efficiency is impaired (repair time rises). For the estimated parameters, one finds, as for irreversible binding, that the recognition and repair steps exert the highest control on the repair time (Tab. 8.1, set 3 and 4).

Assuming that the factors bind equally well to their respective substrate ($\kappa_i = \kappa$ and $k_{-i} = k_-$ for $i \leq n$) simplifies the repair time as follows

$$\tau_R = \sum_{i=0}^{n} \left(\frac{k_-}{\kappa}\right)^i \left(\frac{1}{\kappa_R} + \frac{n-i}{\kappa}\right). \tag{8.6}$$

The quantity $k_-/\kappa = k_-/(kT)$ represents the dissociation constant of a factor to its intermediary complex. Equation (8.6) brings to light a condition for NER to be efficient in removing DNA lesions: as NER involves a large number of proteins ($n \geq 5$)[1], these proteins must be sufficiently affine to their substrate ($k_-/\kappa \leq 1$). The importance of this condition is illustrated in Fig. 8.1, when $k_-/\kappa \leq 1$ the repair time increases only moderately with the number of factors, whereas for $k_-/\kappa > 1$ the rise is very pronounced. Already for five repair factors the differences between these two cases can be considerable. According to the estimated parameters, the condition $k_{-i}/\kappa_i < 1$ is fulfilled for nearly all factors (except the 2nd factor in set 3), indicating that NER, for the number of required factors, is a rather efficient pathway (Tab. 7.3).

8.1.2 High initial damage

If a large number of lesions is introduced at $t = 0$, it is not possible to calculate τ_R explicitly. An approximation for the time changes of the damage concentration is given by (Appendix C.4)

$$\frac{dD_T}{dt} = -V_R \approx -V_{max} \frac{D_T}{D_T + K_d}, \tag{8.7}$$

where V_{max} is the maximal repair rate and K_d is the damage concentration at which lesions are removed at half-maximal rate ($V_R = V_{max}/2$). Using Eq. (8.7) one derives (Appendix D.2.2)

$$\tau_R \approx \frac{1}{2} D_T(0) V_{max} + \frac{K_d}{V_{max}}. \tag{8.8}$$

---

[1] In the model, I considered the five most prominent repair factors, however, there are indications that at least two additional proteins, RPA and UV-DDB, are also involved in repair [59, 108, 119, 159]

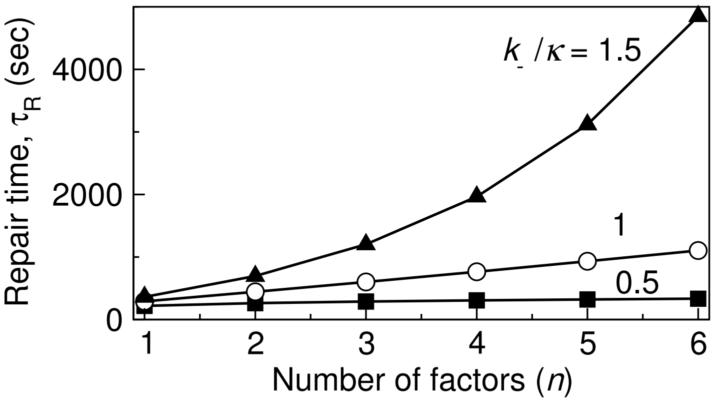

Figure 8.1: Low initial damage: Repair time as function of the number of repair factors, Eq. (8.6). The dissociation rate constant k_- is increased from 0.1 (square), to 0.2 (circle) and 0.3 (triangle). The latter case is considerably less efficient in removing damages. The other parameters are $k_R = 0.007$ and $\kappa = kT = 0.2$/s.

Which indicates that the repair time increases linearly with the initial damage concentration $D_T(0)$. For the control coefficients one obtains

$$C_p^{\tau_R} = \frac{2K_d}{2K_d + D_T(0)} C_p^{K_d} - C_p^{V_{max}}, \tag{8.9}$$

where $C_p^{V_{max}}$ and $C_p^{K_d}$ are the control coefficients of parameter p on the maximal repair rate V_{max} and the half-saturation constant of repair K_d, respectively (defined in analogy to Eq. (8.2)). These two coefficients are specific to the repair system and are independent of the inflicted damage. At a saturating damage concentration ($D_T(0) \gg K_d$), only parameters affecting V_{max} will influence the repair time, $C_p^{\tau_R} = C_p^{V_{max}}$.

The control coefficients shown in Tab. 8.2 demonstrate that each reaction step contributes to the repair time. Increasing the total concentrations of early binding NER proteins appears to have the strongest effect on repair efficiency (largest positive control on V_{max}). In contrast, for the rate constants, the largest positive effect on V_{max} is exerted by the repair rate constant. This is because the repair step is relatively slow compared to the time needed to assemble the PC. Conversely, changes in the binding rate constant of the first NER factor (k_1) have no effect on V_{max} (control coefficient equals zero, Tab. 8.2). The rationale for this is that, under saturating conditions, the first factor will be completely involved in repair. Increasing k_1, on the other hand, has a strong negative effect on K_d, making the system more proficient for repairing low amounts of DNA damage (cf. to the previous section). This analysis, valid for small parameter changes, pinpoints steps that are likely to have the strongest influence on

Control Coefficients for the Maximal Repair Rate and the Half-Saturation Constant						
	XPC-HR23B	TFFIIH	XPG	XPA	ERCC1-XPF	Repair step
Control on V_{max} by binding rate constants and total factor concentrations						
$C_k^{V_{max}}$	0 (k_1)		0.145 (k_2)	0.071 (k_3)	0.016 (k_4)	0.046 (k_5)
$C_T^{V_{max}}$	$\boxed{0.612\ (T_1)}$		0.329 (T_2)	0.221 (T_3)	0.021 (T_4)	0.091 (T_5)
Control on K_d, the half-saturation constant of repair						
$C_k^{K_d}$	$\boxed{-0.632\ (k_1)}$		0.086 (k_2)	0.068 (k_3)	0.01 (k_4)	0.04 (k_5)
$C_T^{K_d}$	-0.148 (T_1)		0.322 (T_2)	0.279 (T_3)	0.017 (T_4)	0.1 (T_5)

Table 8.2: The term in brackets refers to the parameter for which the control coefficient has been calculated (using parameter set 1, Table 1). One has $V_{max} = 1.92$ nM/s and $K_d = 0.52$ μM. These two values are in agreement with the experimentally estimated values of 1.03–2.24 nM/s for V_{max} and ~ 1 μM for K_d [71, 175].

repair efficiency.

Figures 8.2A and B analyze the effect of large changes in the system parameters on repair efficiency, characterized by the repair time τ_R. Interestingly, changing the value of one of the binding rate constants over a 25-fold range has little or no effect on repair time (Fig. 8.2A). Also increasing the concentration of just one of the protein factors (Fig. 8.2B) has only a limited influence on repair efficiency. The rationale for this is that after an increase in rate, achieved by making one step faster (e.g. by increasing the concentration of one of the protein factors), the repair process as a whole will be limited by one of the other reaction steps. On the other hand, changes in the repair rate constant k_R appear to significantly modulate the repair time (Fig. 8.2B). This is because the repair/release step is slow compared to the other steps, thereby suppressing the availability of free repair proteins.

This analysis reveals an important property of sequential assembly systems: No single component uniquely controls the repair process. There are some processes that seem to have a larger control. I have shown that the last step in the model depicted in Fig. 7.1 has a stronger control on repair efficiency compared to processes characterizing the assembly of the pre-incision complex. In order to verify this hypothesis experimentally it would be useful to measure the maximal rate of damage removal (V_{max}) for different factor concentrations. The results of the simulations are shown in Fig. 8.2C. Different from the previous case, rising the concentrations of all factors simultaneously strongly increases V_{max}, resulting in a more efficient repair. The relationship between V_{max} and

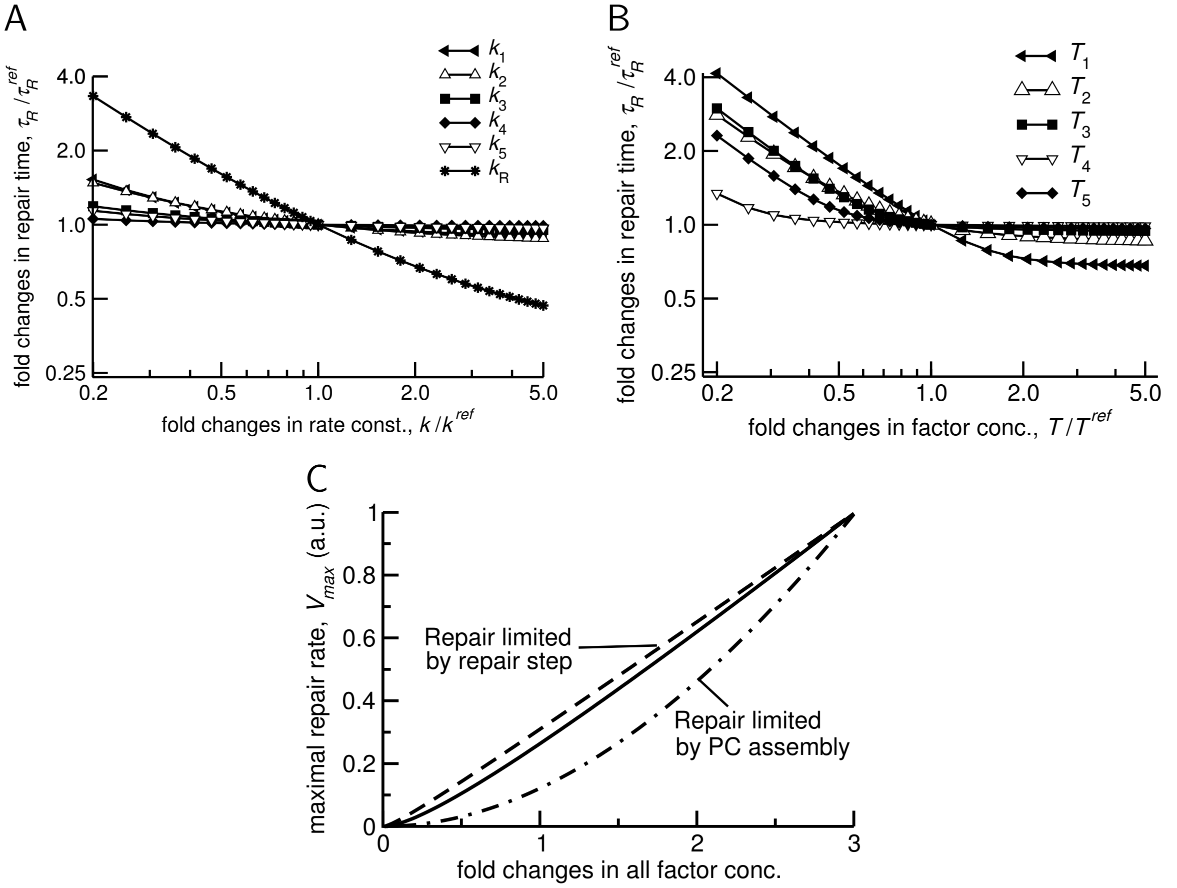

Figure 8.2: Repair efficiency for large parameter changes. An increase in efficiency corresponds to a decrease in repair time τ_R. (A) Fold changes in τ_R due to changes in each of the individual rate constants. τ_R is calculated from Eq. (8.1) for an initial damage of 4 μM given to the whole nucleus (i.e. 7.2×10^5 lesions). Fold changes are relative to reference parameter values k^{ref} and reference repair time ($\tau_R^{ref} = 20.56$ min) obtained from set 1, Tab. 7.2. (B) Fold changes in τ_R due to changes of each of the total NER factor concentrations. (C) Changes in maximal repair rate V_{max} due to variations in total concentrations of all NER factors simultaneously. The total concentrations are increased or decreased by an equal factor. With a slow repair step ($k_R = 0.001$/s, upper dashed line, or 0.007/s, solid line), V_{max} depends nearly linearly on the factor concentrations (first order reaction). For a fast repair step ($k_R = 0.7$/s, lower dashed line), where repair is limited by the assembly of the proteins, the dependency on factor concentrations is of second order. The values for V_{max} have been normalized. Similar results are obtained for parameter set 2 to 4 (Tab. 7.2 and 7.3).

the protein concentrations depends on the process that limits repair. If repair is limited by the rate of the last step, the relation between factor concentrations and V_{max} is approximately linear (Fig. 8.2C, upper dashed and solid line). On the other hand, if repair is limited by the rate of PC assembly, V_{max} depends on protein factor concentrations as in a second order reaction (Fig. 8.2C, lower dashed line). This result can be proved analytically for the case of irreversible binding ($k_{-i} = 0$) and equal total concentrations T (see Appendix C.4). When the limiting process is the repair step, i.e. $k_i \gg k_R$,

$$V_{max} \approx k_R T. \tag{8.10}$$

When repair is limited by the assembly of the factors, i.e. $k_i \ll k_R$,

$$V_{max} \approx k_n \lambda_{n-1} T^2, \tag{8.11}$$

which is second order in T. The constant λ_{n-1} depends on all binding rate constants and the repair rate constant (cf. Appendix C.4, page 172).

The values of V_{max} and K_d as well as of the repair time can be measured experimentally (e.g. [71, 175]). Therefore, several of the model predictions presented here, concerning the perturbation of the factor concentrations, could be tested experimentally.

8.1.3 Relation between repair efficiency and accumulation kinetics

NER is a versatile repair mechanism that recognizes several type of lesions. It is interesting to understand, whether the factor recruitment kinetics can shed light on which type of lesion is repaired and on how efficiently this lesion is removed.

To be specific, I assume that the binding properties of the repair factors to the different type of lesions are not equal. How the accumulation times, characterizing the recruitment kinetics, change for variations in the binding and dissociation rate constants is plotted in Fig. 8.3. I recall that a decrease (increase) in the binding (dissociation) rate constant goes hand in hand with a rise in the repair time, and so a less efficient repair. Surprisingly, the accumulation times can display a maximum as function of the rate constants (Fig. 8.3). This is a counterintuitive result, one would expect that the better a type of damage is repaired, the faster the factors are recruited (low accumulation time).

The theoretical analysis shows that the accumulation kinetics of factors to the local damage is not always correlated with repair efficiency. Recruitment of factors to lesions to which they are less affine, for example due to higher dissociation rate constants, could proceed faster than the recruitment to lesions which are more efficiently repaired (low dissociation rate constants).

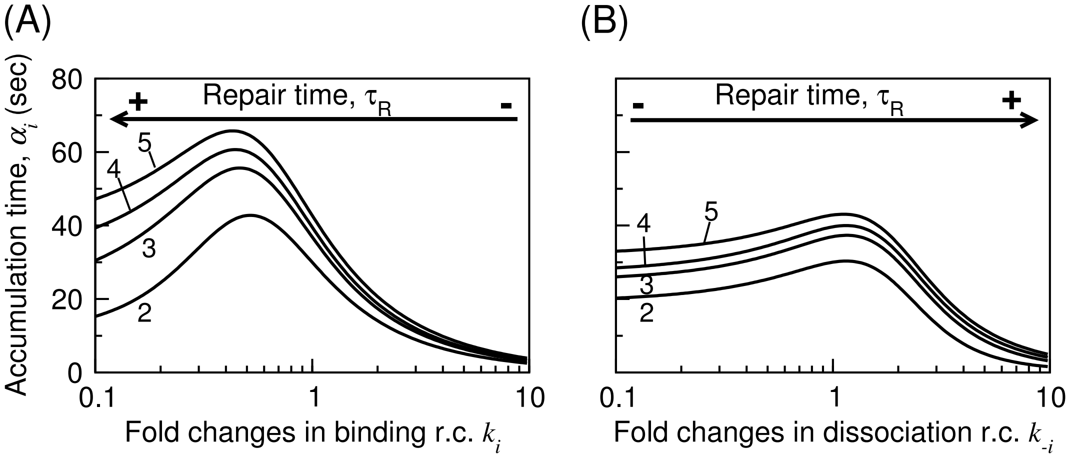

Figure 8.3: The accumulation times are calculated for high damage (see Appendix D.3.2) as function of the binding rate constants (r.c.) k_i (A) or the dissociation rate constants k_{-i} (B). The numbers indicate the repair factor for which the accumulation time is plotted. The rate constants are varied simultaneously by the same coefficient. The reference parameter set is given in Tab. 7.2, set 1. The dissociation rate constants are equal for all factors $k_{-i} = k_- = 0.1/s$. These calculations have been performed for the linearized system ($T_i - I_i \approx T_i$, $i > 1$), similar results are obtained for the complete model and for the other parameter sets (not shown).

8.2 Selectivity of NER

The previous analysis demonstrated that repair efficiency decreases with the number of repair factors (the repair time increases, Eq. (8.6)). Therefore, with respect to efficiency, it would be better to perform the repair task with only one protein. In fact, some organisms use a photolyase for removing 6-4PPs and one for removing CPDs [3]. Which are then the advantages of using a multitude of proteins for performing repair?

NER has a wide range of substrates that all cause distortions of the DNA helix. This fact indicates how unlikely it is to have an extremely high affinity just for a specific substrate, as this would impair the ability to recognize the other type of lesions. It has been shown, *in vitro*, that the differences in NER protein affinity between damage and undamaged DNA are small. For example, the affinity of XPC and UV-DDB for non-damaged DNA is only slightly lower than for thymine dimers. Thymine dimers, however, are still repaired efficiently by NER [132], whereas undamaged DNA, which can have spontaneous helix distortions, is excised to a much lesser extent by the endonucleases [14]. The problem one is faced to, is to minimize excision of undamaged DNA, an energy consuming process and possible source of mutations [49], when the affinity to lesions is only slightly higher than to non-damaged sites. In the following, I will analyze how the usage of several proteins in NER can resolve this problem.

Let assume two types of substrates for NER: The lesions and some slight helix distortions. The two substrates differ in their affinity for the repair factors. A system is highly selective, if it repairs the damage much faster than the excision of non-damaged sites. I define the selectivity of repair by

$$\sigma = \frac{\tau_R^* - \tau_R}{\tau_R^*}. \tag{8.12}$$

where τ_R^* is mean time needed to excise non-damaged sites. It is reasonable to assume that the recognition and repair of damages occurs faster than the excision of non-damaged sites, thus $\tau_R^* > \tau_R$. The selectivity σ varies between 0 and 1, and a value of 1 corresponds to the highest selectivity for the damage. How well NER recognizes the damage compared to the non-damaged substrate can be expressed by the ratio of the dissociation constants, the versatility

$$\omega = \frac{\sum_1^n k_{-i}/k_i}{\sum_1^n k_{-i}^*/k_i^*}. \tag{8.13}$$

Where k_{-i}^* and k_i^* denote the dissociation and binding rate constants of the repair proteins to the non-damaged sites, respectively. The versatility varies between 0 and 1, ω is equal 1 when all helix distortions are repaired with the same efficiency.

In Fig. 8.4 I plotted these two measures against each other. Clearly, the higher the affinity of the factors to the damaged site, low ω, the higher the selectivity. Because for each additional repair factor the substrate is verified anew, the selectivity increases with the number of factors involved in repair. Furthermore, for a multiprotein process the selectivity remains high even if the affinity for the lesions decreases, higher ω, whereas a single protein mediated repair ($n = 1$) loses its selective power. As postulated above, to recognize a multitude of damage types it is desirable to have a moderate affinity for each type of lesion. Therefore, a multiprotein process allows to recognize and selectively repair a larger range of helix-distorting lesions compared to a process relying on a single protein.

The selectivity of NER towards the damaged substrate reminds kinetic proofreading [12, 68]. In my model the selectivity relies on the fact that the system is not in thermodynamic equilibrium. This is because the excision step is irreversible and the excised ssDNA containing the damage is quickly degraded. Strictly speaking, a kinetic proofreading mechanism also includes (i) irreversible, energy consuming, steps before the last catalytic one, and (ii) the possibility for the enzyme complex to fall off its substrate after such irreversible reactions. These latter mechanisms have been shown, using

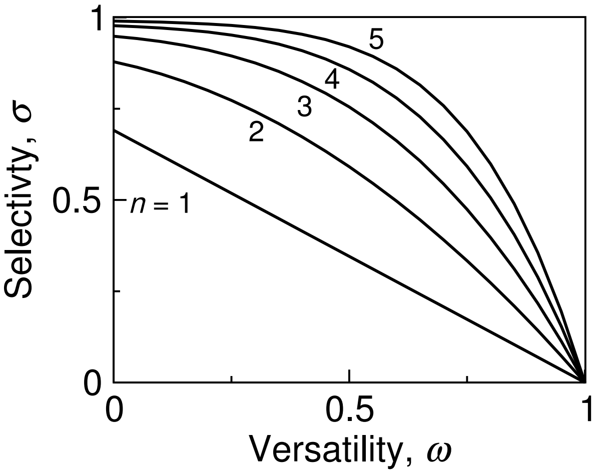

Figure 8.4: Selectivity versus versatility for increasing number of repair factors (labels on curves). Increase in versatility is obtained by increasing the dissociation rate constant for the damaged substrate k_-. The curves are computed using Eq. (8.6) for low amounts of initial substrate. Parameters: $T = 0.44$ μM, $k = k^* = 0.2/\mu$M/s, $k^*_- = 0.2$/s, $k_R = 0.007$/s.

mathematical models, to dramatically increase the selectivity of a system towards the right substrate (see e.g. [103]). In NER, the opening of the DNA by the TFIIH helicases is known to require ATP [3]. It would be interesting to test, whether the introduction of such a step in the model and allowing for the factors to fall off the DNA at once before completion of the PC, could further increase the selectivity of repair.

8.3 Model variants

In the experimental literature, several alternative binding and dissociation mechanisms have been suggested. These will be discussed below and their efficiency compared to the sequential assembly mechanism.

8.3.1 Non-sequential binding of protein factors

The order of binding of the repair factors and whether it is strictly sequential or not has been a matter of controversy in the last years. It has been proposed that other factors, in addition to XPC-HR23B, are involved in the recognition of the damaged DNA [130, 132]. Furthermore, the results of Volker and coworkers indicate that ERCC1-XPF and XPG, the last two factors in our model, can bind randomly after XPA has been recruited to the DNA [180]. In this section, I will analyze the repair efficiency of alternative non-sequential assembly mechanisms.

In Fig. 8.5, I show the results for four alternative pathways to assemble the pre-incision complex (PC). They allow random binding of two factors to damaged DNA or to intermediary complexes (Fig. 8.5A). In assembly mechanism **I**, the first and second factor can recognize the damaged DNA, resulting in two different routes to complex $S_0F_1F_2$. Subsequent assembly of the other factors is assumed to proceed sequentially. For the assembly mechanisms **II** to **IV**, the constraint of strict sequential binding of factors is relieved more downstream. For a low (non-saturating) concentration of lesions D_T, one observes similar repair rates V_R for both the strict sequential assembly and mechanism **I** through **IV** (Fig. 8.5B). At a high DNA damage, mechanisms **II** and **III** are slightly more efficient than strict sequential assembly, which itself is slightly better than mechanism **IV** (inset Fig. 8.5B). Interestingly, the assembly mechanism **I**, which allows independent binding of two different factors to recognize damaged DNA, dramatically alters repair efficiency. The repair rate V_R reaches a maximum beyond which it rapidly declines with increasing damage concentration. This can be understood from the fact that, in the presence of a large number of lesions, many complexes will be formed containing only one of the two factors, hence lowering the probability for the other factor to be recruited, which in turn interrupts the assembly chain towards establishing a complete PC.

Therefore, albeit V_{max} for mechanism **I** hardly differs from that of a sequential assembly mechanism (Fig. 8.5B), non-sequential factor binding can readily become unfavorable at high concentrations of DNA damage. Consideration of more complex random binding mechanisms led to similar conclusions (data not shown). In particular, if more

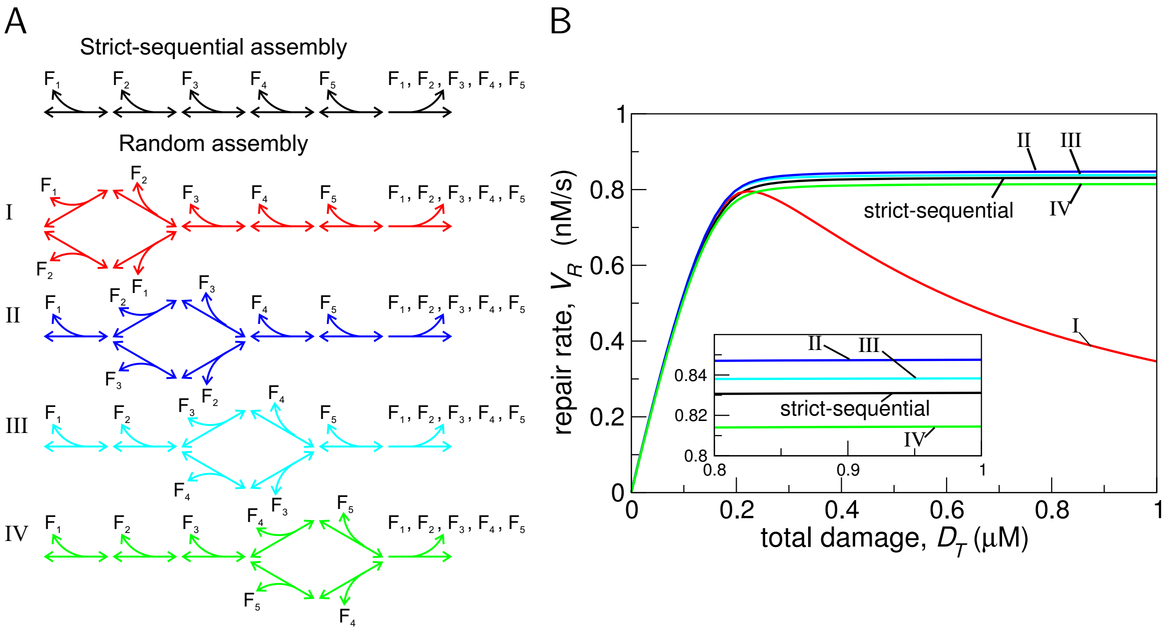

Figure 8.5: Random binding of repair factors. (A) Five possible assembly mechanisms for the formation of the PC. Mechanism **I** to **IV** describe the random reversible binding of in each case two factors at a different step of the repair process. As in the previous model, after removal of the damage all factors are released. For clarity, the intermediary complexes are not shown. It is assumed that all factors bind equally well (same association/dissociation rate constants) to their respective binding sites and have equal total concentrations. This avoids bias, when comparing the alternative mechanisms. (B) Steady state repair rate versus total damage concentration. The colors and Roman numbers refer to the assembly mechanisms shown in (A). Inset is a magnification. For mechanism **I** repair is inhibited at high damage (red line). Parameters: each total factor concentration is $T = 0.2$ μM; binding and dissociation rate constants are $k = 1$ $(\mu\text{M s})^{-1}$ and $k_{-} = 0.005$/s, respectively; repair rate constant is $k_R = 0.007$/s.

than two factors can bind to the free damage the repair rate will decrease for high amount of lesions (similar curves as for mechanism **I**, Fig. 8.5B).

8.3.2 Non-simultaneous release of factors

Several studies have suggested that XPC-HR23B is released before the PC is established [136, 182, 200]. In addition, recent *in vivo* data showed that XPC-HR23B resides at the DNA damage significantly shorter than TFIIH, XPA, and ERCC1-XPF [66]. I, therefore, explored five mechanistic variants that consider early release of XPC-HR23B

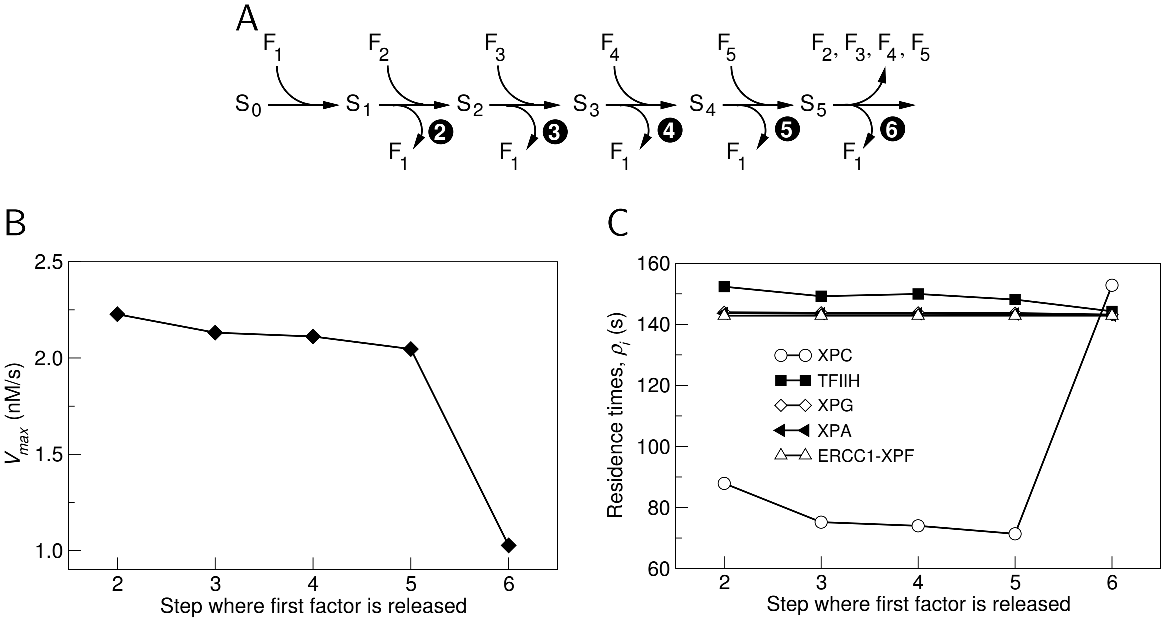

Figure 8.6: Early release of the first factor. (A) Dissociation of the first factor F_1 at different steps of the assembly process. At step six all factors are released simultaneously (as hitherto). (B) Maximal repair rate as a function of the step where the first factor is released (shown in (A), dark encircled numbers). When the first factor is released before the other factors (step 5 to 1) the maximal repair rate increases. Parameter set 1 of Tab. 7.2 is used, except $T_1 = 0.2$ μM. (C) Residence times are calculated for saturating conditions (Appendix D.2.4). Only when the first factor is released before the other factors does its residence time fit with the experimental data.

(Fig. 8.6A) and compared their repair efficiencies and the time that NER proteins reside in the complexes. Figure 8.6B shows that repair efficiency significantly improves if XPC-HR23B is released prior to the other factors (the maximal repair rate V_{max} increases). The rationale for this is that, at any time point, the first factor will now be sequestered in fewer complexes and can therefore initiate more repair events per unit time. This leads to a higher degree of immobilization of the other factors, so that more PCs are formed, and, thus, the maximal repair rate increases.

For distinguishing between the different alternatives, I calculated the mean time the factors reside in the repair complex (cf. Section 7.2.2 and Appendix D.2.4). Figure 8.6C demonstrates how the residence times of each factor depend on the step in which the first factor is released. As pointed in Section 7.3.3, for simultaneous release (step 6), the residence time of the first factor is higher than measured experimentally, whereas the residence times of TFIIH (F_2), XPA (F_4) and ERCC1-XPF (F_5) are in agreement with the data [67, 71, 127]. Early release of the first factor (step 2–5) results in a lowering of its residence time[2]: One obtains a residence time of $\sim$ 70 s, which has the same order of magnitude as what has been measured experimentally ($\sim$ 44 s, [66]).

8.3.3 Preassembled repairosome

It has been a point of controversy whether NER proteins are recruited to lesions as individual factors [1, 67, 127, 180], larger protein complexes [50, 131, 183], or as a fully pre-assembled repairosome [160]. Although the current consensus is that the PC is assembled at sites of DNA damage, this does not imply that such on-the-spot assembly strategy is the most favorable per se. I already showed that repair mediated by the binding of a single protein, in this case the holocomplex, shows less selective power in distinguishing damaged and non-damaged sites than repair mediated by factors assembled at the DNA (Section 8.2). Here, I will analyze how both mechanisms differ with respect to repair efficiency.

Consider n factors that can interact with each other. For $n = 3$, all possible interactions to form a holocomplex are shown in Fig. 8.7A. Since repair by a pre-established repairosome complex involves only two steps, the repair time under non-saturating conditions, in analogy to Eq. (8.6), reads

$$\tau_R^h = \frac{1}{kH} + \frac{1}{k_R} + \frac{k_-}{kH}\frac{1}{k_R}, \tag{8.14}$$

with H, k, k_-, and k_R being the concentration of the holocomplex, the binding and the dissociation rate constants at the damaged site, and the repair rate constant, respectively. In steady state, the concentration of the holocomplex H is given by the implicit expression (Appendix C.3)

$$\left(\sqrt[n]{\frac{K_h}{T}} + \sqrt[n]{\frac{H}{T}}\right)^{n-1} \sqrt[n]{\frac{H}{T}} = 1, \tag{8.15}$$

where T is the total concentration of each factor, and K_h is the dissociation constant for factor interactions. Repair efficiency of the holocomplex is compared to the corresponding sequential pathway for which the repair time is, Eq. (8.6),

$$\tau_R^s = \sum_{i=0}^{n} \left(\frac{k_-}{kT}\right)^i \left(\frac{n-i}{kT} + \frac{1}{k_R}\right). \tag{8.16}$$

---

[2] When XPC-HR23B can initiate additional repair complexes the free concentrations of downstream factors decrease. The consequence is that each binding step proceeds more slowly. This effect explains why, when XPC-HR23B is released prior step 5, its residence time slightly increases.

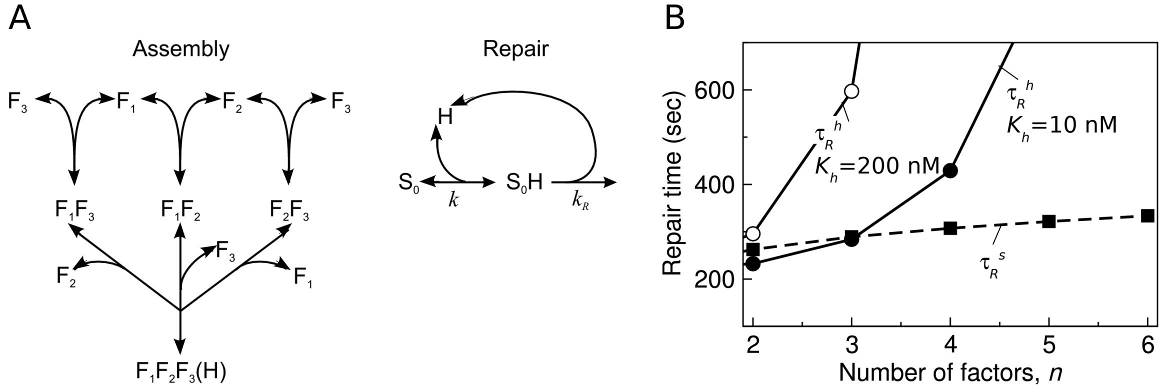

Figure 8.7: Preassembly of repair factors. (A) Repair factors are allowed to reversibly associate in solution to form intermediary complexes and the holocomplex in a damage-independent fashion (shown for the case of three protein factors). The holocomplex (H) contains all factors and is able to repair DNA damage through a single binding step and a single repair step. (B) Repair time of the holocomplex (τ_R^h, solid lines), and of the sequential assembly mechanism (τ_R^s, dashed line) as a function of the number of factors involved (n) for non-saturating damage. For the holocomplex, both weak and strong factor interactions were examined ($K_h = 200$ nM and $K_h = 10$ nM, respectively). Parameters: factors have equal concentrations $T = 0.4$ μM, binding rate constant to the damaged site $k = 0.5/\mu$M/s, dissociation rate constant $k_{-} = 0.1$/s, repair rate constant $k_R = 0.007$/s.

In both models the repair time increases with the number of NER factors involved (Fig. 8.7B), but do so for different reasons: for the sequential pathway, the approximately linear increase in repair time results from the mere fact that each extra step requires extra time (Fig. 8.7, dashed curve). Repair by the pre-assembled holocomplex shows a strong non-linear increase in repair time (Fig. 8.7B, solid lines). Noticeably, pre-assembly of the repair complex is less favorable if the binding between factors is weak (Fig. 8.7B, $K_h = 200$ nM). For strong affinities, repair by the holocomplex may be more efficient if only a few different factors are involved (in Fig. 8.7B if $n < 3$), yet repair readily becomes inefficient if holocomplex formation involves more proteins (Fig. 8.7B, $K_h = 10$ nM). These results can be understood from the fact that holocomplex concentration decreases with increasing n, as the individual factors become spread over more and more intermediary complexes.

Because most DNA-associated complexes that are involved in processes such as transcription, replication, and various repair mechanisms, involve a considerable number of macromolecules, fully pre-assembled complexes are probably less favorable than stepwise complex formation at the genomic site of action.

Chapter 9

Discussion part II: A model for nucleotide excision repair

Many nuclear processes are carried out by multi-component systems that have properties in common with nucleotide excision repair (NER). Sequential recruitment of protein components to their sites of action on chromatin has been suggested for a number of nuclear processes, including DNA double-strand break repair [193], base excision repair [115], transcription initiation by both RNA polymerase I [32] and RNA polymerase II [87], and DNA replication [17]. Therefore, the presented model, which describes the kinetic properties of NER in the nucleus of mammalian cells, may serve as a paradigm for the kinetic architecture of a broad variety of nuclear processes.

Since no mathematical framework for NER had been available to date, I was aimed to reduce the analysis to its essentials. The core model is based on sequential assembly of five repair factors and their simultaneous release after a successful repair event (Fig. 7.1). Clearly, the NER process is more complex than the six-step repair pathway that has been investigated here. Additional steps include, for instance, recruitment of RPA, opening of the DNA double helix by TFIIH, and modulation of chromatin structure. Yet this does not prevent one to unveil general characteristics of the process as a whole, since these characteristics remain valid if the chain of steps is extended or truncated. The assumptions that entered the model led to several important predictions, which will be discussed below.

No single rate-limiting step

In contrast to the often-held view that a multi-step process should be governed by a single rate-limiting step, I showed here that all reaction steps contribute to the efficiency of the sequential binding system. One may ask which step has the largest effect on repair efficiency? XPC-GFP accumulated remarkably slowly at damaged DNA in vivo. As the number of damages is assumed to be in large excess, and the rate XPC-GFP binding is proportional to the amount of damages, the binding to the DNA will be fast as soon as XPC-GFP is in the local damaged area. Therefore, to explain the slow accumulation of XPC-GFP, I proposed a diffusion-limited recruitment to the local damaged area, a process that may constrain the rate of formation of the pre-incision complex. However, the effective diffusion coefficient of XPC-GFP that was estimated computationally appeared ten times lower than those what those measured in living cells [66]. This may indicate that either other nuclear processes limit the recruitment of XPC-HR23B to sites of DNA damage (e.g. chromatin remodeling, recruitment of a repair factor prior to XPC-HR23B), or that the number of damage sites is not in such a high excess as assumed (see next Chapter, Section 10.1). Our analysis also revealed that the DNA repair step (i.e. last step in Fig. 7.1) plays a dominant role (Tables 8.1 and 8.2, and Fig. 8.2). The prediction of the model is that, for high damage, NER is limited by the rate of the repair step, which includes dual incision, removal of the damaged patch, and DNA resynthesis, and not by the time required for assembling the PC. Increasing the concentrations of all protein factors simultaneously and measuring the changes in maximal repair rate can experimentally verify this prediction. Depending on which process has the largest effect on repair efficiency, a first or second order dependency of the maximal repair rate on the factor concentrations is expected (see Fig. 8.2C).

On-site assembly results in more efficient repair

Many other chromatin-associated processes have been proposed to utilize a sequential assembly strategy [89, 146]. Since several nuclear proteins have multiple functions (e.g. TFIIH functions in both transcription and NER), on-site assembly seems advantageous as it allows flexible usage of proteins in different cellular contexts. However, this may not be the only reason why cells prefer a stepwise assembly strategy.

I showed that a strict sequential assembly mechanism can be remarkably efficient compared to alternative assembly schemes. For NER, XPC-HR23B, XPA, and RPA were recently proposed to cooperate in damage recognition through a random binding mechanism [132]. Although such situation is conceivable, my theoretical analysis indicates that it might have a dramatic negative effect on repair efficiency, particularly at high DNA damage loads. Measurements of the amounts of immobilized NER factors *in vivo* have not indicated a decrease towards higher UV dose. Also, I could find no evidence in literature that repair capacity diminishes at high lesion concentrations. Therefore, damage recognition through different NER factors simultaneously (e.g. assembly mechanism **I** in Fig. 8.5A) seems unlikely. Random binding of factors further downstream in the chain cannot be excluded, but this is predicted to have no significant effect on repair efficiency.

Using the modeling approach, I demonstrated that a pre-assembling of NER proteins can dramatically reduce repair efficiency and the selectivity towards damaged sites. In agreement with this, it has been shown experimentally that in absence of DNA, NER factors only weakly interact *in vitro* [5]. Moreover, the *in vivo* diffusion properties of NER proteins strongly support the notion that, in the absence of UV damage, the factors are present as individual proteins, rather than being part of large complexes [67, 71, 127]. Thus, the model-based analysis indicates that a sequential repair mechanism is preferable over other assembly strategies.

In terms of efficiency, there are mechanistic features from which sequential systems benefit. For instance, I predicted that an early release of XPC-HR23B may significantly improve repair efficiency. In general, the shorter the time that a protein needs to reside in the protein complex, the more efficient that pathway will be. Recent experimental studies provide evidence that XPC-HR23B might indeed function as a "molecular matchmaker", leaving the NER complex before it is complete [136, 183]. It is likely that the NER pathway harbors more such differential release steps. To date, however, especially steps that follow the PC formation have remained ambiguous. Insight into the dynamic properties of these later events of the NER process will be essential for its comprehensive understanding (see also next Chapter, Section 10.3).

Usage of NER protein factors and their kinetics

The model shows that a direct consequence of a sequential assembly and simultaneous release mechanism is that the more upstream in the chain a factor is recruited, the higher the amount of that protein is used in the repair process (Fig. 7.4D–E, Fig. 7.5D–E, and Eq. (7.7)). The first factor will even become fully involved if there is an excess of lesions, and so represents a limiting diffusible recognition factor. Interestingly, in contrast to this prediction, experimental observations show that only about 40% of XPC-HR23B is recruited to DNA damage in global damage experiments. Several explanations are possible. For instance, XPC-HR23B may exist in different states of which only one allows participation in the NER process. Alternatively, XPC-HR23B recruitment might not be the first step in NER. UV-damaged DNA binding protein (UV-DDB), for instance, has also been implicated to play a crucial role early in NER, especially for certain types of lesions [108, 162]. Its precise function in damage removal is still largely unclear, but UV-DDB was recently found to modulate XPC-HR23B recruitment by modifying its ubiquitylation state [159].

Although, the above propositions may explain why XPC-HR23B is not fully immobilized at saturating conditions, they cannot account for the differences in immobilized fractions in local and global damage experiments. Recent experiments show that for XPC-HR23B and all repair factors studied so far the fraction immobilized is about four times higher in global ($\sim 40\%$) than in local damage ($\sim 10\%$) experiments (cf. Section 6.2). Provided that the estimated immobile fractions in local and global damage experiments are not due to differences in the method used for estimation, and can therefore be compared, this is a surprising result. According to the assumed dependency of the number of damages on the UV light intensity (Eq. (7.10)), the number of lesions are about the same in local and global damage experiments. Indeed, model simulations show faster factor accumulation kinetics in global damage experiments, as the diffusional time becomes negligible, compared to local damage experiments, but eventually the attained immobilized fractions are the same (see next chapter, Fig. 10.2).

The initial model has been developed using the *in vivo* kinetic data of XPC-HR23B, TFIIH and ERCC1-XPF assembly, which it could reproduce satisfactorily. Recently, the assembly kinetics of XPG and XPA, two other essential repair factors, has also been analyzed. For XPA an extremely slow recruitment is measured, with a characteristic accumulation time of ~ 810 s (M. Luijsterburg, personal communication). Initial modeling results show that, apparently, there is no parameter set for which the sequential assembly model with simultaneous release could reproduce all the five data sets. In particular, the fast accumulation of ERCC1-XPF and the very slow recruitment of XPA seem incompatible. This may indicate that either ERCC1-XPF binds before XPA, something quite improbable according to [180], or that the release does not occur simultaneously. In the next chapter, I will present first ideas and model extensions on how to accommodate these latest experimental facts (Section 10.3).

Chapter 10

Future directions for modeling NER

The considerations made in the discussion show that, for a further development of the NER model, one needs a better understanding on how damages are generated and recognized. Furthermore, it would be necessary to consider alternative release mechanisms in order to accommodate the latest results. In the next sections, I will discuss a few hypothesis to address the problems of NER saturation and assembly kinetics.

10.1 Damage generation

The probability $p(UV)$ to induce, for a given UV dose, a damage in a pair of adjacent bases can be derived from the experimental data. However, the reported dependency on UV dose vary strongly. Whereas Ye et al. (1999) and van Hoffen et al. (1999) claim linear dependencies [175, 198], Perdiz et al. (2000) show a saturation at higher doses [120]. The probabilities that a pair of adjacent nucleotides is a CPD or a 6-4PP, $p_{CPD}(UV)$ and $p_{PP}(UV)$, respectively, are shown in Fig. 10.1A-B. The total probability to have a damage is consequently $p(UV) = p_{CPD}(UV) + p_{PP}(UV)$. Unfortunately, the experiments have been performed at UV light intensities far below the doses used in local damage experiments (0–40 J/m^2 compared to 100–200 J/m^2). Thus, the interpolation to high UV doses may bear some errors. Depending on which $p(UV)$ curve is used the model predictions will be rather different (see section 10.2).

Future developments of the NER model should consider repair of both type of damages created by UV light. What is known from experiments is that 6-4PP are repaired about ten times faster than CPD [108]. Fig. 10.1C show typical data of damage removal. An improved mathematical model will help in elucidating the origins of the differences in repair efficiency between 6-4PP and CPD, and the possible contribution of CPD to

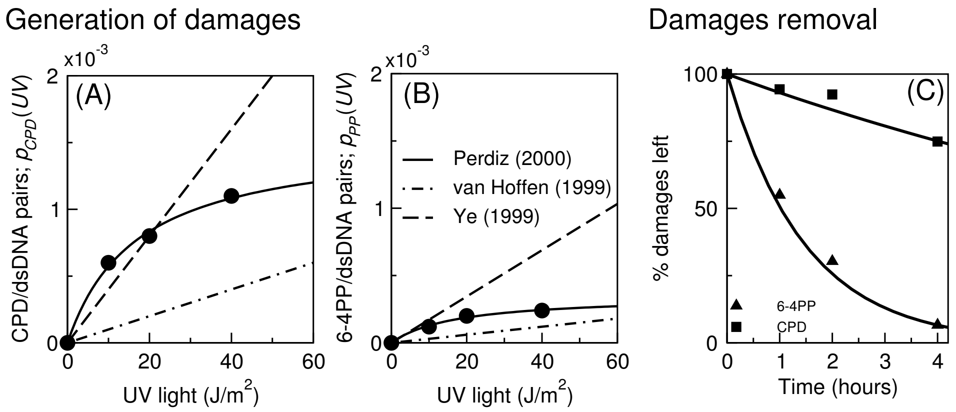

Figure 10.1: Damage generation and removal. The probability to form a CPD (A) or a 6-4PP (B) increases linearly, according to [175, 198], or saturates according to [120] (data points). Compared to 6-4PP, CPD are formed with a 2–4 times higher probability. (C) The removal of CPD is ten times slower than of 6-4PP (data from [108]). One estimates a first order damage removal rate constant of 0.68 ± 0.143/hour for 6-4PP and of 0.071 ± 0.05/hour for CPD.

the observed recruitment kinetics. To account for CPD repair, it will be necessary to include the protein UV-DDB, which is known to be crucial for repairing CPD and which facilitates 6-4PP repair [159].

10.2 How and why NER saturates: a case study

NER is saturated when an increase in UV dose does neither causes further involvement of factors in repair, nor does it produce faster accumulation of repair factors at the local damage (cf. Section 6.2). A plausible explanation was that, at high damage loads, nearly the totality of the recognition factor is bound to damages, so that no further repair complexes can be initiated. As pointed in the discussion, some problems follow the assumption of such a limiting recognition factors. Resolving these problems can give a better understanding of NER.

I will discuss two alternative hypothesis. In the first case, not all damages can be recognized/processed simultaneously, I denote this hypothesis lateral inhibition. In the second case, the number of induced damages per UV light saturates (see above). These two alternatives are tested against three different experiments: (*i*) the immobilized fraction at different UV doses in local damage experiments (LDE) and global damage experiments (GDE), (*ii*) the recruitment kinetics to multiple local damages, and (*iii*) the long time behavior at the local damage. For comparison, I recapitulate below the results obtained with the previous model, which accounted for a limiting diffusible recognition factor.

10.2.1 Limiting recognition factor

When the number of damages is an increasing function of the UV dose (Fig. 10.2A) and the recognition factor is limiting, the maximal amounts of immobilized factors in GDE and LDE become identical for high UV doses (dashed and solid lines in Fig. 10.2B, respectively). The differences in immobile fractions between GDE and LDE at their respective typical doses of 10 J/m^2, solid square, and 100 J/m^2, opaque square, are minimal. This is due to the dissipation of the spatial gradients after the initial transient, so that it is irrelevant if the same number of damages are concentrated locally or evenly distributed throughout the nucleus. The recognition factor is limiting at high UV doses and will be completely bound to the DNA (red lines in Fig. 10.2B). The dose-response curves can be used to read out the effect of augmenting the damaged area. One predict only a small increase of the immobile fraction along the arrows shown in Fig. 10.2B, the changes become negligible for factors binding more downstream in NER (green lines).

If more than one local damage is applied to a nucleus, the accumulation kinetics at each of these local damages is faster and the immobile fraction lower compared to a nucleus with one single local damage (blue and black line respectively, Fig. 10.2C). Characteristic for the presence of a limiting diffusible recognition factor is that, at saturating UV, the sum of the immobile fraction in the three local damages approaches the value obtained with an unique local damage (dotted line, Fig. 10.2C). This is due to the fact that the recognition factor is fully immobilized in both cases.

A further prediction of the model is that an increase in UV dose is reflected in a longer immobilization time (Fig. 10.2D). As shown in Chapter 7, the changes in immobilization/repair time are proportional to changes in the initial damage. This type of kinetics is the proof that, indeed, more damages have been induced by increasing the UV dose.

10.2.2 Limited number of detectable damages: lateral inhibition

The central idea, is that only part of the damages can be recognized/processed at a time, and that the number of detectable damages saturates with increasing number of lesions. This may be due to the limited capacity of chromatin remodeling, thought to

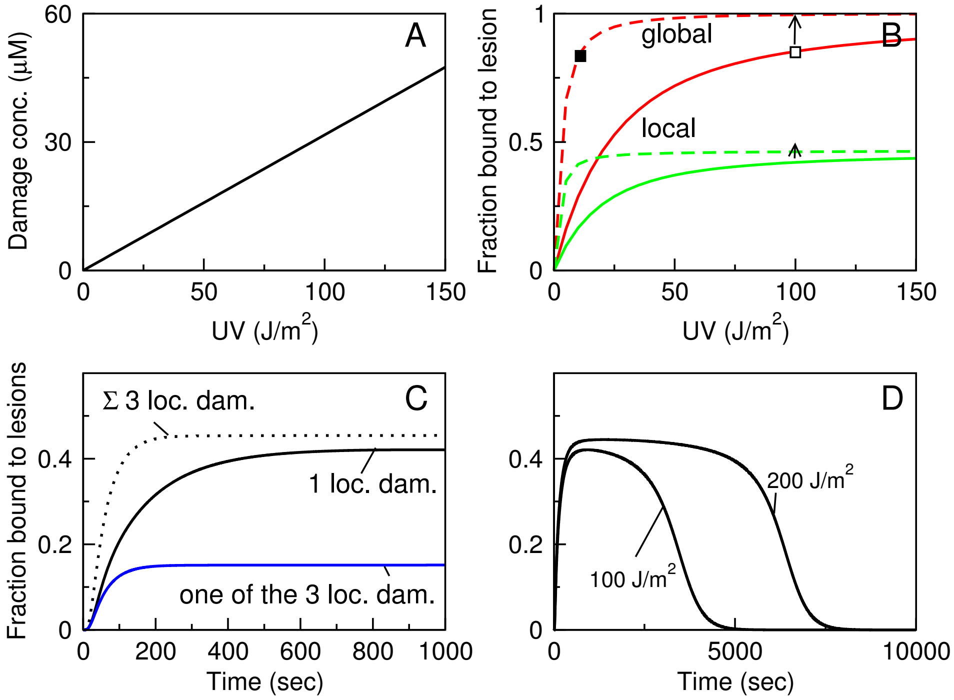

Figure 10.2: Limiting recognition factor. (A) Linear increase in damages with UV intensity, Eq. (7.10). (B) Immobilized fraction of the recognition factor (red lines) and the last factor ERCC1-XPF (green lines) in global and local damage experiments (dashed and solid lines, respectively). The arrows indicate the changes obtained by increasing the size of the local damage. The squares show the typical doses used in GDE and LDE. (C) Kinetics of ERCC1-XPF accumulation in the damaged area, when the nucleus has one (black line) or three different local damages (blue line). After the initial transient, the immobilized fraction in all three local damages (dotted line) is similar to that for one single local damage (solid black line). UV dose is 100 J/m^2. (E) Immobile fraction of ERCC1-XPF after a dose of 100 and 200 J/m^2. Parameters Tab. 7.2, set 1.

be necessary to make the DNA accessible for the protein factors [23, 96]. One can think at an initial event, which mediator is not diffusible, acting locally in the damaged area. Alternatively, physical hindrances may exist. For example, in a volume around a pre-incision complex no other repair complexes can be initiated. Both possibilities could be implemented in the model and I expect similar results. Here, I will elaborate on the situation where physical hindrances exist.

The pre-incision complex is composed of about 10 proteins each with a radius of 4-7 nm, which yields a total radius of 10-23 nm. As 10 bp have a length of about 3.4 nm, the pre-incision complex occupies at least 60–140 bp [3]. This value may be higher if one consider that the DNA is packed. For example, around a nucleosome unit one finds 146 bp and a radius of just 6 nm [3]. In the following, I will derive a mathematical expression that account for the lateral inhibition around a PC.

Let assume that all damages on a DNA string of N nucleotides are recognized as one damage. The generation of damages is assumed to be a random process, so that the probability of having j damages in a string of N nucleotides follow a binomial distribution

$$\binom{N/2}{j} p(UV)^j [1 - p(UV)]^{N/2-j}$$

where $N/2$ is the maximal number of damages physically possible in the string (N even). Thus the probability of having one or more damages in N nucleotides is

$$w(UV) = 1 - [1 - p(UV)]^{N/2}.$$

The average number of initial damages d and detectable damages $\hat{d}$ follows

$$\begin{aligned} d &= \frac{V_d N_T/2}{V_n} p(UV) \\ \hat{d} &= \frac{V_d N_T/2}{V_n N/2} w(UV) = \frac{V_d N_T}{V_n N} [1 - (1 - p(UV))^{N/2}] \end{aligned}$$

Where $N_T = 3.2 \times 10^9$ bp is the total size of dsDNA, V_d and V_n the volumes of the damaged area and the nucleus, respectively. Converting these expressions in concentrations yields a relation, valid for all times, between detectable damage concentration $\hat{S}_0$ and total free damage S_0

$$\hat{S}_0 = \frac{D}{N/2} [1 - (1 - S_0/D)^{N/2}], \tag{10.1}$$

where the concentration of DNA pairs is $D \approx 8.7$ mM.

The function given by Eq. (10.1) is plotted in Fig. 10.3A. Whereas the concentration of detectable damages saturates (dot-dashed line), the concentrations of damages continue to rise linearly with increasing UV dose (solid line). Because the recognition factor binds only to detectable damages, the time evolution of the free damage concentration and the first intermediary complex changes to

$$\frac{dS_0}{dt} = -k_1 \hat{S}_0 F_1 + k_{-1} S_1 \tag{10.2}$$

$$\frac{dS_1}{dt} = k_1 \hat{S}_0 F_1 - (k_{-1} + k_2 F_2) S_1 + k_{-2} S_2 \tag{10.3}$$

The equations for the other repair factors remain unchanged.

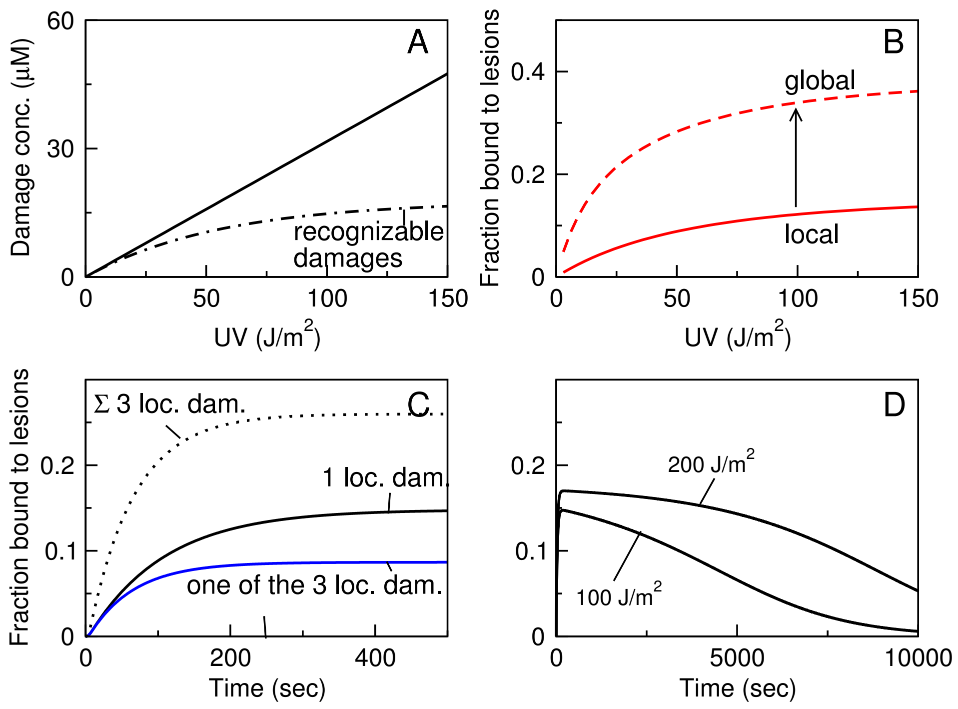

Figure 10.3: Lateral inhibition. (A) Concentration of detectable damages saturates at high UV light intensities (dot-dashed line, Eq. (10.1) $N = 1000$), whereas the concentration of damages increases (solid line). (B) Fraction immobilized of the first factor in global and local damage experiments (dashed and solid lines, respectively). (C) ERCC1-XPF accumulation in nuclei with one or three different local damages (black and blue line, respectively). The total amount of proteins immobilized in all three local damages (dotted line) is higher than for a single local damage. (D) ERCC1-XPF accumulation after a dose of 100 and 200 J/m^2. Parameters are determined by fitting the model, with Eqs. (10.2)–(10.2) and factor diffusion, to the accumulation kinetics. Differently from the original model, the immobile fractions as obtained from local damage experiments are used (Tab. 6.2). Parameters: $T_1 = 0.4$, $T_2 = 0.4$, T_3–T_5 $= 0.2$ μM; $k_1 = 0.0014$, $k_2 = 0.9$, k_3–k_5=5 /μM/s; $k_{-1} = 0.022$, $k_{-2} = 2.54$, k_{-3}–$k_{-5} = 0.273$/s; $k_R = 0.007$/s; $D_1 = 1$ μm^2/s.

Model predictions are shown in Fig. 10.3B–D. As observed experimentally, the model predicts that in GDE the maximal fraction of immobilized factors is higher than in LDE (dashed and solid line in Fig. 10.3B, respectively). The reason are the additional detectable damages in globally irradiated nuclei. An aggrandizement of the local damaged area will cause a significant increase in the immobile fraction (arrow). Since saturation is due to a limited number of recognizable damages, at high UV dose the recognition factor will not be fully immobilized (Fig. 10.3B). Furthermore, different from the previously described model, the recruitment of XPC-HR23B is not solely dependent on its diffusion to the local damage. With a value for the diffusion coefficient of XPC-HR23B similar to what has been found in experiments, 1 μm^2/s compared to 0.16 μm^2/s with a limiting recognition factor, the model well reproduces the experimental data (not shown). In the presence of multiple local damages one finds a faster accumulation kinetics and a lower immobile fraction (Fig. 10.3C, blue line). Here, the main difference to the previous case is that the total amount of immobile factors in a nucleus with several local damages is higher compared to a nucleus with a single local damage (dotted and black solid line, respectively, Fig. 10.3C, compare to Fig. 10.2C). Since the number of damages increases with the dose, one observes a longer immobilization/repair time when the UV intensity is increased (Fig. 10.3D).

10.2.3 Limited number of damages

The model predictions, when the number of damages, as suggested by [120], saturates with increasing UV light intensities, are shown in Fig. 10.4. As for the case of lateral inhibition, one finds, in agreement with the data, that the maximal immobile fraction in GDE is higher than in LDE (dashed and solid lines, Fig. 10.4B) and that the first factor does not become fully immobilized at high UV light intensities. Furthermore, the total immobile fraction in a nucleus which has three local damages is higher than in a nucleus with one local damage (Fig. 10.4C). The main feature, characterizing a limited number of damages, is that the long-time immobilization kinetics at the local damage are very similar for increasing UV light intensities (100 and 200 J/m^2 in Fig. 10.4D). This behavior, which is rather different from the two previously discussed cases, characterizes the fact that for increasing UV dose the number of lesions only minimally increases.

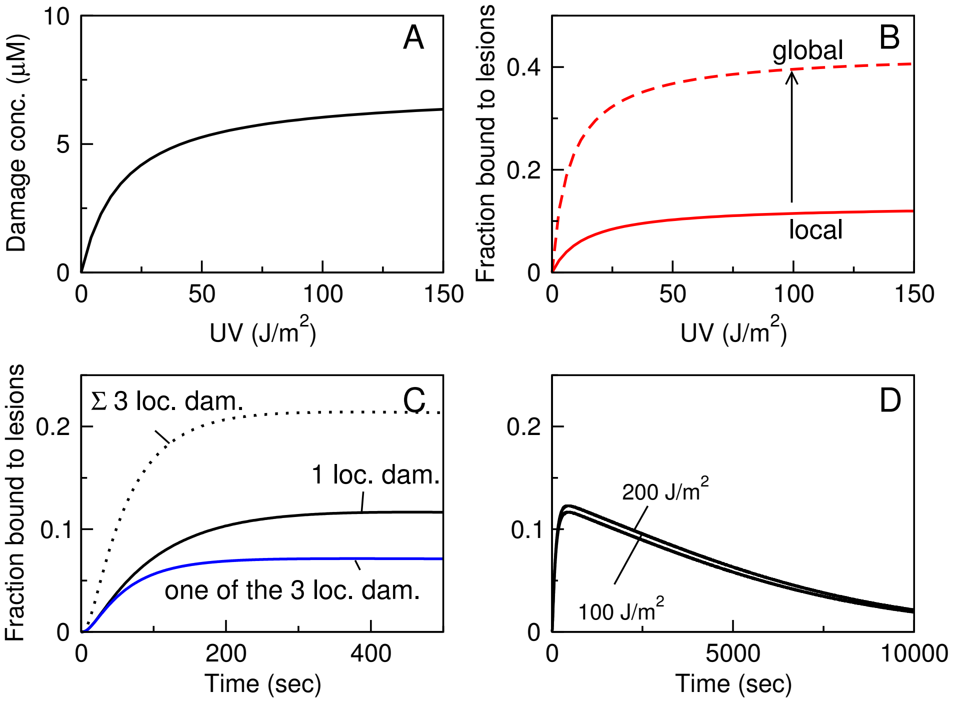

Figure 10.4: Limiting number of damages. (A) Saturating generation of damages as function of UV light intensity. (B) Fraction immobilized of the first factor in global and local damage experiments (dashed and solid lines, respectively). An increase in the size of the local damage causes large changes in the immobile fraction (arrow). (C) ERCC1-XPF accumulation, with one (black line) or three different local damages (blue line). The total amount of proteins immobilized in all three local damages is higher than for a single local damage (dotted line). Dose is 100 J/m^2. (D) Increasing the dose from 100 to 200 J/m^2 does not change the long-time kinetics of ERCC1-XPF. Parameters estimated as in Fig. 10.3: $T_1 = 0.4$, $T_2 = 0.4$, T_3–$T_5 = 0.2$ μM; $k_1 = 0.0263$, $k_2 = 0.3$, k_3–k_5=3.88 /μM/s; $k_{-1} = 3.6$, $k_{-2} = 0.096$, k_{-3}–$k_{-5} = 0.2$/s; $k_R = 0.007$/s; $D_1 = 1$ μm^2/s.

10.3 Understanding the last steps of NER

In the last years more and more cell lines have been developed with a fluorescent version of one of the repair factors, and it will soon be possible to measure the recruitment kinetics and residence times of all known repair factors. The recent data indicate that the recruitment kinetics are not closely correlated to the assumed binding position in the NER pathway. For example XPA accumulates about 10 times slower than ERCC1-XPF although ERCC1-XPF binds only in the presence of XPA (M. Luijsterburg, personal communication). As pointed out in the discussion, this large variance in the accumulation kinetics cannot be accommodated in a model where the factors are released

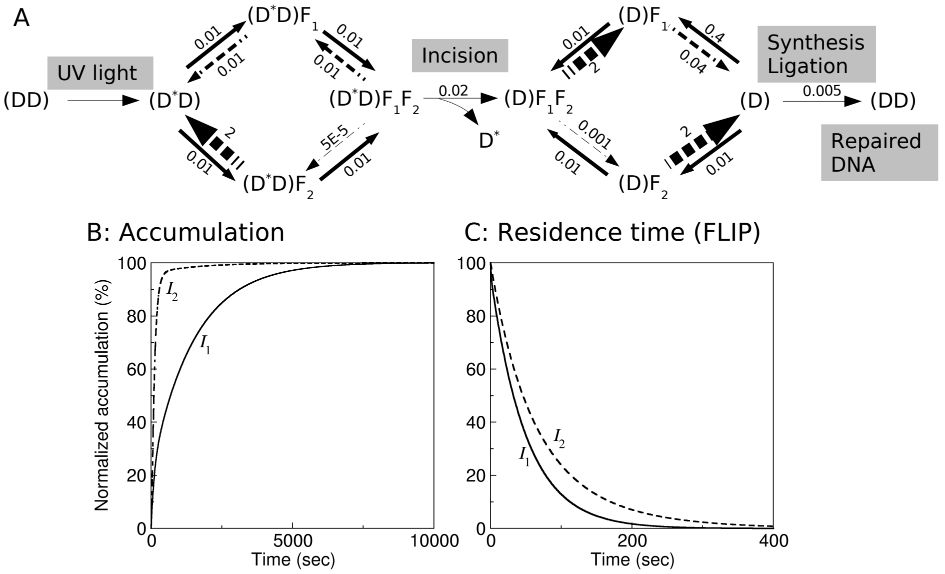

Figure 10.5: Non simultaneous release. (A) Two factors perform repair. The solid and dashed arrows indicate binding and dissociation reactions, respectively. For clarity, I omitted, in the scheme, the free forms of the factors. (B)–(C) Predicted accumulation kinetics and FLIP curves, respectively. Parameters are listed in the scheme in A, total concentrations are 0.5 μM, a low dose of damage has been used. The kinetic rate constants are chosen so that the binding of F_1 and F_2 to the damaged DNA (D*D) and to the single stranded DNA (D) is detailed balanced.

simultaneously. The assumption of simultaneous release was a simplification and did not took into account two differential steps at the end of repair: the incision of the damaged DNA and the resynthesis of the new strand (cf. Section 6.1). First theoretical models indicate that the resolution of the enzymatic steps at the end of repair, which already exerted strong control on the repair efficiency in our initial model (Fig. 8.2), can provide the required answers.

I illustrate this idea with a minimal model containing two repair factors, F_1 and F_2 (Fig. 10.5A). Both F_1 and F_2 can bind to the damage, however, due to its high affinity for the lesion (D*D), factor F_1 will be recruited first[1]. After incision, there is a net dissociation of factors from the single stranded DNA (D). The complex (D)F_1F_2 is unstable and decays to (D)F_1 by releasing F_2 first. The departure of F_1 allows for other proteins, responsible for resynthesis and ligation of the DNA, to dock at the DNA.

---

[1] In fact, when the differences in affinities of the factors to the damage are large, the depicted binding scheme is equivalent to a sequential binding scheme.

As resynthesis and ligation are assumed to be slow processes, the complex (D)F_1 has a delayed accumulation. This is reflected in the simulated accumulation kinetics shown in Fig. 10.5B, where F_1 needs much more time to reach the plateau (solid line, $t_{1/2} = 690$ s) compared to F_2 (dashed line, $t_{1/2} = 96$ s). Although, the accumulation kinetics of the two repair factors are extremely different, their residence times are similar (Fig. 10.5C).

10.4 Concluding remarks

In this last chapter, I showed how the gained knowledge from the initial NER model was used to approach some of the open questions of DNA repair.

I proposed a series of experiments to improve the understanding of the initial events in repair. These experiments can readily be implemented as they are based on the available techniques. They consist in monitoring the factor kinetics on a long time scale at different UV doses, and vary the size and number of local damages. The obtained results can be used to distinguish between several hypothesis.

The theoretical analysis can be helpful in understanding the course of the final events of NER. I showed how the presence of two separate enzymatic steps, e.g. incision and resynthesis, can account qualitatively for the observed recruitment kinetics. After incision, the release of repair factors does not occur simultaneously, and some factors can reside longer on the single stranded DNA. Whether this prolonged permanence has a biochemical significance remains to be elucidated. For example RPA, which complexes with XPA, is thought to protect the single stranded DNA from misfolding and endonucleases [56]. For a more quantitative analysis, it is necessary to estimate the kinetic parameters of different binding and release mechanisms, and compare the model predictions with the numerous experimental data. This procedure could be largely simplified by deriving, for each alternative mechanism, analytical expressions characterizing the repair factor kinetics (cf. Appendix D.1).

Bibliography

[1] A. Aboussekhra, M. Biggerstaff, M.K. Shivji, J.A. Vilpo, V. Moncollin, V.N. Podust, M. Protic, U. Hubscher, J.M. Egly, and R.D. Wood. Mammalian dna nucleotide excision repair reconstituted with purified protein components. *Cell*, 80:859–868, 1995.

[2] S. Adimoolam and J.M. Ford. p53 and DNA damage-inducible expression of the xeroderma pigmentosum group c gene. *Proc. Natl. Acad. Sci. USA*, 99:12985–12990, 2002.

[3] B. Alberts, D. Bray, J. Lewis, M. Raff, K. Roberts, and J. Watson. *Molecular biology of the cell, 3rd ed.* Garland, 1994.

[4] N.L. Allbritton, T. Meyer, and L. Stryer. Range of messenger action of calcium ion and inositol 1,4,5-trisphosphate. *Science*, 258:1812–1815, 1992.

[5] S.J. Araujo and R.D. Wood. Strong functional interactions of TFIIH with XPC and XPG in human DNA nucleotide excision repair, without a preassembled repairosome. *Molecular and cellular biology*, 21:2281–2291, 2001.

[6] T. Balla. Phosphoinositide-derived messengers in endocrine signaling. *J. Endocrinol.*, 188:135–153, 2006.

[7] D.A. Barnes and T. Lindenthal. Repair and genetic consequences of endogeneous dna base damage in mammalian cells. *Annu. Rev. Genet.*, 38:445–476, 2004.

[8] D. Batty, V. Rapic-Otrin, A.S. Levine, and R.D. Wood. Stable binding of human XPC complex to irradiated DNA confers strong discrimination for damaged sites. *J. Mol. Biol.* , 300:275–290, 2000.

[9] M.J. Berridge. Inositol trisphosphate and calcium signalling. *Nature*, 361:315–325, 1993.

[10] I. Bezprozvanny and B.E. Ehrlich. The inositol 1,4,5-trisphosphate (InsP$_3$) receptor. *J. Membr. Biol.*, 145:205–216, 1995.

[11] J.L. Blank, A.H. Ross, and J.H. Exton. Purification and characterization of two G-proteins that activate the $\beta 1$ isozyme of phosphoinositide-specfic phospholipase C. *J. Biol. Chem.*, 266: 18206–18216, 1991.

[12] C. Blomberg and M. Ehrenberg. Energy consideration for kinetic proofreading in biosynthesis. *J. Theor. Biol.*, 88:631–670, 1981.

[13] D. Boehning and S.K. Joseph. Direct association of ligand-binding and pore domains in homo- and heterotrimeric inositol 1,4,5-trisphosphate receptors. *EMBO J.*, 19:5450–5459, 2000.

[14] M. Branum, J. Reardon, and A. Sancar. DNA repair excision nuclease attacks undamaged DNA. *J. Biol. Chem.*, 276:25421–25426, 2001.

[15] P. Camello, J. Gardner, O.H. Petersen, and A.V. Tepikin. Calcium dependence of calcium extrusion and calium uptake in mouse pancreatic acinar cells. *J. Physiol.*, 490.3:585–593, 1996.

[16] T. Capiod, A.C. Field, D.C. Ogden, and C.A. Sandford. Internal perfusion of guinea-pig hepatocytes with buffered Ca^{2+} or inositol 1,4,5-trisphosphate mimics noradrenaline activation of K^+ and Cl^- conductances. *FEBS Lett.*, 217:247–252, 1987.

[17] M.C. Cardoso and H. Leonhardt. Protein targeting to subnuclear higher order structures: a new level of regulation and coordination of nuclear processes. *J. Cell. Biochem.*, 70:222–230, 1998.

[18] A.M. Castellino and M.V. Chao. Differential association of phosphatidylinositol-5-phosphate 4-kinase with the EGF/ErbB family of receptors. *Cell Signal*, 11:171–177, 1999.

[19] K.C. Chen, A. Csikasz-Nagy, B. Gyorffy, J. Val, B. Novak, and J.J. Tyson. Kinetic analysis of a molecular model of the budding yeast cell cycle. *Mol. Biol. Cell*, 11:369–391, 2000.

[20] C. Clair, T. Dien, S. Boucherie, M. Claret, T. Tordjmann, and L. Combettes. Hormone receptor gradients supporting directional Ca^2+ signals: direct evidence in rat hepatocytes. *J. Hepat.*, 39: 489–495, 2003.

[21] T. Cochet, O. Filhol, B. Payrastre, T. Hunter, and G.N. Gill. Interaction between epidermal growth factor receptor and phosphoinositide kinases. *J. Biol. Chem.*, 266:637–644, 1991.

[22] D. Communi, V. Vanweyenberg, and E. Christophe. D-myo-inositol 1,4,5-trisphosphate 3-kinase a is activated by receptor activation through a calcium:calmodulin-dependent protein kinase ii phophorylation mechanism. *EMBO J.*, 16:1943–1952, 1997.

[23] T. Costelloe, J. Fitzgerald, N.J. Murphy, A. Flaus, and N.F. Lowndes. Chromatin modulation and the DNA damage response. *Exp. Cell. Res.*, 312:2677–2686, 2006.

[24] E. Cunningham, G.M.H. Thomas, A. Ball, I. Hiles, and S. Cockcroft. Phosphatidylinositol transfer protein dictates the rate of inositol trisphosphate production by promoting the synthesis of pip2. *Curr. Biol.*, 5:775–783, 1995.

[25] K.S.R. Cuthbertson and T.R. Chay. Modelling receptor-controlled intracellular calcium oscillations. *Cell Calcium*, 12:97–109, 1991.

[26] L.B. Dale, A.V. Babwah, and S.S.G. Ferguson. Mechanisms of metabotropic glutamate receptor desensitization. *Neurochem. Inter.*, 41:319–326, 2002.

[27] W.L. de Laat, N.G.J. Jaspers, and J.H Hoeijmakers. Molecular mechanism of nucleotide excision repair. *Genes Dev.*, 13:768–785, 1999.

[28] G.W. De Young and J. Keizer. A single-pool inositol 1,4,5-trisphosphate-receptor-based model for agonist-stimulated oscillations in Ca^{2+} concentration. *Proc. Natl. Acad. Sci. USA.*, 89:9895–9899, 1992.

[29] E.J. Doedel. Auto, a program for the automatic bifurcation analysis of autonomous systems. *Cong. Numer. 30:265*, 30:265–384, 1981.

[30] R.E. Dolmetsch, K. Xu, and R.S. Lewis. Calcium oscillations increase the efficiency and specificity of gene expression. *Nature*, 392:933–936, 1998.

[31] C.P. Downes, A. Gray, and J.M. Lucocq. Probing phosphoinositide functions in signaling and membrane trafficking. *Trends Cell Biol.*, 15:259–268, 2005.

[32] M. Dundr, U. Hoffmann-Rohrer, Q. Hu, I. Grummt, L. Rothblum, R.D. Phair, and T. Misteli. A kinetic framework for a mammalian rna polymerase in vivo. *Science*, 298:1623–1626, 2002.

[33] G. Dupont and R. Dumollard. Simulation of calcium waves in ascidian eggs: insights into the origin of the pacemaker sites and the possible nature of the sperm factor. *J. Cell Sci.*, 117: 4313–4323, 2004.

[34] G. Dupont and C. Erneux. Simulations of the effects of inositol 1,4,5-trisphosphate 3-kinase and 5-phosphatase activities on Ca^{2+} oscillations. *Cell Calcium*, 22:321–331, 1997.

[35] G. Dupont and A. Goldbeter. One-pool model for Ca^{2+} oscillations involving Ca^{2+} and inositol 1,4,5-trisphosphate as co-agonist for Ca^{2+} release. *Cell calcium*, 14:311–322, 1993.

[36] G. Dupont, S. Swillens, C. Clair, T. Tordjamann, and L. Combettes. Hierarchical organization of calcium signals in hepatocytes: from experiments to models. *Biochem. Biophys. Acta*, 1498: 134–152, 2000.

[37] G. Dupont, G. Houart, and P.D. Koninck. Sensitivity of cam kinase ii to the frequency of ca^{2+} oscillations a simple model. *cell Calcium*, 34:485–497, 2003.

[38] G. Dupont, O. Koukoui, C. Clair, C. Erneux, S. Swillens, and L. Combettes. Ca^{2+} oscillations in hepatocytes do not require the modulation of $InsP_3$ 3-kinase activity by Ca^{2+}. *FEBS Lett.*, 534:101–105, 2003.

[39] B. Efron and R.J. Tibshirani. *An Introduction to the Bootstrap.* Chapman & Hall/CRC, 1998.

[40] E. Evans, J.G. Moggs, J.R. Hwang, J.M. Egly, and R.D. Wood. Mechanism of open complex and dual incision formation by human nucleotide excision repair factors. *EMBO J.*, 16:6559–6573, 1997.

[41] M. Falcke. Buffers and oscillations in intracellular Ca^{2+} dynamics. *Biophys. J.*, 84:28–41, 2003.

[42] C.C. Fink, B. Slepchenko, and L.M. Loew. Determination of time-dependent ionositol-1,4,5-trisphosphate concentrations during calcium release in a smooth muscle cell. *Biophys. J.*, 77: 617–628, 1999.

[43] C.C. Fink, B. Slepchenko, I.I. Moraru, J. Schaff, J. Watras, and L.M. Loew. Morphological control of inositol-1,4,5-trisphosphate-dependent signals. *J. Cell Biol.*, 147:929–935, 1999.

[44] O. Flores, H. Lu, and D. Reinberg. Factors involved in specific transcription by mammalian RNA polymerase II. identification and characterization of factor IIH. *J. Biol. Chem.*, 267:2786–2793, 1992.

[45] E.C. Friedberg, G.C. Walker, and W. Siede. *DNA Repair and Mutagenesis.* Washington DC, ASM Press, 1995.

[46] L.D. Gaspers and A.P. Thomas. Calcium signaling in liver. *Cell Calcium*, 38:329–342, 2005.

[47] G. Gerisch and B. Hess. Cyclic-AMP-controlled oscillations in suspended Dictyostelium cells: their relation to morphogenetic cell interactions. *Proc. Natl. Acad. Sci. USA*, 71:2118–2122, 1974.

[48] N. Geva-Zatorsky, N. Rosenfeld, S. Itzkovitz, R. Milo, A. Sigal, E. Dekel, T. Yarnitzky, Y. Liron, P. Polak, G. Lahav G, and U. Alon. Oscillations and variability in the p53 system. *Mol. Syst. Biol.*, 2:1–13, 2006.

[49] Holmquist. G.P. Endogeneous lesions, S-phase-independent spontaneous mutations, and evolutionary strategies for base excision repair. *Mutat. Res.*, 400:59–68, 1998.

[50] S.N. Guzder, P. Sung, L. Prakash, and S. Prakash. Nucleotide excision repair in yeast is mediated by sequential assembly of repair factors and not by a pre-assembled repairosome. *J. Biol. Chem.*, 271:8903–8910, 1996.

[51] G. Hajnoczky and A.P. Thomas. Minimal requirements for calcium oscillations driven by the IP_3 receptor. *EMBO J.*, 16:3533–3543, 1997.

[52] G. Hajnoczky, L.D. Robb-Gaspers, B.S. Michele, and A.P. Thomas. Decoding of cytosolic calcium oscillations in the mitochondria. *Cell*, 82:415–424, 1995.

[53] G. Halet, R. Tunwell, T. Balla, K. Swann, and J. Carroll. The dynamics of plasma membrane PtdIns(4,5)P(2) at fertilization of mouse eggs. *J. Cell. Sci.*, 115:2139–2149, 2002.

[54] P.C. Hanawalt. Controlling the efficiency of repair. *Mutat. Res.*, 485:3–13, 2001.

[55] A. Harootunian, J. Kao, S. Paranjape, and R. Tsien. Generation of calcium oscillations in fibroblasts by positive feedback between calcium and IP_3. *Science*, 251:75–78, 1991.

[56] Z. He, L.A. Henricksen, M.S. Wold, and C.J. Ingles. RPA involvement in the damage-recognition and incision steps of nucleotide excision repair. *Nature*, 374:566–569, 1995.

[57] R. Heinrich and S. Schuster. *The regulation of cellular systems.* New York, NY, Chapman & Hall, 1996.

[58] R. Heinrich, B.G. Neel, and T.A. Rapoport. Mathematical models of protein kinase signal transduction. *Mol. Cell*, 9:957–970, 2002.

[59] T. Hey, G. Lipps, and G. Krauss. Binding of XPA and RPA to damaged DNA investigated by fluorescence anistropy. *Biochemistry*, 40:2901–2910, 2001.

[60] T. Hey, G. Lipps, K. Sugasawa, I. Shigenori, F. Hanaoka, and G. Krauss. The XPC-HR23B complex diplays high affinity and specificity for damaged DNA in a true-equilibrium fluorescence assay. *Biochemistry*, 41:6583–6587, 2002.

[61] K. Hirose, S. Kadowaki, M. Tanabe, H. Takeshima, and M. Lino. Spatiotemporal dynamics of inositol 1,4,5-trisphosphate that underlies complex Ca^{2+} mobilization patterns. *Science*, 284: 1527–1530, 1999.

[62] C. Hisatsune, K. Nakamura, Y. Kuroda, T. Nakamura, and K. Mikoshiba. Amplification of Ca^{2+} signaling by diacylglycerol-mediated inositol 1,4,5-trisphosphate production. *J. Biol. Chem.*, 280: 11723–11730, 2005.

[63] T. Höfer. Model of intercellular calcium oscillations in hepatocytes: synchronization of heterogeneous cells. *Biophys. J.* , 77:1244–1256, 1999.

[64] T. Höfer, A. Politi, and R. Heinrich. Intercellular Ca^{2+} wave propagation through gap-junctional Ca^{2+} diffusion: a theoretical study. *Biophys. J.* , 80:75–87, 2001.

[65] T. Höfer, L. Venance, and C. Giaume. Control and plasticity of intercellular calcium waves in astrocytes: A modeling approach. *J. Neuros.*, 22:4850–5859, 2002.

[66] D. Hoogstraten. *The spatio-temporal organization of DNA repair: A life cell study.* PhD thesis, Erasmus University Rotterdam, Netherlands, 2003.

[67] D. Hoogstraten, A.L. Nigg, H. Heath, L.H. Mullendersand R. van Driel, J.H. Hoeijmakers, W. Vermeulen, and A.B. Houtsmuller. Rapid switching of TFIIH between rna polymerase i and ii transcription and DNA repair in vivo. *Molecular Cell*, 10:1163–1174, 2002.

[68] J.J. Hopfield. Kinetic proofreading: a new mechanism for reducing errors in biosynthetic processes requiring high specificity. *Proc. Natl. Acad. Sci. USA*, 71:4135–4139, 1974.

[69] G. Houart, G. Dupont, and A. Goldbeter. Bursting, chaos, and birythmicity originating from self-modulation of the inositol 1,4,5-trisphophate signal in a model for intracellular Ca^{2+} oscillations. *Bull. Math. Biol.* , pages 507–530, 1999.

[70] A. B. Houtsmuller and W. Vermeulen. Macromolecular dynamics in living cell nuclei revealed by fluorescence redistribution after photobleaching. *Histochem Cell Biol*, 115:13–21, 2001.

[71] A.B. Houtsmuller, S. Rademakers, A.L. Nigg, D. Hoogstraten, J.H. Hoeijmakers, and W. Vermeulen. Action of DNA repair endonuclease ERCC1/XPF in living cells. *Science*, 284:958–961, 1999.

[72] J. Hsuan and S. Cockcroft. The pitp family of phosphatidylinositol transfer proteins. *Genome Biol.*, 2:3011.1–3011.8, 2001.

[73] J.R. Hwang, J.M. Ford, P.C. Hanawalt, and G. Chu. Expression of the p48 xeroderma pigmentosum gene is p53-dependent and is involved in global genome repair. *Proc. Natl. Acad. Sci. USA*, 96:424–428, 1999.

[74] S. Iben, H. Tschochner, M. Bier, D. Hoogstraten, P. Hozak abd J.M. Egly, and I. Grummt. TFIIH plays an essential role in RNA polymerase I transcription. *Cell*, 109:297–306, 2002.

[75] G. Innamorati, H.M. Sadeghi, N.T. Tran, and M. Birnbaumer. A serine cluster prevents recycling of the v2 vasopressin receptor. *Proc. Natl. Acad. Sci. USA*, 95:2222–2226, 1998.

[76] A. Janicijevic, K. Sugasawa, Y. Shimizu, F. Hanaoka, N. Wijgers, M. Djurica, J.H. Hoeijmakers, and C. Wyman. DNA bending by the human damage recognition complex XPC-hR23B. *DNA Repair*, 2:325–336, 2003.

[77] P.A. Jonmey and U. Lindberg. Cytoskeletal regulation: rich in lipids. *Nat. Rev. Mol. Cell Biol.*, 5:658–666, 2004.

[78] M. Kanehisa and S. Goto. Kegg: Kyoto encyclopedia of genes and genomes. *Nucleic Acids Res.*, 28:27–30, 2000.

[79] A. Kauffmann-Zeh, G.M. Thomas, A. Ball, S. Prosser, E. Cunningham, S. Cockcroft, and J.J. Hsuan. Requirement for phosphatidylinositol transfer protein in epidermal growth factor signaling. *Science*, 268:1188–1190, 1995.

[80] J. Keizer, Y.X. Li, S. Stojilkovic, and J. Rinzel. InsP$_3$-induced Ca^{2+} excitability of the endoplasmic reticulum. *Mol. Biol. Cell*, 6:945–951, 1995.

[81] H. Kleinig and P. Sitte. *Zellbiologie, 3. Auflage.* Gustav Fisher Verlag, 1992.

[82] S.C. Kowalczykowski. Initiation of genetic recombination and recombination-dependent replication. *Trends. Biochem. Sci.*, 25:156–165, 2000.

[83] U. Kummer, L.F. Olsen, C.J. Dixon, A.K. Green, E. Bornberg-Bauer, and G. Baier. Switching from simple to complex oscillations in calcium signaling. *Biophys. J.*, 79:1188–1195, 2000.

[84] T.A. Kunkel and D.A. Erie. DNA mismatch repair. *Annu. Rev. Biochem.*, 74:681–710, 2005.

[85] D.F. Mayers K.W. Morton. *Numerical Solution of Partial Differential Equations.* Cambridge University Press, 2nd edition, 2005.

[86] J. Lechleiter, S. Girard, E. Peralta, and D. Clapham. Spiral calcium wave propagation and annihilation in xenopus laevis oocytes. *Science*, 252:123–126, 1991.

[87] T.I. Lee and R.A. Young. Transcription of eukaryotic protein-coding genes. *Annu. Rev. Genet.*, 34:77–137, 2000.

[88] J.C. Leloup and Goldbeter A. Toward a detailed computational model for the mammalian circadian clock. *Proc. Natl. Acad. Sci. USA*, 100:7051–7056, 2003.

[89] B. Lemon and R. Tjian. Orchestrated response: a symphony of transcription factors for gene control. *Genes Dev*, 14:2551–2569, 2000.

[90] R. Lev Bar-Or, R. Maya, L.A. Segel, U. Alon, A.J. Levine, and M. Oren. Generation of oscillations by the p53-mdm2 feedback loop: a theoretical and experimental study. *Proc. Natl. Acad. Sci. USA*, 97:11250–11255, 2000.

[91] Y. Li and J. Rinzel. Equations for InsP_3 receptor-mediated $[\mathrm{Ca}^{2+}]_i$ oscillations derived from a detailed kinetic model: a hodgkin-huxley like formalism. *J. Theor. Biol.*, 166:461–473, 1994.

[92] Y. Li, J. Rinzel, L. Vergara, and S.S. Stojilkovic. Spontaneous electrical and calcium oscillations in unstimulated pituitary gonadotrophs. *Biophyis. J.*, 69:785–795, 1995.

[93] L.E. Ling, J.T. Schulz, and L.C. Cantley. Characterization and purification of membrane-associated phosphatidylinositol-4-phosphate kinase from human red blood cells. *J. Biol. Chem.*, 264:5080–5088, Mar 1989.

[94] J.C. Loijens, I.V. Boronenkov, G.J. Parker, and R.A. Anderson. The phosphatidylinositol 4-phosphate 5-kinase family. *Adv. Enzyme. Regul.*, 36:115–140, 1996.

[95] V. Luzzi, C. Sims, J. Soughayer, and N. Allbritton. The physiologic concentration of inositol 1,4,5-trsiphosphate in the oocytes of xenopus laevis. *J. Biol. Chem.*, 273:28657–28662, 1998.

[96] D. Lydall and S. Whitehall. Chromatin and the dna damage response. *DNA repair (Amst)*, 4: 1195–1207, 2005.

[97] J. Lytton, M. Westin, S.E. Burk, G.E. Shull, and D.H. McLennan. Functional comparaison between isomorfs of the sarcoplasmic or endoplasmic reticulum family of calcium pumps. *J. Biol. Chem.*, 267:14483–14489, 1992.

[98] Wiznerowicz M., J. Szulc, and D. Trono. Tuning silence: conditional systems for rna interference. *Nat. Methods*, 3:682–688, 2006.

[99] D.D. Mak, S. McBride, and J.K. Foskett. Regulation by Ca^{2+} and insoitol 1,4,5-trisphosphate (InsP_3) of single recombinant type 3 InsP_3 receptor channels. Ca^{2+} activation uniquely distinguishes types 1 and 3 InsP_3 receptors. *J. Gen. Physiol.*, 117:435–446, 2001.

[100] J.S. Marchant and I. Parker. Role of elementary ca(2+) puffs in generating repetitive ca(2+) oscillations. *EMBO J.*, 20:65–76, 2001.

[101] J.S. Marchant and C.W. Taylor. Rapid activation and partial inactivation of inositol trisphosphate receptors by inositol trisphosphate. *Biochemistry*, 37:11524–11533, 1998.

[102] M. Marhl, T. Haberichter, M. Brumen, and R. Heinrich. Complex calcium oscillations and the orle of mitochondria and cytosolic proteins. *Biosystems*, 57:75–86, 2000.

[103] T.W. McKeithan. Kinetic proofreading in t-cell receptor signal transduction. *Proc. Natl. Acad. Sci. USA*, 92:5042–5046, 1995.

[104] T. Meyer and L. Stryer. Molecular model for receptor-stimulated calcium spiking. *Proc. Natl. Acad. Sci. USA.*, 85:5051–5055, 1988.

[105] Roth M.G. Phosphoinositides in constitutive membrane traffic. *Physiol. Rev.*, 84:699–730, 2004.

[106] J. Mishra and U. Bhalla. Simulations of inositol phophate metabolism and its interaction with insp$_3$-mediated calcium release. *Biophys. J.*, 83:1298–1316, 2002.

[107] M.J. Moné, B. Tytus, C. Dinant, F.A. Goedvree, E.M.M. Manders, M. Volker, A.B. Houtsmuller, J.H.J. Hoeijmakers, W. Vermeulen, and R. van Driel. In vivo dynamics of chromatin-associated complex formation in mammalian nucleotide excision repair. *Proc. Natl. Acad. Sci. USA*, 101: 15933–15937, 2004.

[108] J. Moser, M. Volker, H. Kool, S. Alekseev, H. Vrieling, A. Yasui, A. A. van Zeeland, and L. H. Mullenders. The UV-damaged DNA binding protein mediates efficient targeting of the nucleotide excision repair complex to UV-induced photo lesions. *DNA Repair (Amst)*, 4:571–582, 2005.

[109] T. Müller. *Modeling complex systems with differential equations.* PhD thesis, Albert-Ludwigs-Universität Freiburg, 2002.

[110] Y. Nakatsu, H. Asahina, E. Citterio, S. Rademakers, W. Vermeulen, S. Kamiuchi, J.P. Yeo, M.C. Khaw, M. Saijo, N. Kodo, T. Matsuda, J.H. Hoeijmakers, and K. Tanaka. XAB2, a novel tetratricopeptide repeat protein involved in transcription-coupled DNA repair and transcription. *J. Biol. Chem*, 275:34931–34937, 2000.

[111] M.M. Nalaskowski and G.W. Mayr. The families of kinases removing the Ca^{2+} releasing second messenger Ins(1,4,5)P$_3$. *Curr. Mol. Med.*, 4:277–290, 2004.

[112] M.S. Nash, K.W. Young, R.A. Challis, and S.R. Nahorski. Receptor-specific messenger oscillations. *Nature*, 413:381–382, 2001.

[113] M.H. Nathanson, A.D. Burgsthaler, A. Mennone, M.B. Fallon, C.B. Gonzales, and J.C. Saez. Ca^{2+} waves are organized among hepatocytes in the intact organ. *Am. J. Physiol.*, 32:G167–G171, 1995.

[114] J. Ng, W. Vermeulen, G.T. van der Horst, S. Bergink, K. Sugasawa, H. Vrieling, and J.H. Hoeijmakers. A novel regulation mechanism of DNA repair by damage-induced and RAD23-dependent stabilization of xeroderma pigmentosum group C protein. *Genes Dev.*, 17:1630–1645, 2003.

[115] H. Nilsen and H.E. Krokan. Base excision repair in a network of defence and tolerance. *Carcinogenesis*, 22:987–998, 2001.

[116] L.S. Nilssen, O. Dajani, T. Christoffersen, and D. Sandnes. Sustained diacylglycerol accumulation resulting from prolonged G protein-coupled receptor agonist-induced phosphoinositide breakdown in hepatocytes. *J. Cell Biochem.*, 94:389–402, 2005.

[117] J.J. O'Shea, J.B. Harford, and R.D. Klausner. Identification and characterization of the phosphatidylinositol kinase in membranes of murine T lymphocytes. *J. Immunol.*, 137:971–976, 1986.

[118] S. Patel, L.D. Robb-Gaspers, K.A. Stellato, M. Shon, and A.P. Thomas. Coordination of calcium signalling by endothelial-derived nitric oxide in the intact liver. *Nat. Cell Biol.* , 1:467–471, 1999.

[119] S. Patrick and J. Turchi. Xeroderma pigmentosum complementation group A protein (XPA) modulates RPA-DNA interactions via enhanced complex stability and inihibition of strand separation activity. *J. Biol. Chem.*, 277:16096–16101, 2002.

[120] D. Perdiz, P. Grof, M. Mezzina, O. Nikaido, E. Moustacchi, and E. Sage. Distribution and repair of bipyrimidine photoproducts in solar UV-irradiated mammalian cells. possible role of dewar photoproducts in solar mutagenesis. *J. Biol. Chem.*, 275:26732–26742, 2000.

[121] J.F. Perez and M.J. Sanderson. The frequency of calcium oscillations induced by 5-HT, ACH, and KCl determine the contraction of smooth muscle cells of intrapulmonary bronchioles. *J. Gen. Physiol.*, 125:535–553, 2005.

[122] J.F. Perez and M.J. Sanderson. The contraction of smooth muscle cells of intrapulmonary arterioles is determined by the frequency of Ca^{2+} oscillations induced by 5-HT and KCl. *J. Gen. Physiol.*, 125:555–567, 2005.

[123] A. Politi and T. Höfer. Modelling of periodic intercellular Ca^{2+} waves. In *Function and Regulation of Cellular Systems*, pages 99–110. Birkhäuser-Verlag, 2004.

[124] A. Politi, M.J. Moné, A.B. Houtsmuller, D. Hoogstraten, W. Vermeulen, R. Heinrich, and R. van Driel. Mathematical modeling of nucleotide excision repair reveals efficiency of sequential assembly strategies. *Mol. Cell*, 19:679–690, 2005.

[125] W.H. Press, B.P. Flannery, S.A. Teukolsky, and W.T. Vetterling. *Numerical Recipes in C: The Art of Scientific Computing.* Cambridge University Press, 2nd edition, 1992.

[126] E.K. Pye and B. Chance. Sustained sinusoidal oscillations of reduced pyridine nucleotide in a cell-free extract of *S. carlsbergensis*. *Proc. Natl. Acad. Sci. USA*, 55:888–894, 1966.

[127] S. Rademakers, A. Nigg, M. Moné, M. Volkers, J. Hoeijmakers, Houtsmuller, and W. Vermeulen. Dynamics of the xeroderma pigmentosum group A DNA repair protein in living cells. *Mol. Cell Biol.*, pages 5755–5767, 2003.

[128] L.E. Rameh, K.F. Tolias, B.C. Duckworth, and L.C. Cantley. A new pathway for synthesis of phosphatidylinositol-4,5-bisphosphate. *Nature*, 390:192–196, 1997.

[129] J. Ramos-Franco, M. Fill, and G.A. Mignery. Isoform-specific function of single inositol 1,4,5-trisphosphate receptor channels. *Biophys. J.*, 75:834–839, 1998.

[130] J.T. Reardon and Sancar A. Thermodynamic cooperativity and kinetic proofreading in DNA damage recognition and repair. *Cell Cycle*, 3:141–144, 2004.

[131] J.T. Reardon and A. Sancar. Molecular anatomy of the human excision nuclease assembled at sites of DNA damage. *Mol. Cell. Biol.*, 23:5755–5767, 2002.

[132] J.T. Reardon and A. Sancar. Recognition and repair of the cyclobutane thymine dimer, a major cause of skin cancers, by the human excision nuclease. *Genes Dev.*, 17:2539–2551, 2003.

[133] J.T. Reardon, D. Mu, and A. Sancar. Overproduction, purification, and characterization of the XPC subunit of the human DNA repair excision nuclease. *J. Biol. Chem.*, 271:19451–19456, 1996.

[134] M.J. Rebecchi and N.P. Pentyala. Structure, function, and control of phosphoinositode-specific phospholipase c. *Physiol. Rev.*, 80:1291–1335, 2000.

[135] S.G. Rhee. Regulation of phosphoinositide-specific phospholipase C. *Annu. Rev. Biochem.*, 70: 281–312, 2001.

[136] T. Riedl, F. Hanaoka, and J.M. Egly. The comings and goings of nucleotide excision repair factors on damaged DNA. *EMBO J.*, 22:5293–5303, 2003.

[137] L.D. Robb-Gaspers and A.P. Thomas. Coordination of Ca^{2+} signaling by intercellular propagation of Ca^{2+} waves in the intact liver. *J. Biol. Chem.* , 270:8102–8107, 1995.

[138] T.A. Rooney, E. Sass, and A.P. Thomas. Characterization of cytosolic calcium oscillations induced by phenylephrine and vasopressin in single fura-2-loaded hepatocytes. *J. Biol. Chem.*, 264:17131–17141, 1989.

[139] T.A. Rooney, E.J. Sass, and A.P. Thomas. Agonist-induced cytosolic calcium oscillations originate from a specific locus in single hepatocytes. *J. Biol. Chem.*, 265:10792–10796, 1990.

[140] Yong-Chun S., L. Di, T. Xiao-dan, D. Ai-rong, T. Hui-yong, L. Shen-qiu, and D. Qin-kai. Mathematical model of phosphatidylinositol-4,5-bisphosphate hydrolysis mediated by epidermal growth factor receptor generating diacylglycerol. *J. Biotech.*, 124:584–591, 2006.

[141] L. Schaeffer, R. Roy, S. Humbert, V. Moncollin, W. Vermeulen, J.H.J. Hoeijmakers, P. Chambon, and J.M. Egly. DNA repair helicase: a component of BTF2 (TFIIH) basic transcription factor. *Science*, 260:58–63, 1993.

[142] L. Schaeffer, V. Moncollin, R. Roy, A. Staub, M. Mezzina, A. Sarasin, G. Weeda, J.H.J. Hoeijmakers, and J. M. Egly. The ERCC2/DNA repair protein is associated with the class II BTF2/TFIIH transcription factor. *EMBO J.*, 13:2388–2392, 1994.

[143] M. Schmidt, M. Frings, M.L. Mono, Y. Guo, P.A. Weernink, S. Evellin, L. Han, and K.H. Jakobs. G protein-coupled receptor-induced sensitization of phospholipase c stimulation by receptor tyrosine kinases. *J. Biol. Chem.*, 275:32603–32610, 2000.

[144] S. Schuster, M. Marhl, and T. Höfer. Modelling of simple and complex calcium oscillations. *Eur. J. Biochem.*, 269:1333–1355, 2002.

[145] S. Schuster, B. Knoke, and M. Marhl. Differential regulation of proteins by bursting calcium oscillations–a theoretical study. *Biosystems*, 81:49–63, 2005.

[146] T. Seki and J.F. Diffley. Stepwise assembly of initiation proteins at budding yeast replication origins in vitro. *Proc. Natl. Acad. Sci. USA*, 97:14115–14120, 2000.

[147] P. Shen and R. Larter. Chaos in intracellular Ca^{2+} oscillations in a new model for non-excitable cells. *Cell Calcium*, 17:225–232, 1995.

[148] M.K. Shivji, A.P. Eker, and R.D. Wood. DNA repair defect in xeroderma pigmentosum group C and complementing factor from HeLa cells. *J. Biol. Chem.*, 269:22749–22757, 1994.

[149] T. Shuttleworth and J. Thompson. Ca^{2+} entry modulates oscillation frequency by triggering Ca^{2+} release. *Biochem. J.*, 313:815–819, 1996.

[150] C. Sims and N. Allbritton. Metabolism of inositol 1,4,5-trisphosphate and inositol 1,3,4,5-tetrakisphosphate by the oocytes of xenopus laevis. *J. Biol. Chem.*, 273:4052–4058, 1998.

[151] J. Sneyd and J. Dufour. A dynamic model of the type-2 inositol trisphosphate receptor. *Proc. Natl. Acad. Sci. USA*, 99:2398–2403, 2002.

[152] J. Sneyd and M. Falcke. Models of the inositol trisphosphate receptor. *Prog. Biophys. Mol. Biol.*, 89:207–245, 2005.

[153] J. Sneyd, K. Tsaneva-Atanasova, J. Bruce, S. Straub, D. Giovannucci, and D. Yule. A model of calcium waves in pancreatic and parotid acinar cells. *Biophys. J.*, 85:1392–1405, 2003.

[154] J. Sneyd, K. Tsaneva-Atanasova, D.I. Yule, J.L. Thompson, and T.J. Shuttleworth. Control of calcium oscillations by membrane fluxes. *Proc. Natl. Acad. Sci.*, 101:1392–1396, 2004.

[155] J. Sneyd, K. Tsaneva-Atanasova, V. Reznikov, Y. Bai, M. J. Sanderson, and D. I. Yule. A method for determining the dependence of calcium oscillations on inositol trisphosphate oscillations. *Proc. Natl. Acad. Sci. USA*, 103:1675–1680, 2006.

[156] B.A. Sokhansanj, G.R. Rodrigue, J.P. Fitch, and D.M. Wilson 3rd. Quantitative model of human DNA base excision repair. I. mechanistic insights. *Nucl. acids res.* , 30:1817–1825, 2002.

[157] B. L. Sprague, R. L. Pego, D. A. Stavreva, and J. G. McNally. Analysis of binding reactions by fluorescence recovery after photobleaching. *Biophys. J.* , 86:3473–3495, 2004.

[158] K. Sugasawa, J.M. Ng, C. Masutani, S. Iwai, P.J. van der Spek, A.P.M. Eker, F. Hanaoka, D. Bootsma, and J.H.J. Hoeijmakers. Xeroderma pigmentosum group C protein complex is the initiator of global genome nucleotide excision repair. *Mol. Cell*, 2:223–232, 1998.

[159] K. Sugasawa, Y. Okuda, M. Saijo, R. Nishi, N. Matsuda, G. Chu, T. Mori, S. Iwai, K. Tanaka, K. Tanaka, and F. Hanaoka. UV-induced ubiquitylation of XPC protein mediated by UV-DDB-ubiquitin ligase complex. *Cell*, 121:387–400, 2005.

[160] J.Q. Svejstrup, Z. Wang, W.J. Feaver, X. Wu, D.A. Bushnell, T.F. Donahue, E.C. Friedberg, and R.D. Kornberg. Different forms of TFIIH for transcription and DNA repair: holo-TFIIH and a nucleotide excision repairosome. *Cell*, 80:21–28, 1995.

[161] N.A. Tamarina, A. Kuznetsov, C.J. Rhodes, V.P. Bindokas, and L.H. Philipson. Inositol (1,4,5)-trisphosphate dynamics and intracellular calcium oscillations in pancreatic beta-cells. *Diabetes*, 54:3073–3081, 2005.

[162] J. Tang and G. Chu. Xeroderma pigmentosum complementation group E and UV-damaged DNA-binding protein. *DNA Repair*, 1:601–616, 2002.

[163] Y. Tang and H. Othmer. Frequency encoding in excitable systems with applications to calcium oscillations. *Proc. Natl. Acad. Sci. USA*, 92:7869–7873, 1995.

[164] A. Tanimura and R.J. Turner. Inositol 1,4,5-trisphosphate-dependent oscillations of luminal [Ca^{2+}] in permeabilized HSY cells. *J. Biol. Chem.*, 271, 1996.

[165] A. Tapias, J. Auriol, D. Forget, J.H. Enzlin, O.D. Scharer, F. Coin, B. Coulombe, and J.M. Egly. Ordered conformational changes in damaged DNA induced by nucleotide excision repair factors. *J. Biol. Chem.*, 279:19074–19083, 2004.

[166] B.S. Thoma and Vasquez K.M. Critical DNA damage recognition functions of XPC-hHR23B and XPA-RPA in nucleotide excision repair. *Mol. Carcinog.*, 38:1–13, 2003.

[167] A.P. Thomas, J.S. Marks, K.E. Coll, and J.R. Williamson. Quantitation and early kinetics of inositol lipid changes induced by vasopressin in isolated and cultured hepatocytes. *J. Biol. Chem.*, 258:5716–5725, 1983.

[168] A.P. Thomas, J. Alexander, and J.R. Williamson. Relationship between inositol polyphosphate production and the increase of cytosolic free Ca^{2+} induced by vasopressin in isolated hepatocytes. *J. Biol. Chem.*, 259:5574–5584, 1984.

[169] A.P. Thomas, D.C. Renard, and T.A. Rooney. Spatial and temporal organization of calcium signalling in hepatocytes. *Cell Calcium*, 12:111–126, 1991.

[170] A.P. Thomas, G.S. Bird, G. Hajnoczky, L.D. Robb-Gaspers, and J.W. Putney Jr. Spatial and temporal aspects of cellular signaling. *FASEB J.*, 10:1505–1517, 1996.

[171] S. Thore, O. Dyachok, and A. Tengholm. Oscillations of phospholipase C activity triggered by depolarization and Ca^{2+} influx in insulin-secreting cells. *J. Biol. Chem.*, 279:19396–19400, 2004.

[172] T. Tordjmann, B. Berthon, M. Claret, and L. Combettes. Coordinated intercellular calcium waves induced by noradrenaline in rat hepatocytes: dual control by gap junction permeability and agonist. *EMBO J.*, 16:5398–5407, 1997.

[173] T. Urumow and O.H. Wieland. Purification and partial characterization of phosphatidylinositol-4-phosphate kinase from rat liver plasma membranes. Further evidence for a stimulatory G-protein. *Biochim. Biophys. Acta*, 1052:152–158, 1990.

[174] P.J. van der Spek, A. Eker, S. Rademakers, C. Visser, K. Sugasawa, C. Masutani, F. Hanaoka, D. Bootsma, and J.H. Hoeijmakers. Xpc and human homologs of rad23: intracellular localization and relationship to other nucleotide excision repair complexes. *Nucleic Acids Res.*, 24:2551–2559, 1996.

[175] A. van Hoffen, J. Venema, R. Meschini, A.A. van Zeeland, and L.H. Mullenders. Transcription-coupled repair removes both cyclobutane pyrimidine dimers and 6-4 photoproducts with equal efficiency and in a sequential way from transcribed DNA in xeroderma pigmentosum group C fibroblasts. *EMBO J.*, 14:360–367, 1995.

[176] B. Vanhaesebroeck, S.J. Leevers, K. Ahmadi, J. Timms, R. Katso, P.C. Driscoll, R. Woscholski, P.J. Parker, and M.D. Waterfield. Synthesis and function of 3-phosphorylated inositol lipids. *Annu. Rev. Biochem.*, 70:535–602, 2001.

[177] L. Venance, N. Stella, J. Glowinski, and C. Giaume. Mechanism involved in initiation and propagation of receptor-induced intercellular calcium signaling in cultured rat astrocytes. *J. Neurosci.*, 17:1981–1992, 1997.

[178] I. Vivanco and C. L. Sawyers. The phosphatidylinositol 3-kinase akt pathway in human cancer. *Nat. Rev. Canc.*, 2:489–501, 2002.

[179] M. Volker. *Nucleotide excision repair - complexes and complexities. A study of global genome repair in human cells.* PhD thesis, Universiteit Leiden, 2006.

[180] M. Volker, M.J. Moné, P. Karmakar, A. van Hoffen, W. Schul, W. Vermeulen, J.H. Hoeijmakers, R. van Driel, A.A. van Zeeland, and L.H Mullenders. Sequential assembly of the nucleotide excision repair factors in vivo. *Mol. Cell*, 8:213–224, 2001.

[181] J. Wagner, C.P. Fall, F. Hong, C.E. Sims, N.L. Allbritton, R.A. Fontanilla, I.I. Moraru, L.M. Loew, and R. Nuccitelli. A wave of IP_3 production accompanies the fertlization Ca^{2+} wave in the egg of the frog, xenopus laevis: theoretical and experimental support. *Cell Calcium*, 35:433–477, 2004.

[182] M. Wakasugi and A. Sancar. Assembly subunit composition, and footprint of human DNA repair excision nuclease. *Proc. Natl. Acad. Sci. USA*, 95:6669–6674, 1998.

[183] M. Wakasugi and A. Sancar. Order of assembly of human DNA repair excision nuclease. *J. Biol. Chem.*, 274:18759–18768, 1999.

[184] M. Wakasugi, J.T. Reardon, and A. Sancar. The non-catalytic function of xpg protein during dual incision in human nucleotide excision repair. *J. Biol. Chem.*, 272:16030–16034, 1997.

[185] M. Wakui, B.V. Potter, and O.H. Petersen. Pulsatile intracellular calcium release does not depend on fluctuations in inositol trisphosphate concentration. *Nature*, 339:317–320, 1989.

[186] S.S. Wang, A.A. Alousi, and S.H. Thompson. The lifetime of inositol 1,4,5-trisphosphate in single cells. *J. Gen. Physiol.*, 105:149–171, 1995.

[187] Z. Wang, M. Tymianski, O. Jones, and M. Nedergaard. Impact of cytoplasmic calcium buffering on the spatial and temporal characteristics of intercellular calcium signals in astrocytes. *J. Neurosci.*, 17:7359–7371, 1997.

[188] P.A.O. Weernink, M. Schmidt, and K.H. Jakobs. Regulation and cellular roles of phosphoinositide 5-kinases. *Eur. J. Pharm.*, 500:87–99, 2004.

[189] G.B. Willars, S.R. Nahorski, and R.A.J. Challiss. Differential regulation of muscarinic acetylcholine receptor sensitive polyphosphoinositide pools and consequences for signaling in human neuroblastoma cells. *J. Biol. Chem.*, 273:5037–5046, 1998.

[190] G.S. Winkler, K. Sugasawa, A.P. Eker, W.L. de Laat, and J.H. Hoeijmaker. Novel functional interactions between nucleotide excision DNA repair proteins influencing the enzymatic activities of TFIIH, XPG, and ERCC1-XPF. *Biochemistry*, 40:160–165, 2001.

[191] M.S. Wold. Replication protein A: a heterotrimeric, single-stranded DNA-binding protein required for eukaryotic DNA metabolism. *Annu. Rev. Biochem.*, 66:61–92, 1997.

[192] J. Wolf, S. Becker-Weimann, and R. Heinrich. Analysing the robustness of cellular rythms. *Systems Biol.*, 2:35–41, 2005.

[193] B. Wolner, S. van Komen, P. Sung, and C.L. Peterson. Recruitment of the recombinational repair machinery to a dna double-strand break in yeast. *Mol. Cell.*, 12:221–232, 2003.

[194] P.J. Woodring and J.C. Garrison. Expression, purification, and regulation of two isoforms of the inositol 1,4,5-trisphosphate 3-kinase. *J. Biol. Chem.*, 272:30447–30454, 1997.

[195] N.M. Woods, K.S.R. Cuthbertson, and P.H. Cobbold. Repetitive transient rises in cytoplasmic free calcium in hormone-stimulated hepatocytes. *Nature*, 319:600–602, 1986.

[196] D. Wu, Y. Jia, X. Zhan, L. Yang, and Q. Liu. Effects of gap junction to Ca^{2+} and to IP_3 on the synchronization of intercellular calcium oscillations in hepatocytes. *Biophys. Chem.*, 113: 145–154, 2005.

[197] C. Xu, J. Watras, and L.M. Loew. Kinetic analysis of receptor-activated phosphoinositide turnover. *J. Cell Biol.*, 161:779–791, 2003.

[198] N. Ye, M.S. Binachi, N.O. Bianchi, and G.P. Holmquist. Adaptive enhancement and kinetics of nucleotide excision repair in humans. *Mutation Research, DNA Repair*, 435:43–61, 1999.

[199] M. Yokoi, C. Masutani, T. Maekawa, K. Sugasawa, Y. Ohkuma, and F. Hanaoka. The xeroderma pigmentosum group C protein complex XPC-HR23B plays an important role in the recruitment of transcription factor IIH to damaged DNA. *J. Biol. Chem.*, 275:9870–9875, 2000.

[200] J.S. You, M. Wang, and S.H. Lee. Biochemical analysis of the damage recognition process in nucleotide excision repair. *J. Biol. Chem.*, 278:7476–85, 2003.

[201] K.W. Young, M.S. Nash, A.J. Challiss, and S.R. Nahorski. Role of Ca^{2+} feedback on cell inositol 1,4,5-tisphosphate oscillations mediated by G-protein-coupled receptors. *J. Biol. Chem.*, 278: 20753–20760, 2003.

[202] D. Yule, E. Stuenkel, and J. Williams. Intercellular calcium waves in rat pancreatic acini: mechanism of transmission. *Am. J. Physiol.*, 271:C1285–C1294, 1996.

[203] D.I. Yule, S.V. Straub, and J.I. Bruce. Modulation of Ca^{2+} oscillations by phosphorylation of ins(1,4,5)p_3 receptors. *Biochem. Soc. Trans.*, 31:954–957, 2003.

[204] B. Zimmermann and B. Walz. The mechanism mediating regenerative intercellular Ca^{2+} waves in the blowfly salivary gland. *EMBO J.*, 18:3222–3231, 1999.

Part III

Appendices

Appendix A

Ca^{2+} feedbacks on IP_3 metabolism: alternative models

I will discuss exemplarily four mathematical models that have been proposed in the literature and how they respond to $IP_3$3K and IP_3 buffer expression. The model proposed by Houart and coworkers includes Ca^{2+} activation of $IP_3$3K the model by Shen and Larter Ca^{2+} activation of PLC [69, 147]. These two models use similar terms for the description of the IP_3R as the model in the main part. Differently the model by Sneyd and Dufour (1999), which includes covalent modifications of the IP_3R, e.g. phosphorylation [154]. The last model has been proposed by Cuthbertson and Chay [25]. It is a so-called pure IP_3 oscillator where the oscillations in IP_3 are absolutely necessary for the Ca^{2+} oscillations. I show simulations using the parameter set given in the original articles and to highlight some of the conclusions with slightly modified parameters.

The results shown here indicate that my theoretical conclusions are not dependent on the exact choice of kinetic expressions for the different processes considered. The results obtained with the four alternative models are in agreement with the results obtained by using the model presented in the main text.

A.1 Model with $IP_3$3K

The model proposed by Houart and coworkers [69] consider three variables: calcium in the cytosol (Z), Ca^{2+} in the internal stores (Y), and IP_3 (A). The two major feedbacks are the Ca^{2+} and IP_3 activation of the IP_3R and the Ca^{2+} dependent degradation of IP_3 by the $IP_3$3K.

To simulate the overexpression of $IP_3$3K and the presence of the IP_3 buffer, with concentration B_T, the equation for the IP$_3$ concentration in the original article is modified to

$$\frac{dA}{dt} = \frac{V_{M5}}{1 + B_T K_A/(K_A + A)^2}\left(\frac{\beta V_4}{5} - \frac{A^2}{K_5^2 + A^2}\frac{Z^4}{K_d^4 + Z^4} - \frac{\varepsilon}{V_{M5}}A\right) \tag{A.1}$$

The maximal IP$_3$ production rate V_4 is rescaled with the maximal degradation flux by the IP$_3$3K V_{M5}. These modifications avoid the depletion of IP$_3$ after overexpression of the IP$_3$3K. For $V_{M5} = 5$ μM/min one has the original parameter set. The parameter $\beta \in [0, 1]$ accounts for the stimulus dependent activation of the PLC. For further details see the original work [69].

The result of the simulations are shown in Fig. A.1. Using the original parameter set overexpression of IP$_3$3K cannot abolish the oscillations. Nevertheless, one observes a decrease in the maximal period of the oscillations with increasing level of IP$_3$3K (Fig. A.1A). On the other hand, introduction of the IP$_3$ buffer increases the period range (Fig. A.1B). These simulations are in agreement with the results shown in the main text: The role of IP$_3$3K in generating long period oscillations and the requirement of slow IP$_3$ dynamics. After modification of two parameters in the original set (the sensitivity of the IP$_3$R to IP$_3$ and the sensitivity of the IP$_3$3K to Ca^{2+}) one obtains, at high level of IP$_3$3K, a decrease in the period range (Fig. A.1C) and amplitude (not shown), and eventually abolishment of the oscillations. This effect, as in my model, is not due to depletion of IP$_3$ (Fig. A.1D).

A.2 Model with Ca^{2+} activation of PLC, I

The model proposed by Shen and Larter [147] has three dynamic variables: cytoplasmic Ca^{2+} x, internal store concentration y, and IP$_3$ concentration z. In this model PLC is Ca^{2+} dependent. The IP$_3$R is activated by IP$_3$ and shows a bell-shaped dependence on cytoplasmic Ca^{2+} (activated at low and inactivated at high Ca^{2+} concentrations). The equation for IP$_3$ in the original article is modified to account for the IP$_3$ buffer with concentration B_T

$$\frac{dz}{dt} = \frac{1}{1 + B_T K_1/(K_1 + x)^2}\left(AR\frac{x}{K_3 + x} - Bz\right). \tag{A.2}$$

$R \in [0, 1]$ quantifies the stimulus dependent activation of the PLC, which has a maximal activity A. For further details on the model see [147].

The effects of introducing an IP$_3$ buffer are summarized in Fig. A.2. In the presence of high levels of IP$_3$ buffer the oscillations have a reduced amplitude (Fig. A.2A) and a decreased period (Fig. A.2B). By comparing these oscillations with the oscillations

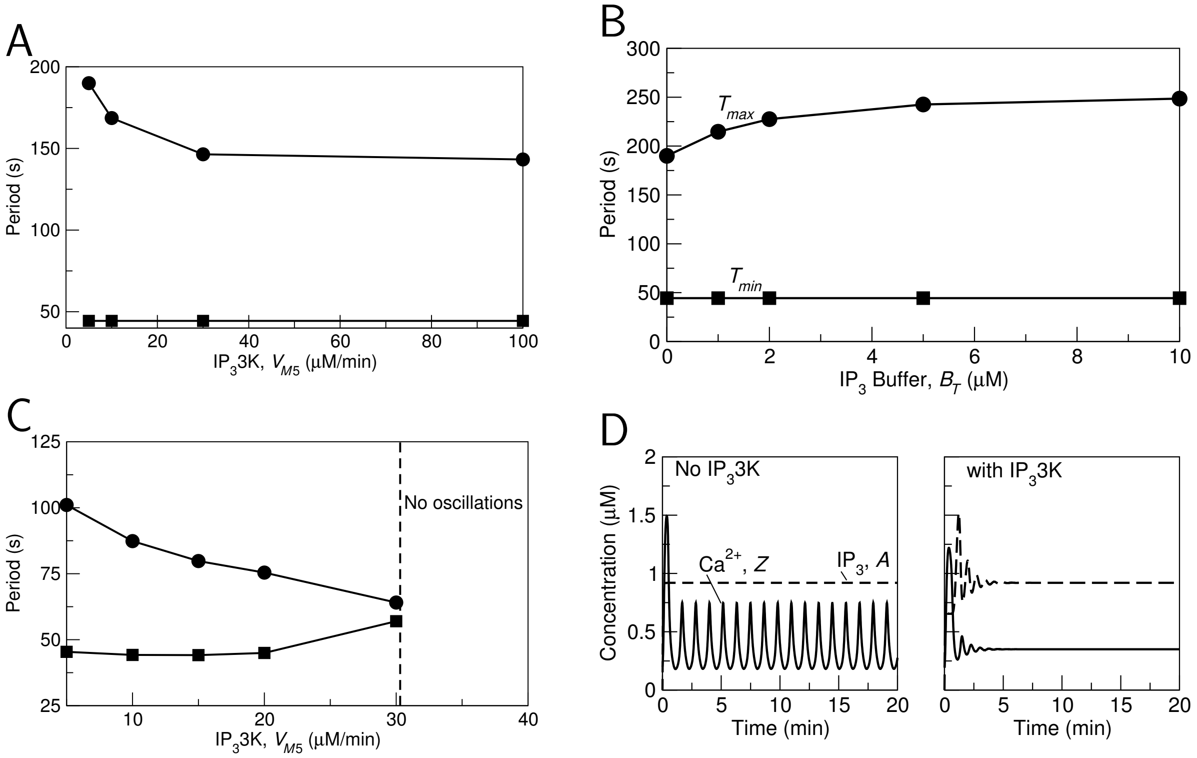

Figure A.1: Effect of IP$_3$3K overexpression and IP$_3$ buffer expression in the model for the Ca^{2+} and IP$_3$ dynamics proposed by Houart and coworkers [69]. (A) Overexpression of IP$_3$3K causes a decrease in the period range. (B) The slowing of the IP$_3$ dynamics by the IP$_3$ buffer causes an increase in the period range. In particular longer period oscillations arise. (C) In the same system overexpression of IP$_3$3K can abolish the oscillations, when e.g. the sensitivity of the IP$_3$R to IP$_3$ and the sensitivity of the IP$_3$3K to Ca^{2+} are modified. (D) The impairment of Ca^{2+} oscillations by IP$_3$3K is not due to depletion of IP$_3$. Ca^{2+} oscillates in the absence of IP$_3$3K (left panel), whereas at high level of IP$_3$3K, although the IP$_3$ concentration is the same, one observes only a transient increase in $[\mathrm{Ca}^{2+}]_c$ (right panel). Parameters: (A) and (B) See [69]. (C) and (D) as in [69] except (C) $K_A = 0.5$ μM and $K_d = 0.3$ μM. (D) left panel $K_A = 0.5$ μM, $K_d = 0$, $V_4 = 3.07$ μM/min, $\beta = 0.75$; right panel $K_A = 0.5$ μM, $K_d = 0.3$ μM, $V_{M5} = 30$ μM/min, $V_4 = 2$ μM, $\beta = 0.75$. The parameters are chosen so that at $\beta = 0.75$ the steady states are identical with and without IP$_3$3K.

obtained in the absence of Ca^{2+} feedback on PLC (by setting $K_3 = 0$), one observes that both have similar amplitude and period range. This shows that, on the one hand positive feedback on PLC increases the period range, on the other hand, an IP_3 buffer erases this effect. In Fig. A.2C I show the location of the two Hopf bifurcations as function of the buffer concentration B_T and stimulus strength R. The picture is qualitatively similar to Fig. 3.3. A slight modification of the parameters of the core oscillator strengthens the effect of the IP_3 buffer (dashed line in Fig. A.2C). Introducing an IP_3 buffer extinguishes the oscillations in a large stimulatory domain. For the parameter used, at high IP_3 buffer concentrations oscillations can persist, but with reduced amplitude and high frequency. In Fig. A.2D typical oscillations in the absence of the IP_3 buffer (left panel) and a slow unique Ca^{2+} spike in the presence of IP_3 buffer (right panel) are shown.

A.3 Model with Ca^{2+} activation of PLC, II

The model proposed by Sneyd and Dufour [151] for the IP_3R dynamics considers recent experimental facts on the inactivation mechanisms of the IP_3R type 2. The kinetic description of the IP_3R differs strongly from the previous two models and the model I used. I was interested whether the theoretical results depend on the particular IP_3R model. The model used to simulate the Ca^{2+} and IP_3R dynamics is given in [154]. I implemented it with an extra equation for the IP_3 concentration (in the original model the IP_3 concentration is a parameter), which accounts for Ca^{2+} activation of PLC and expression of the IP_3 buffer

$$\frac{dp}{dt} = \frac{1}{1 + B_T/K_B}(V_{PLC}\frac{c^2}{K_{PLC}^2 + c^2} - k_{5P}p). \tag{A.3}$$

I also slightly modified the term describing the Ca^{2+} influx from the extracellular medium

$$J_{influx} = \alpha_1 + \alpha_2 V_{PLC}. \tag{A.4}$$

This modification conserves the property of a stimulation dependent influx, which does not oscillate together with Ca^{2+}.

The effects of slowing the IP_3 dynamics with the IP_3 buffer are illustrated in Fig. A.3. The results are similar to the results shown in Fig. 3.3. High concentrations of IP_3 buffer completely abolish the oscillations. Instead, one observes a slow transient increase in $[Ca^{2+}]_c$.

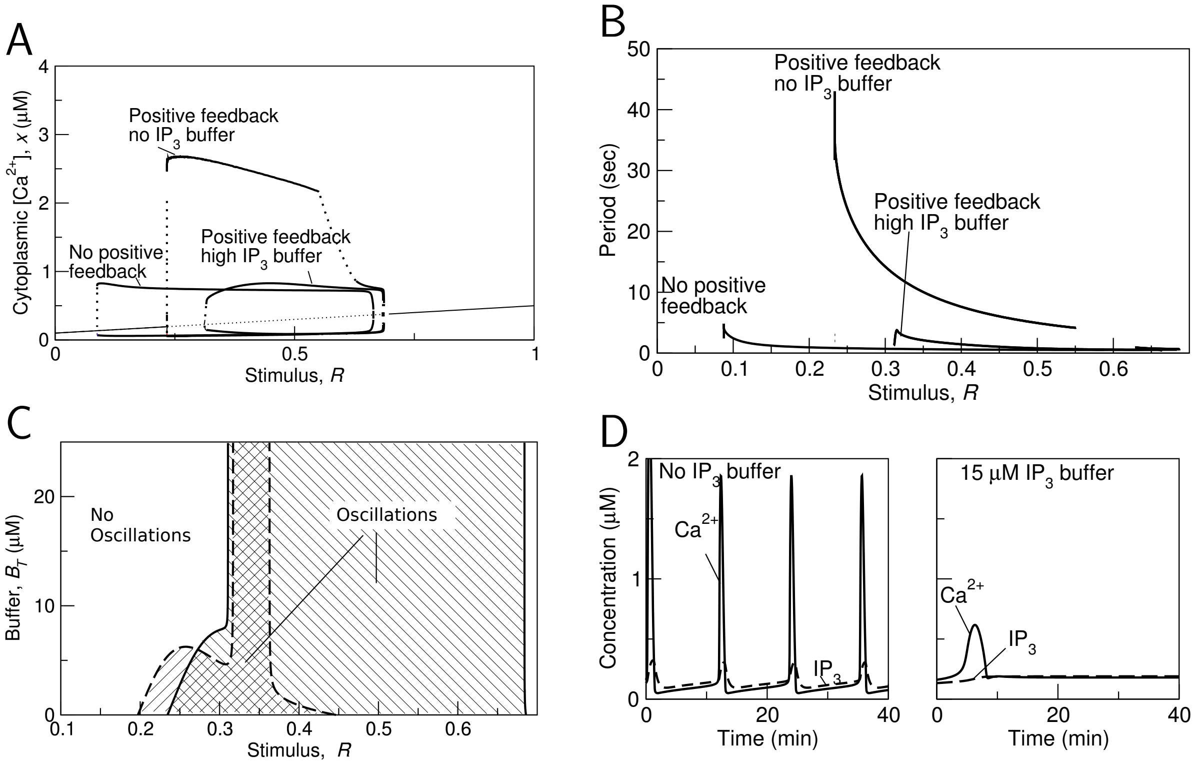

Figure A.2: Effect of an IP_3 buffer in the model proposed by [147], which includes Ca^{2+} activation of PLC. (A) Slowing of the IP_3 dynamics with an IP_3 buffer reduces the oscillatory domain and amplitude and (B) considerably decreases the period range. In particular, long period oscillations disappear (circle and square denote the longest ans shortest period, respectively, obtained when varying the stimulus). (C) Locus of the two Hopf-bifurcations as function of stimulus R and IP_3 buffer concentration for the original parameter set (solid line). With a slight parameter change, the effect of the IP_3 buffer becomes more pronounced (dashed line). (D) Example of the Ca^{2+} (solid) and IP_3 (dashed) dynamics prior (left panel) and after (right panel) addition of IP_3 buffer. The oscillations disappear, instead a broad and slow Ca^{2+} spike is observed. Parameters: (A), (B) as given in Shen and Larter (1995) the IP_3 buffer concentration is 100 μM. (C) solid line: as given in [147], dashed line: Ca^{2+} activation constant of the IP_3R is $K_5 = 0.4\,\mu$M (instead of 0.69 μM) and of PLC $K_3 = 0.2$ μM (instead of 1 μM.). (D) $K_3 = 0.2$ μM, $K_5 = 0.4$ μM. At $t = 0$ s R is increased from 0.15 to 0.25. Left panel: $B_T = 0$. Right panel: $B_T = 15$ μM.

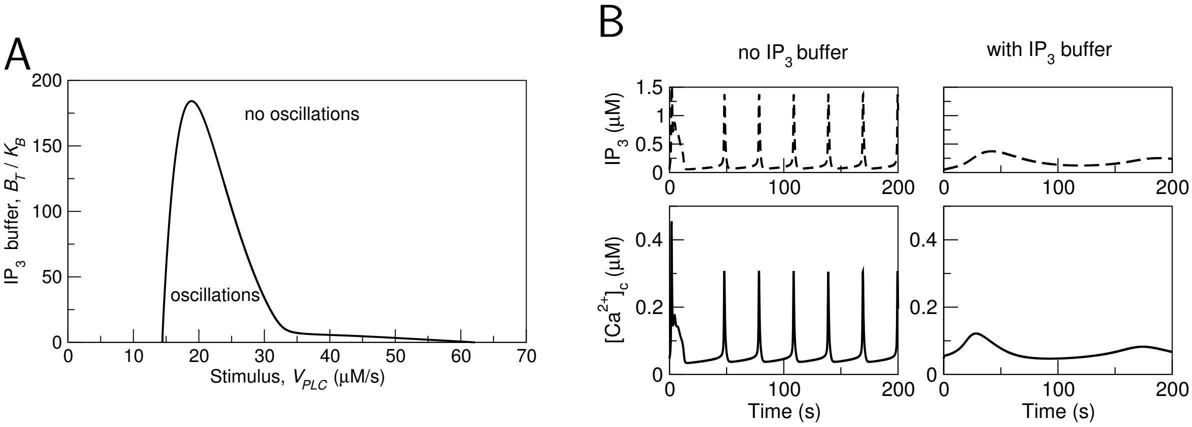

Figure A.3: Model for the IP_3R and Ca^{2+} dynamics proposed by [154] with Ca^{2+} activation of PLC, Eq. A.3. (A) Location of the Hopf-bifurcations as function of the IP_3 buffer concentration and the stimulus dependent V_{PLC}. High concentrations of IP_3 buffer completely abolish the oscillations. (B) Example of Ca^{2+} oscillations for $V_{PLC} = 20$ μM/s (left panel) and $B_T/K_B = 200$. Parameters as in Sneyd et al. (2004), except strength of plasma membrane fluxes $\delta = 0.2$, $\alpha_2 = 0.3$. Activation constant of PLC $K_{PLC} = 0.2$ μM. The high value of V_{PLC} is due to the fast degradation of IP_3 (life time in the absence of IP_3 buffer is 0.1 s, $k5P = 10$/s).

A.4 Pure IP_3/DAG oscillator

Cuthbertson and Chay [25] analyzed different oscillator models. The common point between all these models is that the oscillation mechanism is upstream the Ca^{2+} release, Ca^{2+} barely follows the oscillations in IP_3. In all models the positive action of Ca^{2+} on the IP_3R is not considered. The principal positive feedback mechanism is the activation of PLC by diacylglycerol (DAG), the other product of the PLC mediated hydrolysis of PIP_2. Although the activation of PLC by DAG has not been clearly demonstrated experimentally [62], these models allow to analyze the effect of an IP_3 buffer on a so called pure IP_3 oscillator.

Here, I show the simulation results for one of the models developed in [25] (called example 1). This model accounts for the activation of PLC by DAG and the inactivation of the G_α by protein kinase C (PKC). PKC depends on both DAG and Ca^{2+}. In the original article the model variables are Ca^{2+} in the cytoplasm, the concentration of G_α bound to GTP, and DAG. IP_3 was assumed to be equal to DAG, to analyze the effect of the IP_3 buffer I add an equation for the IP_3 concentration, which reads:

$$\frac{dp}{dt} = \frac{1}{1 + B_T K_s/(K_s + p)^2}(k_d R_{PLC} - h_d p + l_d). \tag{A.5}$$

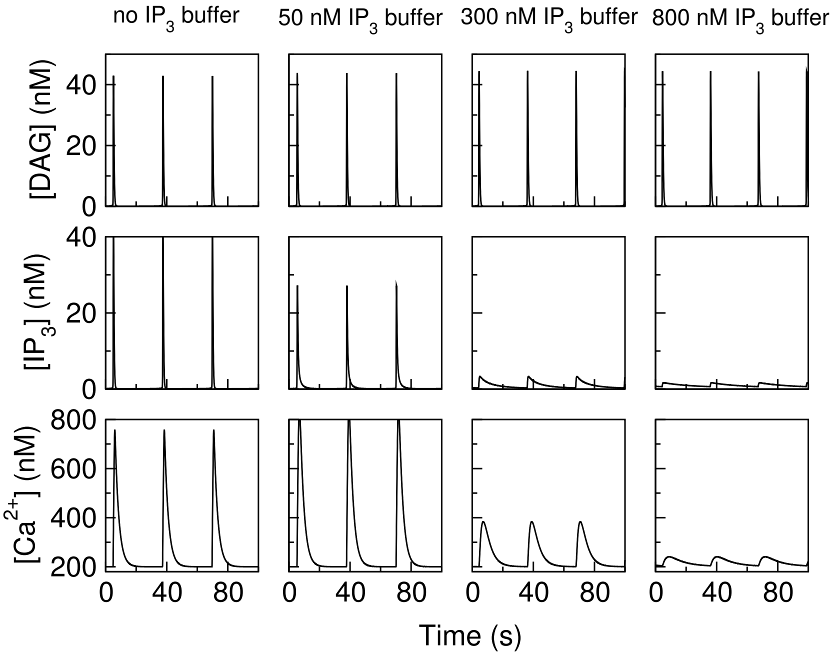

Figure A.4: Model proposed by Cuthbertson and Chay ([25]) implemented with the IP_3 dynamics, Eq. A.5. Typical oscillations observed for four different IP_3 buffer concentrations. DAG appears to be only minimally affected by the buffer. The oscillations in IP_3 and Ca^{2+} have a strong reduced amplitude but the period is unaffected as it is dictated by the oscillations in DAG. Parameters as in [25].

The other equations are described in [25]. As expected for a pure IP_3/DAG oscillator mechanism, the presence of an IP_3 buffer strongly damps the IP_3 oscillations and so the Ca^{2+} oscillations (Fig. A.4). Strictly speaking, although the Ca^{2+} oscillations are very small in amplitude they never cease. This is because the DAG and G_α oscillations remain practically unaffected by the IP_3 buffer. In fact, the oscillations in DAG persist even after clamping Ca^{2+} and IP_3 (not shown). This is because, in the model by Cuthbertson and Chay, PKC is mainly controlled by DAG and is not very sensitive to Ca^{2+} variations.

Appendix B

Phosphoinositide metabolism

B.1 IP$_3$ signal duration and amplitude

To calculate the signal duration and amplitude (Eqs. (4.18)–(4.19)) one must first derive the integrals. Writing the linear ordinary differential equation system in matrix form yields

$$\frac{d\mathbf{X}(t)}{dt} = \mathbf{M}\mathbf{X}(t),$$

where $\mathbf{X}(t) = (X_1(t), \cdots, Y_1(t))^T$ is the vector of concentrations and $\mathbf{M}$ the matrix characteristic for the pathway. Integrating from $t = 0$ to ∞ gives a vector containing the 0-moments in time of the concentration distributions

$$\int_0^\infty \Delta\mathbf{X}(t)dt = -\mathbf{M}^{-1}\Delta\mathbf{X}(0), \tag{B.1}$$

with $\Delta\mathbf{X}(t) = \mathbf{X}(t) - \mathbf{X}(\infty)$. Integration by part gives following relation between the vector of the $n-1$-moments and the vector of the n-moments

$$\begin{aligned} \int_0^\infty t^{n-1}\Delta\mathbf{X}(t)dt &= \frac{t^n}{n}\Delta\mathbf{X}(t)\Big|_{t=0}^{\infty} - \int_0^\infty \frac{t^n}{n}\frac{d\mathbf{X}(t)}{dt}dt \\ &= -\mathbf{M}\int_0^\infty \frac{t^n}{n}\Delta\mathbf{X}(t)dt. \end{aligned} \tag{B.2}$$

Combining Eq. (B.1) and (B.2) leads to the general expression

$$\int_0^\infty t^n \Delta\mathbf{X}(t)dt = n!(-1)^{n+1}\mathbf{M}^{-(n+1)}\Delta\mathbf{X}(0). \tag{B.3}$$

Matrix inversion and multiplication gives the integrals required for calculating signal duration and amplitude. For the case without phosphatases and PI 3/5 kinase these two measures are given in Eq. (4.20) and (4.21).

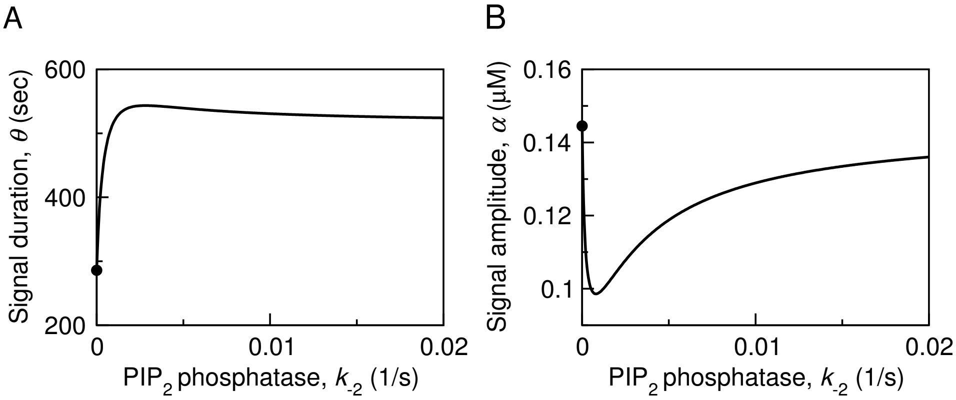

Figure B.1: (A) Duration and (B) amplitude of the [IP$_3$] transient as function of PIP$_2$ phosphatase activity (Eqs. (B.4)–(B.5) and (4.12)). The solid circles indicate the values when PIP$_2$ phosphatase is not present. PLC rate constant during stimulation is $k_3^* = 0.007/s$.

The phosphatases are introduced by conserving the reference unstimulated steady state concentrations. This is guaranteed when the corresponding kinase rate constant is increased according to Eq. (4.11). In the absence of PIP$_2$ phosphatase the formulas for the signal duration and amplitude are not modified when PIP phosphatase is active ($k_{-1} \neq 0$, $k_{-2} = 0$). The result is different, when instead of PIP phosphatase, PIP$_2$ phosphatase is active ($k_{-1} = 0$, $k_{-2} \neq 0$). The signal duration and amplitude are given by

$$\theta = 2\sqrt{\frac{1}{k_3^{*2}} + \frac{1}{k_4{}^2} + \frac{\left(k_3^* + k_{-2}\right)^2 + 2k_2k_{-2}}{k_2^2 k_3^{*2}} - \left(k_2 + k_{-2}\right)^{-2}} \tag{B.4}$$

and

$$\alpha = \frac{\overline{Y}_1 \left(\frac{1}{k_3} - \frac{1}{k_3^*}\right)}{\theta} \frac{k_2 + k_{-2}}{k_2}, \tag{B.5}$$

respectively. In both equations the PIP 5-kinase rate is determined by Eq. (4.12).

The expression for the signal duration and amplitude when both phosphatases are present, but the PI 3/5 kinase is inactive ($k_{-1}, k_{-2} \neq 0$, $\kappa = 0$), is very lengthy and I forbear from listing it here. However, one can show, using symbolic computation as provided by *Mathematica*, that for this situation the signal duration further increases.

B.2 Agonist dependent kinases

There are indications that some of the enzymes involved in the phosphoinositide pathway are activated by agonist dependent G-proteins (see reviews [94, 188]). This putative mechanism represents a possible way to upregulate the [IP$_3$] during stimulation. In the absence of the additional PI degradation pathway ($\kappa = 0$), a sustained elevation in [IP$_3$] can be achieved if the PI production flux v increases (Eq. (4.17)). However, activation of PLC and PI synthase leads to an increase in the PI and PIP level (Eqs. (4.7)–(4.8)), a result that is not observed experimentally. Therefore, PI 4-kinase and PIP 5-kinase must also be activated during stimulation (see Fig. B.2A). Under these premises model simulations show a good agreement with the experimental data (Fig. B.2B, C). As in Fig. 4.5 introduction of receptor desensitization improves the model fit to the data (insets in Fig. B.2B, C). Here, both the rate constant of PIP phosphorylation, k_2, as well of PIP$_2$ hydrolysis, k_3, relaxes in time to lower values. When $\kappa \neq 0$, activation of the PI 4-kinase, PIP 5-kinase, and PLC is sufficient to account for the experimental data (not shown).

Stimulus dependent control of the whole phosphoinositide pathway represents a simple and energy efficient way to regulate the [IP$_3$] in the cytosol. The ATP used to maintain the phosphoinositide pool at rest is much lower than in the presence of phosphatases (0.045 μM/s compared to over 7 μM/s with futile cycles). According to the model there must be strong activation of PI 4-kinase and PIP 5-kinase (rate constants increase by a factor of 10 and 25, respectively). Whether such a change is observed for agonists connected to PLC activation remains to be shown experimentally.

B.3 Linear chain with substrate inhibition

An increase in enzymatic rates does not consequently implies that the enzymes must be activated by the stimulus. If some of the enzymes are inhibited by their substrate the activation of PLC could lead to an overall increase in flux, and so to a prolonged increase in [IP$_3$]. Indeed, for PI 4-kinase and PIP 5-kinase substrate inhibition has been reported [93, 117]. To assess the potential role of substrate inhibition for sustained IP$_3$ signals, the rate of phosphorylation by PI 4-kinase and PIP 5-kinase are described by

$$v_1 = V_1^{max} \frac{A_1 X_1}{1 + A_1 X_1 + A_2 X_2} \text{ and } v_2 = V_2^{max} \frac{B_2 X_2}{1 + B_2 X_2 + B_3 X_3}, \tag{B.6}$$

respectively. Where A_1 (B$_2$) is the affinity of PI 4-kinase (PIP 5-kinase) for its substrate PI (PIP) and A_2 (B_3) the affinity to its product PIP (PIP$_2$). The two enzymes catalyze phosphorylation of their substrate with consumption of ATP. The rather improbable reverse reaction, dephosphorylation of the phosphoinositide and transformation of ADP into ATP is neglected. The PLC reaction and IP$_3$ degradation are described as shown before.

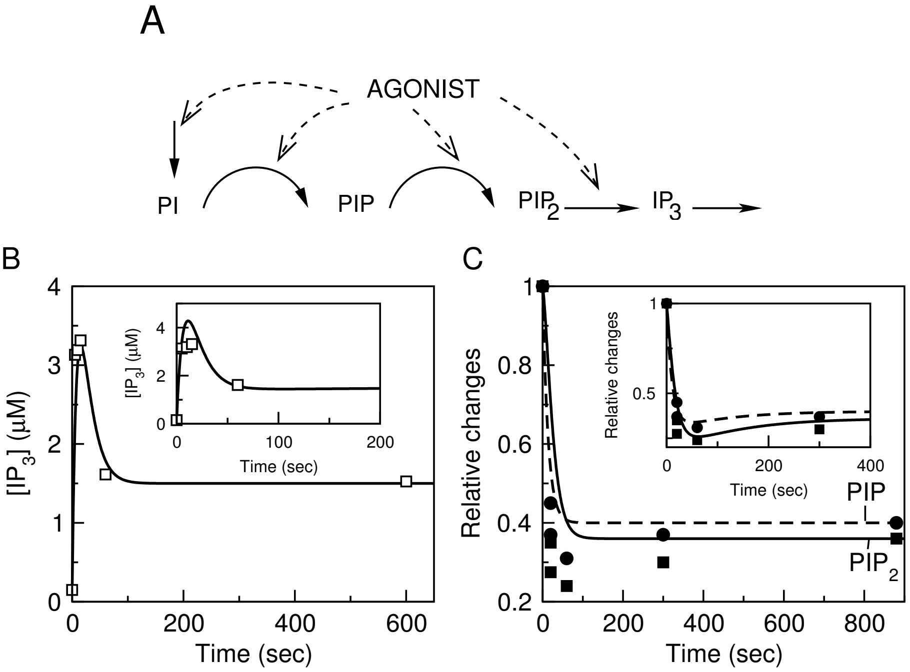

Figure B.2: Stimulating the kinases produces a steady increase in the [IP$_3$]. (A) Agonist activates all forward reactions (PI synthase, PI 4-kinase, PIP 5-kinase and PLC). (B) [IP$_3$] remains elevated during stimulation as observed experimentally (data points). (C) The densities of phosphoinositides decrease during stimulation. Data points for PI, PIP and PIP$_2$ from [189]. Rate constants during stimulation are determined from the steady state in stimulated cells (see Tab. 4.3) $k_1 = 0.0079/\text{s}$, $k_2 = 0.074/\text{s}$, $k_3 = 0.066/\text{s}$. A better agreement with data is obtained with partial receptor desensitization (insets in B and C). This is modeled similar to Fig. 4.5 by $k_2 = 0.074(1 + 0.3e^{-t/100})/\text{s}$ and $k_3 = 0.066(1 + 0.7e^{-t/100})/\text{s}$.

The increase in IP$_3$ production flux mediated by substrate inhibition works as follows: the activated PLC causes a decrease in PIP$_2$ density (X_3). This relieves product inhibition of PIP 5-kinase and v_2 increases. The ensuing fall in PIP density (X_2) leads to an increase in v_1. Given the concentrations of metabolites before and during stimulation, one can evaluate the increase in phosphorylation flux brought about by this mechanism. The ratio γ_1 between the steady state PI phosphorylation rate in stimulated and unstimulated state is

$$\gamma_1 = \frac{v_1^*}{v_1} = \frac{\overline{X}_1^*/\overline{X}_1(1 + A_1\overline{X}_1 + A_2\overline{X}_2)}{1 + A_1\overline{X}_1^* + A_2\overline{X}_2^*}. \tag{B.7}$$

Where * indicates the lipid densities and phosphorylation rate during stimulation. From the previous equation one can express the affinity of PI 4-kinase for its product PIP as

$$A_2 = \frac{A_1 \overline{X}_1^*(\gamma_1 - 1) + \gamma_1 - \overline{X}_1^*/\overline{X}_1}{\overline{X}_2 \overline{X}_1^*/\overline{X}_1 - \gamma_1 \overline{X}_2^*}. \tag{B.8}$$

The nominator of this equation is, according to data, positive ($\gamma_1 > 1$ and $\overline{X}_1^*/\overline{X}_1 \geq 1$, see Tab. 4.3), therefore, for a positive affinity A_2 the denominator has to be positive. This means that there is an upperbound γ_1^{max}, corresponding to a singularity in Eq. (B.8), for the increase in PI phosphorylation rate during stimulation. This upper bound is a function of the concentration ratio in stimulated and unstimulated state, that is

$$\gamma_1 < \gamma_1^{max} = \frac{\overline{X}_2 \overline{X}_1^*}{\overline{X}_2^* \overline{X}_1} \tag{B.9}$$

According to the experimental data in Tab. 4.3 $\gamma_1^{max} = 4 - 5$.

Similarly, one derives an equation for B_3, the affinity of the PIP 5-kinase for its product PIP$_2$, which yields when $B_3 \rightarrow \infty$ a maximal fold increase in PIP phosphorylation during stimulation

$$\gamma_2^{max} = \frac{\overline{X}_3 \overline{X}_2^*}{\overline{X}_3^* \overline{X}_2}. \tag{B.10}$$

As PIP and PIP$_2$ densities decrease of about the same amount $\gamma_2^{max} \approx 1$.

In steady state the phosphorylation of PI and PIP must have equal rates ($v_1 = v_2$). Therefore, the fold increase in IP$_3$ production flux, γ^{max}, obtained after activating PLC is limited by the slowest enzyme, that is $\gamma^{max} = \min(\gamma_1^{max}, \gamma_2^{max})$. As $\gamma_2^{max} \approx 1$, product inhibition alone does not explain the observed sustained increase in [IP$_3$] during stimulation.

Appendix C

Steady state, holocomplex, and unspecific binding in NER

C.1 Binding of repair proteins to undamaged sites

Factor F_i reversibly associates to an undamaged site u_i and forms a complex U_i according to the reaction $\mathrm{u}_i + \mathrm{F}_i \leftrightarrow \mathrm{U}_i$. The balance equations for the concentrations of U_i and the free form of the factors are

$$\frac{dU_i}{dt} = k_{+u_i}(T_{u_i} - U_i)F_i - k_{-u_i}U_i \tag{C.1}$$

and

$$\frac{dF_i}{dt} = k_R S_n - \tilde{k}_i F_i S_{i-1} + k_{-i} S_i - \frac{dU_i}{dt}, \tag{C.2}$$

respectively. k_{+u_i} and k_{-u_i} are the binding and dissociation rate constants of F_i to the undamaged site u_i, respectively, and $T_{u_i} = U_i + u_i$ is the total concentration of undamaged sites. The conservation relation (7.6) changes to

$$T_i = F_i + I_i + U_i. \tag{C.3}$$

If the binding of factors to undamaged sites is fast compared to other processes, one can apply a quasi-steady state approximation ($dU_i/dt \approx 0$) to obtain $U_i = T_{u_i}F_i/(K_{u_i} + F_i)$ for the concentration of the complexes, where $K_{u_i} = k_{-u_i}/k_{+u_i}$. For low affinity binding sites ($K_{u_i} \gg F_i$) one has

$$U_i \approx \frac{T_{u_i}}{K_{u_i}} F_i. \tag{C.4}$$

With this formula and after addition of Eq. (C.1) and (C.2) one yields

$$\frac{dF_i}{dt} = (k_R S_n - \tilde{k}_i F_i S_{i-1} + k_{-i} S_i)/\beta_i,$$

where $\beta_i = 1 + T_{u_i}/K_{u_i}$ is referred to as the buffering coefficient.

Equations (C.3) and (C.4) give

$$F_i = (T_i - I_i)/\beta_i, \tag{C.5}$$

indicating that in the absence of damage ($I_i = 0$) the fraction of repair factor transiently immobilized to non-damaged sites is $1/\beta_i$. With the latter formula, the model which considers non-damaged binding sites reads

$$\frac{dS_0}{dt} = V_{dam} - k_1(T_1 - I_1)S_0 + k_{-1}S_1 \tag{C.6}$$

$$\frac{dS_i}{dt} = k_i(T_i - I_i)S_{i-1} - k_{-i}S_i - k_{i+1}(T_{i+1} - I_{i+1})S_i + k_{-(i+1)}S_{i+1} \tag{C.7}$$

$$\frac{dS_n}{dt} = k_n(T_n - I_n)S_{n-1} - k_{-n}S_n - k_R S_n, \tag{C.8}$$

$i = 1, \cdots, n-1$. The buffering coefficients are included in the effective binding rate constants $k_i = \tilde{k}_i/\beta_i$. Equation (C.7) corresponds to Eq. (7.9).

C.2 Quasi steady state repair rate

A stationary state in the intermediary complex concentrations is reached, when the DNA is damaged constantly at a rate V_{dam} lower than the maximal repair rate V_{max}. One derives from Eqs. (C.6)–(C.8)

$$S_i = \frac{V_{dam} + k_{-(i+1)}S_{i+1}}{k_{i+1}(T_{i+1} - I_{i+1})} \text{ and } S_n = \frac{V_{dam}}{k_R}, \tag{C.9}$$

where the concentration of the immobilized ith factor is defined by $I_i = \sum_{j=i}^{n} S_j$. With Eq. (C.9) one calculates recursively, starting from $i = n$, the steady state concentrations as a function of the damage-induction rate V_{dam}.

Plotting the steady state concentration of DNA lesions D_T against V_{dam} results in a hyperbolic curve (Fig. C.1A). Obviously, a steady state can only be established if V_{dam} is lower than the maximal repair rate V_{max}. When V_{dam} approaches V_{max} the concentration of damaged sites dramatically increases. For $V_{dam} > V_{max}$ the system can no longer cope, resulting in a continuous accumulation of lesions. At steady state the damage induction rate equals the repair rate, one can therefore plot the steady state repair rate V_R as function of the total damage concentration (Fig. C.1B, black solid line). Although in most experimental NER studies all DNA damage is introduced during a short time interval only, rather than continuously, the time dependent repair rate does

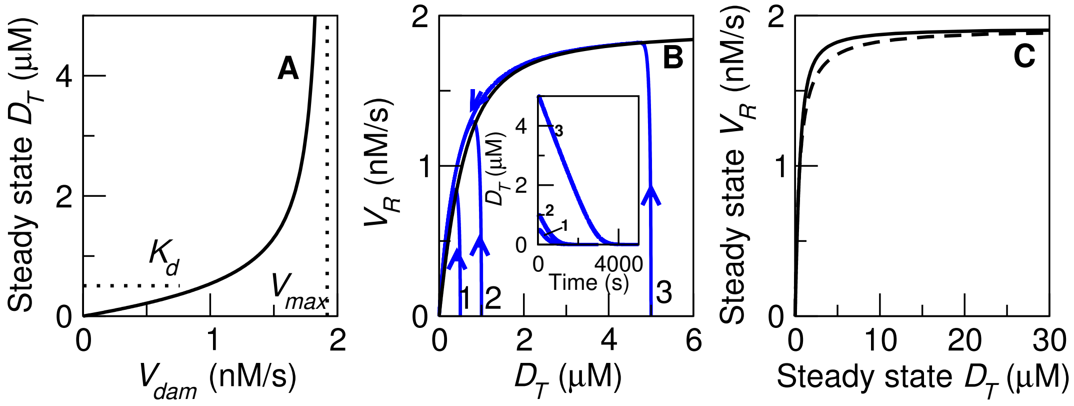

Figure C.1: (A) Total damage steady state concentration D_T as a function of the damage induction rate V_{dam}. At steady state the damaging rate equals the repair rate $V_{dam} = V_R$. V_{max} and K_d are the maximal repair rate and half-saturation constant (total damage for which $V_{dam} = V_{max}/2$) of the repair process, respectively. Both quantities characterize repair efficiency. (B) Time dependent repair rate V_R as a function of the damage concentration D_T. Initial damage concentrations to the whole nucleus: 0.5 μM, 1 μM, and 5 μM (blue lines 1, 2 and 3, respectively). Arrows indicate progression in time. Within a large time interval the repair rate is well represented by its steady state value (black line). Differences are observed during the comparatively fast binding phase, which is characterized by a nearly constant D_T and a strong increase in repair rate V_R. Inset: total damage as a function of time. (C) Exact steady state repair rate and approximation Eq. (C.10) (solid and dashed line, respectively). Parameter set 1 of Tab. 7.2 has been used.

not strongly deviates from its steady state value (Fig. C.1B, blue solid lines). This is true during both the repair phase, where the repair rate is nearly constant and the number of lesions decreases linearly, and during the release phase, in which the repair rate drops sharply. Thus, the steady state relationship can be employed as a measure for repair efficiency.

An approximation for the steady-state repair rate curve is

$$V_R \approx V_{max} \frac{D_T}{D_T + K_d} \tag{C.10}$$

where K_d is the damage concentration for which $V_R = V_{max}/2$. This approximated curve shows good agreement with the exact solution (Fig. C.1C, solid and dashed line, respectively).

C.3 Holocomplex concentration

The repair factors interact with each other to form a holocomplex. A simple expression for the steady state is obtained when equal total concentrations ($T_i = T$), and equal dissociation constants K_h between factors are assumed. Then the concentrations of free diffusing complexes that contain the same number of factors are identical. One derives following conservation relation

$$T = I + \sum_{i=0}^{n-1} \binom{n}{i} f_{i+1}. \tag{C.11}$$

The concentration of a free diffusing complex containing i factors is denoted by f_i. Thus the holocomplex concentration is $H = f_n$. I is the concentration of the holocomplex bound to the damaged site and $\binom{n}{i}$ is the binomial coefficient. In the absence of damage ($I = 0$) and in steady state, one derives

$$f_i = \frac{f_1^i}{K_h^{i-1}}. \tag{C.12}$$

Using the above formula Eq. (C.11) simplifies to

$$T = f_1 \left(1 + \frac{f_1}{K_h}\right)^{n-1}. \tag{C.13}$$

From Eq. (C.12) one has $f_1 = \sqrt[n]{f_n/K_h^{n-1}}$ which together with Eq. (C.13) gives an implicit expression for the holocomplex concentration $H = f_n$

$$\left(\sqrt[n]{\frac{K_h}{T}} + \sqrt[n]{\frac{H}{T}}\right)^{n-1} \sqrt[n]{\frac{H}{T}} = 1 \tag{C.14}$$

This formula has been used to calculate the holocomplex concentration and hence the repair time by the holocomplex.

C.4 Maximal repair rate

C.4.1 Condition for maximal repair rate

Theorem C.4.1 *The repair system defined by the set of differential equations* (C.6)–(C.8)*, reaches its maximal repair rate when the first factor is completely bound to the damage*

$$V_R = V_{max} \text{ for } T_1 = I_1. \tag{C.15}$$

Proof Theorem C.4.1 is analogous to enzymatic reactions where the maximal reaction rate is reached when all enzyme molecules are bound to substrate. By taking the derivative of S_i (Eq. (C.9)) with respect to V_{dam} one easily shows that the immobilized concentrations I_i of the factors increase monotonously with V_{dam}. However, for any factor an upper limit is given by

$$I_i \leq T_i. \tag{C.16}$$

For calculating the maximal repair rate one needs to identify the value of V_{dam} at which one of the above conditions is violated. From Eq. (C.9) one obtains

$$I_i = \frac{V_{dam}}{k_R} + \sum_{j=i+1}^{n} \frac{V_{dam} + k_{-j} S_j}{k_j (T_j - I_j)}.$$

Clearly, for any $j > i$ one obtains $I_i \to \infty$ for $I_j \to T_j$, contradicting condition (C.16). Therefore, when increasing V_{dam}, the condition for the first factor, $I_1 \leq T_1$, is violated first. The maximal repair rate is reached accordingly when condition (C.15) is fulfilled. One yields a polynomial of order 2^{n-1} for V_{max}. Only the smallest positive real root is of interest, since all other solutions would violate condition (C.16). By searching the roots of the polynomial numerically one obtains the maximal repair rate V_{max}. ▮

C.4.2 Formula for the maximal repair rate

I was able to derive a formula for the maximal repair rate in the case of equal total concentrations and when the unbinding reactions are slow ($k_{-i} \approx 0$). First some algebraic transformations of the steady state equations need to be done. From Eq. (C.9) one obtains $T - I_n = T - V/k_R = V/(k_n S_{n-1})$ which gives a relation between S_{n-2} and S_{n-1}

$$S_{n-2} = S_{n-1} \frac{k_n}{k_{n-1}} \frac{V}{V - k_n S_{n-1}^2}.$$

For clarity sake, here and in all subsequent formulas, the damaging rate V_{dam} is denoted by V. Similarly, from Eq. (C.9) one obtains $T - I_{i+2} = V/(k_{i+2} S_{i+1})$ which gives

$$S_i = S_{i+1} \frac{k_{i+2}}{k_{i+1}} \frac{V}{V - k_{i+2} S_{i+1}^2} \quad \text{for } i \leq n-2 \tag{C.17}$$

Lemma C.4.2 *The concentration of the intermediary complexes and the free damage can be expressed by* ($i \leq n-2$)

$$S_i = S_{i+1} \frac{k_{i+2}}{k_{i+1}} \frac{C_{i+1}}{C_{i+1} - V_{i+1}}, \tag{C.18}$$

where the coefficients C_i *and* V_i *are obtained recursively from*

$$C_i = k_{i+1}(C_{i+1} - V_{i+1})^2 \text{ and } V_i = k_{i+2}V_{i+1}C_{i+1}, \tag{C.19}$$

with $C_{n-1} = k_n(T - V/k_R)^2$ *and* $V_{n-1} = V$. *These coefficients satisfy*

$$V - k_{i+2}S_{i+1}^2 = V\frac{C_{i+1} - V_{i+1}}{C_{i+1}} \tag{C.20}$$

Proof Lemma C.4.2 is proven using complete induction. For $i = n-2$ it is easy to see that

$$V - k_n S_{n-1}^2 = V - \frac{V}{k_n(T - V/k_R)^2} = V\frac{k_n(T - V/k_R)^2 - V}{k_n(T - V/k_R)^2} \tag{C.21}$$

which yields

$$S_{n-2} = S_{n-1}\frac{k_n}{k_{n-1}}\frac{C_{n-1}}{C_{n-1} - V_{n-1}}$$

This relation together with Eq. (C.21) gives the next denominator of Eq. (C.17) for $i = n-3$

$$\begin{aligned} V - k_{n-1}S_{n-2}^2 &= V - V\frac{k_n V_{n-1}C_{n-1}}{k_{n-1}(C_{n-1} - V_{n-1})^2} \\ &= V\frac{k_{n-1}(C_{n-1} - V_{n-1})^2 - k_n V_{n-1}C_{n-1}}{k_{n-1}(C_{n-1} - V_{n-1})^2} \\ &= V\frac{C_{n-2} - V_{n-2}}{C_{n-2}} \end{aligned}$$

with C_{n-2} and V_{n-2} given by Eq. (C.19). Using Eq. C.17 one derives that, for $i = n-3$, Eqs. (C.18)–(C.20) hold

$$S_{n-3} = S_{n-2}\frac{k_{n-1}}{k_{n-2}}\frac{C_{n-2}}{C_{n-2} - V_{n-2}}.$$

Assuming that the lemma is valid for $i \geq j$, with $j < n-2$, it is sufficient to prove that its validity for $i = j-1$. From (C.20) one has $S_{j+1} = \sqrt{VV_{j+1}/(k_{j+2}C_{j+1})}$ so that

$$\begin{aligned} V - k_{j+1}S_j^2 &= V - V\frac{k_{j+2}V_{j+1}C_{j+1}}{k_{j+1}(C_{j+1} - V_{j+1})^2} \\ &= V\frac{k_{j+2}(C_{j+1} - V_{j+1})^2 - k_{j+2}V_{j+1}C_{j+1}}{k_{j+1}(C_{j+1} - V_{j+1})^2} \\ &= V\frac{C_j - V_j}{C_j}. \end{aligned}$$

This gives

$$S_{j-1} = S_j\frac{k_{j+1}}{k_j}\frac{C_j}{C_j - V_j}$$

Therefore, Lemma C.4.2 is true for $i \leq j-1$ and so for $i = 0, \cdots, n-2$. ∎

Theorem C.4.3 *For a system defined by Eq.* (C.9)*, and assuming equal total factor concentrations (*$T_i = T, \forall i$*) and negligible dissociation rate constants (*$k_{-i} \approx 0$*), the maximal repair rate where* $I_1 = T$ *is given by*

$$V_{max} = \frac{k_R}{2\lambda_{n-1}k_n}\left(2\lambda_{n-1}k_nT + k_R - \sqrt{4\lambda_{n-1}k_Rk_nT + k_R^2}\right) \tag{C.22}$$

where the coefficient λ_{n-1} *is obtained recursively from*

$$\lambda_i = \frac{2\lambda_{i-1}k_i + k_{i+1} - \sqrt{4\lambda_{i-1}k_ik_{i+1} + k_{i+1}^2}}{2\lambda_{i-1}k_i} \tag{C.23}$$

for $i = 2, \cdots, n-1$ *with* $\lambda_1 = 1$*.*

Proof According to Lemma C.4.2 (Eq. (C.18)), the free damage is given by

$$S_0 = S_1\frac{k_2}{k_1}\frac{C_1}{C_1 - V_1}. \tag{C.24}$$

The condition for the maximal repair rate is when $I_1 = T$ which corresponds to a singularity in the formula for S_0 (Eq. (C.9)). Using the new formulation (C.24), the singularity $T = I_1$ is equivalent to $C_1 = V_1$. With $V_1 = k_3V_2C_2$ and $C_1 = k_2(C_2 - V_2)^2$ (Eq. (C.19)). The condition $C_1 = V_1$ gives a quadratic equation in V_2, which roots are

$$V_2 = C_2\frac{k_3 + 2k_2 \pm \sqrt{4k_2k_3 + k_3^2}}{2k_2}.$$

C_2 and V_2 can be replaced by V_3 and C_3, which yields again a quadratic equation in V_3. One finds following recursive relation

$$V_i = C_iL_i, \text{ for } i = 1, \cdots, n-1$$

with the coefficient L_i given by

$$L_i = \frac{2L_{i-1}k_i + k_{i+1} + \pm\sqrt{4L_{i-1}k_ik_{i+1} + k_{i+1}^2}}{2L_{i-1}k_i}. \tag{C.25}$$

The last equation for $i = n-1$ gives a quadratic expression in V, which roots are

$$V = \frac{k_R}{2L_{n-1}k_n}\left(2L_{n-1}k_nT + k_R \pm \sqrt{4L_{n-1}k_Rk_nT + k_R^2}\right)$$

This equation, together with (C.25), gives all the 2^{n-1} roots of $T = I_1$ (as we have 2^{n-2} different L_{n-1}). By taking the smallest of these roots, one obtains V_{max} as given by Eq. (C.22). ▮

C.4.3 Consequences of the theorem

The dependency of V_{max} on T given by Eq. (C.22) can be checked experimentally by measuring V_{max} at different factor concentrations (see Fig. 8.2C). In particular, these experiments allow to distinguish which processes are limiting for repair.

I) If repair is limited by the binding of the factors, the maximal repair rate has a second order dependency on the total factor concentrations

$$V_{max} \approx \lambda_{n-1} k_n T^2. \tag{C.26}$$

The above formula is valid, when the total concentrations of the factors are small and/or the binding rate constants are low compared to the repair rate constant ($k_i \ll k_R$). Then $4k_n T \lambda_{n-1}/k_R \ll 1$ and the root of Eq. (C.22) is given by a second-order Taylor series approximation

$$\sqrt{4k_R k_n T \lambda_{n-1} + k_R^2} \approx k_R + 2k_n T \lambda_{n-1} - 2\frac{k_n^2 T^2 \lambda_{n-1}^2}{k_R}.$$

Using this Equation one obtains (C.26).

II) Conversely, if repair is limited by the repair step (i.e $k_i \gg k_R$ and/or high factor concentrations) one can approximate the numerator of Eq. (C.22) with $2\lambda_{n-1} k_R k_n T$ yielding

$$V_{max} \approx k_R T, \tag{C.27}$$

which is first order in T.

Appendix D

Metrics of NER

In the introduction, I described how local damage experiments with fluorescent-protein tagged repair factors are performed and data collected (Chapter 6, Section 6.2). In this appendix I will first define, for comparison of experimental and simulated data, their counterparts in the model. Then, I will present measures for the time needed to recruit the repair factor to the damaged sites, the *accumulation time*, and the time spent in a repair complex, the *residence time*. Together with the time needed to remove the damage, the *repair time*, one has a "metric" system to characterize kinetics and efficiency of NER. If the system is simplified in the case of low and saturating damage, these three characteristic times can be calculated analytically. The obtained formulas are used to deduce general properties of NER.

D.1 Mapping of experimental data

D.1.1 Fluorescence

Fluorescence emitted by a repair factor is directly proportional to its concentration. In experiment, fluorescence is monitored in the local damaged area $Fl_{1,i}$ and in a control region $Fl_{2,i}$. The corresponding model definitions are given in Fig. D.1.

The accumulation curve of the ith factor in the local damaged area, i.e. the fraction of factors involved in repair as obtained from experiments, is defined by

$$Acc_i(t) = \frac{[Fl_{1,i}(t)/V_d - Fl_{2,i}(t)/V_c]V_d}{T_i V_{nuc}}. \tag{D.1}$$

Where V_d, V_c and V_{nuc} are the volumes of the damaged region, the control region, and the nucleus, respectively (Fig. D.1). The life time of a protein in the repair complex

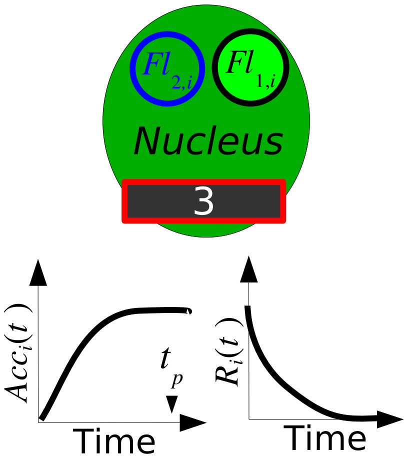

$$
\begin{aligned}
Fl_{1,i}(t) &= \oint_{V_d} [I_i(\vec{x},t) + F_i(\vec{x},t) + U_i(\vec{x},t)]dV \\
&= \oint_{V_d} [I_i(\vec{x},t) + F_i(\vec{x},t)\beta_i]dV \\
Fl_{2,i}(t) &= \oint_{V_c} F_i(\vec{x},t)\beta_i dV
\end{aligned}
$$

Figure D.1: Fluorescence is monitored in the local damaged area ($Fl_{1,i}(t)$) and in a control region ($Fl_{2,i}(t)$). In the model fluorescence is the sum of factors bound to damaged and undamaged DNA, and freely diffusing factors. During FLIP experiments fluorescence is bleached in region 3. V_d, V_c: volume of damaged and control area, respectively; $\vec{x} = (x, y, z)$: spatial coordinate.

is measured using the FLIP technique (Chapter 6, section 6.2). In such an experiment fluorescence is continuously bleached in a region opposite to the local damage (region 3 in Fig. D.1). In the model the residence curve corresponds to

$$R_i(t) = Fl_{1,i}(t)/Fl_{1,i}(0). \tag{D.2}$$

The accumulation and residence curves can be computed for a particular choice of geometry after solving the corresponding system of partial differential equations. This rather time consuming procedure has been used to fit the model parameters to the experimental data (Appendix E).

D.1.2 Accumulation and residence time

For comparing the accumulation and residence curves of different repair factors, it is useful to summarize their course using characteristic times. I define the mean accumulation time of the ith factor

$$\alpha_i = \frac{\int_0^{t_p} [Acc_i(t_p) - Acc_i(t)]dt}{Acc_i(t_p) - Acc_i(0)}, \tag{D.3}$$

and its residence time

$$\rho_i = \frac{\int_0^{\infty} R_i(t)dt}{R_i(0)}. \tag{D.4}$$

Both quantities can be estimated from data. The time t_p is when maximal accumulation, i.e. the plateau, is reached.

Further simplification is obtained if the factors are homogeneously distributed so that $F_i(\vec{x},t) = F_i(t)$ and $I_i(\vec{x},t) = I_i(t)$. This is justified by the fact that diffusion is fast compared to the time needed for a repair event. Measured residence and accumulation times are 2–5 minutes, the diffusion coefficients are around 5 μm^2/s (see Chapter 6). Thus, it takes about 10 sec to diffuse through a typical nucleus of 10 μm diameter. In FLIP experiments, one can assume that fluorescence of the free factors will be completely bleached at the beginning of the experiment. Therefore, during FLIP experiments, solely the unbinding of the protein from the repair complex is monitored, its binding to the DNA cannot be observed as the free factors do not fluoresce. This corresponds to $F_i(t > 0) = 0$. Under these two assumptions, the accumulation and residence time curves read

$$Acc_i(t) = \frac{I_i(t)V_d}{T_i V_{nuc}} \tag{D.5}$$

$$R_i(t) = \frac{I_i(t)}{I_i(0)} \tag{D.6}$$

The time evolution of $I_i(t)$ is described by a system of ODE's instead of PDE's. The solution is quickly obtained by numerical integration. Application of formula (D.5) and (D.6) gives the accumulation and residence time of each factor. In the following sections, I will derive analytical expressions for the characteristic times when the initial damage is low or saturating.

D.2 Non-saturating damage

D.2.1 Definitions

The central idea is that the free factor concentrations do not change significantly during the measurements ($F_i \approx const$). This is indeed the case for residence time measurements, which are performed after a plateau in the immobilized fraction has been reached. Additionally, for most of the factors studied with local damage experiments, the fraction immobilized is around 10% of the total concentration so that one can assume $F_i \approx T_i$. Together with the assumed homogeneous distribution (see above), the system is described by a set of linear ordinary differential equations

$$\frac{d\mathbf{S}(t)}{dt} = \mathbf{M}\mathbf{S}(t). \tag{D.7}$$

The vector $\mathbf{S}(t)$ contains the free damage and intermediary complex concentrations. The matrix $\mathbf{M}$ characterizes the stoichiometry and kinetics of NER. I introduce the matrix $\mathbf{W}$, which computes, from the concentrations of the intermediary complexes, the concentration of the immobile factors

$$(I_1, \cdots, I_n)^T = \mathbf{W}\mathbf{S}_0.$$

The superscript T stands for the transposed. $\mathbf{S}_0$ is a subvector of $\mathbf{S}$ without the free damage.

For a pathway with sequential binding and simultaneous release of the factors one has

$$\mathbf{S} = (S_0, \cdots, S_n)^T \text{ and } \mathbf{S}_0 = (S_1, \cdots, S_n)^T.$$

The $(n-1) \times (n-1)$ matrix $\mathbf{W}$ reads

$$\mathbf{W} = \begin{pmatrix} 1 & 0 & \cdots & 0 \\ 1 & 1 & \ddots & \vdots \\ \vdots & \vdots & \ddots & 0 \\ 1 & \cdots & 1 & 1 \end{pmatrix},$$

the $n \times n$ system matrix $\mathbf{M}$ is

$$\mathbf{M} = \begin{pmatrix} -\kappa_1 & k_{-1} & 0 & \cdots & 0 \\ \kappa_1 & -\kappa_2 - k_{-1} & k_{-2} & \cdots & 0 \\ 0 & \kappa_2 & -\kappa_3 - k_{-2} & \cdots & 0 \\ \vdots & \vdots & \vdots & \ddots & \vdots \\ 0 & \cdots & & \kappa_n & -\kappa_{n+1} - k_{-n} \end{pmatrix} \tag{D.8}$$

For clarity sake, I introduced $\kappa_i = k_i T_i$ for $i \leq n$ and $\kappa_{n+1} = k_R$.

D.2.2 Repair time

General definition

The repair time is defined by

$$\tau_R = \frac{\int_0^\infty D_T(t)dt}{D_T(0)} = \frac{\sum_{i=0}^n \int_0^\infty S_i(t)dt}{\sum_{i=0}^n S_i(0)}.$$

The integrals over time are given by

$$\int_0^\infty \mathbf{S}(t)dt = -\mathbf{M}^{-1}\mathbf{S}(0).$$

Where $\mathbf{M}^{-1}$ is the inverse of $\mathbf{M}$. The initial condition is $\mathbf{S}(0) = (D_T(0), 0, \cdots, 0)^T$. This leads to a definition of the repair time under non-saturating conditions

$$\tau_R = \frac{-[\mathbf{M}^{-1}\mathbf{S}(0)]^T\mathbf{1}}{\mathbf{S}(0)^T\mathbf{1}}. \tag{D.9}$$

Where $\mathbf{1} = (1, \cdots, 1)^T$ is the unit vector.

This formula for the repair time can be applied to any pathway structure (different binding schemes, and kinetics) characterized by different system matrices $\mathbf{M}$ and $\mathbf{W}$. Therefore, this approach is suited to fast compute the efficiency of pathway alternatives. The expressions derived for the sequential pathway are given in the main text (Section 8.1).

D.2.3 Accumulation time

General definition

If the time for accumulation of the factors is short compared to the time needed to remove the damage, so that $S_0(t) \approx const$, the kinetics of accumulation are described by

$$\frac{d\mathbf{S}_0(t)}{dt} = \mathbf{M}_0\mathbf{S}_0(t) + \mathbf{b}_0.$$

Where $\mathbf{M}_0$ is the $(n-1) \times (n-1)$ submatrix of $\mathbf{M}$ without the first column and row, $\mathbf{S}_0$ contains the concentration of the intermediary complexes only. The inhomogeneity vector $\mathbf{b}_0$ of size $n-1$ gives the flux of the intermediary complexes resulting from the binding of free factors to the damage.

As the free damage is assumed constant, the integration to calculate the mean accumulation times (Eq. (D.5)) can be carried till $t_b = \infty$

$$\alpha_i = \frac{\int_0^\infty [I_i(\infty) - I_i(t)]\, dt}{I_i(\infty) - I_i(0)}.$$

The steady state is $\mathbf{S}_0(\infty) = -\mathbf{M}_0^{-1}\mathbf{b}_0$ and $(I_1(\infty), \cdots, I_n(\infty))^T = -\mathbf{W}\mathbf{M}_0^{-1}\mathbf{b}_0$. The integrals of the intermediary complexes are

$$\int_0^\infty [\mathbf{S}_0(\infty) - \mathbf{S}_0(t)]dt = \mathbf{M}_0^{-2}\mathbf{b}_0,$$

where $\mathbf{M}_0^{-2}$ is the product of the inverse $\mathbf{M}_0^{-1}$. The accumulation times read in a compact notation

$$(\alpha_1, \cdots, \alpha_n)^T = \mathbf{D}^{-1}\mathbf{W}\mathbf{M}_0^{-2}\mathbf{b}_0. \tag{D.10}$$

D is the diagonal matrix containing the steady state immobilized factor concentrations

$$\mathbf{D} = \begin{pmatrix} I_1(\infty) & 0 & \cdots & 0 \\ 0 & I_2(\infty) & \ddots & \vdots \\ \vdots & \vdots & \ddots & 0 \\ 0 & \cdots & 0 & I_n(\infty) \end{pmatrix}.$$

Using this general definition, the accumulation times obtained from pathways alternatives can easily be computed.

Application to the sequential pathway

For a sequential binding and simultaneous release of repair factor one has $\mathbf{b}_0 = (k_1 S_0, 0, \cdots, 0)$ and $\mathbf{S}_0 = (S_1, \cdots, S_n)^T$. When binding is irreversible ($k_{-i} \approx 0$) the accumulation time reads

$$\alpha_i = \frac{\displaystyle\sum_{j=i+1}^{n+1} \frac{1}{\kappa_j} \left(\sum_{l=2}^{j} \frac{1}{\kappa_l} \right)}{\displaystyle\sum_{j=i+1}^{n+1} \frac{1}{\kappa_j}}. \tag{D.11}$$

The difference in accumulation time between two successive factors (the ith and $(i+1)$th) is always positive for any i

$$\alpha_{i+1} - \alpha_i = \frac{\displaystyle\sum_{j=i+2}^{n+1} \frac{1}{\kappa_j} \left(\sum_{l=i+2}^{j} \frac{1}{\kappa_l} \right)}{\kappa_{i+1} \left(\displaystyle\frac{1}{\kappa_{i+1}} + \sum_{j=i+2}^{n+1} \frac{1}{\kappa_j} \right) \left(\displaystyle\sum_{j=i+2}^{n+1} \frac{1}{\kappa_j} \right)} > 0.$$

This shows that early binding factors accumulate faster than late binding factors. The same is true when binding of repair factors to the damaged DNA is reversible ($k_{-i} > 0$). In this case the expressions become very lengthy and I was not able to derive a compact notation as for irreversible binding. However, the hierarchy in accumulation times appears to be conserved. Using symbolic computation as provided by programs like *Mathematica* for solving Eq. D.10, one can prove that

$$\alpha_j > \alpha_i \text{ for } j > i. \tag{D.12}$$

This appears to be true at least up to 100 repair factors ($n = 100$).

D.2.4 Residence time

General definition

During FLIP experiments with a GFP-tagged ith factor, $F_i(t > 0) \approx 0$. The loss in fluorescence in the local damage is described by

$$\frac{d\mathbf{S}_i}{dt} = \mathbf{M}_i \mathbf{S}_i. \tag{D.13}$$

$\mathbf{M}_i$ is a submatrix of $\mathbf{M}$ which describes the reactions of the intermediary complexes that contain the ith factor, but not the binding reactions of the ith factor. The vector $\mathbf{S}_i$ is a subvector of $\mathbf{S}$, where only complexes which contain the ith factor are included. At $t = 0$ bleaching is initiated, the initial condition $\mathbf{S}_i(0)$ is set by the intermediary complex concentrations in the plateau phase after damage induction. Using Eq. (D.13) one obtains the general expression

$$\rho_i = -\frac{[\mathbf{M}_i^{-1}\mathbf{S}_i(0)]^T \mathbf{1}}{\mathbf{S}_i(0)^T \mathbf{1}}. \tag{D.14}$$

The $\mathbf{1}$ is again the unit vector. This definition, like the former ones, can be applied to any putative NER pathway structure.

Application to the sequential pathway

For sequential binding and simultaneous release of the repair factors $\mathbf{S}_i = (S_i, \cdots, S_n)^T$, the matrix $\mathbf{M}_i$ is a $(n-i) \times (n-i)$ submatrix of $\mathbf{M}$ where the rows and columns from 1 to i are omitted, for example

$$\mathbf{M}_2 = \begin{pmatrix} -\kappa_3 - k_{-2} & \cdots & 0 \\ \vdots & \ddots & \vdots \\ \cdots & \kappa_n & -\kappa_{n+1} - k_{-n} \end{pmatrix}. \tag{D.15}$$

The initial condition is set by the steady state for $S_0(t) = const.$ That is $\mathbf{S}_1(0) = -\mathbf{M}_0^{-1}\mathbf{b}_0$ with $\mathbf{b}_0 = (k_1 S_0, \cdots, 0)$. The residence time reads

$$\rho_i = \frac{\sum_{j=i+1}^{n+1} \frac{1}{\kappa_j} \left(\sum_{l=i+1}^{j} \frac{1}{\kappa_l} \right)}{\sum_{j=i+1}^{n+1} \frac{1}{\kappa_j}}. \tag{D.16}$$

From this formula, one can prove that early binding factors reside longer in the repair complex than late binding factors

$$\rho_j < \rho_i \text{ for } j > i. \tag{D.17}$$

Furthermore, one recognizes that the residence time of the first factor equals its accumulation time (Eq. (D.11)).

When the unbinding reactions are included ($k_{-i} > 0$), I was not able to derive a closed expression for the residence times. Nevertheless, a few general conclusions can be formulated. According to Eq. (D.10) and (D.14) the residence time of the first factor equals its accumulation time, $\alpha_1 = \rho_1$, when $\mathbf{S}_1(0) = -\mathbf{M}_0^{-1}\mathbf{b}_0$, that is the plateau concentration reached at the end of the accumulation phase equals the initial concentration for the FLIP experiment. When factors bind equally well at their respective substrate ($\kappa_i = \kappa$ and $k_{-i} = k_-$, $i \leq n$), one can show, using symbolic computation, that early binding factors reside longer in the repair complex than late binding factors, that is Eq. (D.17) holds (formula (D.14) has been computed with *Mathematica* till $n = 100$). The hierarchy in residence times as given by Eq. (D.17) can break when the binding properties of the factors to the damaged sites differ. This is already observed for the last two factors where the repair times read

$$\begin{aligned}\rho_n &= \frac{1}{\kappa_{n+1} + k_{-n}} \\ \rho_{n-1} &= \frac{\kappa_n^2 + [k_{-n} + \kappa_{n+1}]^2 + \kappa_n[\kappa_{n+1} + 2k_{-n} + k_{-(n-1)}]}{[\kappa_n + \kappa_{n+1} + k_{-n}][\kappa_n\kappa_{n+1} + k_{-(n-1)}(\kappa_n + \kappa_{n+1})]}.\end{aligned}$$

For example when the first intermediary complex of the $n-1$ factor is unstable (k_{n-1} is large) then $\rho_{n-1} \approx \rho_n\kappa_n/(\kappa_n + \kappa_{n+1} + k_{-n}) < \rho_n$.

D.3 Saturating damage

D.3.1 Repair time

As shown in Appendix C.2, the time dependent repair rate is well characterized by its steady state value. Using Eq. (C.10) the approximation for the time dependent changes of the total damage reads

$$\frac{dD_T}{dt} \approx -V_{max}\frac{D_T}{D_T + K_d}$$

Separation of variables

$$D_T dt = -\frac{D_T + K_d}{V_{max}} dD_T,$$

and integration leads to an expression for the repair time under saturating conditions

$$\tau_R = \frac{1}{D_T(0)}\int_0^\infty D_T(t)dt \approx \frac{1}{2}\frac{D_T(0)}{V_{max}} + \frac{K_d}{V_{max}} \tag{D.18}$$

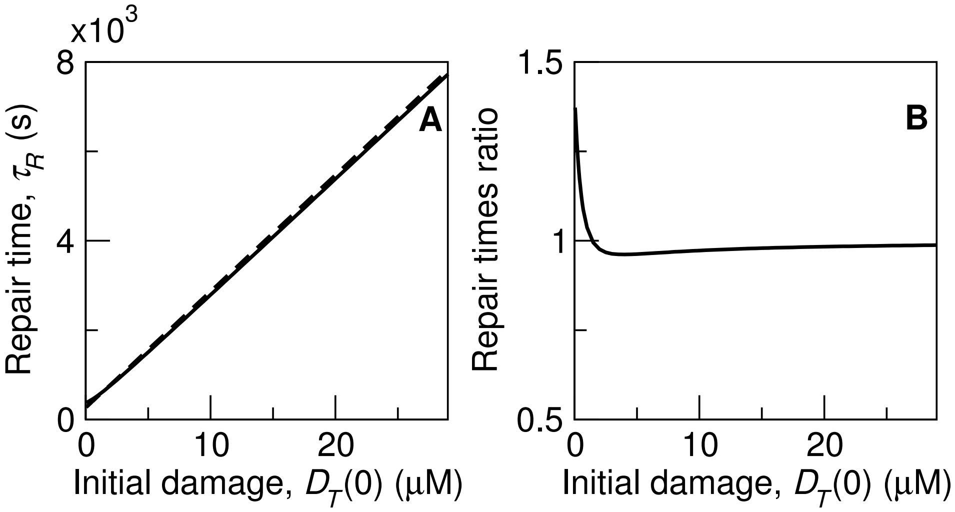

Figure D.2: (A) Solid line: exact repair time calculated numerically by solving the system of differential equations (Eqs. (C.6)–(C.8)) and Eq. (8.1) for different initial damage concentrations. Dashed line: approximation of the repair time obtained from Eq. (D.18). (B) Ratio of the numerically calculated repair time and the approximated value as a function of initial damage. For large initial damages this ratio approaches one. Parameters from set 1, Tab. 7.2.

As shown in Fig. D.2A, this formula well approximates the exact repair time (dashed and solid line, respectively). The two values become practically identical for saturating initial damages (Fig. D.2B).

D.3.2 Accumulation time

At very high damage concentrations, the first factor is nearly completely immobilized to the damage for a long time period (see (C.4)). If its diffusion is fast compared to the binding of the subsequent factors, the initial condition can be approximated by $(S_1(0), \cdots, S_n(0))^T \approx (T_1, \cdots, 0)^T$. Over time, the first factor redistributes between the intermediary complexes. In the sequential pathway following conservation relation holds

$$S_1(t) = T_1 - \sum_{i=2}^{n} S_i(t). \tag{D.19}$$

Assuming constant free factor concentrations the kinetics of the intermediary complexes $\mathbf{S}_2 = (S_2, \cdots, S_n)^T$ are described by a set of linear ODE's

$$\frac{d\mathbf{S}_2}{dt} = \mathbf{M}_2\mathbf{S}_2 + \begin{pmatrix} \kappa_2(T_1 - \sum_{i=2}^{n} S_i) \\ \vdots \\ 0 \end{pmatrix} \tag{D.20}$$

Where $\mathbf{M}_2$ has been defined in (D.15). The concentration of the first intermediary complex is obtained from (D.19).

Due to the high concentration of damaged sites the first factor binds to the DNA as soon as it enters the damaged area. Therefore, its accumulation time is solely determined by the time it takes to diffuse from the undamaged to the damaged area (a process which I do not further consider in this section). To calculate the accumulation time of the other repair factors we can apply the same method as before (section D.2.3). For the sequential accumulation and simultaneous release of the factors the formulas are cumbersome and I forbear of listing them here. Using symbolic computation, one can prove that the repair factors accumulate faster for saturating damage than for low damage, and that the position of binding is positively correlated with a longer accumulation time (i.e. formula (D.12) holds).

D.3.3 Residence time

When the repair system is saturated, the amount of immobilized and free factors does not change during a long time (as the binding and release of the factors is balanced). Thus, one can use the same method as for non-saturating conditions to calculate the residence times (Eq. (D.14)). The initial intermediary complex concentrations $S_i(0)$ and the free factor concentrations F_j are set by the condition $T_1 = I_1$. For a sequential irreversible binding ($k_{-i} \approx 0$) the residence times read

$$\rho_i = \frac{1}{k_R} + \sum_{j=i+1}^{n} \frac{1}{k_j F_j} \left(1 - \frac{I_j(0)}{I_i(0)}\right) \text{ and } \rho_n = \frac{1}{k_R}. \tag{D.21}$$

One has

$$\frac{1}{k_j F_j} \left(1 - \frac{I_j}{I_k}\right) < \frac{1}{k_j F_j} \left(1 - \frac{I_j}{I_i}\right) \tag{D.22}$$

when $I_i > I_k$, which occurs in the sequential pathway when $k > i$ (see Eq. 7.8). Using the above relation, one shows that

$$\rho_j < \rho_i \text{ for } j > i \tag{D.23}$$

holds. This means that early binding factors reside longer in the repair complex than late binding factors also for saturating conditions. For reversible binding, numerical calculations indicate that if the binding and dissociation rate constants are the same for all factors this hierarchy in the residence times (Eq. (D.17)) is conserved (data not shown).

To calculate the residence times in the alternative pathways where the first factor is released prior to the other factors (page 118), one proceeds in a similar way.

Appendix E

Data fitting

E.1 NER model including diffusion

The NER model is extended to include diffusion of the free factors and is used to simulate the data of the local UV-damage experiments and fit the model parameters to the accumulation curves of XPC-HR23B, TFIIH, and ERCC1-XPF. The model accounts for the spatial gradients that arise after application of a high UV dose to a local area of the nucleus.

The nuclear geometry is approximated by a cylinder with radius R_n. As shown in Fig. E.1, I assume that UV irradiation induces damages in a cylindrical volume of radius R_d, thus the system has axial symmetry and is described in cylinder coordinates. The concentration of the diffusible free factor at a distance r from the center is determined by

$$\frac{\partial F_i(r,t)}{\partial t} = k_R S_n + k_{-i} S_i - \tilde{k}_i F_i S_{i-1} + \frac{1}{r}\frac{\partial}{\partial r}\left(\tilde{D}_i r \frac{\partial F_i}{\partial r}\right),$$

where $\tilde{D}_i$ is the diffusion coefficient of the free i-th repair factor. For the intermediary complexes

$$\frac{\partial S_i(r,t)}{\partial t} = \tilde{k}_i F_i S_{i-1} - k_{-i} S_i - \tilde{k}_{i+1} F_{i+1} S_i + k_{-(i+1)} S_{i+1} \tag{E.1}$$

holds. Similar expressions for the free damage S_0 and the PC concentration (S_n) are used. At $t = 0$, DNA damage is induced instantaneously. The initial conditions are

$$S_0(r,0) = \begin{cases} D_T(0) & \text{for } 0 \leq r \leq R_d, \\ 0 & \text{for } R_d < r \leq R_n \end{cases} \tag{E.2}$$

$$S_i(r,0) = 0 \tag{E.3}$$

$$F_i(r,0) = T_i/\beta_i. \tag{E.4}$$

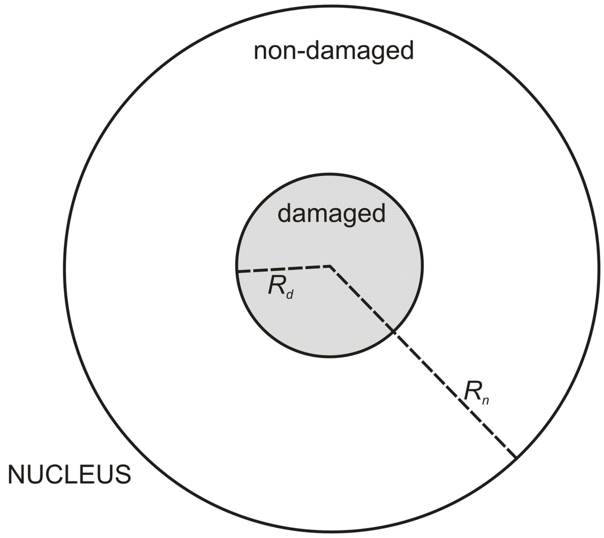

Figure E.1: Geometry used for NER model including diffusion. The nucleus is represented by a cylinder with radius R_n. A cylindrical volume with radius R_d is damaged.

Note that the presence of unspecific binding sites, $\beta_i > 1$, reduces the initial concentration of free factors available for repair (Eq. (E.4)).

In the presence of undamaged binding sites, the equation for the free factors is

$$\frac{\partial F_i(r,t)}{\partial t} = \frac{k_R}{\beta_i} S_n + \frac{k_{-i}}{\beta_i} S_i - \frac{\tilde{k}_i}{\beta_i} F_i S_{i-1} + \frac{1}{r}\frac{\partial}{\partial r}\left(\frac{\tilde{D}_i}{\beta_i} r \frac{\partial F_i}{\partial r}\right) \tag{E.5}$$

where a quasi-steady state approximation is used as in section C.1. This indicates a reduction of the diffusibility of F_i, which diffuses with an effective diffusion coefficient

$$D_i = \tilde{D}_i/\beta_i.$$

When DNA damage is uniform throughout the nucleus ($R_d = R_n$), as is the case in global damage experiments, the spatial gradients vanish ($\partial F_i/\partial r = 0$) and everywhere in the nucleus the conservation relation $T_i = F_i\beta_1 + I_1$ holds. In this case the model with diffusion reduces to the basic model (Eqs. (C.6)–(C.8)).

E.2 Immobile fraction

The parameters and confidence intervals were estimated using the initial accumulation curves of XPC-HR23B, TFIIH, and ERCC1-XPF. In experiments it is not possible to distinguish between freely diffusing factors and immobile factors (see Appendix D.1), so that the amount of immobilized factors involved in repair is approximated by taking the difference between total fluorescence in the damaged area and total fluorescence in an area of equal size outside the damaged region. In the model, this is accounted for by taking the difference M_i between the average concentration of factors in damaged and undamaged volume, that is (see Fig. E.1)

$$M_i = \frac{\int_0^{R_d}(F_i\beta_i + I_i)rdr}{R_d^2} - \frac{\int_{R_d}^{R_n}(F_i\beta_i)rdr}{R_n^2 - R_d^2}.$$

Accordingly, the observable fraction of immobilized factors is given by

$$Fr_i = \frac{M_i R_d^2}{T_i R_n^2}. \tag{E.6}$$

The binding rate constants were estimated by minimizing the sum of squares differences between simulations and data [125]

$$\chi^2 = \sum_i \sum_{j=1}^{N_i} \left[\frac{\overline{I}_i(t_{j,i}) - Fr_i(t_{j,i})}{\sigma_i(t_{j,i})} \right]^2 \tag{E.7}$$

where $i = 1$ (XPC-HR23B), 2 (TFIIH), 5 (ERCC1-XPF). In this formula, $\overline{I}_i(t_{j,i})$ and $\sigma_i(t_{j,i})$ are the observed averages and standard deviations of the immobilized fraction of the i-th factor at time points $t_{j,i}$, respectively. To get the value of Fr_i at the desired time points, Eqs. (E.1)–(E.5) are solved numerically on a regular spaced grid (see Appendix F). For minimization of χ^2, the non-linear curve fitting procedure `lsqnonlin` included in the package `matlab` was used (MathWorks Inc., Natick, MA).

For the distance between two grid points I used $\Delta r = 0.5$ μm, and for the time step $\Delta t = 2.77$ ms. Higher spatial or temporal resolutions did not increase the accuracy of the calculations. The radius of the nucleus is $R_n = 10$ μm. The ratio of damaged volume to total nuclear volume is $\gamma = V_d/V_n = R_d^2/R_n^2$. Thus, the radius of the damaged area is given by $R_d = R_n\sqrt{\gamma} = 3.77$ μM (in the experiments $\gamma \approx 1/7$).

Appendix F

Simulation of reaction-diffusion equations

F.1 Type of problems

A substance c diffuses in a medium with diffusion constant D. In one dimension or with cylindrical, or spherical symmetry, the equation describing the changes in concentration c is given by

$$\frac{\partial c}{\partial t} = D\frac{\partial^2 c}{\partial x^2} + D\frac{\alpha}{x}\frac{\partial c}{\partial x} + f(c) \tag{F.1}$$

with $\alpha = 0$, 1 or 2 for linear, cylindrical, or spherical coordinates, respectively. The term $f(c)$ incorporates all reactions in which c is involved. The boundary conditions at $x = l$ and $x = L$ are

$$-D\left.\frac{\partial c}{\partial x}\right|_{x=l} = J_l \tag{F.2}$$

$$-D\left.\frac{\partial c}{\partial x}\right|_{x=L} = J_L \tag{F.3}$$

Note that due to symmetry in cylindrical and spherical coordinates ($\alpha = 1, 2$) the flux is zero at the boundary $l = 0$. To solve this type of diffusion problems the space is subdivided in N equally spaced points (Fig. F.1). The distance between each grid points is Δx so that $N\Delta x = L$. The concentration at the grid point j situated at $x = \Delta x(j + 1/2)$ is denoted by c_j.

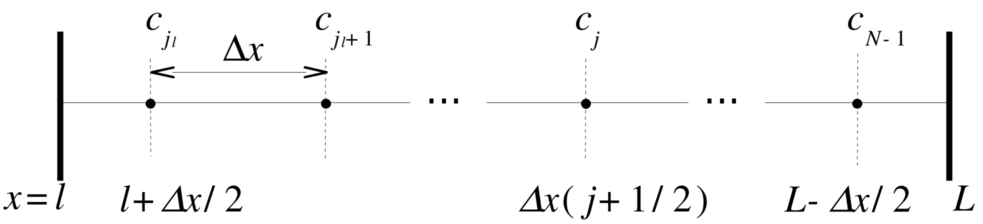

Figure F.1: Scheme of the lattice used for the numerical solution of Eq. (F.1). The first grid point, c_{j_l}, is at $\Delta x(j_l + 1/2) = l + \Delta x/2$, the last point c_{N-1} at $\Delta x(N-1/2) = L - \Delta x/2$, the j-th point at $\Delta x(j+1/2)$. The index varies between $j = j_l$ and $N-1$.

F.2 Difference scheme

F.2.1 Away from the boundaries

A Taylor expansion of the concentrations c_{j+1} and c_j $(N-1 > j > j_l)$, yields

$$c_{j+1} = c_j + \Delta x \left.\frac{\partial c}{\partial x}\right|_{\Delta x(j+1/2)} + \frac{(\Delta x)^2}{2}\left.\frac{\partial^2 c}{\partial x^2}\right|_{\Delta x(j+1/2)} + \frac{(\Delta x)^3}{6}\cdots + O((\Delta x)^4) \tag{F.4}$$

$$c_{j-1} = c_j - \Delta x \left.\frac{\partial c}{\partial x}\right|_{\Delta x(j+1/2)} + \frac{(\Delta x)^2}{2}\left.\frac{\partial^2 c}{\partial x^2}\right|_{\Delta x(j+1/2)} - \frac{(\Delta x)^3}{6}\cdots + O((\Delta x)^4) \tag{F.5}$$

The difference between the previous equations gives an approximation for the first derivative

$$\left.\frac{\partial c}{\partial x}\right|_{\Delta x(j+1/2)} = \frac{c_{j+1} - c_{j-1}}{2\Delta x} + O((\Delta x)^2) \tag{F.6}$$

The sum of Eq. (F.4) and (F.5) yields an approximation for the second derivative

$$\left.\frac{\partial^2 c}{\partial x^2}\right|_{\Delta x(j+1/2)} = \frac{c_{j+1} - 2c_j + c_{j-1}}{(\Delta x)^2} + O((\Delta x)^2) \tag{F.7}$$

F.2.2 At the boundaries

At the left-hand side boundary a Taylor expansion of the first space derivative at $x = l$ and $l + \Delta x$ yields

$$\left.\frac{\partial c}{\partial x}\right|_{l+\Delta x} = \left.\frac{\partial c}{\partial x}\right|_{l+\Delta x/2} + \frac{\Delta x}{2}\left.\frac{\partial^2 c}{\partial x^2}\right|_{l+\Delta x/2} + \frac{(\Delta x)^2}{8}\cdots + O((\Delta x)^3) \tag{F.8}$$

$$\left.\frac{\partial c}{\partial x}\right|_{l} = \left.\frac{\partial c}{\partial x}\right|_{l+\Delta x/2} - \frac{\Delta x}{2}\left.\frac{\partial^2 c}{\partial x^2}\right|_{l+\Delta x/2} + \frac{(\Delta x)^2}{8}\cdots - O((\Delta x)^3). \tag{F.9}$$

By summing the two equations one obtains

$$\left.\frac{\partial c}{\partial x}\right|_{l+\Delta x/2} = \frac{1}{2}\left(\left.\frac{\partial c}{\partial x}\right|_{l+\Delta x} + \left.\frac{\partial c}{\partial x}\right|_{l}\right) + O((\Delta x)^2). \tag{F.10}$$

With Eq. (F.2) and (F.6) the first derivative in space at the left boundary reads

$$\left.\frac{\partial c}{\partial x}\right|_{l+\Delta x/2} = \frac{c_{j_l+1} - c_{j_l}}{2\Delta x} - \frac{J_l}{2D\Delta x} + O((\Delta x)^2). \tag{F.11}$$

Taking the difference of Eq. (F.8) and (F.9) yields

$$\left.\frac{\partial^2 c}{\partial x^2}\right|_{l+\Delta x/2} = \frac{c_{j_l+1} - c_{j_l}}{(\Delta x)^2} + \frac{J_l}{D\Delta x} + O((\Delta x)^2). \tag{F.12}$$

Similarly, at the right boundary one derives for the first derivative

$$\left.\frac{\partial c}{\partial x}\right|_{L-\Delta x/2} = \frac{c_{N-1} - c_{N-2}}{2\Delta x} - \frac{J_N}{2D\Delta x} \tag{F.13}$$

and for the second derivative

$$\left.\frac{\partial^2 c}{\partial x^2}\right|_{L-\Delta x/2} = \frac{c_{N-2} - c_{N-1}}{(\Delta x)^2} - \frac{J_N}{D\Delta x}. \tag{F.14}$$

F.2.3 An explicit scheme

By taking a forward difference for the time derivative

$$\frac{\partial c}{\partial t} = \frac{c(t+\Delta t) - c(t)}{\Delta t} = \frac{c^* - c}{\Delta t}$$

one obtains at the left boundary

$$c^*_{j_l} = \left(1 - \nu\frac{2j_l + 1 + \alpha}{2j_l + 1}\right) c_{j_l} + \nu\frac{2j_l + 1 + \alpha}{2j_l + 1} c_{j_l+1} + \frac{\Delta t}{\Delta x}\frac{2j_l + 1 - \alpha}{2j_l + 1} J_l \tag{F.15}$$

where $\nu = D\Delta t/(\Delta x)^2$, away from the boundaries

$$c^*_j = \nu\frac{2j + 1 - \alpha}{2j + 1} c_{j-1} + (1 - 2\nu)c_j + \nu\frac{2j + 1 + \alpha}{2j + 1} c_{j+1} \tag{F.16}$$

and at the right boundary

$$c^*_{N-1} = \nu\frac{2N - 1 - \alpha}{2N - 1} c_{N-2} + \left(1 - \nu\frac{2N - 1 - \alpha}{2N - 1}\right) c_{N-1} - \frac{\Delta t}{\Delta x}\frac{2N - 1 + \alpha}{2N - 1} J_L \tag{F.17}$$

F.2.4 A mixed implicit-explicit scheme

The average of an implicit and explicit difference scheme gives a better numerical stability. One obtains

$$-\alpha_j c^*_{j-1} + \beta_j c^*_j - \gamma_j c^*_{j+1} = \delta_j \tag{F.18}$$

with

$$\begin{aligned}
\alpha_{j_l} &= 0\\
\beta_{j_l} &= 1 + \theta\nu\frac{2j_l+1+\alpha}{2j_l+1}\\
\gamma_{j_l} &= \theta\nu\frac{2j_l+1+\alpha}{2j_l+1}\\
\delta_{j_l} &= \left(1-(1-\theta)\nu\frac{2j_l+1+\alpha}{2j_l+1}\right)c_{j_l} + (1-\theta)\nu\frac{2j_l+1+\alpha}{2j_l+1}c_{j_l+1}\\
&\quad +\frac{\Delta t}{\Delta x}\frac{2j_l+1-\alpha}{2j_l+1}J_l
\end{aligned}$$

The averaging coefficient is $\theta \in [0,1]$, with $\theta = 0$ for the explicit scheme and $\theta = 1$ for a pure implicit scheme. Away from the boundaries ($N-1 > j > j_l$)

$$\begin{aligned}
\alpha_j &= \theta\nu\frac{2j+1-\alpha}{2j+1}\\
\beta_j &= 1+\theta 2\nu\\
\gamma_j &= \theta\nu\frac{2j+1+\alpha}{2j+1}\\
\delta_j &= (1-\theta)\nu\frac{2j+1-\alpha}{2j+1}c_{j-1} + (1-(1-\theta)2\nu)c_j\\
&\quad +(1-\theta)\nu\frac{2j+1+\alpha}{2j+1}c_{j+1}
\end{aligned}$$

and

$$\begin{aligned}
\alpha_{N-1} &= \theta\nu\frac{2N-1-\alpha}{2N-1}\\
\beta_{N-1} &= 1+\theta\nu\frac{2N-1-\alpha}{2N-1}\\
\gamma_{N-1} &= 0\\
\delta_j &= (1-\theta)\nu\frac{2N-1-\alpha}{2N-1}c_{N-2} + \left(1-(1-\theta)\nu\frac{2N-1-\alpha}{2N-1}\right)c_{N-1}\\
&\quad -\frac{\Delta t}{\Delta x}\frac{2N-1+\alpha}{2N-1}J_L
\end{aligned}$$

F.2.5 Accuracy and stability

The Crank-Nicolson scheme is when $\theta = 0.5$ in this case the numerical scheme is $(\Delta t)^2$ and $(\Delta x)^2$ accurate. Following stability conditions have to be fulfilled (derived for $\alpha = 0$)

$$\begin{aligned} &\text{when } 0 \leq \theta < 1/2, && \text{stable if and only if } \nu \leq \frac{1}{1-2\theta} \\ &\text{when } 1/2 \leq \theta \leq 1, && \text{stable for all } \nu \end{aligned}$$

Moreover, in order for the solution to be positive at all times (see [85])

$$\nu \leq \frac{1}{4}\frac{2-\theta}{(1-\theta)^2}. \tag{F.19}$$

This is a more severe condition than for stability. In particular, it should be applied if the initial conditions are not smooth. Depending on the problem higher values for ν can be chosen.

The previous stability conditions apply in the absence of reactions. In the presence of reactions the choice of Δt is also determined by their kinetics. In the absence of diffusion, the numerical scheme is a simple forward Euler. Take, for example, following degradation reaction

$$\frac{du}{dt} = -cu, \ \ c > 0.$$

Applying forward Euler one obtains

$$u^* = (1 - c\Delta t)u$$

This map is stable if $1 > 1 - c\Delta t > -1$, that is $\Delta t < 2/c$ and $c > 0$. Thus, when reactions are fast, ν needs possibly to be chosen lower than given in Eq. (F.19).

Abbreviations

IP_3	inositol 1,4,5-trisphosphate
IP_3R	inositol 1,4,5-trisphosphate receptor
IP_35P	inositol 1,4,5-trisphosphate 5-phosphatase
IP_33K	inositol 1,4,5-trisphosphate 3-kinase
PLC	phospholipase C
PI	phosphatidylinositol
PIP	phosphatidylinositol-4-phosphate
PIP_2	phosphatidylinositol-4,5-bisphosphate
DAG	1,2-diacylglycerol
SERCA	sarco endoplasmic reticulum Ca^{2+} ATPase
$[Ca^{2+}]_c$	Ca^{2+}concentration in the cytoplasm
PMCA	plasma membrane Ca^{2+} ATPase
CICR	calcium induced calcium release
XP	Xeroderma Pigmentosum
PC	pre-incision complex
ssDNA	single-stranded DNA
dsDNA	double-stranded DNA
bp	base pair

Acknowledgments

I would like to thank my doctor father Prof. Thomas Höfer who was a mentor and a friend able to create a nice and cooperative atmosphere in the group. I thank the support he brought to my project all the times I needed, and the freedom I had to move independently and work also on projects which, unfortunately, did not find a place inside this thesis. I thank Prof. Reinhart Heinrich, wherever his soul is at this moment, who was in a way my second doctor father and advised me in the DNA repair project. He left me the freedom to develop the project how I wanted to, but was always very passionate in discussing the results.

My sincere thanks go to my collaborators in the USA, Prof. Andrew Thomas and Prof. Lawrence Gaspers, who initiated the project on the IP$_3$ feedbacks and gave the decisive inputs in this work. They made the stays in Newark always very enjoyable and interesting. I thanks also the members of the Newark group, in particular, Dr. Fang Liu and Dr. Nicola Pierobon for the interesting discussions and help. The work on DNA repair would not have existed without Prof. Roel van Driel from Amsterdam. He, Dr. Martijn Moné, and Martijn Luijsterburg, were the driving force behind the project. I spend many days in Amsterdam together with Prof. R. Heinrich and it was always a very nice and productive time. The fun to work with both groups is the true reason for the presence of two so diverse topics in my thesis.

I would like to thank all the members of the theoretical biophysics group in Berlin for the relaxed atmosphere, in particular, I thank Dorothea Busse, Dr. Carlos Salazar, Jana Schütze, and Dr. Jana Wolf, for carefully proofreading large part of the thesis, Luca Mariani, for taking care of my well being in the last months of writing, and Bernd Binder, for his courses in ML.

My parents and my brothers, plus supplement, were always a great help even if I did not saw them very much. During the time I spent in Italy I was able to refill my Fellini batteries. I would like here also to thanks my friends, Michael, Katja, Dirk, Barbara, Felix, Luca, Marion, Ruth who were giving me the balance and the force.

Publications

A.Z. Politi, C. Salazar, T. Höfer. Decoding of calcium oscillations by phosphorylation cycles: analytic results. *Biophys. J.*, doi:10.1529/biophysj.107.113084, 2007.

A.Z. Politi, L.D. Gaspers, A.B. Brümmer, A.P. Thomas, and T. Höfer. Cellular calcium oscillations: from bifurcation analysis to experiment. In *Analysis and Control of Nonlinear Processes in Physics, Chemistry and Biology*, L. Schimanski-Geier et al. (eds.), world scientific lecture notes in complex systems Vol. 5, 2007.

A. Politi, L.D. Gaspers, A.P. Thomas, and T. Höfer. Model of IP_3 and calcium oscillations: frequency encoding and identification of underlying feedbacks. *Biophys. J.*, 90:3120-3133, 2006.

A. Politi, M.J. Moné, A.B. Houtsmuller, D. Hoogstraten, W. Wermeulen, R. Heinrich, and R. van Driel. Mathematical modeling of nucleotide excision repair reveals efficiency of sequential assembly strategies. *Mol. Cell*, 19:679-690, 2005.

A. Politi and T. Höfer. Modelling of periodic intercellular Ca^{2+} waves. In *Function and Regulation of Cellular Systems*, Birkhäuser-Verlag, pages 99-110, 2004.

C. Salazar, A. Politi, and T. Höfer. Decoding of calcium oscillations by phosphorylation cycles. Proceedings of the *Fourth International Workshop on Bioinformatics and Systems Biology*, p. 50-51, 2004.

T. Höfer, A. Politi, and R. Heinrich. Intercellular Ca^{2+} wave propagation through gap-junctional Ca^{2+} diffusion: a theoretical study. *Biophys. J.*, 80:75-87, 2001.

A. Politi. Modell für Kalziumoszillationen in durch *gap junctions* gekoppelten Zellen. *Humboldt Universität zu Berlin*, Diplom, 2000.

In preparation

L.D. Gaspers, P. Burnett, J. Johnston, A.Z. Politi, T. Höfer, S.K. Joseph and A.P. Thomas. Receptor-mediated $[Ca^{2+}]_i$ transients and intracellular $[Ca^{2+}]_i$ waves require Ca^{2+}-evoked $InsP_3$ oscillations (submitted).

S. Brune, A.Z. Politi, and T. Höfer. Regulation of mitochondrial calcium by calcium microdomains.

A.Z. Politi, P. Müller, and T. Höfer. Control of spatial gradients in phosphorylation cascades.

A.Z. Politi and T. Höfer. Positive feedback of Ca^{2+} on the IP_3 metabolism obviates for futile cycling: A mathematical model of the phosphoinositide pathway.

Selbständigkeitserklärung

Ich versichere hiermit, die vorliegende Arbeit selbständig und ausschließlich unter Verwendung der angegebenen Mittel und ohne unerlaubte Hilfen angefertigt zu haben.
Berlin, 26. November 2006
Antonio Politi